Faculteit
Bio-ingenieurswetenschappen

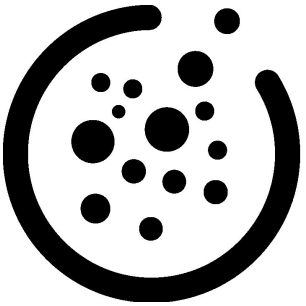

Academiejaar 2004 – 2005

Modelling the activated sludge flocculation process: a population balance approach

Modelleren van het actief-slib flocculatieproces: een populatiebalansbenadering

door
ir. INGMAR NOPENS

Thesis submitted in fulfillment of the requirements for the degree
of Doctor (Ph.D.) in Applied Biological Sciences

Proefschrift voorgedragen tot het bekomen van de graad van
Doctor in de Toegepaste Biologische Wetenschappen
Milieutechnologie

op gezag van
Rector: **Prof. Dr. ir. A. De Leenheer**

Decaan:
Prof. Dr. ir. H. Van Langenhove

Promotor:
Prof. Dr. ir. P.A. Vanrolleghem

ISBN 90-5989-067-1

voor Marleen

voor Jostin

en iedereen die mij dierbaar is

Copyright

Gent, May 2005

De promotor:

Prof. Dr. ir. Peter A. Vanrolleghem

De auteur:

ir. Ingmar Nopens

Dankwoord

In de eerste plaats wil ik uiteraard Peter, mijn promotor, bedanken zonder wie dit werk nooit mogelijk was geweest. Maar Peter is meer dan een promotor. Nooit ontmoette ik een persoon die zo gedreven is als hij. Een brok pure energie die er op een ongelofelijke manier in slaagt zijn energie over te dragen op andere mensen. Of dit allemaal het werk is van zijn dagelijkse portie koffie laat ik hier in het midden. Verder is Peter iemand die mensen de kans geeft zich ten volle te ontplooiien door hen de nodige bewegingsruimte te geven, zowel fysiek als wetenschappelijk. Naast het pure wetenschappelijke leerde ik ook veel bij met betrekking tot het 'managen' van een groep en het organiseren van evenementen. Ik heb dan ook geen minuut spijt gehad van mijn beslissing na mijn studie nog wat te blijven plakken aan de universiteit.

Een werk als een doktoraat tot een goed einde brengen wordt zeker ook bevorderd door de juiste atmosfeer waarin men dag in dag uit vertoeft. Hiervoor wil ik dan ook alle mensen van Biomath bedanken met wie ik de eer had samen te werken. Een individuele opsomming zou me hier veel te ver leiden. Wel wil ik het sociaal en multi-cultureel karakter van Biomath even in de verf zetten, wat aanleiding gaf tot het op een andere manier leren kennen van collega's. Hierbij denk ik aan de Biomath-fuiven, de Biomath-cocktails, Biomath-weekends, Biomath @ De Gentse Feesten, de gezellige bierintroductiecursussen voor niet-Belgen en zeker ook niet te vergeten het Biomatch-minivoetbalteam met zijn vele internationale transfers.

Op gebied van onderzoek wil ik enkele mensen extra bedanken voor hun aandeel in het succes van dit werk. Was het nu East of West, Jurgen en Dirk losten in sneltempo al mijn redelijk specifieke problemen op. Zin om je doctoraat in Latex te schrijven, dan staat Gaspard altijd paraat. Voor specifieke problemen in Matlab was Jo dan weer een helpende hand. Bedankt! *Furthermore, special thanks goes out to the thesis students I guided: Carlo, Koen, Thilo and Daan. Their efforts had a substantial positive impact on the booklet in front of you.*

Verder zijn er natuurlijk mensen die ondertussen Biomath reeds hebben verlaten. Klaas wil ik bedanken voor zijn onaflaatbare inzet bij het tot stand brengen van de succesvolle PBM-conferentie. Bloed, zweet en tranen spoelden we maar wat graag door met een Duvelke. Met Bob zijn we aanbeland bij de Sedifloc groep, een schoolvoorbeeld van een groepsinspanning om een kluif als het beter begrijpen van nabezinking vanuit verschillende hoeken te bekijken zonder in elkaars vaarwater te komen en elkaar perfect aan te vullen. Bob legde de basis hiervoor, zowel op financieel als wetenschappelijk gebied, waarvoor dank. *Special thanks also goes to Ruxandra and Griet, who put an enormous effort in conducting all experiments with the Flocunit, a tedious task resulting in a goldmine of data. Also Dave should be mentioned. I remember him from the in-depth discussions on every wastewater-related topic, the golf lesson and barbecue in Charlotte and his football skills. Also worth mentioning are my best Turkish friends*

Guclu and Gurkan with whom I spent several weekends in the simulation lab driven by science. Their hospitality is remarkable. Remember the Turkish night and the Tequila special.

During February-March-April 2004, I was honoured to be hosted by the group of Prof. Ramkrishna at Purdue University in famous office 'B5'. Apart from the scientific work I was also involved in lots of social activities. Special thanks goes to Rob and Eric, who introduced me into respectively American nightlife, the whereabouts of College basketball and disc-golf. For the scientific work, a huge thanks goes to Nandu alias Dr. Nere and of course Prof. Ramkrishna. In Lafayette as well as afterwards, they introduced me to the inverse world. Their efforts were of utmost importance for the success of this work. Thanks a lot! Thanks to Swati I now also know how a low-spiced Indian dish tastes like. I also won't forget the games basement over at Ramki's! Thank you all for your hospitality!

Verder wil ik uiteraard ook mijn familie en vrienden bedanken die me door de jaren heen hebben gesteund.

Mijn ouders verdienen een extra plaatsje in dit dankwoord. Zonder hen had ik nooit bereikt waar ik nu sta. Zij gaven mij de kans om mij educatief te ontplooiien. Zij hebben mij steeds gesteund, moreel en financieel, ook in de moeilijkere perioden en zijn ondanks alles altijd in mij blijven geloven. Woorden schieten hier tekort. Bedankt! Ik zal ook nooit vergeten hoe we samen de mobiele Flocunit in elkaar knutselden!

Tenslotte is er nog een speciaal iemand die ik uitzonderlijk wil bedanken: mijn allerliefste Marleentje. Zij gaf me de kracht en creëerde de ideale omgeving om een werk als dit uit te voeren. Ik wil haar bedanken voor haar geduld en het trotseren van eenzame momenten wanneer ik weer maar eens in het buitenland vertoefde (waaronder 2 verjaardagen). Bovendien gaf ze me het mooiste geschenk waar men (naast het behalen van een doctoraat) kan van dromen: ons zoontje Jostin. Ook hem wil ik danken om mij 's nachts wakker te houden zodat ik geen koffie nodig had om wakker te blijven bij het finaliseren van dit werk ;-))

Finaal wil ik ook nog iedereen danken die ik hier niet expliciet heb vermeld.

ir. Ingmar Nopens

Contents

CHAPTER 1

Introduction and objectives

To date, over *1.2 billion* people have no access to safe drinking water and over *2.4 billion* lack basic sanitation. The need to focus on this issue has been strongly affirmed by the World Summit on Sustainable Development that fixed clear targets for halving this dramatic situation by 2015. As a consequence, also the UN Commission on Sustainable Development has put Water Supply and Sanitation as two of the three priorities of work for 2004-2005.

The protection of our clean water resources, and the sustainability of our water systems as such, is one of the biggest challenges of the 21st century. Water is essential for most living organisms on this planet. However, the growth of the earth's population and industrialisation has increased the need for clean water enormously, putting a large pressure on our water resources. Apart from this, the environment is also exposed to a growing amount of (untreated) wastewater.

The European Union recognised this problem for the first time in the seventies and has, since then, introduced several water directives in its environmental policy. The most recent is the *EU Water Framework Directive* (Directive 2000/60/EC), which has among its goals 'water management based on river basins' and 'getting the citizens more involved' (EU, 2004). On the other side of the ocean, the US Environmental Protection Agency (EPA) adopted the National Pollution Discharge Elimination System (NPDES) as part of the clean water act (CWA) in the early seventies (EPA, 2004). In their latest regulation, the EPA requires states to develop prioritised lists of polluted or threatened water bodies and to establish the maximum amount of pollutant that a water body can receive while still meeting water quality standards, the so-called total maximum daily load (TMDL).

Today's municipal wastewater treatment is commonly achieved through the activated sludge process. This process consists of

1. mineralisation and conversion of the biodegradable components by a broad variety of microorganisms
2. separation of the grown activated sludge from the purified water

The efficiency of the entire process depends on the efficiency of both processes. The first, biological step has found considerable attention in research, which resulted in a sufficient understanding of the various biological processes and conversions that take place. This knowledge was translated into models which are able to describe this degradation process adequately (Henze et al., 1987, 1995; Gujer et al., 2000).

In the second step, the separation of the purified water from the activated sludge, biological degradation processes are less important even though they can not be fully neglected. More important for the final clarification are physical processes, mainly the floc formation (i.e. flocculation and deflocculation) and the gravitational settling of the flocs. The latter two processes are highly influenced by hydrodynamics and further by the shape and density of the flocs themselves. In practice the effectiveness of the clarification process suffers repeatedly from a poor settling ability of small particles which remain in the supernatant and deteriorate the effluent quality. Even though various studies of the activated sludge flocculation and settling characteristics have been performed during the last decades, a thorough understanding of the process and the external influencing factors is still missing.

In their study, Ekama et al. (1997) give an overview of the state-of-the-art of theory, modelling, design and operation of secondary settling tanks. They also provide a list of research needs. Many of these listed items were tackled in a large research project conducted at the Department of Applied Mathematics, Biometrics and Process Control (BIOMATH, Ghent University). This so-called SEDIFLOC project (acronym for Sedimentation and Flocculation) tried to gain better insight into activated sludge flocculation and its external influences (Govoreanu, 2004) and compile this knowledge into a flocculation model (using a population balance framework, i.e. the subject of this work) that can be incorporated into a 2D CFD-model describing the fluid dynamics and particle transport in a secondary settling tank (De Clercq, 2003). The final step of the project is to investigate how predictions of this calibrated model can be used to calibrate 1D sedimentation models (De Clercq, 'Modelling of batch and continuous settling', in preparation) on the basis of CFD simulation results obtained under process conditions specified by using the optimal experimental design technique in a virtual fashion (De Pauw, 'Optimal experimental design for calibration of bioprocess models: a validated software toolbox'). The project resulted in 5 PhD's (including this one). A summary of the project can be found in Fig. 1.1 where the black boxes represent the separate PhD studies.

Mathematical modelling can serve as a tool for improving process insight, process optimisation and process control. In this work, the problem of activated sludge flocculation is tackled by means of a population balance framework. This modelling framework allows to balance one or more properties of a population's individuals. It has been widely used in chemical engineering applications and to some extent in environmental applications (e.g. flocculation in drinking water production). However, very few researchers have tried to apply it to the activated sludge flocculation problem, mainly due to the difficulty of measuring the dynamics of the particle size distribution in an on-line way. Recent developments in measurement technology have opened a new research track that should enable us to explore at least some of the mysteries of the activated sludge flocculation process. The latter is needed to be able to optimise and control the separation and clarification process.

In this particular work, it will be investigated whether a population balance framework is appropriate for the description of the activated sludge flocculation process. This problem statement involves the analysis of several issues that will be treated in this dissertation. They are organised in a number of logical steps, which are summarised in Fig. 1.2 and briefly introduced below.

First, a thorough analysis and comprehension of the population balance framework is needed, which is the main subject of the literature review (Chapter 2).

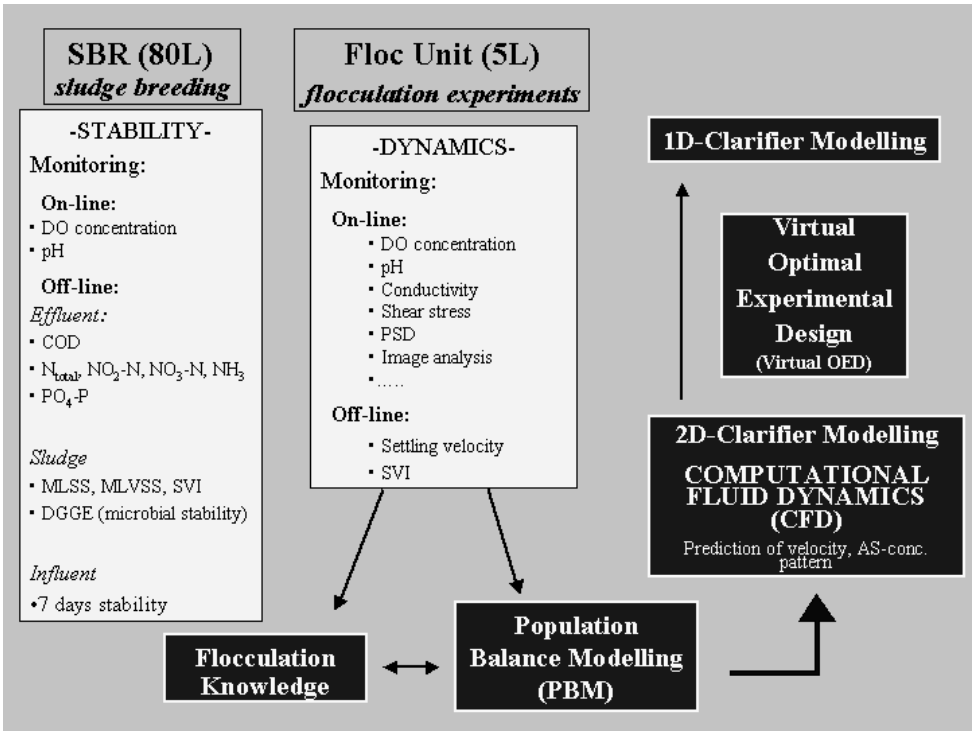

Figure 1.1: Overview of the Sedifloc project

Following this, the methods used throughout this work are described in Chapter 3. Among these methods, a fast, accurate and software compatible numerical solution method will be looked for. This is treated in Chapter 4 by means of a detailed simulation study of several specific solution methods selected from literature applied to simple model structures. It is tried to identify the pros and cons of each solution method and to spot possible pitfalls. One of the latter is studied in more detail in Chapter 5. It was the first time that such a detailed simulation study using a comprehensive set of degrees of freedom was conducted.

Once a numerical solution technique is available to work efficiently with the population balance model, the model should be confronted with reality, i.e. its parameters should be selected such that the model describes the experimental data well. For that, a calibration procedure is needed to fit the model to the experimental data that are produced from flocculation experiments. Such data are discussed in Chapter 6, where, for the first time in activated sludge flocculation modelling, focus lies on the distribution dynamics rather than summarising parameters such as the average floc size. The development of a comprehensive calibration methodology is focused on in Chapter 7, which treats several aspects related to calibration such as how to deal with experimental errors, possible data conversions that are needed for enabling compatibility between the experimental data and the model and the choice of the variable to which the model is fitted. Another novelty is introduced here, i.e. fitting on number distributions rather than on volume distributions.

Up to now, the model structure received little attention since it is not really important in the investigation of solution methods nor to develop a calibration strategy. However, at this stage of the research, it becomes of utmost importance. In the 'quest' for the correct model structure that can describe activated sludge flocculation, two different approaches were investigated. A first approach is treated in Chapter 8

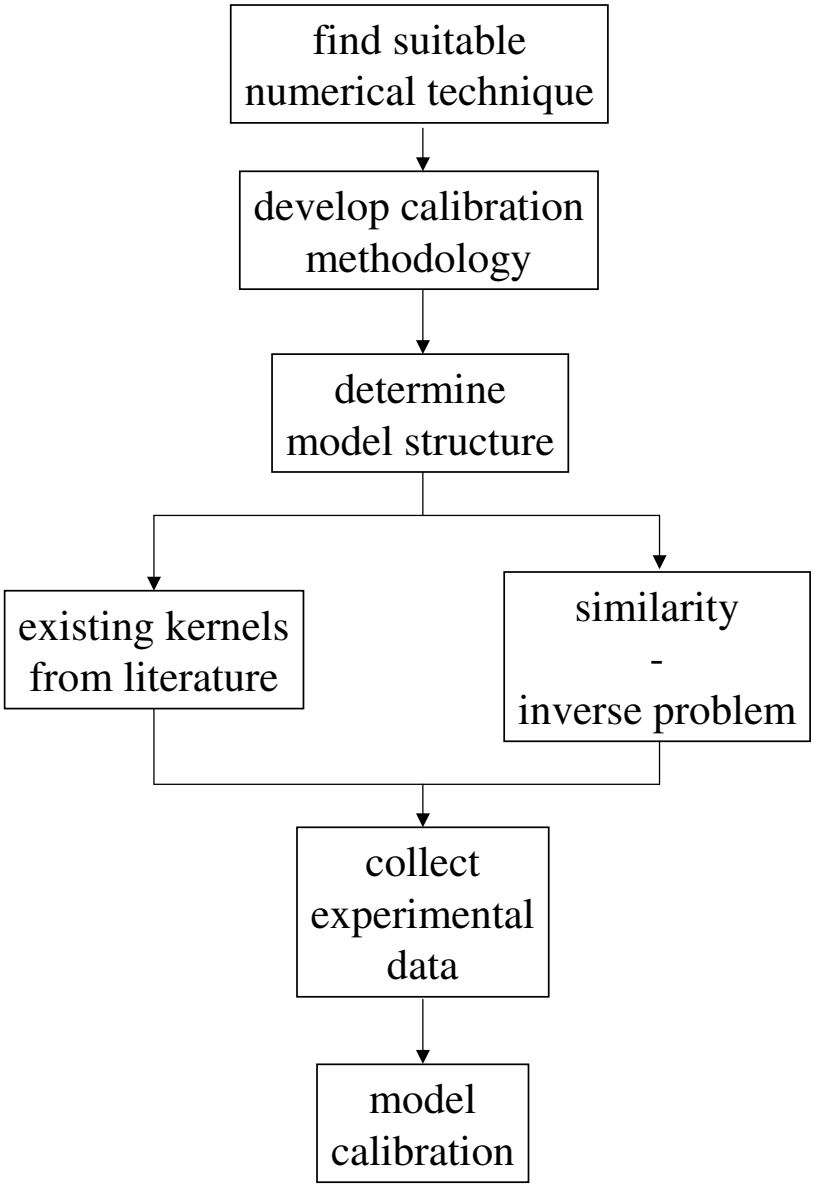

Figure 1.2: Schematic overview of the different steps for investigating the appropriateness of a population balance framework for describing the activated sludge flocculation process

and checks the applicability of several existing model structures that are available in literature. A second approach aims at recovering the model structure from the experimental data by means of a mathematical technique called inversion. As part of this second approach, a similarity analysis is recommended as it might reduce the complexity of the inverse problem solution. Therefore, this second approach starts with a similarity analysis which is the subject of Chapter 9. Finally, the inverse problem solution for both the aggregation and breakage case are treated in Chapter 11. The application of the inverse problem to experimental data is another new aspect of this dissertation, since this exercise has so far remained limited to a few cases in literature.

The most important findings of the dissertation and the perspectives for further research are synthesised in Chapter 12.

CHAPTER 2

Literature review

2.1 Introduction

This chapter gives an overview of the state-of-the-art literature concerning secondary settling in wastewater treatment and activated sludge flocculation. It starts with a brief introduction to biological wastewater treatment, thereby focusing on the secondary settling step. Next, the state-of-the-art findings with regard to activated sludge flocculation are discussed. The major part of this chapter deals with population balance models (PBMs), discussing the general framework, solution methods (in particular the discretisation techniques used in this work) and kernel structures. Also, two useful techniques for kernel structure determination are discussed: self-similarity and the inverse problem. Finally, some state-of-the-art sizing techniques that are available for on-line particle characterisation are briefly discussed.

2.2 Wastewater treatment

Wastewater collected from municipalities and communities must ultimately be returned to receiving waters, to the land or reused. Unit operations (physical treatment methods) and unit processes (chemical and biological methods) can be combined to reach a certain level of treatment. An overview of these levels is given in Table 2.1. Whereas conventional secondary treatment was the most common method of treatment up until the late 1980s, nutrient removal has become the standard nowadays (Tchobanoglous et al., 2003).

The secondary treatment, also called activated sludge process, was first introduced by Ardern and Lockett (1914). The wastewater is mixed with a consortium of microorganisms, which is responsible for the degradation of organic compounds and/or nutrients (depending on the process configuration) from the wastewater. Removal of Biochemical Oxygen Demand (BOD) and ammonium (nitrification) requires an aerobic tank. When nitrate removal (denitrification) is required, an anoxic tank or zone is required.

Table 2.1: Levels of wastewater treatment (from Tchobanoglous et al. (2003))

Treatment level	Description
Preliminary	Removal of wastewater constituents such as rags, sticks, floatables, grit, and grease that might cause maintenance or operational problems with the treatment operations, processes, and ancillary systems
Primary	Removal of a portion of the suspended solids and organic matter from the wastewater
Advanced primary	Enhanced removal of suspended solids and organic matter from the wastewater. Typically accomplished by chemical addition or filtration
Secondary	Removal of biodegradable organic matter (in solution or suspension) and suspended solids. Disinfection is also typically included in the definition of conventional secondary treatment
Secondary with nutrient removal	Removal of biodegradable organics, suspended solids and nutrients (nitrogen, phosphorus, or both)
Tertiary	Removal of residual suspended solids (after secondary treatment)
Advanced	Removal of dissolved and suspended materials remaining after normal biological treatment when required for various water reuse applications

Enhanced biological phosphorus removal also requires an anaerobic tank or zone.

The suspended solids (SS) can be removed gravitationally by means of a secondary settling tank (SST). The thickened sludge is partly recirculated to the secondary treatment (in order to retain biomass in the system) and partly wasted. Alternatively, membranes can be used to perform this separation. It has the advantage of yielding higher levels of removal, but produces more sludge and still is expensive.

The excess sludge that is produced and separated should then be disposed. This is typically done by incineration, disposal into landfills or reuse in e.g. agriculture. Due to higher constraints on these disposal methods, sludge treatment has become a new challenge in wastewater treatment. Therefore, prior to disposal, some steps might be incorporated into the process to reduce the sludge volume: thickening, dewatering, anaerobic digestion.

A schematic overview of the biological treatment process is given in Fig. 2.1.

2.3 The secondary settling tank

As mentioned before, the separation of the cleaned water from the biosolids is often obtained by gravitational settling in a SST. In this section, some aspects of SSTs and their relation to activated sludge flocculation are briefly discussed. For a more detailed and complete overview about theory, modelling, design and operation of SSTs, the reader is referred to Ekama et al. (1997).

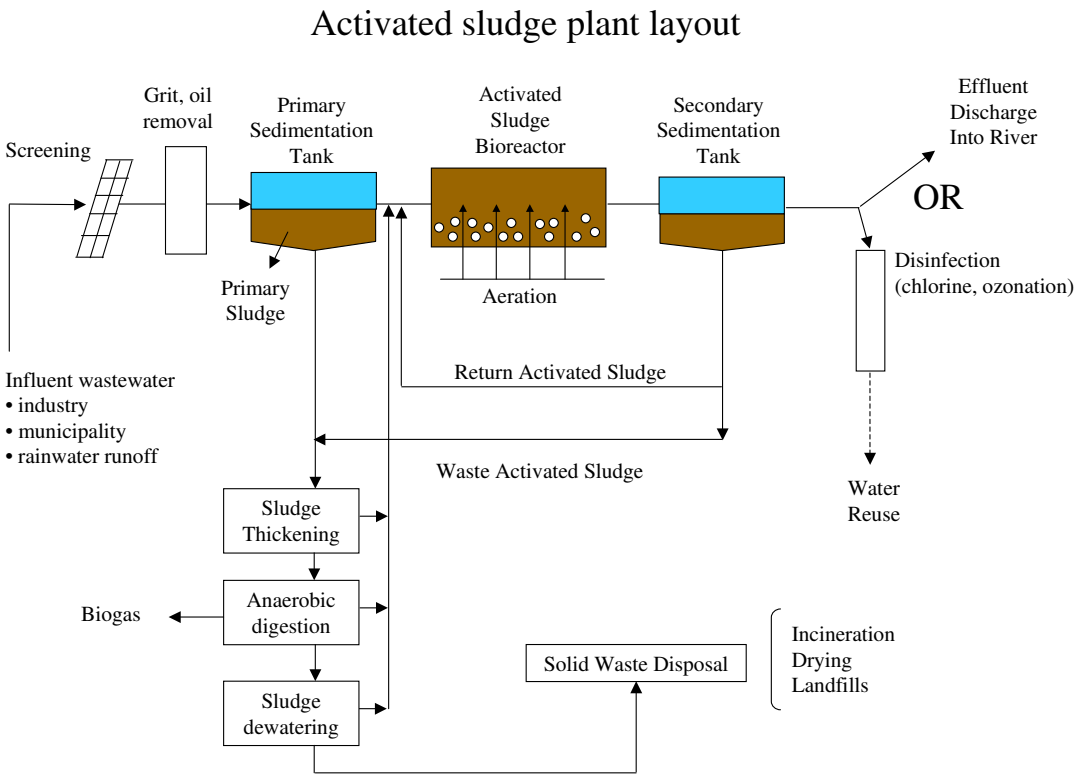

Figure 2.1: Overview of a biological wastewater treatment facility

2.3.1 Layout and working principle of the secondary settling tank

A schematic of a circular secondary clarifier is given in Fig. 2.2. The sludge, coming from the biological reactor, enters the SST through the centre feed inlet, after which it enters the flocculation or energy dissipation well, where baffles might be present to avoid short circuits. The hydrodynamics of the system forces the sludge to move downwards in order to exit the flocculation well and peripherally to reach the peripheral launder or weir. On its way to the launder, the sludge gets the opportunity to settle gravitationally and a sludge blanket is formed. The bottom of the tank is slightly tilted to guide the thickened sludge toward the sludge hopper, where it is removed. Often, this flow is also governed by means of a scraper attached to the bridge, which is moving around tangentially. If the SST works well, the sludge has settled by the time the fluid reaches the effluent launder and effluent with a small amount of suspended solids (effluent suspended solids - ESS) is removed from the system.

2.3.2 Functions of the secondary settling tank

The SST is a vital component of the activated sludge system. It combines the function of (1) a thickener to produce a continuous underflow of thickened sludge for return to the biological reactor, (2) a clarifier

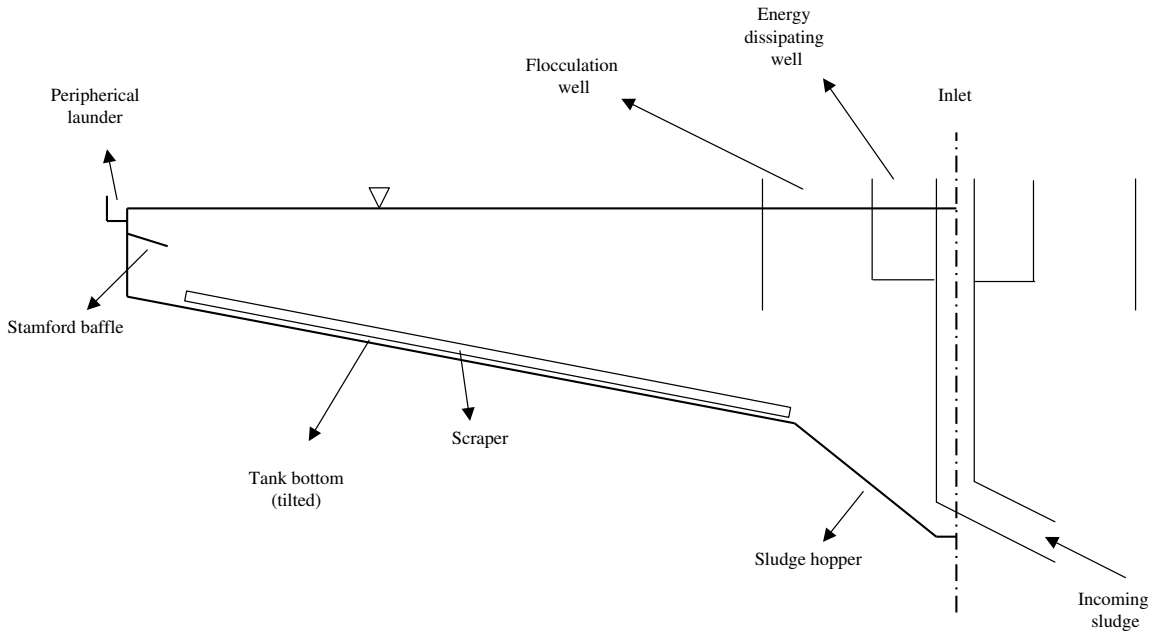

Figure 2.2: Schematic of a circular secondary clarifier

to produce a clarified final effluent and (3) a storage tank to store sludge during peak flows. Should the settling tank fail one of these three functions, SS will be carried over the effluent weirs and escape with the effluent. Besides delivering an effluent of poor quality, excessive loss of SS could affect the behaviour of the biological process by uncontrolled decrease in mixed liquor suspended solids (MLSS), and hence the sludge age, to values below that required for proper plant performance.

Whether or not the SST will successfully perform the aforementioned functions depends on its design features and its operation. The factors affecting these aspects can be grouped in: (1) hydraulic features, (2) physical features, (3) site conditions and (4) sludge characteristics. The latter factor, including settling, flocculation and thickening characteristics, is of great importance in the design phase and is directly affected by the conditions and configuration of the biological reactor(s). For example, under-aeration that might be wanted to create anaerobic or anoxic zones for nutrient removal, might lead to excessive growth of filamentous organisms deteriorating the settleability and the thickenability. Over-aeration, on the other hand, can lead to poor flocculation and pin-point floc formation. High shear zones (e.g. due to aeration or inlet design) might cause floc breakup and, therefore, poor clarification characteristics.

The thickening function is governed by the settleability and thickenability of the sludge and the solids concentration. It requires the majority of the sludge mass (over 98%) that enters the SST to be stored and eventually returned to the biological reactor. The extent of thickening determines the plant treatment *capacity*. The clarification extent determines the *performance* of the SST in terms of ESS. It is governed by the flocculation and settling characteristics of the sludge. Since both settleability and thickenability are dependent on sludge flocculation, the latter is very important for the SST to achieve good thickening and clarifying performances. Therefore, flocculation wells have been incorporated in the design of SSTs. The activated sludge flocculation will be more extensively discussed in section 2.4. First, some more details concerning sludge settling behaviour and SST modelling will be discussed.

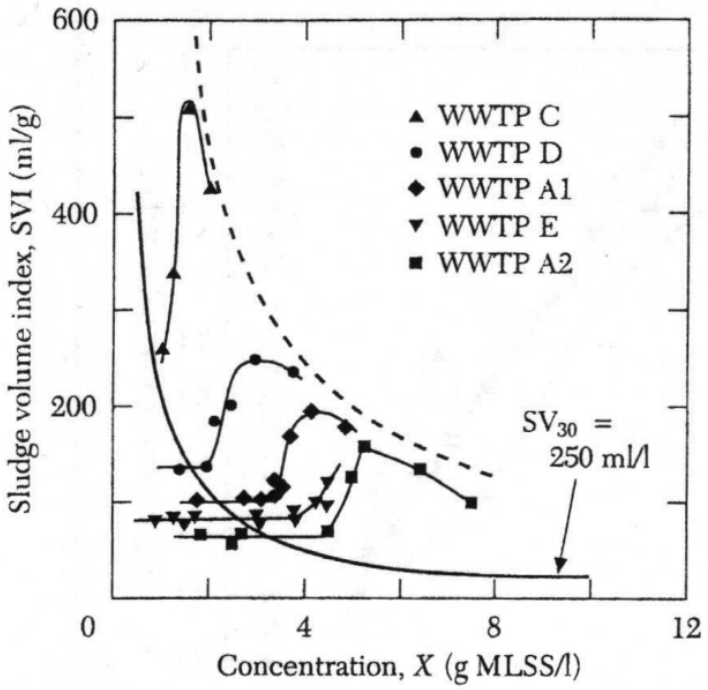

Figure 2.3: The SVI plotted against concentration for five sets of data from different WWTP (from Dick and Vesilind (1969))

2.3.3 Practical determination of the sludge settling behaviour

A widely used measure for sludge settleability (due to its simplicity) is the sludge volume index (SVI), which is defined as the volume in ml occupied by 1 g of activated sludge after settling for 30 min. Dick and Vesilind (1969) questioned the physical meaning and the validity of the SVI as settleability measure since two sludges with the same SVI can have completely different settling properties (SVI only presents 1 point on the settling curve). In search for its true meaning the same authors could not find a consistent relationship between the SVI and SS concentration (see Fig. 2.3), rheological characteristics and interface velocity. The increase in SVI-value at low sludge concentrations in Fig. 2.3 is due to failure of agglomeration, whereas the decrease is induced by the increasing sludge concentration. Moreover, the test is influenced by the cylinder diameter, initial depth, temperature and stirring, making it a doubtful measure for design. Several alternatives have been proposed throughout the past decades: diluted SVI (DSVI) (Stobbe, 1964), stirred SVI (SSVI) (White, 1975) and stirred specific volume index at fixed SS concentrations (e.g. $\mathrm{SSVI}_{3.5}$) (White, 1975). The first one was introduced to avoid the dependency on SS at high concentrations, whereas the second was introduced to better mimic reality since settling in a SST does not occur in a quiescent liquid and, moreover, to avoid wall effects in the (small) measuring cylinder. The third alternative aimed to avoid SS concentration dependency. Lee et al. (1983) found the diluted SVI to be the best index, when correlating with sludge filament content. However, more than 2 decades later, the SVI is still being used in practice, probably due to its simplicity.

An alternative approach for practical determination of the sludge settling behaviour is the solid flux theory, which is often used in the design and operation of SSTs. It involves setting up a solid flux curve, in which the solids flux (product of SS concentration and zone settling velocity [$\mathrm{V_{ZS}}$]) is plotted versus the SS concentration. $\mathrm{V_{ZS}}$ determination as function of SS concentration requires measurement

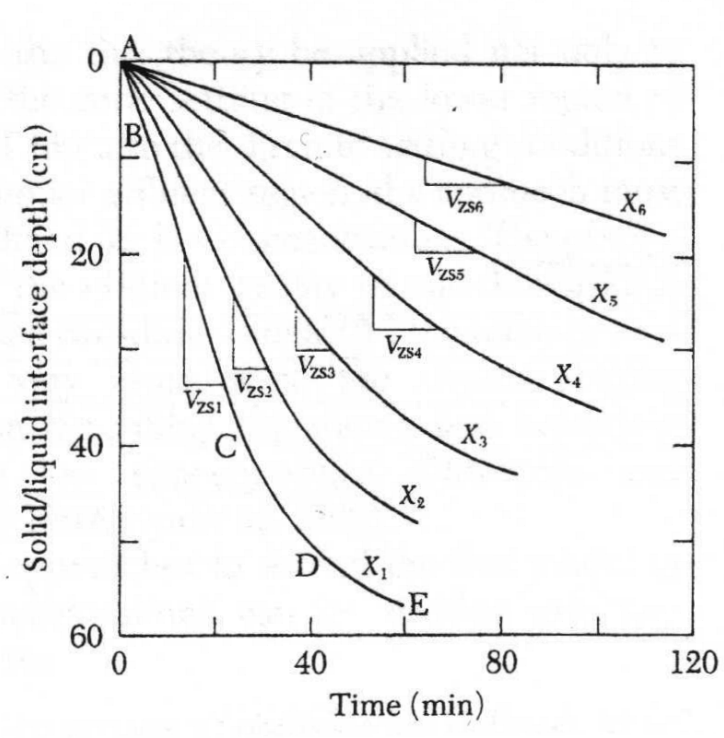

Figure 2.4: Solid-liquid interface height plotted against time. The slope of the straight line section gives the zone settling velocity (V_{ZS}), which decreases as concentration (X) increases (Vanrolleghem et al., 1996; Ekama et al., 1997).

of hindered settling curves at different SS concentrations (see Fig. 2.4), which can be automated using a Settlometer (Vanrolleghem et al., 1996).

Typically, the $V_{ZS}(X)$ curve is then fitted using the Vesilind equation

$$V_{ZS} = V_0 \, exp\,(-nX) \tag{2.1}$$

yielding values for parameters V_0 and n, which reflect the settling characteristics of the sludge. On the one hand, these values can be used for SST design. On the other hand, the flux curve can be used in a state point analysis (SPA) to determine whether the SST is either underloaded, critically loaded or overloaded (Ekama et al., 1997).

The major drawback of this method is its labour intensiveness compared to the SVI measurement (which is one point on one of the hindered settling curves of Fig. 2.4). Another drawback is the fact that hindered settling tests at high SS concentration have a long duration and might cause problems due to denitrification or flotation (Lee et al., 1983; Ekama et al., 1997). This is another reason why the simpler sludge settleability parameters SVI, DSVI or SSVI are preferred.

In literature, authors have tried to merge the benefits of flux theory analysis and the simplicity of SVI-type measurements by proposing relationships between SVI, DSVI and SSVI and the flux theory parameters V_0 and n. An extensive overview of such relationships can be found in Ekama et al. (1997). These relationships should, however, be used with caution since uncritical and ill-disciplined use of these kind of relationships can lead to serious errors (Ekama et al., 1997; Bye and Dold, 1998).

2.3.4 Practical determination of the sludge flocculation behaviour

The clarification function performed by activated sludge SSTs ensures a relatively solids-free effluent. In an SST where hydraulic flow currents do not impact effluent quality, the success of the clarification function depends on the extent to which the mixed liquor has been flocculated before settling and any additional flocculation that occurs during settling. Flocculation is necessary not only to produce flocs of sufficient mass to settle in the SST, but also to decrease the concentration of small, dispersed solids that do not have sufficient mass to settle in the SST. Ekama et al. (1997) give 3 mechanisms why these dispersed solids may exist: (1) they have not been incorporated into a floc particle owing to a surface chemistry reaction that prevents flocculation, (2) they have not been incorporated into a floc particle owing to insufficient time for flocculation to occur, or (3) they have been sheared from a floc particle owing to excessive turbulence in the mixed liquor transport system between the aeration system and the SST. The first mechanism can be caused by toxicants and/or chemical dispersants in the influent stream or by excessive chemical dosing to control bulking. The fact that flocculation takes time was shown by several authors (Wahlberg et al., 1994). It was proposed that at least 20 min of retention time are required in a flocculator to ensure completion of the flocculation. Das et al. (1993) reported that floc breakup is inversely related to the distance from surface aerators and that certain structures in mixed liquor transfer systems had deleterious effects on floc integrity.

Wahlberg et al. (1995) proposed a procedure for making the distinction between clarifier failing due to hydraulics or flocculation, the so-called DSS-FSS test. Dispersed suspended solids (DSS) are defined as those SS remaining in the supernatant after 30 min of settling, whereas flocculated suspended solids (FSS) are defined as those SS remaining in the supernatant after 30 min of settling preceded by 30 min of flocculation. Samples for DSS are taken near the inlet of the SST and the biological reactor outflow by using a Kemmerer sampler. The settling test is performed within the same apparatus to avoid changes in flocculation state due to sample transfer and, hence, measures the state of flocculation at the moment and location at which it was taken. Samples for FSS can be collected everywhere between the aeration basin and the SST and are taken by using a square flocculation jar equipped with a six-paddle stirrer. This test attempts to simulate the optimal degree to which the sample can be flocculated. The duration of 30 min was inspired by Wahlberg et al. (1994). The stirrer speed was chosen to be 50 rpm. In addition, the effluent is also analysed for SS (ESS). It is important that all three analysis (DSS, FSS an ESS) are performed at approximately the same time.

As to interpret the results, 4 scenarios are possible when a high ESS is measured:

1. *High DSS, low FSS* — This situation indicates either insufficient flocculation time or breakup due to some conveyor structure. In both cases, a flocculator should be incorporated (either before or in the SST).

2. *Low DSS, low FSS* — This situation indicates a hydraulic or a sludge blanket management problem. A means of handling this problem is to model the hydraulics with computational fluid dynamics (CFD).

3. *High DSS, high FSS* — This situation also indicates a flocculation problem, but not one that can be solved by additional flocculation. Most likely, it is of biological nature or the consequence of a chemical dispersant or toxicant in the plant influent.

4. *Low DSS, high FSS* — This situation is very unlikely to occur. If it does, repetition of the tests is recommended.

Table 2.2: Classification of separation problems (Wanner, 1994)

Type	Description
dispersed growth	no floc formation
pinpoint flocs	lots of small unsettleable flocs present
filamentous bulking	abundance of filamentous organisms
rising sludge	N_2-gas produced by denitrification causes sludge to rise
viscous bulking	overproduction of exocellular polymers (slime)
foam and scum	accumulation of biomass at the surface caused by non-degradable detergents or by specific filamentous organisms

2.3.5 Factors influencing the capacity and performance of the secondary settling tanks

The previous sections described how the capacity (settleability/thickening) and the performance (flocculation) of the SST can be determined for an existing plant or applied for the design of a new plant. In this section, the different influences on both capacity and performance are briefly highlighted. They can be categorised as biological, hydraulic or physical-chemical.

Biological influences

Activated sludge is grown in flocs of microorganisms, which interact with their environment. The presence of certain types of organisms is related to the operation and configuration of the treatment plant and the external environmental conditions. Changes in the latter (wanted or unwanted) can cause shifts in microbial community. In some cases, these shifts can affect the floc size and shape and, hence, their settleability. Some reported separation problems related to biological influences are summarised in Table 2.2.

Although some cause-effect relations exist, not all cases are completely understood. Dispersed growth and pinpoint flocs might be caused by low solids residence time (SRT), not allowing the flocs to form properly. Barbusinski and Koscielniak (1995) concluded that the organic loading rate (i.e. the amount of BOD_5 or chemical oxygen demand (COD) available per unit solids mass and time) and the availability of dissolved oxygen per unit of organic loading rate were the two most significant factors influencing the size distribution. Low organic loading resulted in smaller floc sizes. Filamentous bacteria grow faster than floc forming bacteria at low substrate concentrations, due to their higher surface-to-volume ratio. This is better known as the kinetic selection theory (Chudoba et al., 1973). Low oxygen concentration has also been shown to enhance growth of filamentous organisms (Wilén and Balmér, 1999). When the mixed liquor entering the SST contains appreciable amounts of NO_3, N_2-gas can be produced by denitrification (Henze et al., 1993), causing the sludge to rise due to increased buoyancy. Viscous bulking is caused by an overproduction of EPS. As to foaming, two species have been associated with foaming (*Nocardia* and *Microthrix Parvicella*). These organisms have hydrophobic cell surfaces and attach to air bubbles.

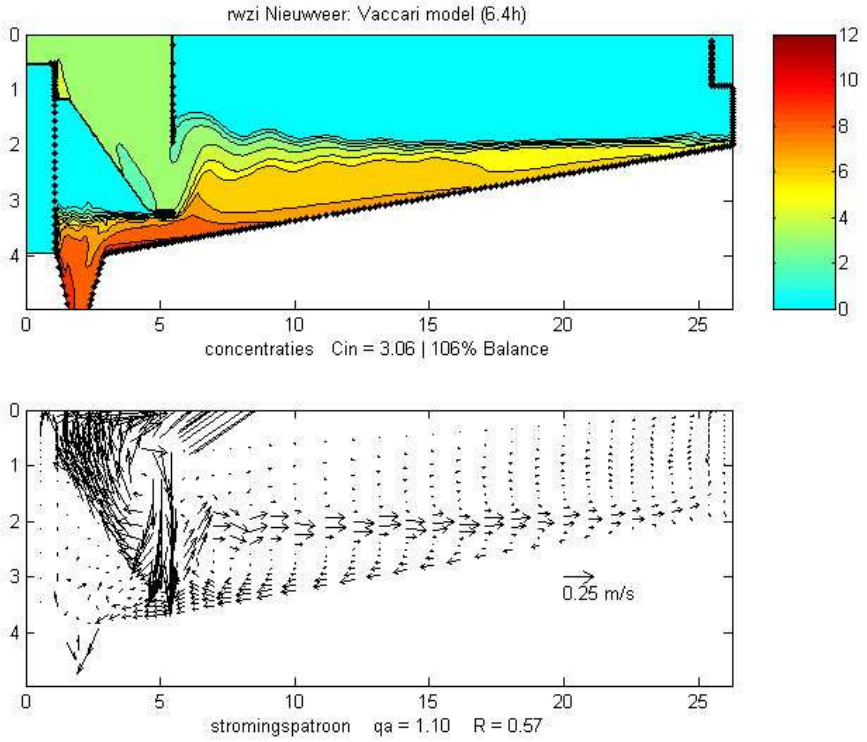

Figure 2.5: Illustration of a sludge concentration profile (top) and a fluid velocity profile (bottom) in a half cross-section of a circular secondary clarifier (from STOWa (2002))

Physical-chemical influences

Physical-chemical influences are mainly related to flocculation and will be thoroughly addressed in section 2.4.

Hydraulic influences

It is quite obvious that the flow field will influence both the (orthokinetic) flocculation and settling processes. The flow field in a SST is far from uniform due to the density stratification. The solids-loaded influent has a higher density than the ambient water and, hence, plunges as a density jet to the bottom of the tank. This is called the density current. This will induce a secondary countercurrent at the surface of the tank or even a multi-layer flow. This density current is characterised by high velocities and appears in the vicinity of the sludge blanket. Therefore, settled solids may be resuspended and can be transported to the effluent weirs, deteriorating the effluent quality. On the other hand, the density current might reduce short circuiting, which is beneficial. Temperature is another factor that might induce currents since it brings about changes in density. In order to improve the insight in the hydraulic behaviour, SSTs have been modelled using computational fluid dynamics (CFD). In the latter, the Navier-Stokes equations (continuity and momentum) are combined with a solids transport model and a settling model and are solved numerically in either 2 or 3 dimensions. This results in fluid velocity field and solids concentration profiles as shown in Fig. 2.5. These can be compared with experimental data (De Clercq, 2003).

2.4 Activated sludge flocculation

2.4.1 Activated sludge characteristics

In aquatic systems microorganisms commonly occur as flocs or biofilms (Marshall, 1981). This 'organisation' seems to bring advantages to the microorganisms such as enhanced nutrient supply or protection from shear forces (Fowler, 1988). Besides the microorganisms themselves, extracellular polymeric substances (EPS) have been found of great importance for the formation of dense flocs and biofilms, since they act as ion exchange compounds and attract ions and molecules. By use of EPS, microorganisms in flocs or biofilms can also establish close interactions with each other protecting them from dehydration (Liu and Fang, 2003).

Activated sludge flocs consist of a complex mixture of microorganisms, dead cells, particulate organic and inorganic material and EPS. The structure of the flocs is very heterogeneous and porous. The size ranges from a few to approximately 1000 μm (Li and Ganczarczyk, 1990, 1991). The organic matter within the floc varies from 60 % to 70 %. About half of the organic fraction is composed of EPS. The total chemical composition of the activated sludge flocs changes with wastewater composition and applied treatment. Floc formation and flocculation of activated sludge flocs is very complex and cannot be described by a single mechanism. The vast variety of organisms involved in activated sludge is one factor that contributes to the complexity of flocculation.

Microorganisms in activated sludge

Activated sludge is composed of a large variety of microorganisms. The major reason for this is the diversity of substrates in the wastewater it is exposed to. Over time, particular microbial species adapt to particular kinds of substrates. The microorganisms are in continuous competition for the substrate under given environmental conditions (pH, temperature, substrate concentration, oxygen supply,...). Moreover, phenomena like commensalism, parasitism and predation exist, leading to further diversity of the community.

Microorganisms in activated sludge can roughly be divided into two categories: floc forming species and filamentous species. The presence of filamentous microorganisms is closely related to the flocculation behaviour since they are believed to provide a network to which floc formers and microcolonies (small clusters of microorganisms) can attach. In this regard Parker et al. (1970) observed that activated sludge flocs containing filaments are stronger when they are subjected to shear and that the diameter is closely related to the size of the filaments. In contrast to this positive effect, it has been shown that excessive occurrence of filamentous bacteria results in poor settling flocs (filamentous bulking) (Wanner, 1994).

Exocellular polymeric substances (EPS)

EPS are extracellular biopolymers typically consisting of proteins, polysaccharides, humic compounds, nucleic acids, and lipids. The biopolymers form a matrix which encapsulates the microorganisms and aids in their aggregation and the floc formation (Wilén et al., 2003). Furthermore, EPS retains exoenzymes near the cell surface to bind organic matter. EPS is produced by the bacterial metabolism and lysis of microorganisms (Urbain et al., 1993). Andreadakis (1993) suggested that, in the case of low sludge age, EPS originates from substrate absorption and storage, whereas for high sludge ages this

would be due to decay of biomass. The total mass of EPS in a floc has been found to represent up to 80 % of the total floc mass. Wilén et al. (2003) investigated the relationship between activated sludge flocculation and the composition of the EPS and found a negative correlation between flocculation ability and amount of EPS. EPS contain hydrophobic sections and differently charged functional groups with high binding capacity for metals, particles and microorganisms (Urbain et al., 1993). This feature is certainly the main reason for the significant role of EPS in activated sludge flocculation although the distinct mechanisms are not yet fully understood.

Regarding the poor SVI values observed when high amounts of EPS are present, Mikkelsen and Keiding (2002) showed that an increase of EPS was related to an increased negative charge of the sludge flocs. The expected high electrostatic repulsion of highly negatively charged flocs would therefore deteriorate the settling behaviour of the flocs, which is also described by the DLVO theory (see section 2.4.2). Similar observations were made by other researchers (Wilén et al., 2003; Liao et al., 2001).

An in-depth discussion about EPS is beyond the scope of this literature review. A critical review about many aspects of EPS can be found in Liu and Fang (2003).

Bound water

Bound water (BW) in activated sludge flocs consists of three components based on different binding forces (Liao et al., 2000): *interstitial water* (water entrapped in the floc matrix), *vicinal water* (water held by surface forces), and *water of hydration* (water held by chemical bonds). It has been shown that poorer settling and dewatering properties of sludge are related to a larger BW content. Liao et al. (2000) found larger amounts of BW for smaller flocs. The total amount of EPS was positively correlated to the BW content on bench-scale, but no conclusive correlation was found in full-scale. The same authors also found a positive correlation between BW content and SVI. The BW is likely associated with EPS that form a complex matrix and large surface area that retains water (Liss et al., 1996). No correlation existed between BW and SRT nor surface charge.

Floc size and strength

Andreadakis (1993) reports a typical range of floc sizes between 10 μm and 70 μm for well mixed activated sludge systems. Other authors report a bimodal floc size distribution (Parker et al., 1970; Li and Ganczarczyk, 1991): flocs within the size range of 25 μm – 300 μm and primary particles (or bacterial cells) of about 0.5 μm - 5 μm (Li and Ganczarczyk, 1991; Jorand et al., 1995). Mikkelsen (2001) suggests the upper boundary for flocs to be around 1000 μm. Primary particles are regarded as colloids exhibiting different physical properties than flocs. Flocculation in these bimodal distributed systems is explained by adhesion of primary particles to floc surfaces whereas breakage is governed by erosion of primary particles from the floc surface due to shear (Parker et al., 1970). It is generally accepted that the average final floc size is due to a dynamic equilibrium between breakage and aggregation mechanisms (Lu and Spielman, 1984; Spicer and Pratsinis, 1996b; Mikkelsen, 2001). Both mechanisms depend on floc properties as well as external factors. They will be discussed in a later stage (sections 2.5.4 and 2.5.5).

With regard to floc strength, a maximum stable floc diameter ($\mathrm{d_{max}}$) has been suggested (Parker et al., 1970; Kusters, 1991; Dobias, 1993)

$$d_{max} = \frac{C}{G^n} \tag{2.2}$$

where C is the floc strength constant, n is the stable floc size exponent and G is the average velocity gradient given by

$$\bar{G} = \sqrt{\frac{\bar{\epsilon}}{\nu}} \tag{2.3}$$

with ϵ the energy dissipation rate and ν the kinematic viscosity. Parker et al. (1970) suggests that floc strength is governed by filamentous bacteria (functioning as floc backbone) due to their tensile strength. Kusters (1991) states that floc strength is proportional to the amount of particles and to different types of bonds between the particles within the activated sludge floc. Wilén et al. (2003) found a lower shear sensitivity (or higher floc strength) for sludges containing lower amounts of EPS.

Floc structure and density

Microphotographs of activated sludge flocs showed that microorganisms, water and EPS are irregularly dispersed within the floc (Li and Ganczarczyk, 1990; Jorand et al., 1995; Liss et al., 1996). The random occurrence of water channels and reservoirs of variable sizes in the floc clearly indicated that a uniform distribution of microorganisms did not exist. In their examinations of activated sludge flocs, Li and Ganczarczyk (1990) noted a general resemblance, in a statistical sense, under different magnifications. This self-similar property, as well as the lack of a characteristic size for water gaps, implies that the sections may be characterized by the fractal concept within a certain size range. The concept of the fractal dimension is based on the relation between the aggregate size and the aggregate mass (M). If the aggregate size is expressed by the radius of gyration $\mathrm{r_G}$, the fractal relationship is generally expressed by (Mandelbrot, 1987)

$$M \propto r_G^{D_f} \tag{2.4}$$

where $\mathrm{D_f}$ is the fractal dimension. The radius of gyration is the root-mean-square distance of the primary particles (that build up the floc) from their centre of mass or

$$r_G = \sqrt{\langle d^2 \rangle} = \sqrt{\frac{1}{N}\sum_{i=1}^{N} d_i^2} \tag{2.5}$$

with d_i the distance of a particle to the centre of mass. Note that this expression only holds for monodispersed primary particles.

For linear, planar, and three dimensionally compact objects, the exponent $\mathrm{D_f}$ in eq. 2.4 will have values of 1, 2 and 3 respectively, whereas for porous aggregates $\mathrm{D_f}$ may take a fractal value. In such cases, the exponent is known as the mass fractal dimension. More porous or open structures will have a smaller fractal dimension. If the relationship between mass and length is independent of the scale of observation the structure of the aggregate is described as being self-similar. This is illustrated in Fig.2.6.

The assumption of the fractal nature brings about two important practical consequences. First, the effective density of aggregates decreases as their size increases (Gregory, 1997) leading to a faster growth of aggregates and, hence, an increased collision probability, which is governed by an effectively larger volume fraction. This is beneficial for orthokinetic flocculation (flocculation mechanism based on velocity gradients, see section 2.4.4). Second, large and low density fractal aggregates settle slower than compact dense spheres due to their lower density and, moreover, are more susceptible for breakup. The former is also influenced by the permeability of the floc. Indeed, if water is able to penetrate the floc, the settling velocity will again increase due to a lower drag compared to an impermeable floc. Floc size and density are, therefore, very important factors with regard to the performance (large and less dense flocs

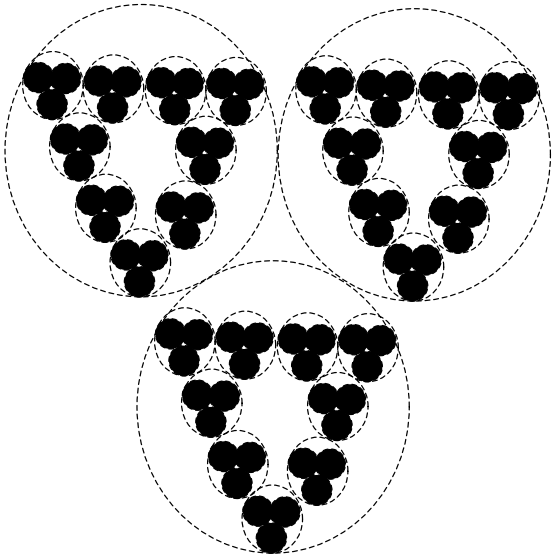

Figure 2.6: Two dimensional model of self similar aggregate structure (after Gregory (1997))

are beneficial) and the capacity of the SST (compact and dense flocs are beneficial) as was discussed before. It is clear that a compromise between these two factors should be found. It is difficult, however, to control the floc density in practice.

Several techniques are available to measure fractal dimension. An overview is given by Bushell et al. (2002). Guan et al. (1998) used small angle light scattering and predicted the fractal dimension for activated sludge to be in the range of 2.0 - 2.2, which is similar to the values reported by Li and Ganczarczyk (1989) who used image analysis. Gregory (1997) suggested that the fractal dimension of formed flocs also depends on the mechanism that leads to aggregation. When a single particle is added to a cluster, a more compact structure may be expected since a single particle is able to penetrate somewhat into the cluster before making contact. When two clusters encounter, a more open structure is likely, due to sterical hindrance. This is illustrated in Fig. 2.7. Furthermore, it has been observed that the fractal dimension of flocs increases with time. As a possible reason Clark and Flora (1991) suggest that breakup and reformation of the flocs in sheared suspensions lead to more compact structures. This has also been observed in latex particle systems (Selomulya et al., 2001).

2.4.2 Conceptual activated sludge flocculation models

Four conceptual models describing the activated sludge flocculation, i.e. the alginate theory, the polymer bridging model, the colloidal interaction model and the model of three structural levels are briefly introduced.

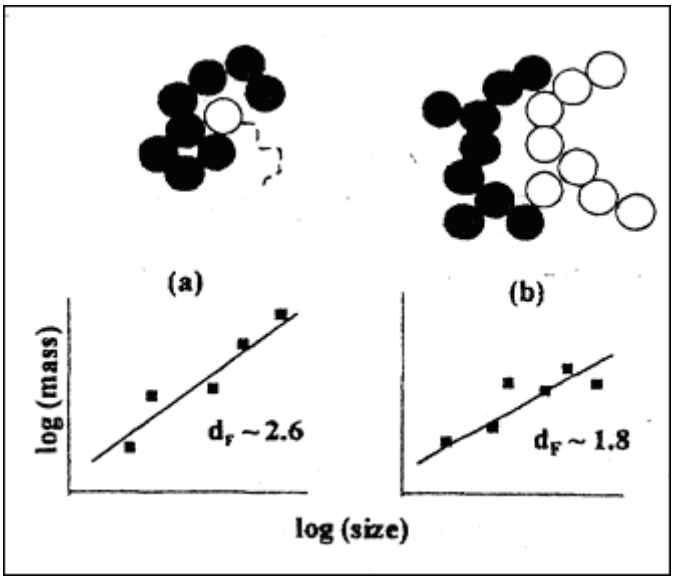

Figure 2.7: Illustration of aggregation mechanism dependency of the fractal dimension (from Gregory (1997))

The alginate theory

The alginate theory for the role of cations in the bioflocculation of activated sludge was first proposed by Bruus et al. (1992). Alginate is a polysaccharide produced by bacteria and is typically made up of repeating mannuronic and glucuronic acids. Its unique composition results in the formation of alginate gels in the presence of calcium ions. Sobeck and Higgins (2002) argued that this could not be the only mechanism present, since they found improved bioflocculation as well when adding magnesium ions, which is not supported by the alginate theory since the affinity of alginate toward magnesium ions is lower.

Polymer bridging model

The polymer bridging or divalent cation bridging (DCB) model, which is widely supported (Busch and Stumm, 1968; Sobeck and Higgins, 2002), stresses the role of divalent cations (e.g. $\mathrm{Ca}^{2+}, \mathrm{Mg}^{2+}$) in activated sludge flocculation. According to this theory, divalent cations bridge negatively charged functional groups present in the EPS matrix, thereby promoting the aggregation process and stabilising the matrix of polymer and microorganisms. The latter enhances bioflocculation. The DCB theory suggests a non specific binding of divalent cations rather than specific interactions (e.g. alginate theory) and also supports findings of deflocculation by addition of monovalent cations like Na^{+} (Sobeck and Higgins, 2002). Higgins and Novak (1997) proposed a monovalent to divalent cation ratio lower than 2 in order to avoid floc property deterioration. The conceptual model is illustrated in Fig.2.8.

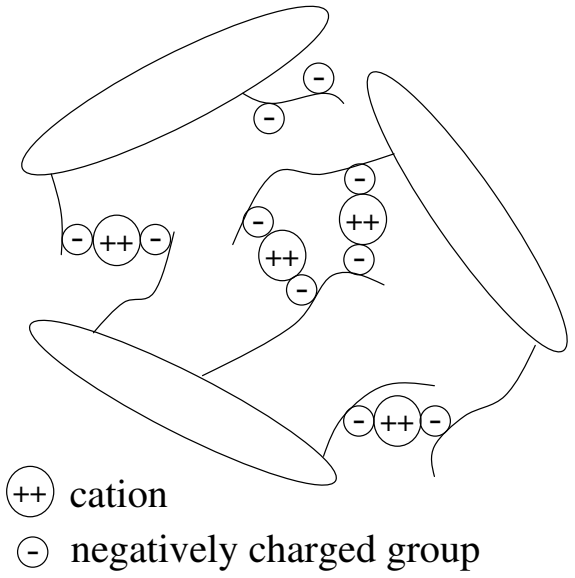

Figure 2.8: Illustration of the cation bridging concept (after Sobeck and Higgins (2002))

Colloidal interaction model

Zita and Hermansson (1994) suggested that bioflocculation can be explained by the colloidal interaction model, which assumes that interactions between particles can be described through the DLVO theory for colloidal stability, which has been used to explain interactions between colloids in general (Hiemenz and Rajagopalan, 1997; Verwey and Overbeek, 1948). Colloidal particles are in the size range of 1 nm to 1 μm. Colloids are non-settleable and are affected by Brownian motion.

The DLVO theory describes the interactions between particles according to their surface potential and the thickness of their electrical double layer. Based on the fact that most natural surfaces are negatively charged in aquatic systems, these surfaces are surrounded by oppositely charged ions. Some of these ions are bound to the surface, the stern layer, but most of them are located in a diffuse layer (Fig. 2.9). Therefore, if two equally charged objects approach one another, they experience *repulsive electrostatic forces*. The electrostatic repulsion is a function of the thickness of the double layer, which is inversely proportional to the ionic strength. Therefore, the electrostatic repulsion is reduced if the electrolyte concentration is high. Large amounts of divalent and trivalent ions also lead to an increase of the ion strength and a reduction of the particles surface potential.

A second short range interaction between colloids is the *van der Waals attraction*. The van der Waals force is a function of the separation distance, the geometry of the system and the Hamaker constant, which depends on the hydrophobicity of the concerned particles.

The DLVO theory defines a total so-called *Gibbs interaction energy*, summing the van der Waals attraction and electrostatic repulsion forces. This total interaction energy is a function of the separation distance of two particles (Fig. 2.10). When repulsion exceeds attraction, there is a potential energy barrier, which hinders contact between particles. For two particles to aggregate, this energy barrier must be overcome (e.g. through kinetic energy obtained by the flow) or lowered (e.g. by adding coagulant). Once the barrier has been overcome, the particles are strongly held in the deep primary minimum. It is

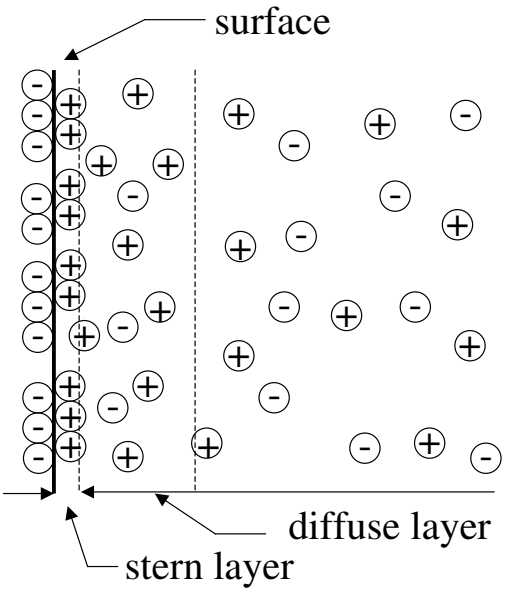

Figure 2.9: Illustration of the formation of an electrical double-layer

assumed that flocculation of activated sludge is due to attraction forces of the secondary minimum since sludge aggregates tend to deflocculate under turbulent conditions and at relatively low shear rates.

Sobeck and Higgins (2002) argue the validity of this theory since it suggests an improvement of the flocculation when monovalent cations are added (since this increases the ionic strength and, hence, decreases the thickness of the double layer). The latter is, however, not always observed in practice. The same authors state that the discrepancy between experimental studies to investigate the influence of cations on bioflocculation is governed by the different experimental set-ups that have been used to study the influence of cations on bioflocculation (i.e. batch versus continuous).

Model with three structural levels

This model, suggested by Jorand et al. (1995) on the basis of sonication experiments, describes an activated sludge floc population as being composed of three different structural levels: microflocs, which are primary particles, 2.5 μm in size (single bacteria); secondary particles of about 13 μm (microcolonies) which link together through exopolymers to, finally, form tertiary structures having a mean diameter of about 125 μm. Examining activated sludge from a wastewater treatment plant by transmission electron microscopy the authors predicted a fractal dimension for the primary particles of about 3, whereas that of the third level was found to be in the range 2.4 - 2.6. An illustration of a simplified activated sludge floc is given in Fig.2.11.

2.4.3 Influencing factors on floc size and structure

As mentioned before the average final floc size and in particular the particle size distribution (PSD) is determined by a dynamic steady state between aggregation and breakup processes. These processes are

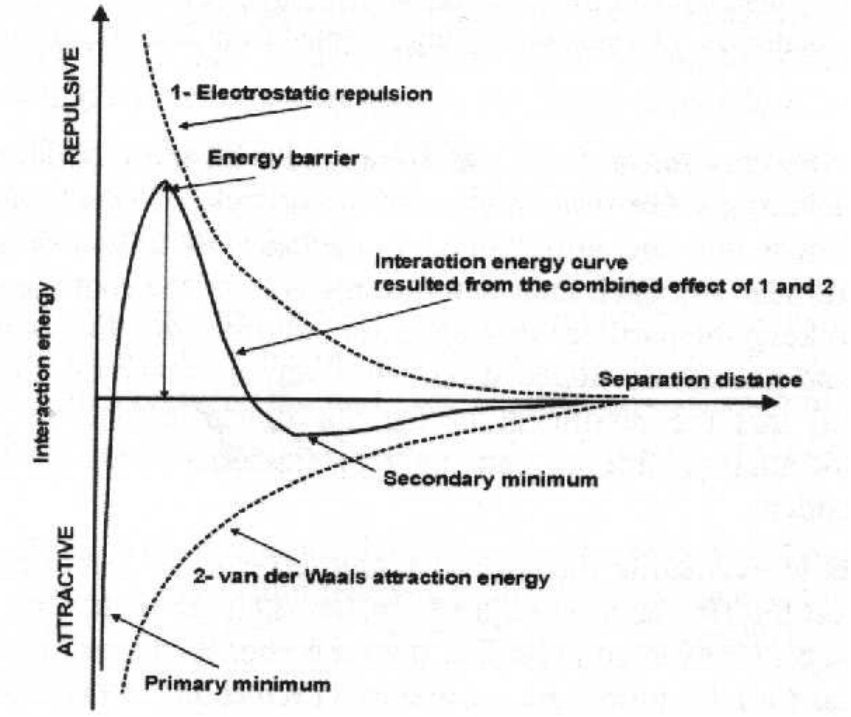

Figure 2.10: Interaction energy between two particles as a function of separation distance according to the DLVO theory

dependent on the actual shear force, induced by mixing, various properties of the fluid and properties of the activated sludge. Often diverse influencing factors of floc size and structure are closely related and hard to distinguish.

Mixing

Mixing is important for the formation and breakup of activated sludge flocs. A certain degree of shear rate is necessary to provoke collisions between particles and, hence, to provide kinetic energy to overcome repulsive forces between approaching flocs allowing them to aggregate. With regard to the floc breakup, mixing imposes shear stresses on the floc surface which are larger than the floc's resistance to stress (floc strength). Breakup of flocs can be of two kinds: erosion of small primary particles from the floc surface and floc rupture in two or more smaller flocs (Parker et al., 1970). Erosion is likely to happen when the shear forces exceed the strength of the bond between the primary particles and the floc. At higher shear forces, floc rupture is more likely. Mikkelsen and Keiding (2002) argued that floc erosion is more common in wastewater treatment plants than floc rupture because the EPS within the flocs is very much cross-linked requiring high forces to break the flocs. Eq. 2.2 has been proposed to express a maximum stable floc diameter as a function of experienced surface shear stress and shear strength or simply the shear stress only (Parker et al., 1970; Tambo and Watanabe, 1979; Tambo and Hozumi, 1979). A more detailed description of aggregation and breakage and how they are translated into models will be given later (sections 2.5.4 and 2.5.5). A study by Clark and Flora (1991) revealed that different mixing strategies lead to differences in the final floc structure and density. The authors included a period of high mixing during a flocculation experiment at low mixing intensity and observed higher densities

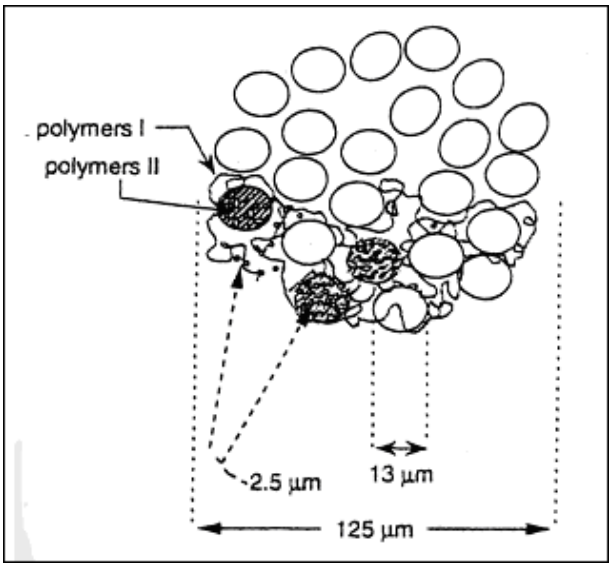

Figure 2.11: Simplified activated sludge floc (from Jorand et al. (1995))

and fractal dimensions compared to the standard (low) mixing conditions. A clear correlation between mixing intensity and floc size was found by Biggs and Lant (2000) and Govoreanu (2004). Both studies used on-line laser diffraction to follow the floc size distribution in time and used the mass mean average diameter at steady state to obtain the correlation. Govoreanu (2004) concluded from a Response Surface Model (RSM), summarising her extensive experimental data set that the mixing intensity should be lower than $15\,\mathrm{s}^{-1}$, i.e. the lowest mixing intensity used in the study, in order to maximise the mass mean average floc size and to minimise the SVI.

Sludge age

It has been observed by various researchers that the floc size increases with higher sludge ages (Knocke and Zentkovitch, 1986; Jiwani et al., 1997; Andreadakis, 1993). The latter authors studied the morphology of activated sludge flocs for different operation modes of an activated sludge pilot plant. They observed that relatively small flocs were obtained at short HRTs (hydraulic retention times) (less than 10 hours) and for sludge ages less than 8 days; larger flocs were obtained when increasing both parameters. Moreover, lower levels of turbidity were measured in the effluent. A possible explanation could be a higher accumulation of EPS in the flocs with higher sludge age (Keiding and Nielsen, 1997) or a more firm linkage between older flocs, which makes them less susceptible to shear (Eriksson et al., 1992). Samimi et al. (2003), however, did not find a strong correlation between total EPS and sludge age. They suggest that the change in ESS (or supernatant turbidity) is related to the surface properties of the flocs (i.e. hydrophobicity and surface charge), which is governed by the EPS composition and not by the level of EPS.

Organic loading rate

While investigating variations in the operation of the activated sludge process, Li and Ganczarczyk (1993) found that at high organic loading rates the number of primary particles ($< 2\,\mu\mathrm{m}$) increased significantly. A possible explanation for this might be a stimulated growth of dispersed bacteria in the bulk water. Barbusinski and Koscielniak (1995) performed a detailed study on the influence of organic loading rate on the size of activated sludge flocs. They observed a direct proportionality between floc size and changes of organic loading rate in the range of 0.17 - 1.8 $\mathrm{kg\,COD.kg\,MLSS^{-1}.d^{-1}}$: average floc size increased with increasing loadings and floc size distributions shifted to larger size ranges. When the organic loading rate exceeded 0.5 $\mathrm{kg\,COD.kg\,MLSS^{-1}.d^{-1}}$, a rapid increase of filamentous bacteria appeared. This might be due to a reduction of the DO concentration at high organic loading rates which favours filamentous bacteria (Sezgin et al., 1978). In all experiments it was found that the floc size curves for increasing and decreasing organic loading rate were not the same but revealed a significant hysteresis effect. The final floc size was larger than the initial floc size at equal low organic loading rates. However, this effect became smaller when the gradual change in organic loading rate was performed faster.

Ionic strength

As explained by the DLVO theory, low ionic strength can cause deflocculation, since it weakens the floc strength. Zita and Hermansson (1994) studied the influence of ionic strength on the overall floc strength. As evidenced by a lower turbidity, they observed an increasing floc strength with increasing electrolyte concentration. The researchers explained this through the DLVO theory. If the ionic strength was increased beyond 0.1 M, the floc stability diminished again. A proper explanation for the latter has not been given yet. Govoreanu (2004) also found a relationship between increased ionic strength (in terms of $\mathrm{Ca^{2+}}$) and floc strength by proving that the mass mean average floc diameter could still be increased at high mixing intensities when $\mathrm{Ca^{2+}}$ was added. Cousin and Ganczarczyk (1998) showed that, as a result of physicochemical effects, increased sodium ion concentrations significantly affected both floc size and their internal structure. Mean floc size was found to increase linearly with NaCl addition. In some experiments, increased NaCl concentrations resulted in an increase of the floc porosity, indicating a change in physical structure of individual flocs. This is in disagreement with the findings of others (Higgins and Novak, 1997; Sobeck and Higgins, 2002) who found different effects for the addition of monovalent (e.g. $\mathrm{Na^{+}, K^{+}}$) and divalent (e.g. $\mathrm{Ca^{2+}, Mg^{2+}}$) cations. They state that the monovalent to divalent ratio is more important than the total ionic strength. This ratio should be lower than 2 to avoid deterioration of the floc structure and, hence, deflocculation. Biggs and Lant (2000) observed an increase in mass mean average diameter with increasing concentrations of $\mathrm{Ca^{2+}}$. Govoreanu (2004) confirmed these findings and found that the optimal $\mathrm{Ca^{2+}}$-addition is in the range of 14-18 $\mathrm{meq.l^{-1}}$. However, it was postulated that this is highly dependent on the initial $\mathrm{Ca^{2+}}$-content of the sludge.

Temperature

Temperature affects the physical properties (e.g. viscosity, structure of EPS) and the biological properties (nature and rate of metabolism) of activated sludge. Higher temperatures lead to increased deflocculation (Sürücü and Cetin, 1989; Morgan-Sagastume and Allen, 2003; Govoreanu, 2004). Increased amounts of suspended solids in the effluent were observed when the temperature was increased from 15 to 25 °C. Further increase of the temperature up to 35 °C led to an even higher concentration of suspended solids. Govoreanu (2004) observed larger mass mean average floc sizes at lower temperatures and proposed an

optimal temperature of 7-8 °C based on an optimisation using a response surface model (RSM).

Dissolved oxygen concentration

Li and Ganczarczyk (1993) concluded from their studies that the DO-concentration and the organic loading, as very closely related parameters, are the two most significant factors determining the size distribution of activated sludge flocs. Sürücü and Cetin (1989) found that, on average, activated sludge flocs were larger at DO concentrations of 2 - 5 $\mathrm{mg.l^{-1}}$ than they were at DO concentrations of 0.5 - 1.5 $\mathrm{mg.l^{-1}}$. Starkey and Karr (1984) found deterioration in effluent turbidity when DO levels were decreased. They reported two causes: decrease in EPS production reducing the adsorptive capacity of the sludge and washout of protozoa, which are believed to graze bacteria and other colloids. Wilén and Balmér (1999) investigated the influence of DO on the structure, size and size distribution. At high DO concentrations, more compact flocs were found. No clear correlation between DO concentration and floc size was found. 80% of the particles in the supernatant were found to be smaller than 2 $\mu\mathrm{m}$. With regard to supernatant turbidity, similar results were found by Starkey and Karr (1984). Wilén et al. (2000) found that deflocculation due to anaerobic conditions is irreversible to a certain extent, which is most likely due to changes in microbial activity. All mentioned studies focused on long-term effects (order of magnitude of days). Govoreanu (2004) studied short-term DO-effects and concluded that they were absent.

Combined effect of influencing factors

Govoreanu (2004) was the first to investigate the combined effect of 5 influencing factors on activated sludge flocculation simultaneously: mixing intensity (G), dissolved oxygen concentration (DO), temperature (T), calcium addition ($\mathrm{Ca^{2+}}$) and sludge concentration (X). Seven so-called response variables (R) were evaluated: floc size (D[4,3]), SVI, zeta potential (zeta), turbidity (turb), supernatant suspended solids (TSS), conductivity (cond) and pH. In a first approach the functionality between separate response variables (one by one) and all factors were investigated separately using a quadratic response surface model (RSM). The latter is defined as a pure statistical model (not knowledge based) that is obtained through multivariate (more than one measured variable) non-linear regression. Such a model considers both linear, quadratic and interaction terms. Since all responses were measured before and after the different factor values were applied, two criteria were used for the response variables:

1. the difference between the initial and steady state response variable, $\Delta\,\mathrm{R} = \mathrm{R_{ss}} - \mathrm{R_{init}}$
2. the steady state response variable, $\mathrm{R_{ss}}$

From the derived models optimal factorial points were derived by optimising the respective response variable. The findings are summarised in Table 2.3. Here, the different criteria that were tested are listed, along with their target, which is either minimisation (min), or maximisation (max) (taking into account the physical boundaries), and whether the influencing factors either have a positive (+), negative (-) or negligible (0) effect.

In a second approach the model was optimised using a combination of target values for the different responses. Since a conductivity target is hard to define and pH had little influence, only 5 response variables were retained. D[4,3] was targeted at 1800 $\mu\mathrm{m}$ and SVI at 40 $\mathrm{ml.g^{-1}}$. Zeta potential, turbidity and TSS were all targeted at 0. The optimisation resulted in the following optimal conditions: T=

Table 2.3: Summarising results from the optimisations using response surface models (from Govoreanu (2004)). +,- and 0 means that the factor has a positive, negative or negligible effect respectively.

criterion	goal	G	DO	X	Ca^{2+}	T
Δ D[4, 3]	max	-	0	+	0	-
$D[4,3]_{ss}$	max	-	0	+	+	-
Δ SVI	min	-	0	+	0	-
SVI_{ss}	min	-	0	+	+	-
Δ zeta	max	not reliable				
$zeta_{ss}$	min	not reliable				
Δ turb	min	-	+	0	0	0
$turb_{ss}$	min	-	+	0	0	0
Δ TSS	min	+/-	0	0	-/+	0
TSS_{ss}	min	not reliable				
Δ cond	max	0	0	-	+	+
$cond_{ss}$	max	0	0	-	+	+
Δ pH	0	no effect observed				
pH_{ss}	0	no effect observed				

17.6 °C G = 15 s^{-1} (i.e. the minimum value tested), Ca^{2+} = 14.09 $meq.l^{-1}$, DO = 0.99 $mg.l^{-1}$ and X = 3.29 $g.l^{-1}$. Some of the experimental results are discussed in more detail in chapter 6.

2.4.4 Mathematical modelling of activated sludge flocculation

The mathematical representation of flocculation, i.e. the process whereby destabilised suspended particles are aggregated, has conventionally been based on considering the process as two discrete steps: transport and attachment (Thomas et al., 1999). The transport step, leading to the collision of two particles, is achieved by virtue of local variations in fluid/particle velocities arising through

- the random thermal 'Brownian' motion of particles (*perikinetic flocculation*)
- imposed velocity gradients from mixing (*orthokinetic flocculation*)
- differences in settling velocities of individual particles (*differential sedimentation*)

This is illustrated in Fig. 2.12. Attachment is dependent upon a number of short range forces largely pertaining to the nature of the surfaces themselves. These two concepts can be expressed mathematically as a rate of successful collision:

$$rate\,of\,flocculation = \alpha\beta(i,j)n_i n_j \tag{2.6}$$

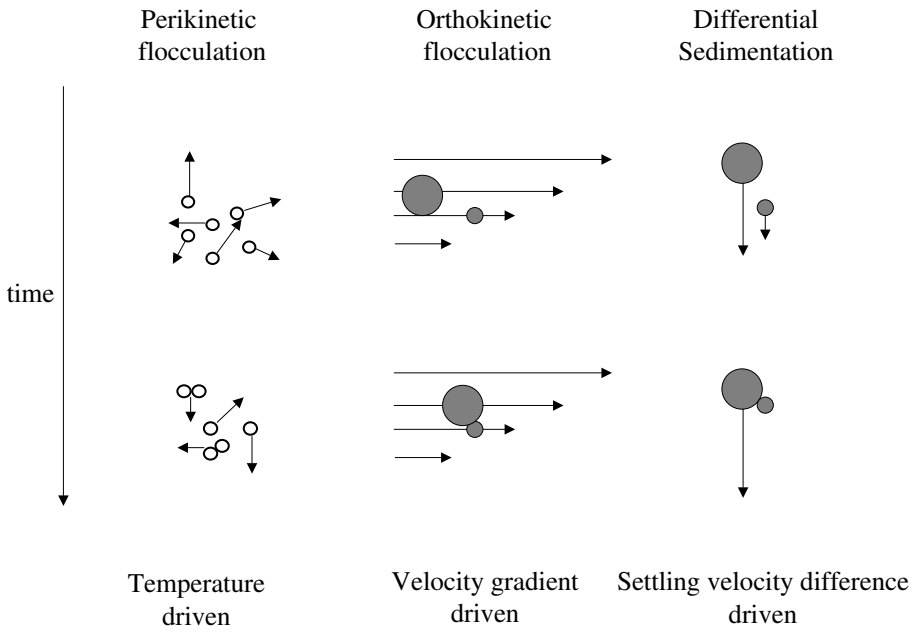

Figure 2.12: Illustration of the different flocculation mechanisms that induce particle collisions

where α is the the collision efficiency, $\beta(i,j)$ is the collision frequency between particles of size i and j and n_i and n_j are the particle concentrations for particles of size i and j. This approach leads to the first major attempt at modelling the flocculation process by Smoluchowski (1917), which formed the basis for almost all subsequent research into flocculation:

$$\frac{dn_k}{dt} = \frac{1}{2}\sum_{i+j=k}\beta(i,j)n_i n_j - \sum_{i=1}^{\infty}\beta(i,k)n_i n_k \tag{2.7}$$

The first term on the right hand side of eq. 2.7 defines the increase in number of particles of size k, whereas the second term on the right hand side of eq. 2.7 describes the loss of particles of size k due to aggregation with other particle sizes. The one half factor in the first term ensures for not counting collisions twice. The overall equation defines the rate of change in the number concentration of particles of size k. Hence, a set of k equations like eq. 2.7 needs to be solved simultaneously. Smoluchowski (1917) made a number of simplifying assumptions:

- the collision efficiency factor α is unity for all collisions
- fluid motion undergoes laminar shear
- particles are monodisperse
- no breakage occurs
- all particles are spherical in shape and remain so after aggregation (coalescing assumption)
- collisions involve only two particles

Later on, the more general framework of population balances was developed and some of the assumptions of Smoluchowski (1917) were discarded by developing new expressions for α and β and adding models for breakage of particles. This will be the subject of section 2.5.4 and 2.5.5.

2.5 Population Balance Modelling

When modelling a population of individuals, one can choose 2 different approaches:

- *continuum approach* — The population is considered as one lumped entity. All properties of the population are either homogeneously distributed, or a mean value of a heterogeneous distribution. In both cases the properties are represented by one number. For example, a population of particles would have one average settling velocity, independent of the particle size and/or density.
- *segregated approach* — The population is considered as a population of individual objects. All properties of the population are distributions. In this case the aforementioned population of particles would have a distribution of settling velocities depending on size and/or density, which is more realistic.

The continuum approach is easier in use, but leads to a loss of realism. In some cases the continuum approach can be derived from the segregated approach by making some assumptions. Hence, the segregated approach leads to a better understanding of the limitations of the continuum approach and will answer the question whether the continuum approach can be used without introducing a severe error. The continuum model has been widely used because of a lack of measurement techniques to collect the required data to feed the segregated models.

Recently, however, improved particle sizing techniques have been developed (e.g. flow cytometry, image analysis, laser scattering, coulter counter,...) which are further described in section 2.6. This has enhanced the capacity to identify a population balance model from experimental data. Therefore, the interest in population balance modeling has risen steeply in recent times (Ramkrishna and Mahoney, 2002).

The first appearance in literature of the general framework of population balances was by Hulburt and Katz (1964). An excellent review of the state-of-the-art in population balances was due to Ramkrishna (2000) and formed the basis of this literature review on population balances.

2.5.1 General framework

In this section, the population balance equation will be introduced. However, before doing so, some notation and terminology needs to be addressed.

The particle state and continuous phase vectors

As mentioned before, a segregated model considers individual objects. In what follows, these objects shall be denotes as 'particles', which should be regarded as any individual object in a segregated system (i.e. a floc, a crystal, a bubble,...) and not solely solid particles. Every object is considered to

be in a certain state, which can be defined by a number of (heterogeneous) properties of these objects. These properties are specified and summarized in the *particle state vector*. It is convenient to distinguish between external coordinates $\mathrm{r} \equiv (\mathrm{r}_1, \mathrm{r}_2, \mathrm{r}_3)$, which may be used to denote the position vector of the particle, and internal coordinates $\mathrm{x} \equiv (\mathrm{x}_1, \mathrm{x}_2, \ldots, \mathrm{x}_\mathrm{d})$, representing different quantities/properties associated with the particle. The choice of the particle state vector is determined by the variables considered important to specify (1) the rate of change of those variables of direct interest in the application, and (2) the birth and death processes. The domains of internal and external coordinates will further be denoted as Ω_x and Ω_r respectively.

The phase in which the particles are dispersed will be referred to as the continuous phase. This continuous phase can also be heterogeneous and is therefore also summarized in the c-dimensional *continuous phase vector*, which is clearly a function of the external coordinates and time:

$$Y(r,t) \equiv [Y_1(r,t), Y_2(r,t), \ldots, Y_c(r,t)] \tag{2.8}$$

The evolution of this field in space and time is governed by the laws of transport and interaction with the particles. The actual governing equations must involve the number density of particles in the particulate phase, which must first be identified.

In some situations, a continuous phase balance may not be necessary because interaction between the population and the continuous phase may not bring about any (or a substantial enough) change in the continuous phase. In such cases, analysis of the population involves only the population balance equation. The latter will be the case in this work.

The number and volume (or mass) density function

The number of objects that have a given state vector (x,r) is expressed by the *number density function* $\mathrm{f}_1(\mathrm{x}, \mathrm{r}, \mathrm{t})$. This implies that the number of particles in the infinitesimal volume $\mathrm{dV_x}\,\mathrm{dV_r}$ (in particle state space) about the particle state (x,r) is $\mathrm{f}_1(\mathrm{x}, \mathrm{r}, \mathrm{t})\ \mathrm{dV_x}\,\mathrm{dV_r}$. The number density function allows one to calculate the number of particles in any region of particle state space. The total number of particles in the entire system is given by:

$$\int_{\Omega_x} dV_x \int_{\Omega_r} dV_r\ f_1(x,r,t) \tag{2.9}$$

The total number of particles per unit of physical space, denoted as N(r,t) is then given by:

$$N(r,t) = \int_{\Omega_x} dV_x\ f_1(x,r,t) \tag{2.10}$$

Other densities such as volume or mass may also be defined for the particle population. Thus, if v(x) is the volume of the particle of internal state x, then the volume density may be defined as $\mathrm{v(x)\,f_1(x,r,t)}$. When using only volume as an internal state, the volume fraction $\phi(\mathrm{x}, \mathrm{r}, \mathrm{t})$ of particles of volume v(x) becomes:

$$\phi(x,r,t) = \frac{1}{\phi(r,t)}\, v(x)\, f_1(x,r,t) \tag{2.11}$$

where

$$\phi(r,t) \equiv \int_{\Omega_x} dV_x\ v(x)\ f_1(x,r,t) \tag{2.12}$$

represents the total volume fraction of all particles. In contrast with the number density, the volume and mass densities are concerned with the amount of dispersed material, and consequently are often physically more relevant. Of course, this depends on the application.

The rate of change of particle state vector

Particle states can vary in time. A change of external coordinates refers to motion through physical space, whereas that of internal coordinates refers to motion through an abstract property space. The velocities for external and internal coordinates, if the process is viewed as a deterministic one, are defined as:

$$\dot{R}\left(x,r,Y,t\right),\dot{X}\left(x,r,Y,t\right) \tag{2.13}$$

This allows to identify particle (number) fluxes, i.e. the number of particles flowing per unit of time per unit of area normal to the direction of the velocity:

$$f_1\left(x,r,t\right)\ \dot{R}\left(x,r,Y,t\right),f_1\left(x,r,t\right)\ \dot{X}\left(x,r,Y,t\right) \tag{2.14}$$

Both fluxes are evaluated at time t and at the point (x,r) in particle state space.

The population balance equation

Having introduced this terminology, one can write down the general multi-dimensional population balance equation. For the complete derivation, the reader is referred to Ramkrishna (2000).

$$\frac{\partial}{\partial t}f_1+\nabla_x\cdot\dot{X}f_1+\nabla_r\cdot\dot{R}f_1=h \tag{2.15}$$

where h is the net rate of generation of particles due to birth and death processes. The structure of h will be discussed in the next section.

In order to be solvable, eq. 2.15 needs to be supplemented with *initial* and *boundary* conditions. The initial condition $\mathrm{f_1\left(x,r,0\right)}$ must clearly stipulate the distribution of particles in the particle state space, including internal and external coordinates. The boundary condition is basically a specification of the component of the particle flux normal to the boundary or the number density at each point on "'appropriate"' parts of the boundary. These parts are the origins of the characteristic curves along which the solution of eq. 2.15 evolves. For examples of initial and boundary conditions, the reader is referred to Ramkrishna (2000). The initial and boundary conditions are also dependent on the application.

Birth and death functions

Changes in the number of particles can be driven by the boundary condition. The focus of this section, however, will be the modelling of processes in which particles may appear or disappear at any point in the particle state space. Birth and death events are generally a consequence of nucleation, particle breakage and/or aggregation processes. Since nucleation is not of interest in this work, it will not be further discussed. If birth takes place through one of the other processes, or at the expense of existing particles, then the right-hand side of the population balance equation must include a corresponding sink

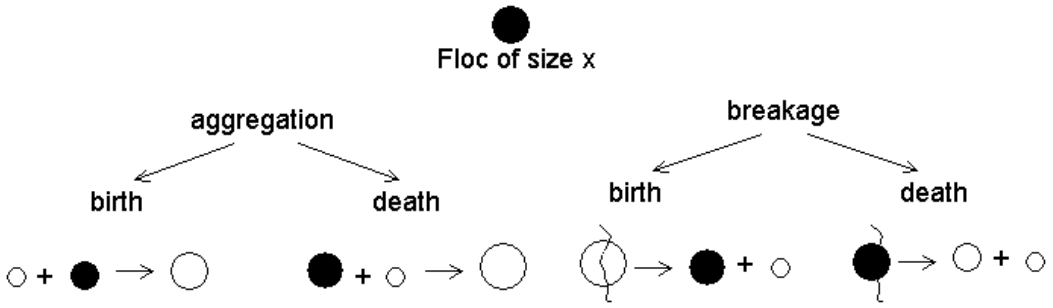

Figure 2.13: Illustration of the birth and death concept for aggregation and breakage

term besides a possible boundary condition term. Hence, the net birth rate consists of source and sink terms:

$$h\left(x,r,Y,t\right)=h^{+}\left(x,r,Y,t\right)+h^{-}\left(x,r,Y,t\right) \tag{2.16}$$

where the first term on the right hand side (source term) represents the number of particles of state (x,r) that are formed due to aggregation and/or breakage, whereas the second term on the right hand side (sink term) represents the number of particles of state (x,r) that is disappearing due to aggregation and/or breakage. The structure of these terms is further discussed, hereby differentiating between aggregation and breakage processes.

Breakage processes in the broad sense not only include mechanical fracture of particles, but also other mechanisms where new particles arise from existing particles like e.g. asexual cell division. The underlying theme stresses independent behaviour of individual particles with respect to breakage. This limitation would imply that breakage of particles due to collision with other particles cannot be modelled using the strategy outlined below. However, those operations where particles are in intimate contact with one another have been traditionally modelled using the same methodology assuming independency of breakage towards other particles. The justification of this may come from viewing the environment of each particle as an average medium of particles transmitting forces (stress) leading to particle breakup.

If breakup of particles occurs independently of each other, the *specific breakage rate* of particles of state (x,r) at time t in an environment Y can be represented by b(x,r,Y,t). It represents the fraction of particles of state (x,r) breaking per unit of time. The sink term from breakage simply becomes:

$$h_{break}^{-}\left(x,r,Y,t\right)=b\left(x,r,Y,t\right)f_{1}\left(x,r,t\right) \tag{2.17}$$

The function b(x,r,Y,t) has the dimension of reciprocal time and is often called the *breakage frequency*. This sink term $\mathrm{h_{break}^{-}\left(x,r,Y,t\right)}$ can be viewed as the death of particles with size x due to breakage and is therefore also called *breakage death*. This is illustrated in Fig. 2.13.

In order to characterise the source term from breakage, some additional quantities have to be introduced:

$\upsilon\left(\mathrm{x',r',Y,t}\right)$ The *average number* of particles formed from the breakup of a single particle of state (x',r') in an environment of state Y at time t ;

$\mathrm{P\left(x,r|x',r',Y,t\right)}$ The *probability density function* or *daughter distribution function* for particles of state (x',r') in an environment of state Y at time t that break into particles of state (x,r). This is a continuously distributed fraction over particle state space

The former quantity is often (but not always) known. It has a minimum value of 2 but, being an average number, is not restricted to being an integer. In a multiple-splitting process, detailed modelling of the breakage process is essential to arrive at the value of v. Alternatively, its value could be determined from experiments. The latter quantity also needs to be determined either by experimental observation or by detailed modelling of the breakage process. This function, however, inherits certain properties from conservation laws which must constrain the breakage process. It must satisfy the normalisation condition:

$$\int_{\Omega_x} P\left(x, r|x', r', Y, t\right) dV_x = 1 \tag{2.18}$$

Conservation of mass is required too. If m(x) is assumed to be the mass of a particle of internal state x, this yields the restriction:

$$P\left(x, r|x', r', Y, t\right) = 0 \quad m\left(x\right) \geq m\left(x'\right) \tag{2.19}$$

Eq. 2.19 expresses the fact that breakage into larger particles is impossible. The following restriction expresses the fact that no mass can be "created", in other words, the mass of all the fragments from breakage formed within the system should be no more than the mass of the parent particle:

$$m\left(x'\right) \geq v\left(x', r', Y, t\right) \int_{\Omega_x} m\left(x\right) P\left(x, r|x', r', Y, t\right) dV_x \tag{2.20}$$

If the equality in this equation holds, this means that no mass is lost during the breakage process.

Now these functions have been characterised, the source term from breakage can be calculated as:

$$h^{+}_{break}\left(x, r, Y, t\right) = \int_{\Omega_r} dV_{r'} \int_{\Omega_x} dV_{x'} \upsilon\left(x', r', Y, t\right) b\left(x', r', Y, t\right) P\left(x, r|x', r', Y, t\right) f_1\left(x', r', t\right) \tag{2.21}$$

This source term can be viewed as the birth of particles of size x due to breakage of larger particles and is therefore also called *breakage birth* and is illustrated in Fig. 2.13. The structure of the different breakage functions will be dealt with in section 2.5.5.

Aggregation processes include all particulate events in which two or more particles collide and remain together as one entity. The amount of particles involved is application-specific and depends on the degree of dilution. In crowded systems, it is conceivable that several adjacent particles could simultaneously aggregate. Aggregation can lead to complete merging of two particles along with their interiors, but also covers processes in which flocs of particles are formed that are loosely held together by surface forces and are thus not involving physical contact. The former is also known as coalescence, the latter as coagulation. Of course, intermediate situations also exist. In the framework described here, it is assumed that the dilution is sufficient to only allow binary aggregation. It is also insensitive to the degree of physical contact.

The main phenomenological instrument of the population balance model meant to describe an aggregation process is the *aggregation frequency*. The latter represents the probability of aggregation per unit of time of a pair of particles of specified states. As mentioned before, it is assumed that the population density is so small that the probability of more than two particles colliding is negligible. The fraction of particle pairs of states (x,r) and (x',r') aggregating per unit of time is represented by:

$$\beta\left(x, r; x', r'; Y, t\right) \tag{2.22}$$

which is a symmetric function with regard to x and r. Since the time dependency is not a desirable feature in models, it is eliminated in the remainder of the framework development.

It is assumed that if the states of one of the aggregating particles and of the new particle are known, the state of the other aggregating particle can be calculated. Thus, given the state of the newly formed particle (x,r) and the state (x',r') of one of the two aggregating particles, the state of the other aggregating particles is denoted by:

$$\left[\tilde{x}\left(x,r|x',r'\right)\tilde{r}\left(x,r|x',r'\right)\right] \tag{2.23}$$

It is also necessary to define the average number of particle pairs that are present at each time instant with specified states. Therefore, a function $\mathrm{f_2\left(x,r;x',r',t\right)}$ is defined that represents the average number of particle pairs at time t per unit volumes in state space located about (x,r) and (x',r') respectively.

The sink term from aggregation is readily found to be

$$h_{agg}^{-}\left(x,r,Y,t\right)=\int_{\Omega_x}dV_{x'}\int_{\Omega_r}dV_{r'}\beta\left(x,r;x',r';Y\right)f_2\left(x,r;x',r',t\right) \tag{2.24}$$

This sink term can be viewed as the death of particles with size x due to aggregation and is therefore also called *aggregation death*. The concept is illustrated in Fig. 2.13.

The source term from aggregation, representing the rate of production of particles of state (x,r) must account for the fact that the density with respect to coordinates $[\tilde{x}\left(x,r|x',r'\right)\tilde{r}\left(x,r|x',r'\right)]$ must be transformed into one in terms of (x,r) by using the appropriate Jacobian of the transformation and hence may be written as

$$h_{agg}^{+}\left(x,r,Y,t\right)=\int_{\Omega_x}dV_{x'}\int_{\Omega_r}\frac{1}{\delta}dV_{r'}\beta\left(\tilde{x},\tilde{r};x',r';Y\right)f_2\left(\tilde{x},\tilde{r};x',r',t\right)\frac{\partial\left(\tilde{x},\tilde{r}\right)}{\partial\left(x,r\right)} \tag{2.25}$$

where δ represents the number of times identical pairs have been considered. The term $\frac{\partial(\tilde{\mathrm{x}},\tilde{\mathrm{r}})}{\partial(\mathrm{x,r})}$ represents the determinant

$$\begin{vmatrix} \frac{\partial\tilde{x_1}}{\partial x_1} & \cdots & \frac{\partial\tilde{x_1}}{\partial x_n} & \frac{\partial\tilde{x_1}}{\partial r_1} & \frac{\partial\tilde{x_1}}{\partial r_2} & \frac{\partial\tilde{x_1}}{\partial r_3} \\ \vdots & \vdots & \vdots & \vdots & \vdots & \vdots \\ \frac{\partial\tilde{x_n}}{\partial x_1} & \cdots & \frac{\partial\tilde{x_n}}{\partial x_n} & \frac{\partial\tilde{x_n}}{\partial r_1} & \frac{\partial\tilde{x_n}}{\partial r_2} & \frac{\partial\tilde{x_n}}{\partial r_3} \\ \frac{\partial\tilde{r_1}}{\partial x_1} & \cdots & \frac{\partial\tilde{r_1}}{\partial x_n} & \frac{\partial\tilde{r_1}}{\partial r_1} & \frac{\partial\tilde{r_1}}{\partial r_2} & \frac{\partial\tilde{r_1}}{\partial r_3} \\ \frac{\partial\tilde{r_2}}{\partial x_1} & \cdots & \frac{\partial\tilde{r_2}}{\partial x_n} & \frac{\partial\tilde{r_2}}{\partial r_1} & \frac{\partial\tilde{r_2}}{\partial r_2} & \frac{\partial\tilde{r_2}}{\partial r_3} \\ \frac{\partial\tilde{r_3}}{\partial x_1} & \cdots & \frac{\partial\tilde{r_3}}{\partial x_n} & \frac{\partial\tilde{r_3}}{\partial r_1} & \frac{\partial\tilde{r_3}}{\partial r_2} & \frac{\partial\tilde{r_3}}{\partial r_3} \end{vmatrix} \tag{2.26}$$

This source term can be viewed as the birth of particles of size x due to aggregation of smaller particles and is therefore also called *aggregation birth*. The concept is illustrated in Fig. 2.13.

The population balance equation obtained is not closed because the right-hand side involves a fresh unknown in the pair density function f_2, introduced via eq. 2.24-2.25. To close the population balance, it can be approximated that:

$$f_2\left(x,r;x',r',t\right)=f_1\left(x,r,t\right)f_1\left(x',r',t\right) \tag{2.27}$$

presenting the coarsest form of closure hypothesis. This assumption implies that there is no statistical correlation between particles of states (x',r') and (x,r) at any instant time or in other words, they are independent.

2.5.2 Existence of solution and solution methods

Before being able to judge whether a solution for the PBE exists, one should have a closer look at the population balance equation. For reasons of simplicity both internal and external coordinates are combined in a vector z, turning eq. 2.15 into

$$\frac{\partial}{\partial t} f_1 + \nabla_z \cdot \dot{Z} f_1 = h\left(z,t\right) \tag{2.28}$$

The existence of a solution is very much dependent on the characteristics of the right-hand side of eq. 2.28. Three cases can occur for h(z,t):

1. Independent of f_1, i.e. a specified function of z and t. This occurs obviously in systems in which the particles may appear or disappear because of events occurring in the continuous phase;
2. A linear function of f_1, which occurs in systems where particles are lost spontaneously;
3. A non-linear function of f_1 which requires the specification of the number density over a range of particles states.

Cases 1 and 2 can be considered together, since case 2 can be easily transposed into case 1. The obtained equation is a *first-order partial differential equation* in f_1 for which the existence of solution is well known. It is generally solved analytically (when initial and boundary conditions are known) by using the *method of characteristics*.

In case 3, the non-linearity often involves integrals of the population density (e.g. when aggregation and breakage are considered). Also integral boundary conditions can lead to a case 3 PBE. The equation now becomes an *integro-partial differential equation* in f_1. When pretending that f_1 is known, again the method of characteristics can be applied, however, yielding an integral equation in f_1. The existence of a solution of this integral equation can be guaranteed by the convergence of the method of successive approximations (also known as Picard's iteration method). The convergence of the iteration is guaranteed when the criteria for existence of a unique solution are satisfied. The latter is done by using fixed-point methods to analyse the integral equation (also generating criteria for existence of the solution) or the contraction mapping theorem (also assuring the uniqueness of the solution).

From the previous discussion, it can be clearly seen that the format of the right-hand side of the PBE will determine to a certain extent the solution method to be used. A number of possible solution methods are available: the method of successive approximations (Ramkrishna, 2000), the method of successive generations (Liou et al., 1997), the method of Laplace transformation (Ramkrishna, 2000), the method of moments and weighted residuals (Ramkrishna, 2000), the quadrature method of moments (Marchisio et al., 2003), discretisation (Hounslow et al., 1988; Litster et al., 1995; Hill and Ng, 1995; Kumar and Ramkrishna, 1996a,b, 1997; Lee et al., 2001), wavelet-based method (Liu and Cameron, 2001). An in depth discussion of solution methods is beyond the scope of this literature review. Only the methods that were used in this work (discretisation) will be addressed in some more detail in what follows.

2.5.3 Discretisation techniques

A direct solution of the population balance equation by finite difference methods would require a natural discretisation of particle state space to represent derivatives and integrals that appear in the equation. The

fineness of discretisation of particle state space would necessarily be dictated by numerical considerations in approximating the derivative or the integral. However, much coarser discretisation grids will be used, implying that the population balance becomes a macroscopic balance. The method (applying these coarse discretisation grids) has been used successfully in that they greatly reduce the computation effort, making it an attractive attribute with regard to repetitive calculations in optimisation and control of particulate systems. When using this method, the calculations should be designed for selected properties of the system rather than for an estimate of the number density accurate enough for estimating all properties of the population. Several methods have been presented in literature (Batterham et al., 1981; Hounslow et al., 1988; Kumar and Ramkrishna, 1996a,b; Litster et al., 1995; Hill and Ng, 1995; Vanni, 2000). The ones that will be used in this work are discussed in more detail.

Batterham et al. (1981) were the first to propose a set of discretised equations describing the process of aggregation. They considered a discretised size domain in which volumes were in a geometric series such that $\mathrm{v_{i+1}}/\mathrm{v_i} = 2$. They deduced equations that allowed interaction of particles at the appropriate rate and split the so formed particles into the permissible sizes in such a way as to conserve volume. However, the rate of change of particle numbers using their equations is not predicted correctly, which was not surprising given the arbitrary allocation of particle numbers used in the generation of the equations. Hounslow et al. (1988) proposed a set of discretised equations for aggregation that did conserve 2 moments, mass and numbers. They adopted the same geometric grid from Batterham et al. (1981) and considered 4 mechanisms: particle birth in size class i from one particle in size class i-1 and any other particle up to size class i-2; particle birth in size class i from two particles in size class i-1; particle death in size class i by collision with a smaller particle; particle death in size class i by collision with a larger particle. After calculating the occurrence of each of these mechanisms and forcing the moments to be conserved, the following set of equations is found:

$$\frac{dN_i}{dt} = N_{i-1}\sum_{j=1}^{i-2} 2^{j-i+1}\beta\left(i-1,j\right)N_j + \frac{1}{2}\beta\left(i-1,i-1\right)N_{i-1}^2 - N_i\sum_{j=1}^{i-1)} 2^{j-i}\beta\left(i,j\right)N_j - N_i\sum_{j=i}^{\infty}\beta\left(i,j\right)N_j \quad (2.29)$$

where $\mathrm{N_i}$ is the number concentration of class i and $\beta\left(\mathrm{i,j}\right) = \beta\left(\mathrm{v_i,v_j}\right)$. The drawback of this method is that it is not flexible towards the choice of grid, the moments to be conserved and that it is restricted to pure aggregation processes. The grid flexibility was extended by Litster et al. (1995) allowing grids with $\mathrm{v_{i+1}}/\mathrm{v_i} = \mathrm{r}$ where $\mathrm{r} = 1/\mathrm{q}$ and q is an integer. Hill and Ng (1995) derived similar equations for pure breakage events.

Kumar and Ramkrishna (1996a) used another approach to derive a set of discretised equations. They assumed a one-dimensional continuous population balance equation in particle size x (represented by particle volume v) for both breakage and aggregation, integrated over subintervals in an arbitrary partition

$$P_M \equiv \{0 = v_0, v_1, \ldots, v_M, v_{M+1}\} \quad (2.30)$$

The population balance equation for aggregation and breakage (no growth) is given by:

$$\frac{\partial f_1\left(v,t\right)}{\partial t} = H\left[\{f_1\};v,t\right] \quad (2.31)$$

where $\mathrm{H}\left[\{\mathrm{f_1}\}\,;\mathrm{v},\mathrm{t}\right]$ is given by

$$H\left[\{f_1\}\,;v,t\right] \equiv \frac{1}{2}\int_0^v \beta\left(v-v',v'\right) f_1\left(v-v',t\right) f_1\left(v',t\right) dv' - f_1\left(v,t\right)\int_0^\infty \beta\left(v,v'\right) f_1\left(v',t\right) dv' + \int_v^\infty \upsilon\left(v'\right) b\left(v'\right) P\left(v|v'\right) f_1\left(v',t\right) dv' - b\left(v\right) f_1\left(v,t\right) \quad (2.32)$$

and consists respectively of an aggregation birth, aggregation death, breakage birth and breakage death term that were introduced and defined before.

By integrating over the interval $\mathrm{I_i} = [\mathrm{v_i}, \mathrm{v_{i+1}}]$ of the arbitrary partition, the *macroscopic balance* of the particles in the interval is obtained

$$\frac{d}{dt}\int_{v_i}^{v_{i+1}} f_1\left(v,t\right) dv = \int_{v_i}^{v_{i+1}} H\left[\{f_1\}\,;v,t\right] dv \quad i = 0,1,2,\ldots,M \quad (2.33)$$

Defining the total number of particles in $\mathrm{I_i}$ as

$$N_i\left(t\right) \equiv \int_{v_i}^{v_{i+1}} f_1\left(v,t\right) dv \quad (2.34)$$

and expressing the integral with respect to v' (from eq. 2.32) as the sum of integrals over subintervals, eq. 2.33 becomes

$$\frac{dN_i}{dt} = \int_{v_i}^{v_{i+1}} dv \left[\frac{1}{2}\sum_{j=0}^{i-1}\int_{v_j}^{v_{j+1}} \beta\left(v-v',v'\right) f_1\left(v-v',t\right) f_1\left(v',t\right) dv' - f_1\left(v,t\right)\sum_{j=0}^{M}\int_{v_j}^{v_{j+1}} \beta\left(v,v'\right) f_1\left(v',t\right) dv' + \sum_{j=i}^{M}\int_{v_j}^{v_{j+1}} \upsilon\left(v'\right) b\left(v'\right) P\left(v|v'\right) f_1\left(v',t\right) dv' - b\left(v\right) f_1\left(v,t\right)\right] \quad (2.35)$$

These M+1 equations are *unclosed* in the variables $\mathrm{N_i}$ (both $\mathrm{N_i}$ and $\mathrm{f_1}$ are unknown), reflecting a lack of *autonomy*. Restoration of autonomy can be brought about by expressing the double integrals involved in the right hand side of eq. 2.35 entirely in terms of the dependent variables $\{N_i\}$. This can be done by

- using the mean value theorem on the aggregation frequency $\beta\left(\mathrm{x_i},\mathrm{x_j}\right)$ The mean value theorem expresses the following. Let f(x) be a function which is differentiable in an open interval (a,b) and continuous in the closed interval (a,b). Then there is at least one point c in the interval (a,b) such that

  $$f'(c) = \frac{f(b)-f(a)}{b-a} \quad (2.36)$$

  Applying this theorem to e.g. the second term of eq. 2.35 yields

  $$\beta\left(x_i,x_j\right)\int_{v_i}^{v_{i+1}} dv \int_{v_j}^{v_{j+1}} dv' f_1\left(v,t\right) f_1\left(v',t\right) = \beta\left(x_i,x_j\right) N_i N_j \quad (2.37)$$

where x_i and x_j may be described as *pivotal points* or simply *pivots* in I_i and I_j respectively. The pivot concentrates the particles in the interval at a single representative point. This allows to write the number density $f_1(v,t)$ as being given by

$$f_1(v,t) = \sum_{i=0}^{M} N_i \delta(v - x_i) \tag{2.38}$$

Using eq. 2.38 in eq. 2.35 (illustrated here for the second term) will yield the right-hand side of eq. 2.37. The pivots x_i and x_j must depend on the frequency function $a(v,v')$ as well as the number densities in the two intervals so that they must strictly be regarded as time dependent in a dynamic problem. The pivots would also not remain the same for all terms in eq. 2.35. Hence, this again illustrates that an exact calculation of all the properties of the population by such a method is not a reasonable expectation.

- using the mean value theorem on number density $f_1(v,t)$ turning for example the second term on the right hand side of eq. 2.35 into

$$N_i N_j \frac{1}{(v_{i+1} - v_i)(v_{j+1} - v_j)} \int_{v_i}^{v_{i+1}} dv \int_{v_j}^{v_{j+1}} dv' \beta(v, v') \tag{2.39}$$

This requires calculation of the integral of the aggregation frequency at each step.

In either of the preceding categories, since the integrand contains the unknown number density, the mathematically rigorous choice of the pivot, which is consistent with the mean value theorem is of course not accessible. The finer the interval, the less crucial would be the location of the pivot in I_i. The fineness required would depend on the extent to which the phenomenological functions of the population balance model such as the aggregation and breakage functions vary in the interval.

Using the former to restore the autonomy of eq. 2.35 yields

$$\frac{dN_i}{dt} = \frac{1}{2} \sum_{j=0}^{i-1} N_j \sum_{(x_j + x_k) \in I_i} N_k \beta(x_k, x_j) - N_i \sum_{j=0}^{M} N_j \beta(x_i, x_j) + \sum_{j=i}^{M} N_j \upsilon(x_j) b(x_j) \int_{v_i}^{v_{i+1}} P(v|x_j)\, dv - b(x_i N_i) \tag{2.40}$$

where it is understood that terms involving indices other than i=0.1,...,M are automatically set to zero. Both birth terms on the right-hand side of eq. 2.40 contribute particles to the size interval I_i so that the number balance in each subinterval of the partition is exactly upheld. This also implies that the total number balance in the entire interval (i.e. the zeroth moment) is satisfied.

When deriving the r^{th} integral moment from this equation (r being an integer value)

$$\mu_r(t) = \sum_{i=0}^{M} \mu_r^{(i)}(t) \quad r = 0, 1, 2, \ldots \tag{2.41}$$

where the r^{th} sectional moment is given by

$$\mu_r^{(i)}(t) \equiv \int_{v_i}^{v_{i+1}} v^r f_1(v,t)\, dv = x_i^r N_i \quad r = 0, 1, 2, \ldots \tag{2.42}$$

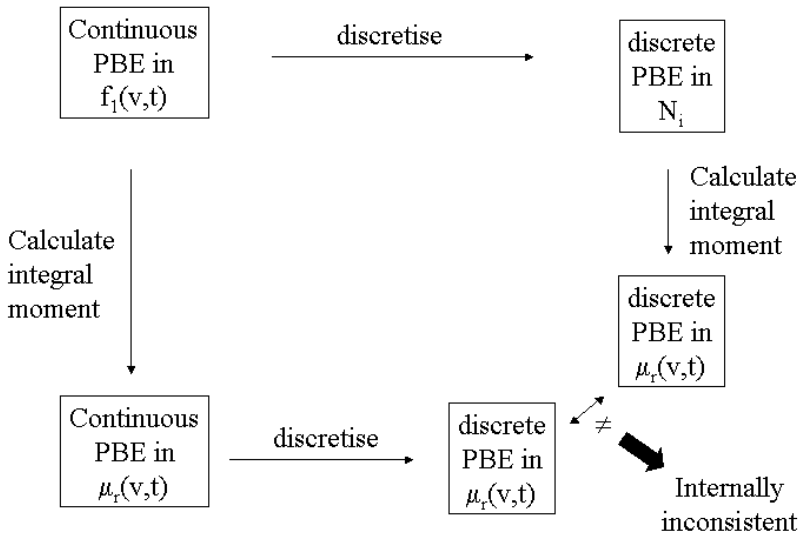

Figure 2.14: Illustration of the two different approaches that can be followed in order to obtain the discretised PBE in terms of a chosen integral moment

one obtains

$$\frac{d\mu_r}{dt} = \frac{1}{2}\sum_{i=0}^{M}\sum_{j=0}^{M} N_j \sum_{(x_j+x_k)\in I_i} N_k a\left(x_k, x_j\right)\left(x_j + x_k\right)^r - \mu_r \sum_{j=0}^{M} N_j a\left(x_i, x_j\right) + \sum_{i=0}^{M}\sum_{j=i}^{M} v\left(x_j\right) b\left(x_j\right) N_j \int_{v_i}^{v_{i+1}} v^r P\left(v|x_j\right) dv - \sum_{i=0}^{M} b\left(x_i\right)\mu_r^{(i)} \quad (2.43)$$

The evolution of the r^{th} integral moment can also be derived in another way. Instead of first discretising eq. 2.31 and then calculating the integral moment, one can also first express the continuous PBE in terms of the integral moment and subsequently discretise the obtained equation. The difference between both approaches is illustrated in Fig. 2.14. When doing so, this turns out to be *internally inconsistent* with the same integral moment derived directly from the original continuous PBE (eq. 2.31), which is given by

$$\frac{d\mu_r}{dt} = \frac{1}{2}\sum_{i=0}^{M}\sum_{j=0}^{M} N_j \sum_{(x_j+x_k)\in I_i} N_k a\left(x_k, x_j\right)\left(x_i\right)^r - \mu_r \sum_{j=0}^{M} N_j a\left(x_i, x_j\right) + \sum_{i=0}^{M}\sum_{j=i}^{M} v\left(x_j\right) b\left(x_j\right) N_j x_i^r \int_{v_i}^{v_{i+1}} P\left(v|x_j\right) dv - \sum_{i=0}^{M} b\left(x_i\right)\mu_r^{(i)} \quad (2.44)$$

Restoring this inconsistency requires

1. $\mathrm{x_j} + \mathrm{x_k} = \mathrm{x_i}$, which will eliminate the inconsistency due to the source term for aggregation (in an exact way)

2. $\int_{v_i}^{v_{i+1}} v^r P(v|x_j)\,dv = x_i^r \int_{v_i}^{v_{i+1}} P(v|x_j)\,dv$, which can only be satisfied exactly for r=0 and approximately for lower order moments for sufficiently fine grids.

It should be stressed though that internal consistency does not guarantee a number density sufficiently accurate for the calculation of all associated properties of the population unless the partition of the size interval is suitably fine. Hence, fineness of the partition of the size interval is indeed an underwriting requirement for accurate calculations of the number density.

The fixed pivot

Kumar and Ramkrishna (1996a) used the rationale of internal consistency of the moment equations for the redistribution of particles that have sizes different from the pivotal sizes and, hence, to derive a discrete set of equations. A newly formed particle in the size range x_i, x_{i+1} due to breakup or aggregation is represented by assigning fractions $a(v, x_i)$ and $b(v, x_{i+1})$ to particle populations at x_i and x_{i+1}, respectively. In order to conserve two properties $f_1(v)$ and $f_2(v)$, the following set of equations needs to be satisfied:

$$\begin{aligned} a(v,x_i) f_1(x_i) + b(v,x_{i+1}) f_1(x_{i+1}) &= f_1(v) \\ a(v,x_i) f_2(x_i) + b(v,x_{i+1}) f_2(x_{i+1}) &= f_2(v) \end{aligned} \tag{2.45}$$

It is clear from these equations that for preservation of two properties, the particle population at x_i gets net particles assigned to it for every new particle that is born in the size range $\{x_{i-1}, x_{i+1}\}$. By using this simple technique, a set of discretised equations for aggregation and breakage, conserving both numbers and mass, can be derived (Kumar and Ramkrishna, 1996a; Ramkrishna, 2000)

$$\begin{aligned} \frac{dN_i}{dt} = & \sum_{\substack{j,k \\ x_{i-1} \le (x_j + x_k) \le x_{i+1}}}^{j \ge k} \left[1 - \frac{1}{2}\delta_{j,k}\right] \eta_i a_{x_j,x_k} N_j N_k - N_i \sum_k a_{x_i,x_k} N_k \\ & + \sum_{\substack{k \\ j \ge i}} n_{i,k} b(x_j) N_j - b(x_i) N_i \end{aligned} \tag{2.46}$$

where

$$\eta_i = \begin{cases} \frac{x_{i+1} - (x_j + x_k)}{x_{i+1} - x_i} & \text{when} \quad x_i \le (x_j + x_k) \le x_{i+1} \\ \frac{(x_j + x_k) - x_{i-1}}{x_i - x_{i-1}} & \text{when} \quad x_{i-1} \le (x_j + x_k) \le x_i \end{cases} \tag{2.47}$$

and

$$n_{i,k} = \int_{x_i}^{x_{i+1}} \frac{x_{i+1} - v}{x_{i+1} - x_i} P(v|x_k)\,dv + \int_{x_{i-1}}^{x_i} \frac{v - x_{i-1}}{x_i - x_{i-1}} P(v|x_k)\,dv \tag{2.48}$$

The technique, which was given the name *fixed pivot*, is illustrated in Fig. 2.15. These equations are flexible in the sense that they are independent of the functional forms for the breakage frequency, daughter particle size distribution and the aggregation kernel. Moreover, the moments to be conserved can be freely chosen as well as the grid, which is an advantage over the previously described technique by Hounslow et al. (1988). For a geometric grid with factor 2, eq. 2.46 reduces to eq. 2.29.

Kumar and Ramkrishna (1996a) tested the performance of the fixed pivot technique by comparing he simulation results with analytical solutions of a simple PBE for pure breakage (Ziff and McGrady,

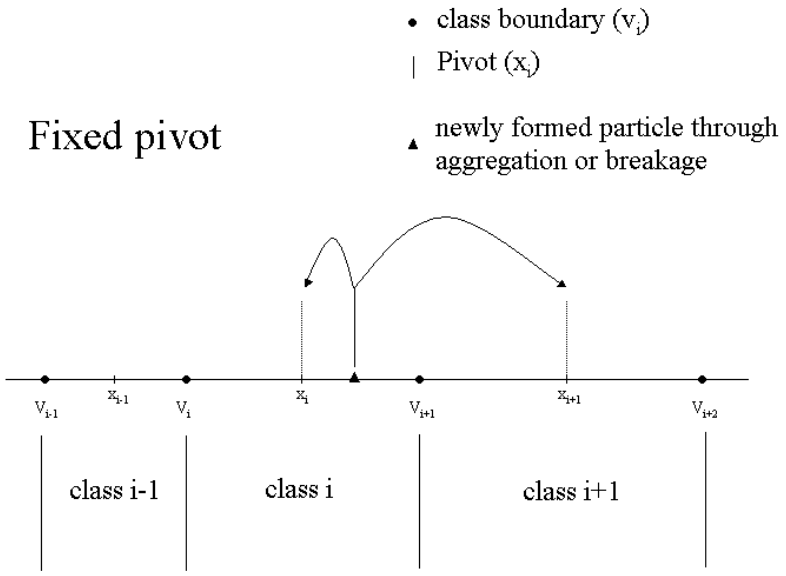

Figure 2.15: Schematic representation of how the fixed pivot deals with newly formed particles that do not coincide with an existing pivot

1985), pure aggregation (Scott, 1968) and simultaneous aggregation-breakup (Blatz and Tobolsky, 1945) preserving the zeroth and first moment on a volume basis, for different coarse geometric grids and a monodispersed initial condition.

For pure, uniform, binary breakage, the numerical results were in good agreement with the analytical results throughout the simulation, getting more accurate as the grid is further refined. Similar results were found for pure, multiple breakage. In this case even a coarse grid yielded accurate results. Similar numerical-analytical comparisons were performed for pure, uniform aggregation for different aggregation kernels (constant, i.e. independent of particle size; sum of particle sizes; product of particle sizes), a kernel being another name frequently used to address aggregation or breakage functions as defined earlier in section 2.5.1. Results show excellent agreement for small to moderate particles (even for coarse grids), but reveal overprediction in the large particle region, where the number density gets smaller and steep changes occur (Fig. 2.16). This steep part of the number density in an aggregating system will be further referred to as a front‘ moving to the higher size ranges as the aggregation proceeds. The overprediction gets worse (1) when time progresses in the simulation, (2) when the degree of homogeneity of the aggregation kernel increases (from a constant over a sum to a product kernel). Results evidently improve when using finer grids. For simultaneous aggregation-breakup good results were obtained too, although the overprediction-problem observed with the pure aggregation exercise persists.

The same authors tried to give an explanation for the overpredictions and illustrated this with a straightforward example in which they look at the aggregation of particles in a size range $\{v_i, 2v_i\}$ starting from different initial number densities in the size range, i.e. uniform and exponentially decreasing. The number density of new particles in $\{2v_i, 4v_i\}$ can be calculated analytically using a certain aggregation kernel. The discretised solution of the same problem assumes N_i particles at x_i representative for $\{v_i, 2v_i\}$ and will form $N_i/2$ particles at x_{i+1} representative for $\{2v_i, 4v_i\}$. It is shown that this results holds for the initial uniform number distribution (Fig. 2.17), but not at all for the exponential one (Fig. 2.18). In the

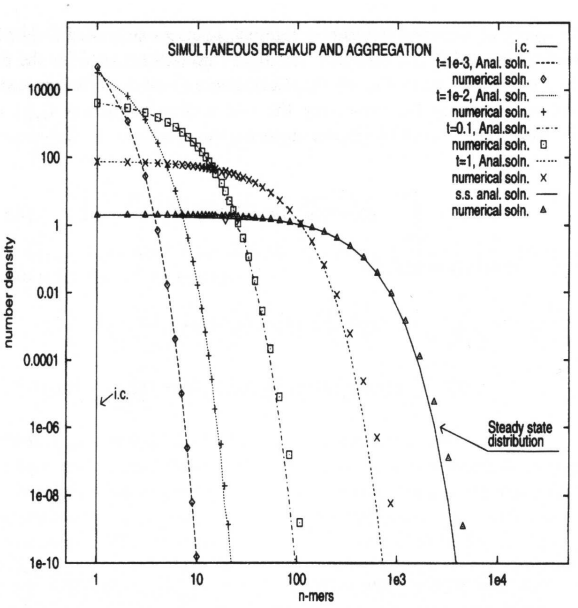

Figure 2.16: Comparison of the number density calculations of Kumar and Ramkrishna (1996a) using the discretisation algorithm (eq. 2.46) with the analytical solution of Blatz and Tobolsky (1945) for a polymerisation-depolymerisation process (i.c. = initial condition)

latter case the newly formed particles are situated at the lower end of the particle range $\{2v_i, 4v_i\}$, clearly showing that the discretised solution results in an overprediction of the evolution of the number density. The front mentioned earlier is an example of such a non-uniform number density and moves towards the higher size ranges. In the discretised case, the front moves at a faster rate than its actual rate explaining the increase of overprediction as the aggregation proceeds. For size dependent kernels, the kernel would be calculated only at the frequency at x_i instead of at a more relevant frequency corresponding to the most populated size in $\{v_i, v_{i+1}\}$. Obviously, the stronger the size-dependency, the larger the degree of overprediction will be as was observed when comparing constant, sum and product kernels (not shown). It is also clear that a refinement of the grid will reduce this source of error. For every aggregating system, the discretised solution will always suffer from these problems. The problem is on the other hand not fixed at a certain size range, but moves through the particle size space as the front is moving towards the larger particle size region.

To overcome this problem, two strategies can be followed: (1) use a variable grid instead of a fixed geometric grid or (2) allow the pivot to change at each time-step taking into account the particle distribution within the size class at that time instant. The former approach was briefly introduced by Kumar and Ramkrishna (1996a), but has been fully developed by Lee et al. (2001). The idea is to avoid large variations in the number density across a section by choosing the section widths appropriately. Replacing the geometric grid with a non-regular grid that is fine in steeply varying size ranges and coarse elsewhere, resulted in a better estimate in the higher particle size range even if the total number of sections or classes remains the same. A similar improvement with a geometric grid would require the double number of sections and, hence, imply a significantly higher computation time. As the front moves, size regions exist that initially contain large variations and evolve to regions with much less variation and vice versa. A locally fine grid that no longer contains the front can then be changed to a coarse grid. The computational effort can, therefore, be further decreased by allowing the grid to vary in time.

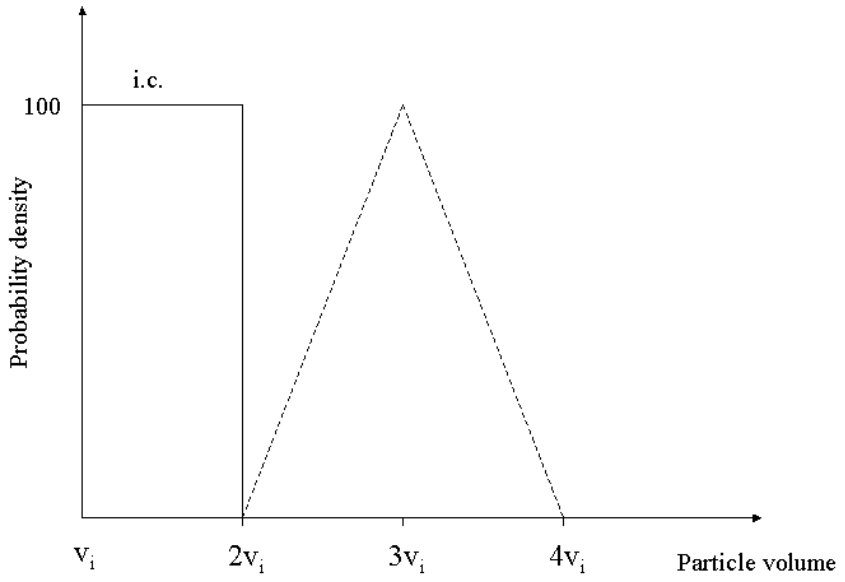

Figure 2.17: Distribution of particles before and after aggregation (constant kernel) when particles are initially uniformly distributed (i.c. = initial condition) (from Kumar and Ramkrishna (1996a))

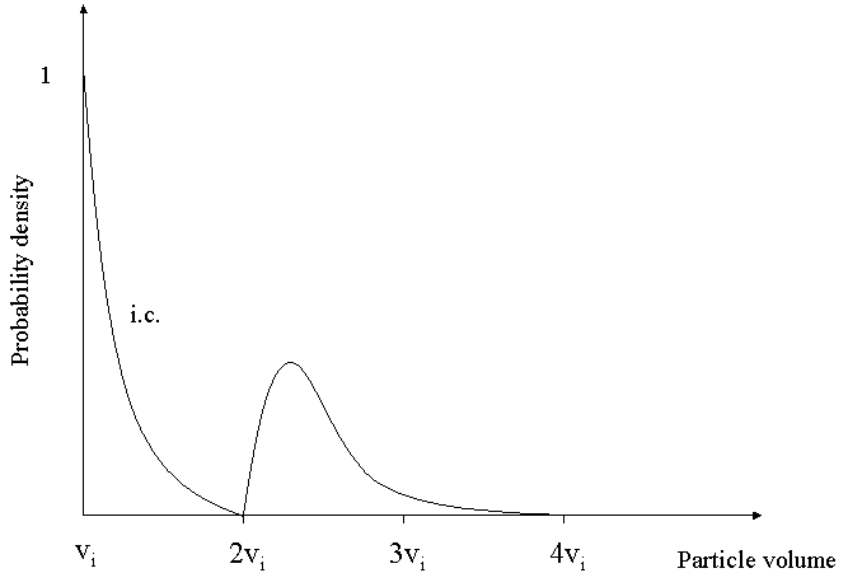

Figure 2.18: Distribution of particles before and after aggregation (constant kernel) when particles are initially exponentially distributed (i.c. = initial condition) (from Kumar and Ramkrishna (1996a))

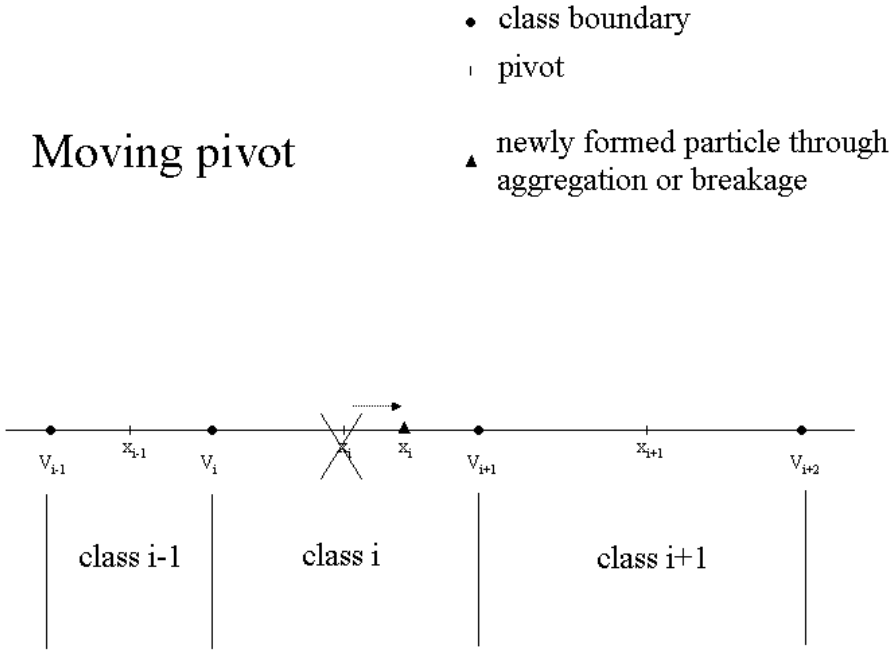

Figure 2.19: Schematic representation of how the moving pivot deals with newly formed particles that do not coincide with an existing pivot

The moving pivot

The second approach has been presented by Kumar and Ramkrishna (1996b) and is referred to as the *moving pivot technique*. The approach consists of an incorporation of details of the variation of the number density within a size range without loosing the properties of the fixed pivot technique. This technique accounts for the evolving non-uniformity of the distribution in each interval by allowing a varying pivot location within the interval (Fig. 2.19). The other features (arbitrary choice of grid and integral properties to be conserved) were maintained.

Next to the equations for N_i, equations describing the changes in location of the pivots (x_i) are needed too. For the derivation of the equations, the reader is referred to the literature (Kumar and Ramkrishna, 1996b). The equations conserving numbers and mass are given below:

$$\frac{dN_i}{dt} = \sum_{\substack{j,k \\ v_i \le (x_j + x_k) \le v_{i+1}}}^{j \ge k} \left[1 - \frac{1}{2}\delta_{j,k}\right] \beta_{x_j,x_k} N_j N_k - N_i \sum_{k=1}^{M} \beta_{x_i,x_k} N_k + \sum_{j \ge i} b\left(x_i\right) N_j \bar{B}_{i,j}^{(1)} - b\left(x_i\right) N_i \quad (2.49)$$

$$\frac{dx_i}{dt} = \frac{1}{N_i} \sum_{\substack{j,k \\ v_i \le (x_j + x_k) \le v_{i+1}}}^{j \ge k} \left[1 - \frac{1}{2}\delta_{j,k}\right] \left[(x_j + x_k) - x_i\right] \beta_{x_j, x_k} N_j N_k - \frac{1}{N_i} \sum_{j \ge i} S\left(x_j\right) N_j \left[\bar{B}_{i,j}^{(v)} - x_i \bar{B}_{i,j}^{(1)}\right] \quad (2.50)$$

where

$$\bar{B}_{i,j}^{(1)} = \int_{v_i}^{v_{i+1}} P\left(v|x_j\right) dv \quad and \quad \bar{B}_{i,j}^{(v)} = \int_{v_i}^{v_{i+1}} vP\left(v|x_j\right) dv \quad (2.51)$$

Eq. 2.49 describes the time variation of $\mathrm{N_i}$ and looks similar to the one of the fixed pivot method. It also contains 4 terms (aggregation birth/death and breakage birth/death). However, the first and the third term are different compared to eq. 2.46. An important difference in the first term is the fact that the summation now involves aggregated particles that are formed between the class boundaries $\mathrm{v_i}$ and $\mathrm{v_{i+1}}$ (and not between the pivots as was the case in the fixed pivot approach). A similar difference occurs in the third term where the integrals (eq. 2.51) have different integration limits as the ones for $\mathrm{n_{i,k}}$ (eq. 2.48). A closer look at eq. 2.50 reveals that only 2 terms are responsible for changes of the pivots $\mathrm{x_i}$, one for aggregation birth and one for breakage birth. In fact, the equation is nothing but a determination of the average diameter (in this case volume) of every size class when new particles are born into them (also taking into account the ones that were already present). In this way, the pivots are allowed to move inside the class boundaries depending on the number and the volume of particles that are born into the class through either aggregation or breakage.

The technique was compared with the fixed pivot technique, but only for its additional features (Kumar and Ramkrishna, 1996b). It was found that the moving pivot technique did not overpredict the analytical solution (Scott, 1968) in the large particle size range, but instead a small underprediction was observed (Fig. 2.20). However, more importantly, the results for the moving pivot technique were much closer to the analytical solution compared to the fixed pivot technique with exactly the same grid. Further refinement of the grid improved the accuracy of the solution. It was concluded that the moving pivot is more accurate.

2.5.4 Kernel structures for aggregation

In this section, an overview will be given of the different kernel structures for aggregation that have been suggested in literature to describe flocculation processes and that can be adopted to describe the aggregation part of the activated sludge flocculation process. As mentioned before, aggregation is considered to be based on two distinct steps: transport and attachment. The former is described by the collision frequency, the latter by the collision efficiency (Thomas et al., 1999).

Collision frequency

As mentioned before, the transport of particles to one another can be brought about by three mechanisms: Brownian motion (*perikinetic flocculation*), imposed velocity gradients by mixing (*orthokinetic flocculation*) and differences in settling velocities (*differential sedimentation*).

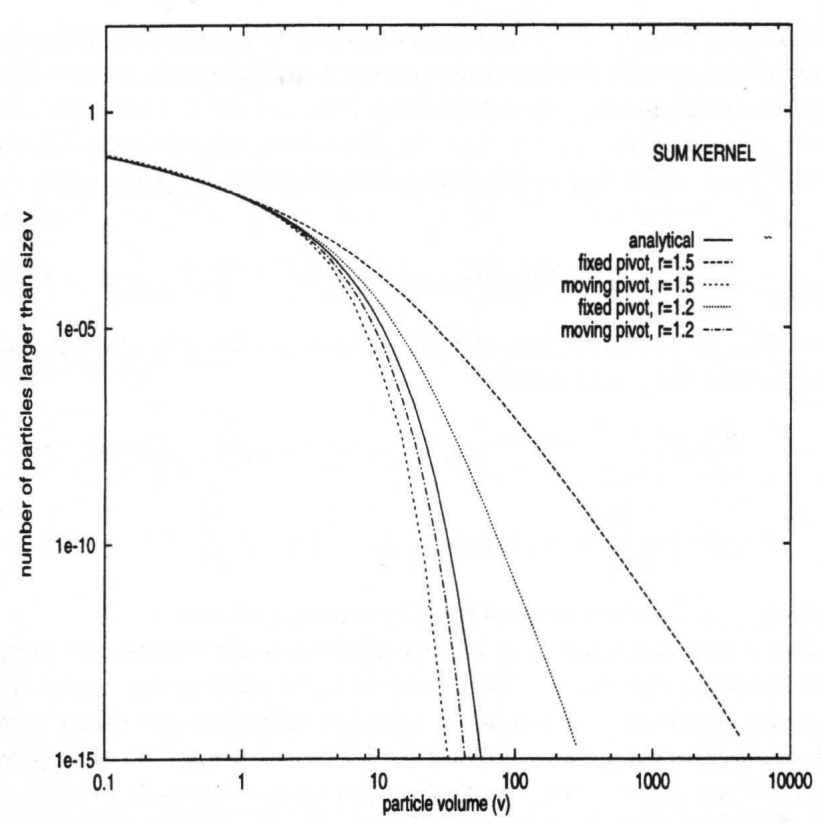

Figure 2.20: Comparison of the fixed and moving pivot techniques on the solution of the pure aggregation problem for the sum kernel (for different geometric grid factors r) with its analytical solution

The collision frequency of particles of sizes i and j for transport by Brownian motion is given by (Smoluchowski, 1917):

$$\beta(i,j)_{perikinetic} = \left(\frac{2kT}{3\mu}\right)\left(\frac{1}{d_i}+\frac{1}{d_j}\right)(d_i+d_j) \tag{2.52}$$

where k is Boltzmann's constant ($1.38.10^{-23}$ J.K^{-1}), T the absolute temperature of the fluid and μ the dynamic fluid viscosity. This type of flocculation is important for relatively small particles ($< 1\,\mu$m) and is, therefore, often not considered to be important in activated sludge flocculation compared to the order of magnitude of the other transport mechanisms.

Smoluchowski (1917) proposed the following expression for the orthokinetic transport of particles of sizes i and j induced by *laminar shear*

$$\beta(i,j)_{orthokinetic} = \frac{1}{6}\frac{du}{dy}(d_i+d_j)^3 \tag{2.53}$$

where $\mathrm{du/dy}$ is the velocity gradient of the fluid perpendicular to the flow direction. Before describing expressions for *turbulent shear*, a brief introduction to turbulent flow is necessary. For more detailed information concerning turbulence, the reader is referred to the literature (e.g. Bradshaw (1978)).

Turbulent flow consists of a 'continuum of eddies' (i.e. turbulent length scales) ranging in size from the dimensions of the turbulence generating device (e.g. the impeller blade) to the Kolmogorov microscale

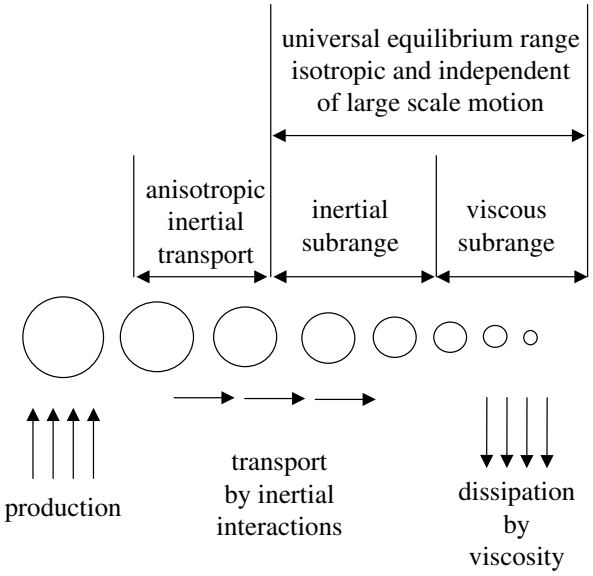

Figure 2.21: Idealized visualization of turbulent length scales (after Stanley and Smith (1995))

(will be defined later). An eddy can be considered as a component of the fluid motion which is characterised by different velocities $\Delta \mathrm{u}(\mathrm{l})$ and by the distance l over which these velocities change significantly (scale of eddy motion). Eddies of a scale approximating the size of the particles control the aggregation process. The eddy sizes in a turbulent flow can be separated into three groups:

- energy containing eddies
- inertial subrange
- viscous subrange

Energy containing eddies (also called the macro scale of turbulence) in a stirred vessel are generated by the impeller, and their length scale (l=L) is expected to be roughly the same order as the size L of the impeller blade. The impeller provides these large scale eddies with a certain amount of kinetic energy per unit mass. The large scale eddies do not loose energy to viscous dissipation since the Reynolds numbers are large for the fluid motion with these length scales. However, they produce smaller eddies for which the Reynolds number rapidly decreases with decreasing length scale l. At a certain value of l=η (Kolmogorov microscale of length), the Reynolds number becomes approximately unity, meaning that in these regions viscous forces begin to have a noticeable effect on the fluid motion. Kolmogorov scale eddy motion is accompanied by dissipation of energy, which is continuously withdrawn from the large scale motion. Hence, there is a continuous transfer of energy from large scale eddies to small scale eddies until Kolmogorov microscale eddies, where energy is converted into heat. This is illustrated in Fig. 2.21. The parameters determining the smallest scale of motion (or Kolmogorov microscale) are the energy dissipation rate per unit mass ϵ and the kinematic viscosity ν. The Kolmogorov microscale of length is given by

$$\eta = \left(\frac{\nu^3}{\epsilon} \right)^{1/4} \tag{2.54}$$

Table 2.4: Conversions between G, ϵ and η (using eq. 2.54 and 2.3) for $\nu = 1.005\,\mathrm{m^2 s^{-1}}$

G ($\mathrm{s^{-1}}$)	$\eta(\mu\mathrm{m})$	$\epsilon(\mathrm{m^2.s^{-3}})$
1	1002	1.005E-6
10	317	1.005E-4
50	142	2.513E-3
100	100	1.005E-2
200	71	4.020E-2
500	45	2.513E-1

Table 2.5: Eddy subranges with corresponding expressions for the differential velocity fluctuations (from Kusters (1991))

subrange	eddy size l	$\Delta\, u(l)$
viscous	$l < 10\eta$	$\left(\frac{1}{15}\right)^{1/2} \left(\frac{\epsilon}{\nu}\right)^{1/2} l$
inertial	$10\eta \leq l < L/2$	$1.37\,(\epsilon\, l)^{1/3}$
macro	$L/2 \leq l \approx L$	$\sqrt{2}\,(\epsilon\, L)^{1/3}$

Table 2.4 gives examples of the conversions between G, ϵ and η (by means of eq. 2.54 and 2.3).

The *inertial subrange* is the range of eddies intermediate between the large scale eddies and the Kolmogorov microscale. They merely transfer energy between large and small scale eddies and are, therefore, only governed by the energy transfer rate ϵ.

Because of their importance in the transport of aggregating particles, Kusters (1991) derived expressions for the differential velocity fluctuations $\Delta\mathrm{u(l)}$ (i.e.the velocity difference over a distance l) for the three regions and also defined a range of length scales in which they are valid. These expressions are summarised in Table 2.5 Saffman and Turner (1956) derived the collision rate of particles of sizes i and j from the flux of particles j into the collision envelope (or collision sphere or collision radius, i.e. the sum of the radii of the colliding particles) multiplied by the number concentration of particles i. Assuming *homogeneous* and *isotropic* turbulent flow, they found

$$\beta(i,j)_{orthokinetic} = (8\pi)^{1/2} \left(a_i + a_j\right)^2 \Delta\, u(a_i + a_j) \tag{2.55}$$

where a_i and a_j are the respective particle radii. This expression reveals that the orthokinetic flocculation rate is function of the collision radius ($\mathrm{a_i + a_j}$) and the velocity difference over the latter ($\Delta\mathrm{u}$). The differential velocity fluctuation expressions from Table 2.5 can be substituted in eq. 2.55 to obtain expressions for the particle transport in the different turbulent subranges. Only the expression for the viscous subrange is given here since the sludge floc size range is in this length scale for typical energy

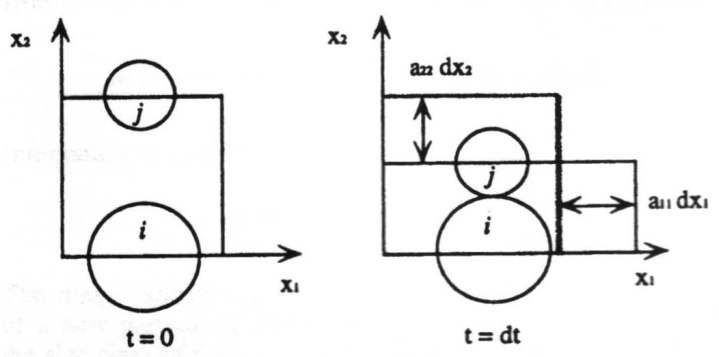

Figure 2.22: Pure normal-strain motion of a fluid element (from Kramer and Clark (1997))

dissipation rates:

$$\beta(i,j)_{orthokinetic} = 1.29 \left(\frac{\epsilon}{\nu}\right)^{1/2} (a_i + a_j)^3 \tag{2.56}$$

This expression was adopted to model various aggregating systems (Flesch et al., 1999; Kusters et al., 1997).

Camp and Stein (1943) obtained a similar result for the viscous subrange to the above mentioned more rigorous equation derived by Saffman and Turner (1956) by substitution of $(\epsilon/\nu)^{1/2}$ for the velocity gradient ($\frac{\mathrm{du}}{\mathrm{dy}}$) in Smoluchowski's equation for laminar shear (eq. 2.53). They defined the *absolute velocity gradient G* as

$$G = (\epsilon/\nu)^{1/2} \tag{2.57}$$

and obtained a similar expression as Saffman and Turner (1956), but with a different coefficient (1.33 versus 1.29)

$$\beta(i,j)_{orthokinetic} = \frac{4}{3} G (a_i + a_j)^3 \tag{2.58}$$

This expression has been widely used for modelling a variety of aggregating systems (both biological and inorganic) in turbulent environments (Koh et al., 1987; Serra et al., 1997; Serra and Casamitjana, 1998; Biggs and Lant, 2001).

Eq. 2.58 was questioned by several authors (Cleasby, 1984; Clark, 1985; Kramer and Clark, 1997). Cleasby (1984) concluded that G is only a valid parameter for the flocculation of particles smaller than the Kolmogorov microscale, which is not common in water and wastewater treatment. Kramer and Clark (1997) argued that the global or average velocity gradient should not be used to calculate collision rates. Instead, a new concept called the maximum principal strain rate $\mathrm{a}'_{\max}$ was introduced (see also Appendix A). The motion of a fluid element and the forces acting on it generate velocity gradients across the surfaces of the element. This can be expressed by the velocity gradient tensor, which includes the 9 partial derivatives of the velocity components to the spatial coordinates (for a 3D system). This tensor can be separated into symmetric and antisymmetric components, respectively corresponding to the strain-rate tensor and the rotational tensor. The former results in distortion of the fluid element, changing the relative position of particles present in the fluid element. The distortion can either be due to

- normal strain motion (Fig. 2.22), where the fluid element is compressed in direction x_2 and elongated in direction x_1 caused by the normal strain rate components $\mathrm{a}_{11} - \mathrm{a}_{22}$

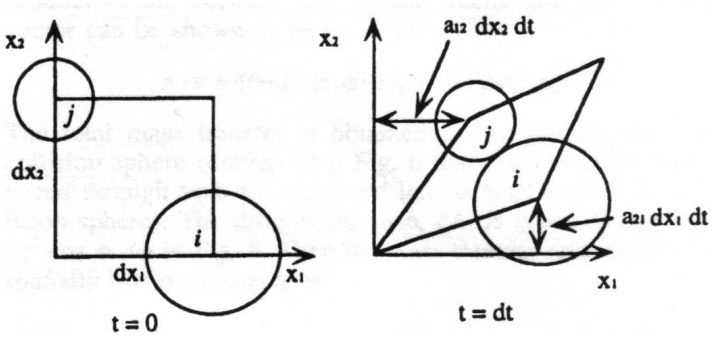

Figure 2.23: Pure shear-strain motion of a fluid element (from Kramer and Clark (1997))

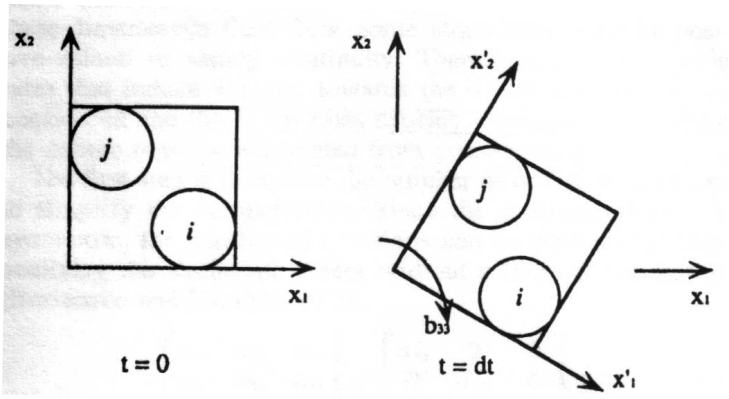

Figure 2.24: Rotating motion of a fluid element (from Kramer and Clark (1997))

- shear strain motion (Fig. 2.23), where the fluid element is distorted by the shear strain rate components $\mathrm{a}_{12} - \mathrm{a}_{21}$
- a combination of both

The rotational tensor should not be considered since it does not change the relative position of two particles comprised in the fluid element as illustrated by Fig. 2.24. Derivation of the collision rate resulted in

$$\beta(i,j)_{orthokinetic} = \frac{4\pi}{3} a_{lm} \left(a_i + a_j\right)^3 \tag{2.59}$$

where a_{lm} represents the elements of the strain-rate tensor, resulting in 9 equations (one for each combination of l and m, which can both take values 1, 2 and 3; see Appendix A). In order to decrease the number of equations and to correct for the fact that only strain-rates causing movement of particles toward each other should be considered, some extra steps are required. Since the strain-rate tensor is symmetric, it can be diagonalised resulting in the principal strain-rates that act in the principal directions (using principal component analysis (PCA)). The absolute value of the largest component (of the largest and smallest principal component) allows for computation of the equivalent value of mass entering the collision sphere. This is called the *maximum principal strain rate* and results in the following collision rate (see Appendix A)

$$\beta(i,j)_{orthokinetic} = \frac{4\pi}{3} \left|a'_{max}\right| \left(a_i + a_j\right)^3 \tag{2.60}$$

Lee et al. (2000) introduced fractal theory in their conceptual framework called the coalesced fractal sphere assumption (CFS) and suggested the following expression for orthokinetic flocculation of fractal aggregates

$$\beta(i,j) = \frac{\bar{G}}{\pi} v_0^{1-\frac{3}{Df}} \left(v_i^{\frac{1}{Df}} + v_j^{\frac{1}{Df}} \right)^3 \tag{2.61}$$

This expression was successfully used by Ducoste (2002) for modelling aggregation in a water treatment process.

Finally, based on Stokes' law, Camp and Stein (1943) proposed the collision frequency for differential sedimentation to be

$$\beta(i,j)_{differential} = \frac{g\pi}{72\mu}(\rho_p - \rho_l)\left(d_i + d_j\right)^3 |d_i - d_j| \tag{2.62}$$

where g is the gravity constant and ρ_p and ρ_l are the particle and fluid densities. Note that this assumes both particles to have the same density, which is not true for fractal particles.

It is commonly assumed that the three mechanisms for interparticle collisions are independent and that their collision frequency functions are additive (Han and Lawler, 1992)

$$\beta(i,j) = \beta(i,j)_{perikinetic} + \beta(i,j)_{orthokinetic} + \beta(i,j)_{differential} \tag{2.63}$$

Collision efficiency

The collision frequencies described in the previous section were based on a *rectilinear* view of collisions, i.e. one that ignores the short-range forces and changes in fluid motion as particles approach one another. This means that all collisions are successful, being one of the assumptions made by Smoluchowski (1917), which is clearly unrealistic. In order to account for short-range forces a *curvilinear* approach, taking into account hydrodynamic effects and attractive/repulsive forces of charged particles, is needed. Possible particle trajectories for both approaches are given in Fig. 2.25. The collision efficiency describes the probability of successful collisions and, therefore, has a value between 0 and 1 (Thomas et al., 1999). In the rectilinear approach, all particles whose centers penetrate the collision envelope (sum of the particle radii) are captured. In the curvilinear case, this collision envelope becomes a lot smaller. The latter has consequences for the relative importance of the three transport mechanisms that were described above. Han and Lawler (1992) concluded that orthokinetic flocculation became far less important. The combined effect of electrostatic repulsion and van der Waals attraction between particles is described by the DLVO theory, which has been discussed earlier (section 2.4.2). This theory describes the attraction/repulsion forces as function of the interparticle distance (Fig. 2.10).

Adler (1981a) was the first to apply the theory of hydrodynamic interactions to heterodispersed systems. The author showed, using equations based on laminar flow, that in the presence of a combination of hydrodynamic, electrostatic and van der Waals forces, collision frequencies were highest when colliding particles were of the same size. The same author concluded that this had led to an overestimation of flocculation collision frequencies.

Over the past decades, the modelling of the hydrodynamic forces between colliding particles has tried to pertain to a more realistic definition of aggregate structures. Rogak and Flagan (1990) represented the flow around self-similar clusters of spheres by the superposition of single-sphere velocity fields in order to calculate the Stokes drag. Veerapaneni and Wiesner (1996) calculated the flow and associated drag on a sphere with nonuniform porosity and, hence, permeability. They concluded that the resistance to the

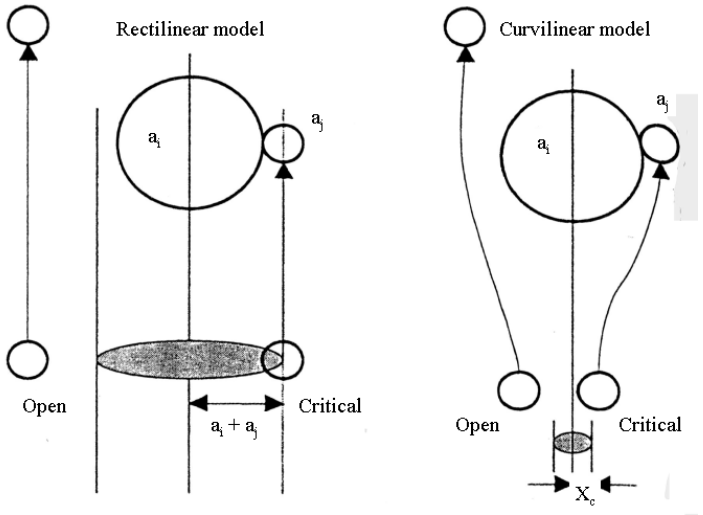

Figure 2.25: Possible particle trajectories for rectilinear and curvilinear approaches (from Han and Lawler (1992))

fluid flow through the aggregate increases with increasing fractal dimension, while the fluid collection efficiency decreased. Hsu and Hsieh (2003) concluded that for the same volume-averaged permeability, the drag coefficient of a spherical floc with a non-homogeneous structure is much larger than that of a floc with a homogeneous structure. Chung et al. (2003) developed a technique to measure the hydrodynamic drag force exerted on an activated sludge floc.

Li and Logan (1997b) measured permeabilities and collision frequencies of fractal aggregates with small particles by differential sedimentation. Their calculated aggregate permeabilities from measured settling velocities were 3 orders of magnitude larger than predicted by a permeability model based on homogeneous distribution of primary particles within the aggregates. They developed a permeability model based on the Brinkman equation to describe permeability as a function of aggregate size. Collision frequencies were 1 order of magnitude higher than predicted by a curvilinear model and about 2 orders of magnitude lower than predicted by a rectilinear model. In a similar study for microbial aggregates Li and Yuan (2002) found lower fluid collection efficiencies, but higher removal efficiencies compared to non-microbial systems. The former was argued to be caused by EPS material clogging the pores, whereas the latter might be addressed to the more narrow nature of the internal flow passages. Similar studies were conducted in turbulent shear conditions (Li and Logan, 1997a; Serra and Logan, 1999). Collision frequencies were found to be as much as 2 orders of magnitude smaller than values predicted by a rectilinear model and as much as 5 orders of magnitude higher than predicted by a curvilinear model. These results demonstrate that fractal aggregates of particles collide much more frequently than expected based on spherical-particle flocculation and based on impermeable spheres.

Others have focused on fluid mechanics of porous, fractal aggregates (Adler, 1981b,a; Chellam and Wiesner, 1993). Adler (1981b) calculated streamlines in and around porous particles, whereas Adler (1981a) calculated capture cross sections and collision frequencies numerically. Chellam and Wiesner (1993) suggested to use a rectilinear model for fractal dimensions up to 2 and a curvilinear model for D_f larger than 2.3. Kusters et al. (1997) used the results of Adler (1981a) in terms of the flow number, being the ratio of hydrodynamic shear forces to van der Waals forces between colliding particles, and the ratio

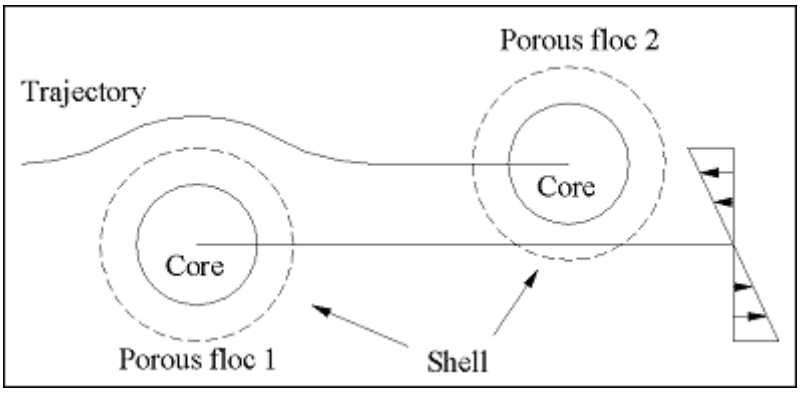

Figure 2.26: The concept of the shell-core model (from Kusters et al. (1997))

of particle sizes to propose an expression for the collision efficiency of impermeable porous flocs

$$\alpha_{i,j} = \alpha_0 \left[\left(\frac{3\pi\mu \left(d_i + d_j\right)^3 G}{32 A_{ham}} \right) \left(\frac{1}{d_0 \left(\frac{1}{d_i} + \frac{1}{d_j} \right)} \right) \right]^{-0.18} \tag{2.64}$$

where $\mathrm{A_{ham}}$ is the Hamaker constant (3.10^{-17} J) and $\mathrm{d_i}$ is the floc diameter. However, when the flocs are considered to be permeable, implying that liquid can flow through the flocs, the forces for the large particles will be considerably smaller. Kusters et al. (1997) tackled this problem by introducing the shell-core model (SCM) concept, which approximates the floc as a spherical body with an impermeable core and a completely homogeneous, permeable shell (Fig. 2.26). The outer collision radius r of the floc represents the distance within which another floc must approach for collision to occur, whereas the smaller core radius describes the drag the floc experiences in the flow field. The latter corresponds to the hydrodynamic radius $\mathrm{r_H}$ which is approximated by

$$\frac{r_H}{r} = \frac{1 - \xi^{-1} tanh(\xi)}{1 + \frac{3}{2}\xi^{-2} - \frac{3}{2}\xi^{-3} tanh(\xi)} \tag{2.65}$$

where ξ represents the dimensionless normalised diameter or Debye's shielding ratio

$$\xi = \frac{r}{\sqrt{\kappa}} \tag{2.66}$$

where κ is the permeability of the porous floc. The latter is function of porosity and the structure of the medium, which is normally represented by a packing factor (Veerapaneni and Wiesner, 1996). A frequently used model is the model of Happel (1958)

$$\kappa = \frac{3 - \frac{9}{2}\varphi^{1/3} + \frac{9}{2}\varphi^{5/3} - 3\varphi^2}{9\varphi\left(3 + 2\varphi^{5/3}\right) C_s} 2a^2 \tag{2.67}$$

where a is the primary particle radius, $\mathrm{C_s}$ a constant accounting for the short-range interactions and φ represents the floc density which, for a fractal aggregate, is given by

$$\varphi = \varphi_0 \left(r/a_0\right)^{D_f - 3} \tag{2.68}$$

where φ_0 represents the packing density and $\mathrm{a_0}$ the primary particle radius. A similar expression as the one proposed by Adler (1981a) can be written for the collision efficiency by using the hydrodynamic radius:

$$\alpha = \alpha_0 \left[\left(\frac{6\pi\mu r_{H,i}^3(\lambda_H + 1)G}{8A} \right) \left(\frac{2\lambda_H r_{H,i}}{a_0(\lambda_H + 1)} \right) \right]^{-0.18} \tag{2.69}$$

where $\lambda_\mathrm{H} = \mathrm{r_{H,j}}/\mathrm{r_{H,i}}$ and α_0 a constant. The model was successfully used to model the aggregation of a polystyrene system. Ducoste (2002) used a similar expression for modelling flocculation in a water treatment process.

2.5.5 Kernel structures for breakage

Breakup of particles is expected to be brought about by hydrodynamic stresses acting on the particles. Breakup through collisions between particles is questionable since no concentration dependencies on the breakage rate have been observed (Kusters, 1991). Two distinct breakage mechanisms have been proposed (Parker et al., 1972; Pandya and Spielman, 1983; Thomas et al., 1999):

- Floc splitting – due to bulk stresses induced within the aggregate structure by instantaneous turbulent velocity differences across the aggregate;
- Surface erosion – due to surface shearing stresses arising from the turbulent fluid drag

To propose criteria for floc breakup Kusters (1991) determined the magnitude of both types of stresses in the different turbulent regimes and compared them with the floc strength. Parker et al. (1970) only considered surface erosion in the viscous and inertial subrange of turbulence when writing down a balance for primary particles. The same authors used the concept of maximum stable floc size to determine which flocs are susceptible to surface shear (see section 2.4.1).

Breakage frequency

Parker et al. (1970) stated that the frequency of primary particle erosion from metastable flocs (i.e. flocs larger than the maximum stable floc size) is related to the frequency of the disturbance. The disturbance is closely related to the action of the eddy producing maximum shear, and, therefore, the disturbance frequency b is close to the eddy frequency. In the inertial subrange, this frequency was determined to be

$$b_{erosion,inertial} = \frac{\beta^{\frac{1}{2}} \epsilon^{\frac{1}{3}}}{\left[\frac{2}{k_f}\right]^{\frac{2}{3}} d_m^{\frac{2}{3}}} \tag{2.70}$$

where β is a constant, $\mathrm{k_f}$ the turbulent drag friction and $\mathrm{d_m}$ the metastable floc diameter. For the viscous subrange, Parker et al. (1970) found

$$b_{erosion,viscous} = \delta^{\frac{1}{2}} \left(\frac{\epsilon}{\nu}\right)^{\frac{1}{2}} \tag{2.71}$$

where δ is a constant combining several constants, see Parker et al. (1970). The same authors did not determine a breakage frequency due to floc splitting. Pandya and Spielman (1983) described the instantaneous rate of change of the volume of a parent floc of size v due to erosion by

$$b_{erosion}(v) = -kG \left(\frac{v_p}{\bar{v}_e}\right) \tag{2.72}$$

where k is the erosion rate coefficient, $\mathrm{v_p}$ is the mean of all erosion product particles and $\bar{\mathrm{v}}_\mathrm{e}$ is the mean erosion product particle size over the entire size range. The latter 2 are determined by the daughter size distribution of erosion product particles (see next section).

The breakage frequency for splitting has been described by a power law function of the particle size v for various systems (Pandya and Spielman, 1983; Ramkrishna, 2000; Spicer and Pratsinis, 1996a; Biggs and Lant, 2001)

$$b_{splitting} = Av^a \tag{2.73}$$

where A and a are coefficients to be determined experimentally. The first coefficient is found to be positively correlated with the velocity gradient G (Spicer and Pratsinis, 1996a; Biggs and Lant, 2001; Pandya and Spielman, 1983). Spicer and Pratsinis (1996a) and Biggs and Lant (2001) took a to have a value of 1/3, assuming the breakage rate to be proportional to the floc diameter. Pandya and Spielman (1983) estimated this parameter using experimental data and found a similar value.

As mentioned before, Kusters (1991) determined values of fluid velocity differences across a certain length scale l ($\Delta\mathrm{u(l)}$). When the velocity difference across the diameter d of a particle exceeds a certain critical value ($\Delta\mathrm{u_b(d)}$), the particle will break up. Assuming the probability density function for occurrence of velocity differences to be Gaussian, the breakage frequency (i.e. the probability that $\Delta\mathrm{u(l)}$ exceeds $\Delta\mathrm{u_b}$) is given by

$$b_{splitting} = \left(\frac{2}{\pi}\right)^{\frac{1}{2}} \frac{\Delta\, u}{d} exp\left(\frac{-\Delta\, u_b^2}{2\Delta\, u^2}\right) \tag{2.74}$$

Expressions for the different turbulent subranges can be derived by using the velocity differences in Table 2.5. For the viscous subrange, this yields the following expression for particles smaller than the Kolmogorov microscale and used by several authors (Ducoste, 2002; Flesch et al., 1999)

$$b_{splitting}\,(x) = \left(\frac{4}{15\pi}\right)^{1/2} \left(\frac{K_i\bar{\epsilon}}{\nu}\right)^{1/2} exp\left(\frac{-C_1}{dK_i\bar{\epsilon}}\right) \tag{2.75}$$

where $\mathrm{K_i}$ is the ratio between the local energy dissipation rate ϵ and the average energy dissipation rate $\bar{\epsilon}$ and $\mathrm{C_1}$ is a constant.

Ducoste (2002) used another expression for the large-scale breakup frequency borrowed from Ducoste and Clark (1998b). In this approach, which was derived from turbulence measurements in the impeller discharge region, the magnitude of the root mean square velocity difference across the particle diameter was approximated by the product of the tip speed and $\mathrm{N_p^{0.5}}$ (with $\mathrm{N_p}$ the dimensionless impeller power number which can be derived from power curves).

Daughter size distribution

Since Parker et al. (1970) only included surface erosion, the daughter size distribution was developed from the peeling-off of the outer unstable layers of the metastable floc. They assumed sphericity and determined the number of primary particles liberated by erosion as the total volume of primary particles in the outer layer divided by the volume of a primary particle, multiplied by an erosion success factor

$$N_1 = 3\sigma^{\frac{2}{3}} k\pi_{\frac{1}{3}} \left(\frac{d_{max}}{2a_0}\right)^2 \zeta \tag{2.76}$$

where σ is the fraction of floc volume that is primary particles, k is a particle arrangement factor and r_m and r_1 are the metastable and primary particle radii, respectively. Pandya and Spielman (1983) used a

log-normal probability distribution for the erosion product

$$p_e(v) = \frac{1}{v\sqrt{2\pi} ln \sigma_{ge}} exp\left[\frac{-\left(ln\, v - ln\, \bar{v}_{ge}\right)^2}{2ln^2\sigma_{ge}}\right] \tag{2.77}$$

where $\bar{v}_{ge}$ and σ_{ge} are the geometric mean and the geometric standard deviation of the erosion product, respectively, taken to be independent of parent floc size v. The same authors showed that a Gaussian probability distribution for the erosion proved to be worse on the basis of experimental data. Another interesting finding of Pandya and Spielman (1983) was that the mean erosion product size was 5-10 times that of the primary particles, suggesting that the erosion product consists of small clusters rather than primary particles.

For floc splitting, several expressions have been used. Binary fragmentation into equal fragments can, for a geometric grid with factor 2, be described as (Flesch et al., 1999; Biggs and Lant, 2001)

$$\begin{aligned} P(v|v') &= \tfrac{v_j}{v_i} \quad j = i+1 \\ P(v|v') &= 0 \quad j \neq i+1 \end{aligned} \tag{2.78}$$

This approach is easy to use, but probably not close to reality.

Others (Pandya and Spielman, 1983; Flesch et al., 1999) have successfully used a normal distribution for the daughter size distribution resulting from a splitting event

$$P(v|v') = \frac{1}{\sqrt{2\pi}\sigma_s(v')} exp\left[\frac{-\left(v - \bar{v}_s(v')\right)^2}{2\sigma_s^2(v')}\right] \tag{2.79}$$

Other possible daughter size distributions have been proposed

- Power law — $v(v')P(v|v') = (\eta+2)\frac{v^\eta}{v'^{\eta+1}}$ (η is a constant)
- Equal size kernel — $v(v')P(v|v') = \eta\,\delta\left(v - \frac{v'}{\eta}\right)$ (η is a constant)
- Uniform kernel — $v(v')P(v|v') = \frac{2}{v'}$
- Sum kernel — $v(v')P(v|v') = \frac{(m+1)}{v'}\left[\left(\frac{v}{v'}\right)^m + \left(1 - \frac{v}{v'}\right)^m\right]$ (m is a constant)

2.5.6 Self-similarity and the inverse problem

The determination of quantitative scientific information from experimental observations can be obtained by solving the so-called *inverse problem*. In the case of population balances, the inverse problem allows the extraction of the aggregation frequency, the breakage frequency and the daughter size distribution from measurements of transient size distributions in either aggregation or breakage experiments. The approaches discussed here take advantage of the self-preserving or *self-similar* distributions. The latter will be discussed first before elaborating further on the solution of the inverse problem.

Similarity behaviour of population balance equations

The self-similar solution of a PBE identifies invariant domains in the space of the independent variables along which the solution remains the same or contains a part that is the same (Ramkrishna, 2000). When $\mathrm{f_1(x,t)}$ satisfies (i.e. is a solution of) a population balance equation such as eq. 2.15, a self-similar solution would be of the form:

$$f_1(x,t) = g(t)\Psi(\eta) \qquad \eta \equiv \frac{x}{h(t)} \tag{2.80}$$

where η is the similarity variable and the scaling functions $\mathrm{g(t)}$, $\mathrm{h(t)}$ as well as $\Psi(\eta)$ are as yet unknown but assumed to be nonnegative, smooth and bounded functions. Hence, the time-dependent solution $\mathrm{f_1(x,t)}$ is written as a product of a time-variant function (g(t)) and a time-invariant function, which is function of the similarity variable (i.e. scaled x) only. $\Psi(\eta)$ remains constant along the invariant curve $\eta = \mathrm{c}$ in the $\mathrm{(x,t)}$-plane. In other words, the rescaling of $\mathrm{f_1(x,t)}$ at different time instants causes all distributions to collapse into one single distribution.

For the cumulative mass fraction $\mathrm{F_1(x,t)}$ defined as

$$F_1(x,t) = \frac{\int_0^x x' f_1(x',t)dx'}{\int_0^\infty x' f_1(x',t)dx'} \tag{2.81}$$

the self-similar form will lead to (see appendix B.2)

$$F_1(x,t) = \frac{\int_0^\eta \eta'\Psi(\eta')d\eta'}{\int_0^\infty \eta'\Psi(\eta')d\eta'} \equiv \Phi(\eta) \tag{2.82}$$

This reveals that the cumulative distribution is itself time-invariant along $\eta = c$ (g(t)=1) and, hence, is a direct candidate for the self-similar solution of the population balance equation.

The functions $\mathrm{g(t)}$, $\mathrm{h(t)}$ and $\Psi(\eta)$ must clearly depend upon the structure of the PBE. Depending on the singularity behaviour of the self-similar form ($\Psi(\eta)$) near the origin (since $\mathrm{f_1(x,t)}$ usually vanishes for large x), expressions for the aforementioned functions $\mathrm{g(t)}$ and $\mathrm{h(t)}$ can be written down in terms of higher integral moments (see appendix B.1)

$$h(t) = \frac{\mu_{k+1}(t)}{\mu_k(t)} \qquad g(t) = \frac{[\mu_k(t)]^{k+2}}{[\mu_{k+1}(t)]^{k+1}} \tag{2.83}$$

provided that

$$\int_0^\infty \eta^k \Psi(\eta)d\eta = \int_0^\infty \eta^{k+1}\Psi(\eta)d\eta = 1 \tag{2.84}$$

The value of k depends on the order of singularity of $\Psi(\eta)$, which determines the existence of the integrals in eq. 2.84. The determination of k must proceed through trial and error. When k is found to be 0, the scaling function $\mathrm{h(t)}$ turns out to be the *average particle mass*. A more in depth discussion about this can be found in Wright and Ramkrishna (1992).

The question whether a population balance equation has a self-similar solution can be answered through what is known as *similarity analysis*. These analyses are somewhat different for pure aggregation, pure breakage and combined cases. They will be shortly discussed.

Pure breakage — The population balance equation for pure breakage in terms of cumulative volume fraction can be written as (Ramkrishna, 2000)

$$\frac{\partial F_1(x,t)}{\partial t} = \int_x^\infty b(x')G(x|x')\partial_{x'}F_1(x',t) \tag{2.85}$$

where $\mathrm{F_1(x,t)}$ is given by eq. 2.81 and $\mathrm{G(x|x')}$ is the cumulative volume fraction of particles of size less than or equal to x formed from the breakage of a particle of size $\mathrm{x'}$:

$$G(x|x') \equiv \frac{v(x')}{x'} \int_0^x \xi P(\xi|x') d\xi \tag{2.86}$$

It can be shown that under the conditions of a power law breakage rate, i.e. $\mathrm{b(x) = kx^n}$, and similar breakage, i.e. $\mathrm{G(x|x') = g(x/x')}$, eq. 2.85 admits a similarity transformation ($\mathrm{F_1(x,t) \rightarrow \Phi(\eta)}$, the latter being the self-similar form of the former) of the form $\mathrm{\eta = x^n t}$ (Ramkrishna, 2000). This form of self-similarity can be generalised somewhat to accommodate more general breakage frequencies (i.e. not only the power law) by assuming

$$G(x|x') = g\left(\frac{b(x)}{b(x')}\right) \tag{2.87}$$

In this case, the similarity transformation is of the form $\mathrm{\eta = b(x)t}$ giving rise to the following PBE in terms of the similarity variable η (see appendix B.3)

$$\eta\Phi'(\eta) = \int_\eta^\infty g\left(\frac{\eta}{\eta'}\right) \eta'\Phi'(\eta') d\eta' \tag{2.88}$$

which is not restricted to power law breakage only.

Narsimhan et al. (1980) developed a procedure to test experimental data for this type of similarity. If the similarity transformation $\mathrm{\eta = b(x)t}$ is valid, for a fixed value of $\mathrm{F_1(x,t)}$, x and t would be related by $\mathrm{b(x)t = constant}$, since the similarity variable would be constant at constant $\mathrm{F_1}$. Differentiating with respect to x yields

$$t\frac{db(x)}{dx} + \left(\frac{\partial t}{\partial x}\right)_{F_1} b(x) = 0 \tag{2.89}$$

where the subscript $\mathrm{F_1}$ in the second term on the left-hand side stresses that this derivative should be taken at a fixed value of $\mathrm{F_1}$, and hence is function of $\mathrm{F_1}$. Multiplying by x and rearranging yields

$$\frac{d\,ln\,b(x)}{d\,ln\,x} = -\left(\frac{\partial\,ln\,t}{\partial\,ln\,x}\right)_{F_1} \tag{2.90}$$

Eq. 2.90 provides the test of the similarity hypothesis. Since the left hand side of the equation is indepedent of F_1, so should be the right hand side. This means that for a plot of $\mathrm{\ln t}$ versus $\mathrm{\ln x}$ for various values of $\mathrm{F_1(x,t)}$ from the experimental data, the slopes of these various curves at any value of x should be independent of $\mathrm{F_1}$. This implies that a translation along the $\mathrm{\ln t}$ axis must result in one single collapsed curve (Narsimhan et al., 1980). This translation requires the choice of a reference curve into which all other curves would be translated and the choice of a reference particle volume for the translation. Sathyagal et al. (1995) proposed an alternative method based on the arc length and the curvature after fitting quadratic curves to the data to smooth out experimental error.

In addition, if the experimental data show this similarity behaviour, the collapsed curve gives additional information on the rate of breakage. Integrating eq. 2.90 yields

$$b(x) = b(x_0) exp\left[-\int_{ln\,x_0}^{ln\,x} \left(\frac{\partial\,ln\,t}{\partial\,ln\,x}\right)_{F_1} d\,ln\,x\right] \tag{2.91}$$

where $\mathrm{b(x_0)}$ is the unknown breakage rate of a particle of volume $\mathrm{x_0}$. The breakage rate is now determined up to a multiplicative constant. An example of a similarity distribution calculated from experimental data taken from Sathyagal et al. (1995) is shown in Fig. 2.27.

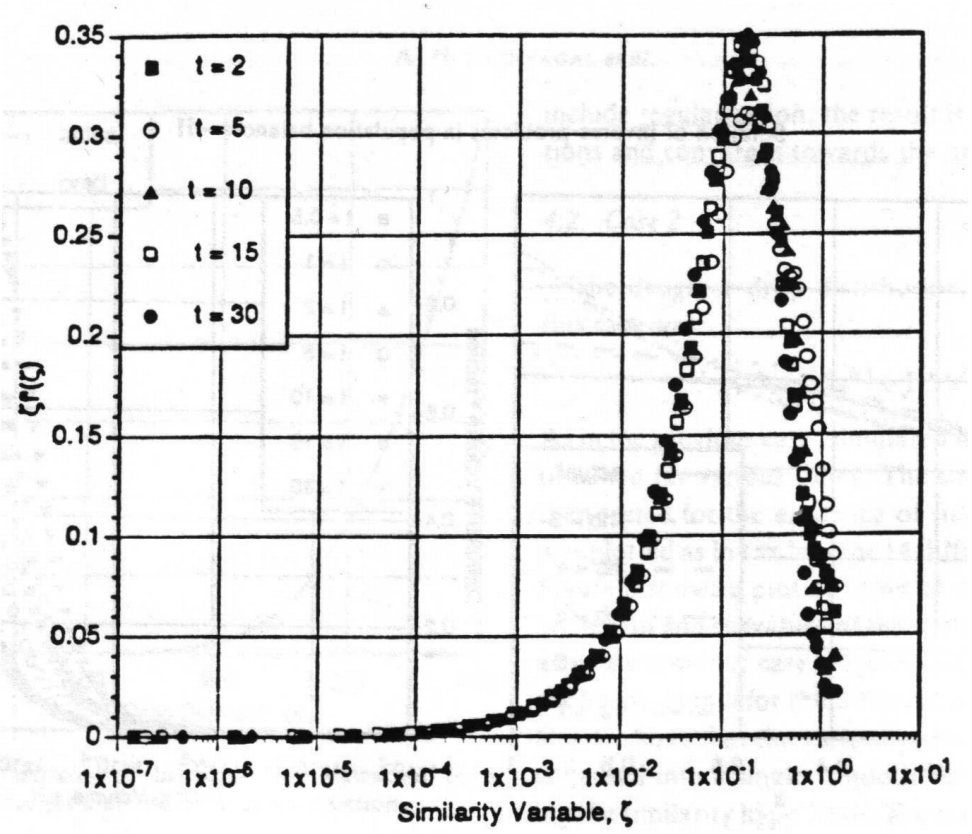

Figure 2.27: Example of a similarity distribution derived from experimental data (from Sathyagal et al. (1995))

Through this self-similar behaviour and collapse, the experimental noise can be reduced by fitting a curve to the collapsed self-similar data. Eq. 2.88 can now be used along with the collapsed curve to solve the inverse problem (instead of the original PBE and the dynamic 'noisy' data), which is a clear advantage.

Pure aggregation — The population balance equation for pure aggregation in terms of cumulative volume fraction can be written as (Ramkrishna, 2000)

$$\frac{\partial F_1(x,t)}{\partial t} = -\int_0^x \partial_\xi F_1(\xi,t) \int_{x-\xi}^{\infty} \frac{a(\xi,u)}{u} \partial_u F_1(u,t) \tag{2.92}$$

Substituting $F_1(x,t)$ by the self-similar form $\Phi(\eta)$ and insisting on time-independency yields the following condition necessary for self-similarity (Ramkrishna, 2000)

$$\frac{\partial}{\partial t}\left[\frac{a(\eta' h(t), \eta'' h(t))}{h'(t)}\right] = 0 \tag{2.93}$$

Hence, we may impose the general requirements that

$$a(\eta' h(t), \eta'' h(t)) = \alpha(\eta', \eta'') H(h(t)) \qquad h'(t) = cH(h(t)) \tag{2.94}$$

where c is a positive constant and H is any positive-valued function that remains to be specified. The positivity requirement on c and H is imposed so that the scaling size is increasing with time, since it is

presumably related to increasing the average particle size in an aggregating population. A homogeneous aggregation frequency

$$a(\lambda x, \lambda y) = \lambda^m a(x, y) \quad m \geq 0 \tag{2.95}$$

with m being the degree of homogeneity, clearly satisfies eq. 2.94 with $\mathrm{H(h)} = \mathrm{h^m}$ and $\mathrm{a}(\eta, \eta') = \alpha(\eta, \eta')$. The self-similar cumulative distribution satisfies the following integral equation (see Appendix B.4)

$$c\eta\Phi'(\eta) = \int_0^\eta d\Phi(\eta') \int_{\eta-\eta'}^\infty \frac{d\Phi(\eta'')}{\eta''} \alpha(\eta', \eta'') \tag{2.96}$$

which leads to the corresponding equation in the self-similar solution $\Psi(\eta)$

$$c\eta^2\Psi(\eta) = \int_0^\eta \eta'\Psi(\eta')d\eta' \int_{\eta-\eta'}^\infty \Psi(\eta'')\alpha(\eta', \eta'')d\eta'' \tag{2.97}$$

which has been solved for different types of aggregation kernels in literature (Ramkrishna, 2000).

The self-similarity study for the combined aggregation and breakage case will not be discussed here, but can be found in Ramkrishna (2000).

Inverse problems in Population Balances

Let us now return to the solution of the inverse problem. For the pure breakage case, eq. 2.91 still contains the not exactly known function $\mathrm{b(x_0)}$ and, therefore, the similarity variable $\eta = \mathrm{b(x)t}$ is also not explicitly known. However, a redefinition of the similarity variable as (through rewriting eq. 2.91)

$$\hat{z} = \frac{b(x)t}{b(x_0)} = exp\left[-\int_{ln\, x_0}^{ln\, x} \left(\frac{\partial\, ln\, t}{\partial\, ln\, x}\right)_{F1} d\, ln\, x\right] \tag{2.98}$$

results in an explicitly known similarity variable since the right hand side of eq. 2.98 can be obtained from the experimental data. The transformed cumulative PBE in the new similarity variable $\hat{\mathrm{z}}$ becomes (see appendix B.3)

$$\hat{z}\hat{\Phi}'(\hat{z}) = b(x_0) \int_z^\infty g\left(\frac{\hat{z}}{\hat{z}'}\right) \hat{z}'\hat{\Phi}'(\hat{z}')d\hat{z}' \tag{2.99}$$

which can be rewritten as (see appendix B.3)

$$\hat{z}\hat{\Phi}'(\hat{z}) = \beta \int_0^1 \frac{\hat{z}^2}{u^3}\hat{\Phi}'\left(\frac{\hat{z}}{u}\right) g(u)du \tag{2.100}$$

where u represents the ratio of the breakage rate of the fragment to that of the parent particle. Solving the inverse problem requires calculating the unknown function $\mathrm{g(u)}$ over the unit interval and the constant β given the self-similar curve in the form of $\hat{\Phi}'$ versus $\hat{\mathrm{z}}$. Since $\mathrm{g(u)}$ is a cumulative distribution function over the interval $0 \leq \mathrm{u} \leq 1$, the solution of eq. 2.100 for the function $\beta\mathrm{g(u)}$ at u=1 automatically yields the value of β as $\mathrm{g}(1) = 1$.

The solution of eq. 2.100 was accomplished by Sathyagal et al. (1995) by expanding the function $\beta\mathrm{g(u)}$ in terms of an appropriate set of basis functions as

$$\beta g(u) = \sum_{j=1}^{n_b} a_j G_j(u) \tag{2.101}$$

where $\mathrm{n_b}$ is the number of basis functions and $\mathrm{a} = \{\mathrm{a_1}, \mathrm{a2}, \ldots, \mathrm{a_{n_b}}\}$ are the coefficients of expansion. The similarity coordinate $\hat{\mathrm{z}}$ is discretised into several (m) discrete intervals $\hat{\mathrm{z}}_\mathrm{i}$ to get a corresponding discrete version of the self-similar distribution $\hat{\mathrm{z}}_\mathrm{i}\hat{\Phi}'(\hat{\mathrm{z}}_\mathrm{i})$ denoted by the vector Φ. The discrete version of the inverse problem becomes

$$\Phi = Xa \tag{2.102}$$

where X is a matrix which components are given by

$$X_{ij} = \int_0^1 \frac{\xi_i^2}{u^3}\Phi'\left(\frac{\xi_i}{u}\right) G_j(u)du \tag{2.103}$$

The solution of the discrete inverse problem is to seek a vector a by minimising the magnitude of the residual vector

$$min\left[\|Xa - \Phi\| + \lambda_{reg}\|a\|\right] \tag{2.104}$$

where λ_reg is a regularisation parameter introduced to cure the ill-posedness of the problem. The latter means that small errors in Φ will induce large errors in the vector a. The choice of the basis functions is strongly dependent on the behaviour of the similarity distribution. However, this is beyond the scope of this review but a discussion can be found in Sathyagal et al. (1995). The same authors successfully applied the techniques described above for the pure breakage case. They were able to recover different breakage kernels from dynamic experimental data produced by simulating models with chosen breakage kernels. Also, they determined the breakage functions for a real experimental data set.

Wright and Ramkrishna (1992) state the inverse aggregation problem starting from the following transformed PBE (see Appendix B.4)

$$\eta\Phi'(\eta) = \int_0^\eta d\eta'\Phi'(\eta')\int_{\eta-\eta'}^\infty d\eta''\frac{\Phi'(\eta'')}{\eta''}\frac{\alpha(\eta',\eta'')}{\langle\alpha\rangle} \tag{2.105}$$

where $\langle\alpha\rangle$ is the average value of the scaled aggregation frequency (Ramkrishna, 2000) and where $\alpha(\eta',\eta'')/\langle\alpha\rangle$ is the unknown function to be extracted. The solution of eq. 2.105 can be achieved by using the same methods that were used for solving the inverse problem for pure breakage. The unknown function $\alpha(\eta',\eta'')/\langle\alpha\rangle$ is expanded in a set of $\mathrm{n_b}$ basis functions

$$\frac{\alpha(\eta',\eta'')}{\langle\alpha\rangle} = \sum_{j=1}^{n_b} a_j A_j(\eta',\eta'') \tag{2.106}$$

The similarity variable η is discretised into $\mathrm{n_d}$ discrete intervals and a matrix X is defined as

$$X_{ij} \equiv \int_0^{\eta_i} d\eta\Phi(\eta)\int_{\eta_i-\eta}^\infty d\eta'\frac{\Phi(\eta')}{\eta'}A_j(\eta,\eta') \tag{2.107}$$

The discretised version of the inverse problem can again be written as

$$\Phi = Xa \tag{2.108}$$

and eq. 2.104 can be used to solve the inverse problem. For examples, the reader is referred to Wright and Ramkrishna (1992).

2.6 Floc sizing

In order to model the dynamics of activated sludge flocculation, one needs to be able to collect quantitative information concerning the floc size distribution. This has long been (and to a certain extent still is) the bottleneck in the attempt to understand the activated sludge flocculation process. To date, several tools have been developed to monitor populations of particles and their behaviour.

Early efforts were based on the analysis of sludge samples by microscopy (Parker et al., 1970; Barbusinski and Koscielniak, 1995). Later on, other techniques like image analysis (Li and Ganczarczyk, 1991), electron microscopy (Jorand et al., 1995) and Coulter counting (Li and Ganczarczyk, 1991; Andreadakis, 1993) were used. All aforementioned techniques (except Coulter counter) have the disadvantage of being time consuming and, hence, they are not suitable for on-line monitoring of activated sludge flocculation. Moreover, they require sample handling, which might affect floc properties. The Coulter counting technique exhibits the disadvantage of being limited to relatively small sizes, being prone to clogging when using activated sludge and requiring a sample treatment that affects the sample's ionic strength (which makes the measurement unreliable).

Recently, however, small angle laser light scattering (SALLS) has been extensively used to monitor floc size and structure (Jorand et al., 1995; Guan et al., 1998; Waite, 1999b; Bushell and Amal, 2000; Biggs and Lant, 2001; Selomulya et al., 2001; Wu et al., 2002; Wilén et al., 2003; Govoreanu et al., 2004). Govoreanu et al. (2004) also used a 'time of transition' method to monitor activated sludge flocculation. De Clercq et al. (2004) measured floc size distributions in-situ by means of the 'Focused Beam Reflectance Method' (FBRM) using a Lasentec (Mettler Toledo, Switzerland). These three techniques will be briefly discussed below.

2.6.1 Laser light scattering

Laser light scattering techniques involve measurement of light intensity I as a function of the wave vector Q. This vector is defined as the difference between the incident and scattered wave vectors of the radiation beam in the medium. The magnitude of the wave vector can be approximated by (Wu et al., 2002):

$$\left|\vec{Q}\right| = Q = \frac{4\pi n sin\left(\theta/2\right)}{\lambda} \tag{2.109}$$

where n, θ and λ respectively represent the refractive index of the medium, the scattered angle, and the wavelength of radiation in vacuum. A typical plot of log I versus log Q is shown in Fig. 2.28.

Three regimes can be observed. In the regime $\mathrm{QR_p} >> 1$, where $\mathrm{R_p}$ is the primary particle size, Porod's law is applicable:

$$I\left(Q\right) \propto Q^{-4} \tag{2.110}$$

This region reflects scattering from the primary particle surfaces. The region where $\mathrm{QR} << 1$ is called the Guinier regime. Here, the scattering intensity is free from the effects of aggregate structure and is only function of the linear measure of the cluster size in the form of its radius of gyration $\mathrm{r_G}$ (Selomulya et al., 2001), which is the root-mean-square distance of the mass elements from their centre of mass. In this regime $\mathrm{I\left(Q\right)}$ is a constant given by:

$$\frac{I\left(Q\right)}{I\left(0\right)} = \left(1 - \frac{1}{3}\left(QR_G\right)\right) \tag{2.111}$$

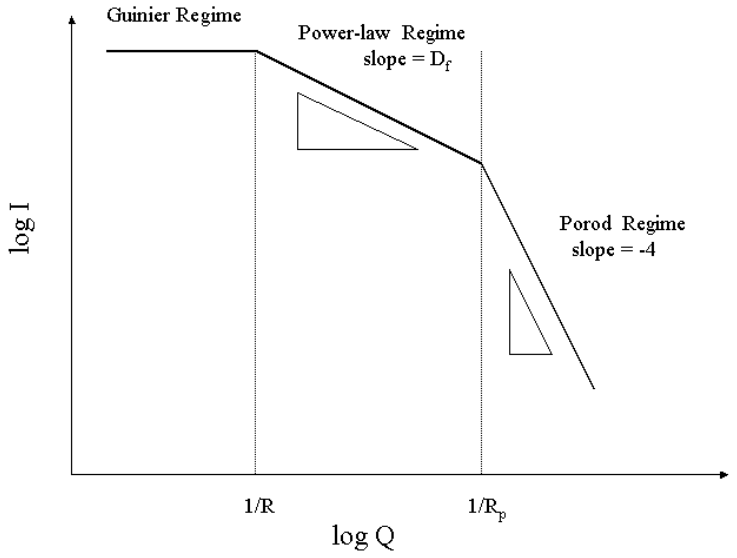

Figure 2.28: A typical I(Q) plot showing the different scattering regimes (after Wu et al. (2002))

For polydisperse cluster size distribution, the radius of gyration that can be obtained in the Guinier region is the root-mean-square of the mass squared-weighted radius of gyration of each aggregate in the distribution $(\mathrm{r_{Gi}})$ (Bushell and Amal, 2000):

$$r_G = \sqrt{\frac{\sum_i m_i^2 r_{Gi}^2}{\sum_i m_i^2}} \tag{2.112}$$

If the inequality $1/\mathrm{R} << \mathrm{Q} << 1/\mathrm{R_p}$ holds and individual particles scatter light independently such that the total scattered wave is the sum of the scattered waves from all individual particles (Rayleigh-Gans-Debye approximation), then I and Q are related via a power law:

$$I\left(Q\right) \propto Q^{-D_F} \tag{2.113}$$

This region is called the fractal regime, where the mass fractal dimension $(\mathrm{D_F})$ reflects the internal structure of the fractal clusters. The mass fractal dimension describes the space-filling ability of an aggregate and can vary between 1 (linear aggregate) and 3 (a compact aggregate). When the length scale corresponding to the Q-value approaches the length scale of the aggregate (Q=1/R), the fractal relationship (eq. 2.113) starts to be influenced by the edge of the aggregate and, hence, the structure cannot be determined in such regions. High polydispersity, as might be expected from activated sludge flocs, would be expected to limit the length scale over which fractal behaviour is observed (Bushell and Amal, 2000).

In order to fulfill the aforementioned Rayleigh-Gans-Debye approximation, certain conditions need to be fulfilled:

$$|m-1| << 1 \tag{2.114}$$

$$\left(2\pi n/\lambda\right) R\,|m-1| << 1 \tag{2.115}$$

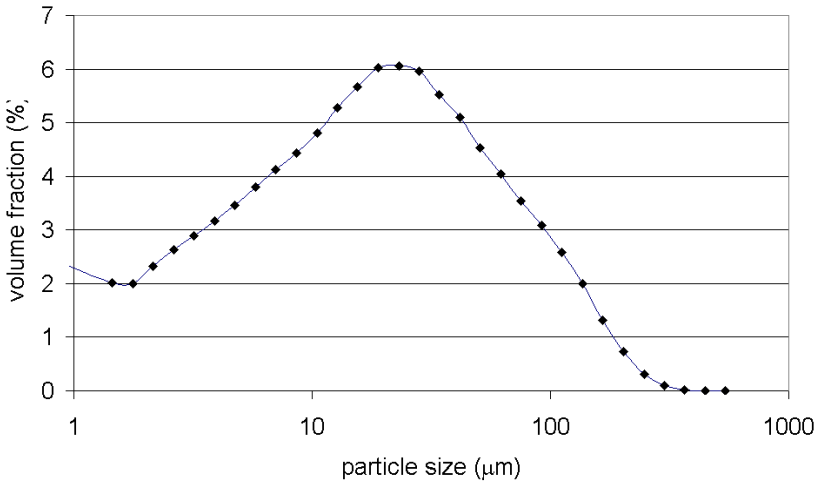

Figure 2.29: Illustration of a volume distribution of an activated sludge sample produced by a Malvern Mastersizer (Malvern, UK)

where m is the relative refractive index of the scatterers and R is the length of the scattering body. Selomulya et al. (2001) noted that the range of validity of the Rayleigh-Gans-Debye approximation can be extended beyond the range specified above. For aggregates constructed from primary particles with low refractive index (which is the case for bacterial aggregates), the assumption is valid for much larger assemblages than indicated by eq. 2.115.

In summary, the scattering pattern as shown in Fig. 2.28 yields the mean radius of gyration, the scattering intensity at Q=0 and the mass fractal dimension.

Commercial devices (e.g. Malvern Mastersizer, Malvern, UK) derive particle size distributions from these scattering patterns by using light diffraction theories (e.g. Fraunhofer, Mie). The procedure is as follows. A possible distribution is proposed and converted into a scattering pattern by using an optical model (which can be chosen by the user). Subsequently, this scaterring pattern is compared with the measured one and a discrepancy measure is calculated. This procedure is repeated iteratively until the discrepancy measure is minimised by proposing different possible distributions. The obtained distribution should be interpreted with caution since the diffraction theories are all based on the assumption of particle sphericity. Moreover, several possible distributions can result in a similar scattering pattern, so that the obtained solution is probably not unique.

The distributions given by these devices are typically volume-based. An example of a Malvern distribution is shown in Fig. 2.29.

2.6.2 Time of transition

Some 15 years ago, a technique known as time of transition (TOT) was introduced (Weiner et al., 1998). It is a direct measurement made on individual particles by means of a rotating laser beam. A photodiode placed directly behind the particles measures the difference in signal. When a particle is hit by the beam, the signal is lower. A size measure is calculated from the time τ during which the signal is lowered (=

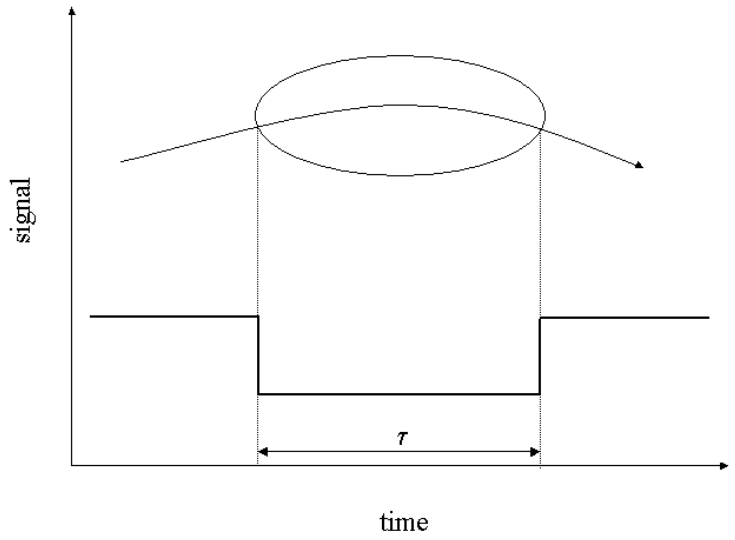

Figure 2.30: Illustration of the TOT-principle

pulse width) and the tangential velocity of the rotating laser. An illustration of the principle is given in Fig. 2.30. The technique is easily adaptable to different size ranges by changing the focal length, the deflection angle and the rotational frequency. This technique measures number concentrations and is actually a counting method. Comparison of this method with the earlier mentioned light diffraction method for the same sludge sample yielded different results (Govoreanu et al., 2004). The same authors state that knowledge of the measurement principle is important when interpreting size distributions from different sizing devices.

Commercial devices exist that apply the TOT-method (e.g. Ankersmid NV, Belgium). In these devices some corrections are performed by the software in order to deal with non-ideal interactions like off-center interactions, out of focus particles, small and large particle limitations, particle motion and non-sphericity of particles. The latter is quite important since the device might ignore particles that are non-spherical. A combination with a shape analysis method (e.g. image analysis) is recommended (Weiner et al., 1998). An example of a CIS-100 distribution is shown in Fig. 2.31.

2.6.3 Focused Beam Reflectance Method

The FBRM technique is based on laser light reflection and is very similar to the time-of-transition method described earlier. Its major advantage is, however, its operating range for solids concentration which goes as far as $50\,\mathrm{g.l^{-1}}$. In order to obtain a statistically acceptable particle size distribution, more than 2000 particles need to be sampled, expressing the need for sample mixing. Intense mixing of the suspension increases the frequency of particle detection and decreases the measurement duration. On the other hand, mixing might disturb the sample to be analysed.

The FBRM probe consists of a laser that is focused in some focal plane outside the probe and rotates at a high fixed speed, i.e. $2\,\mathrm{m.s^{-1}}$, making particle motion insignificant to the measurement. As par-

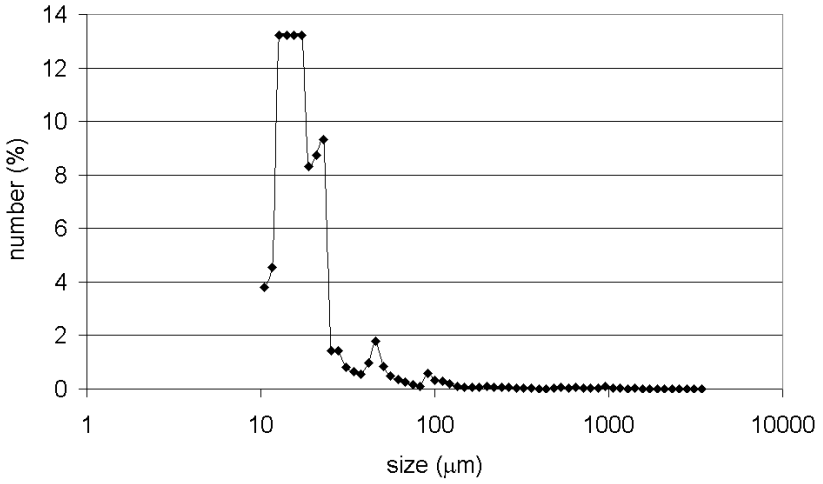

Figure 2.31: Illustration of a number distribution of an activated sludge sample produced by the CIS-100 (Ankersmid NV, Belgium)(from Govoreanu et al. (2004))

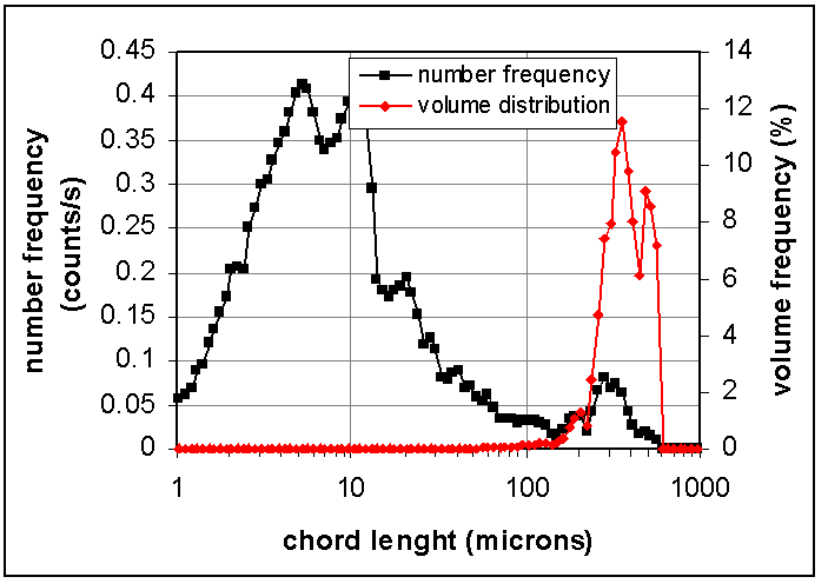

Figure 2.32: Illustration of a chord length distribution in a full-scale secondary clarifier produced by the Lasentec (Mettler Toledo, Switzerland)(from De Clercq et al. (2004))

ticles pass the focal plane, the focused beam intersects the edge of a particle, forcing the laser light to be backscattered. Backscattering continues until the opposite edge of the particle is reached. The backscatter is collected by the FBRM and converted into an electronic signal. From the time period of backscatter and the speed of the rotating laser, the so-called chord-length is calculated. The final result of such a measurement is a 'chord length distribution' (see Fig. 2.32), which is not straightforward to interpret. However, first steps have been taken to convert these chord length distributions into particle size distributions (Wynn, 2003).

Recently, De Clercq et al. (2004) successfully used the FBRM to measure particle size distributions in a full-scale clarifier.

CHAPTER 3

Materials & Methods

3.1 Introduction

This section consists of 4 parts. In a first part the lab-scale *sequencing batch reactor* that was used for breeding the sludge used in the flocculation experiments is shortly described. A second part deals with the *flocculation unit* that was used to perform the flocculation experiments. A third part deals with the determination of *sludge densities*. Finally, a short part describing the *modelling and simulation platform WEST* (Hemmis NV, Kortrijk, Belgium) that was used for modelling, simulation and parameter estimation throughout this dissertation is briefly introduced.

3.2 Sequencing Batch Reactor

3.2.1 Set-up and operation

In order to minimise sources of sludge variability, it was decided to build a lab-scale sequencing batch reactor (SBR). Sludge from a full-scale plant suffers from influent-variability and modifications in operation. These types of variability can be minimised in a lab-scale reactor. A SBR was preferred over a continuous system since it is more stable and practically easier to handle (no separate clarifier necessary).

The SBR has a total volume of 80 L and is designed and operated to remove COD as well as nitrogen and phosphorous (Capalozza, 2001). A synthetic sewage, syntho (Boeije et al., 1998), was used as influent. The C:N:P ratio of the influent is 100:13.7:2.1. Weekly 75 L of concentrated influent is prepared. The concentrated influent is kept at pH 3 to prevent bacterial growth and to keep the influent properties as stable as possible. Before the SBR is fed, the concentrated influent is diluted with tap water (softened) in a ratio of 1:19. To achieve purification each cycle of 6 hours consist of 6 phases, as shown in Table 3.1.

Table 3.1: SBR reaction sequences for nutrient removal used in the lab-scale SBR

#	Phase	Purpose	Duration (min)
1	fill (anaerobic+mixed)	P-release, COD removal	60
2	aerobic 1	P-uptake, nitrification, COD removal	150
3	anoxic	denitrification	60
4	aerobic 2	excess COD removal, N_2-stripping	30
5	settling	settling	60
6	decant	decant	15

During each cycle 2 L of activated sludge is wasted from the system at the end of phase 4. Consequently, the approximate solids residence time (SRT) is 10 days. At the end of the final phase, 38 L of effluent is withdrawn, resulting in a hydraulic residence time (HRT) of 12 h.

The set-up is automated by means of a LabView-VI (National Instruments, USA) and is operated continuously. On-line monitoring of dissolved oxygen (DO), pH, ORP, temperature, weight and conductivity is performed for system evaluation. A schematic overview of the set-up is given in Fig. 3.1.

3.2.2 Monitoring of activated sludge and effluent

On-line monitoring

During operation pH, DO, oxidation-reduction potential (ORP), temperature, conductivity and the weight of the SBR are continuously monitored and logged to a text file on the computer. Measurements of DO are used for on/off-control of DO during the aerobic phases. The other on-line measurements can be used to evaluate operational stability and performance of the system with regard to removal of COD, nitrogen and phosphorus. It is beyond the scope of this work to further elaborate on this. Results of the application of data analysis tools using these on-line experimental data can be found in Lee and Vanrolleghem (2002, 2004); Yoo et al. (2004).

Off-line monitoring of effluent

Daily effluent samples (200 ml) are taken from the supernatant after decantation (end of phase 6) and stored in a fridge at 4C to minimise any conversion of the components prior to analysis. Most of the dissolved components (COD, Total-N, NH_4-N, NO_3-N, PO_4-P) are evaluated using analysing kits (Dr. Lange, Germany) combined with spectrophotometry (Xion 500, Dr. Lange , Germany). The BOD of the effluent is measured during 20 days by means of respirometry (OxiTop, WTW GmbH, Germany). This measurement principle is based on the decrease in pressure in the headspace of a closed bottle due to the consumption of oxygen. Effluent suspended solids are measured according to standard methods.

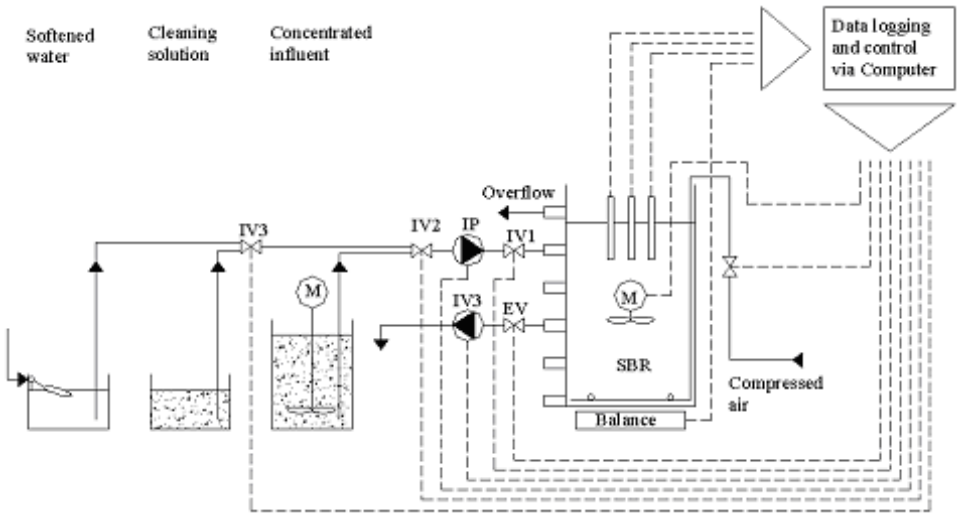

Figure 3.1: Schematic overview of the lab-scale SBR (IV – influent valve; IP – influent pump; EP – effluent pump; EV – effluent valve; M – mixer)

Off-line monitoring of activated sludge

Total suspended solids and settling characteristics are determined daily. For the latter 1 L of sludge is put into a 2 L plastic measuring cylinder and the sludge blanket height is monitored over time (30”, 1’, 3’, 5’, 10’, 20’, 30’ and 45’). The SVI is calculated. Weekly, the microbiological community is monitored using *denaturing gradient gel electrophoresis* (DGGE) to evaluate microbial stability. It was tried to keep a stable microbial community since the goal of the research was to investigate physico-chemical influences on flocculation. By monitoring microbial stability, one can rule out biological causes for experimental observations during the flocculation tests. The results of this microbial monitoring can be found elsewhere (Govoreanu et al., 2003; Govoreanu, 2004).

3.3 Flocunit

The influence of physical and chemical parameters on the (de)flocculation process was investigated in a specially designed flocculation set-up, further referred to as Flocunit. This set-up permits long-term flocculation experiments and allows to control conditions such as pH, conductivity, temperature, dissolved oxygen (DO) concentration and mixing intensity. An on-line evaluation of the dynamics of floc size and structural properties was enhanced by connecting the Flocunit to three sizing devices coupled in series:

- MastersizerS (Malvern Instruments, UK)
- CIS-100 (Ankersmid, Belgium)
- a ICD-46E CCD camera (Ikegami Electronics Inc., USA)) mounted on a CX40 optical microscope (Olympus, Japan) with image analysis software (LabView, NI, USA)

Table 3.2 summarises the settings of the sizing devices.

Table 3.2: Summary of sizing devices used by the Flocunit

device	principle	detection range	meas. frequency
MastersizerS	laser diffraction	4 - 3500 μm	1/30s
CIS-100	Time of transition	10 - 3600 μm	1/30s
IMAN	image analysis	15 - 4000 μm	1/30s

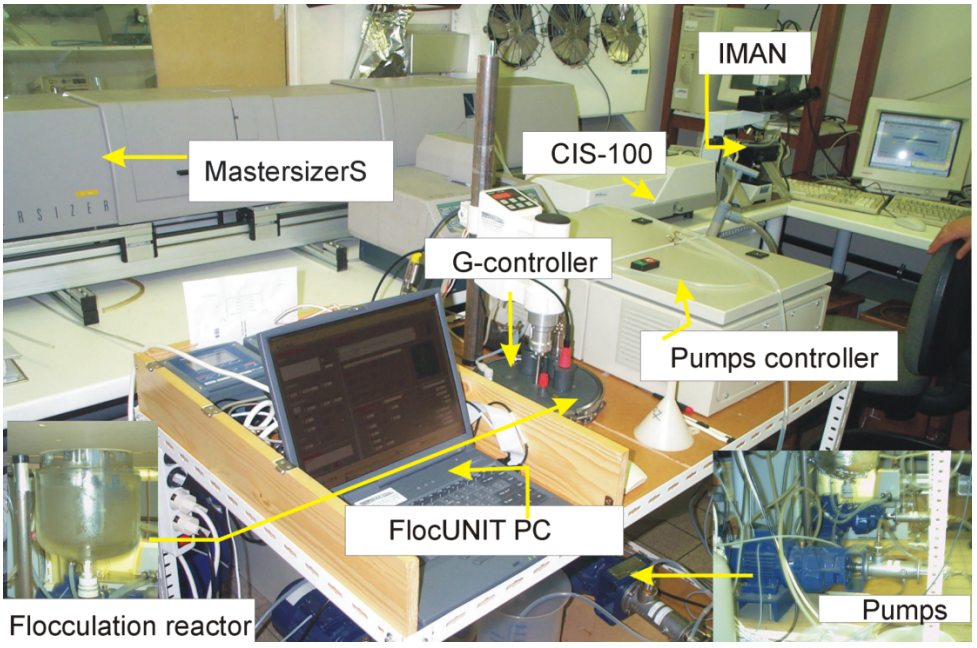

Figure 3.2: The FlocUNIT experimental set-up

A general overview of the set-up is shown in Fig. 3.2. The set-up consists of a 5 L glass vessel (TRGN 7227, KGW Isotherm, Germany) which is built into a mobile unit. The dimensions and configuration of the vessel are given in Fig. 3.3. The vessel has a thermal jacket, allowing temperature control. A plug at the bottom of the vessel allows easy sludge removal for post-experiment analysis. Near the vessel wall four PVC-baffles are introduced to enhance homogeneous mixing. A PVC-cover is used to create a headspace (its gas composition can be controlled) and to avoid heat exchanges. Silicone tubing (9/11 mm), attached to the baffles, is used for controlled oxygen/nitrogen diffusion into the system in order to obtain the desired DO level in the vessel. Bubble-less aeration is preferred since bubbles would induce additional, uncontrolled shear. The PVC mixing blade is designed in a way to approximate uniform mixing in the vessel, and still allowing the use of the aforementioned on-line sensors in the vessel in between the rotating mixer blades. The mixing blade is connected to a viscometer (VT550, Haake GmbH, Germany) allowing to measure and control shear intensity through torque (assuming a constant and known viscosity). Sensors for dissolved oxygen (InPro 6000, Mettler Toledo, Belgium), pH (Xerolyt HA-405 DXK S8 225, Mettler Toledo, Belgium) and conductivity (Kemotron 9222, Kemotron, Denmark) are inserted for on-line measurement. Finally, a PVC-tube is inserted for sludge withdrawal.

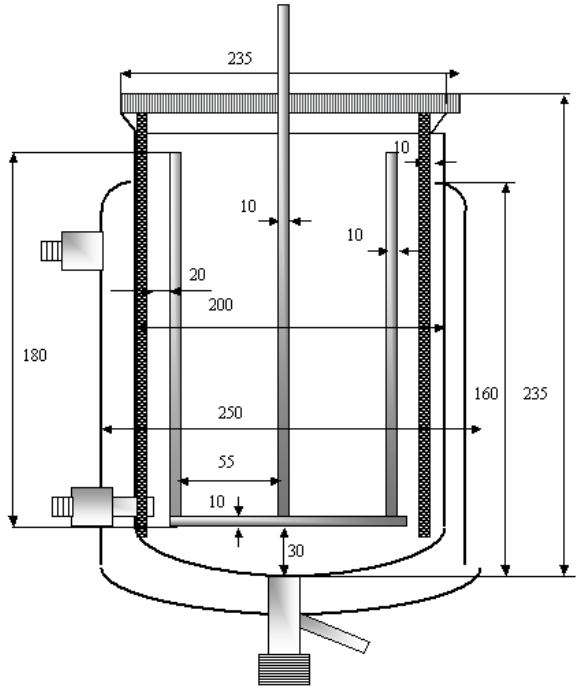

Figure 3.3: The flocculation vessel and its dimensions

The sludge withdrawal tube is connected to the sizing devices and a steady flow is created by suction using a progressive cavity dosing pump (Group D, Seepex Gmbh, Germany), which allows a small flow rate with high accuracy, low fluctuations ($<$1%) and low shear. The pump is placed after the sizing devices (sequentially) to avoid interference with size and structure measurements and the flow rate is chosen to be 3 ml/s. A second, identical progressive cavity dosing pump is used for dilution (required by the sizing devices) with filtered effluent (0.45 μm).

The whole system is connected to a notebook containing a PCMCIA data-acquisition card (DAQ-1200, National Instruments, USA) and controlled using LabView (National Instruments, USA). The data-acquisition system consists of

- on-line measurement of the analog signals (DO, pH, conductivity and temperature)
- control of both progressive cavity dosing pumps
- feedback control of mixing intensity — This is necessary since the liquid level in the vessel is constantly decreasing (no recirculation). The aim is to keep the average shear rate (G) approximately constant. This is done by controlling the power dissipation P which is given by

$$P = 2\pi N_a T_a \tag{3.1}$$

  where $\mathrm{N_a}$ is the agitation speed and $\mathrm{T_a}$ is the torque. By measuring the latter with the viscometer, the former can be adjusted to keep P constant. The viscosity is assumed to be known and to remain constant.
- PID DO-control — In order to obtain the desired DO-level in the system, pure oxygen (larger driving force than compressed air) and pure nitrogen are used. The gas flows are connected to a

3-way air valve (TYP 0330 E, Brkert GmbH, Germany), which state is determined by the value of the difference between the DO-setpoint and the actual measured value. Before entering the vessel the gas line is connected to a flow-controller (Mass Flow Controller 5850S, Brooks Instruments, The Netherlands) to control the gas flow and the pressure in the silicone tube. To speed up the process, the headspace is filled with either pure oxygen or pure nitrogen. The control action is of the PID-type (Proportional, Integral and Derivative) where the control action S is given by

$$S = P\epsilon + I\int \epsilon dt + D\frac{d\epsilon}{dt} \tag{3.2}$$

where ϵ is the difference between the DO-setpoint and the measured DO-value and P, I, D are the proportional, integral and derivative control constants. The latter constants need to be tuned for the desired response to occur . Basically, the controller will change the state of the air valve depending on the value of ϵ.

The operating procedure consists of filling the reaction vessel with activated sludge from the SBR, diluted to the level of the experiment. The Flocunit is then operated at the environmental conditions chosen for the particular experiment. Sludge is continuously withdrawn from the vessel and the particle size is analysed on-line after which the sludge is wasted. At the end of the experiment, the remainder of the sludge (approximately 1 L) is collected from the bottom valve of the vessel and the settling characteristics are measured. The experimental design and the results are further discussed in chapter 6.

3.4 Sludge density

3.4.1 Introduction

Three different types of density can be defined for activated sludge:

1. *bulk density* – This is the density of the dispersion of activated sludge flocs in water. It is often assumed to be equal to the density of water at the same temperature (e.g. in modelling exercises). It is determined by dividing the mass of a known volume through that volume. This density will not be further discussed.

2. *dry sludge density* – This represents the average density of the different solid materials building up the sludge flocs. Since a variety of values has been reported in literature (Ekama et al., 1997; Kinnear, 2002), this type of density was shortly investigated.

3. *sludge floc density* – This is the density of the floc in the sludge dispersion and, hence, takes into account the bound water (i.e. water that is 'part' of the floc). A technique that can be used to determine this density will also be discussed.

3.4.2 Dry sludge density ρ_s

The method for the determination of the dry sludge density is taken from the soil science field. The measurement is based on pyknometry, which uses a recipient with an accurate, certified volume, i.e. a pyknometer (Figure 3.4). The procedure is based on four gravimetric measurements: two of them

Figure 3.4: Illustration of a pyknometer

determine the mass of the sample, whereas the other two are needed to determine its volume (Blake and Hartge, 1986). Here are the steps to be taken to determine the dry sludge density using pyknometry:

1. A certain amount of activated sludge should be dried at 105°Cin order to obtain about 2 g (depending on the biomass concentration). Sludge thickening prior to drying will significantly decrease the duration of this step.

2. The dried solids are pulverised and passed through a 2 mm sieve. They should always be stored in a dessicator to avoid rehydration.

3. The mass of a dry, closed pyknometer (50 or 100 ml) is determined accurately. Let this be the dry, empty mass ($\mathrm{m_{d,e}}$).

4. The dried sludge sample is added to the dry pyknometer. The mass is again determined accurately. Let this be the dry, filled mass ($\mathrm{m_{d,f}}$).

5. The pyknometer is partly (1/3) filled with distilled water (free of air) and placed in a vacuum for three times 20 minutes in order to entirely wet the solids.

6. The pyknometer is then filled completely (up to the measure line). After closing the pyknometer, its mass is determined again. Let this be the wet, solid filled mass ($\mathrm{m_{w,sf}}$). Also, the temperature of the distilled water is determined.

7. After thoroughly cleaning the pyknometer and filling it with distilled air-free water, the mass is again determined. Let this be the wet, water filled mass ($\mathrm{m_{w,wf}}$).

The dry sludge density can then be determined as follows:

$$\rho_s = m_s \frac{1}{V_s} = (m_{d,f} - m_{d,e}) \frac{\rho_w}{(m_{d,f} - m_{d,e})} - (m_{w,sf} - m_{w,wf}) \tag{3.3}$$

where ρ_{w} is the density of water at the temperature measured in step 6 and $\mathrm{V_s}$ is the volume of the dry solids. Hence, the mass of the solids is determined gravimetrically, whereas the volume is calculated based on the buoyancy principle, or in other words by the volume of water that is displaced by the solids.

The method was used to determine the dry sludge density of different sludges (taken from both lab-scale and full-scale). The results are summarised in Table 3.3.

The observed values are significantly larger than those reported in literature, i.e. $1.45\,\mathrm{g.ml^{-1}}$ (Ekama et al., 1997) and can be significantly different for different sludges. The latter is probably caused by a difference in composition. A higher dry sludge density will, however, have a significant influence on calculated settling velocities that are used when modelling sludge settling and predicting the sludge blanket height.

It should be stressed, though, that these measurements were not completely conducted in compliance with the earlier described procedure due to absence of a vacuum bottle and a sieve. The results should, therefore, be viewed as preliminary and interpreted with care. Before applying this fast and cheap method, it should be thoroughly tested and validated, for example by using Helium-pyknometry that uses Helium gas instead of water and measures the change in Helium pressure with and without the sample. This validation is, however, beyond the scope of this work. It should be mentioned that the procedure was reproducible as a standard deviation in repetitive measurements was $0.01\,\mathrm{g.ml^{-1}}$.

3.4.3 Floc density ρ_{f}

Floc density is an interesting property of activated sludge. Indeed, the deviation of the latter from the density of water is regarded as the driving force for settling (e.g. Stokes' law).

Floc density was measured according to a technique based on a discontinuous linear gradient of Percoll solutions with densities ranging from 1.01 to $1.05\,\mathrm{g.ml^{-1}}$ or higher (Dammel and Schroeder, 1991; Kinnear, 2002). This can be done by gently layering appropriate Percoll dilutions of 2 mm thickness (turbulence should be avoided) in a CELLSTAR PP-test tube (15 ml). Dilutions should be prepared using sludge supernatant to avoid disturbances due to differences in osmotic pressure. In a next step, a small amount of thickened sludge is then introduced on the top layer (i.e. lowest density) and allowed to

Table 3.3: Dry sludge densities of different sludges determined by pyknometry

Sludge	origin	ρ_{s} ($\mathrm{g.ml^{-1}}$)
SBR 22-04-03	lab	1.60
SBR 09-05-03	lab	1.61
SBR 25-05-03	lab	1.52
SBR 26-06-03	lab	1.61
WWTP Ossemeersen 05-03	full-scale	1.59
WWTP Heist 05-03	full-scale	1.62
WWTP Halen 09-03	full-scale	1.78

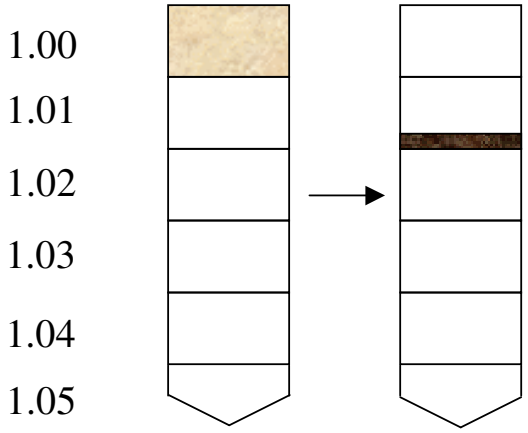

Figure 3.5: Schematic illustration of the floc density measurement based on a Percoll density gradient ranging from 1.01 to 1.05 $\mathrm{g.ml^{-1}}$

settle. The latter will continue until the layer of equal density has been reached. The process might be stimulated by applying centrifugation. The measurement principle is schematically illustrated in Fig. 3.5. A real sample is shown in Fig. 3.6.

On the left the sludge sample is introduced on the top layer. After settling, the sludge has settled up to the interface between 1.01 and 1.02 $\mathrm{g.ml^{-1}}$, further denoted as interface density. This means that the sludge exhibits a density smaller than 1.02 $\mathrm{g.ml^{-1}}$, but larger than 1.01 $\mathrm{g.ml^{-1}}$. Hence, the resolution of the density gradient determines the accuracy of the measurement. Here, a resolution of 0.01 $\mathrm{g.ml^{-1}}$ was used.

Preliminary results have led to the following conclusions:

- Floc densities similar to those reported in literature were found, i.e. 1.02-1.06 $\mathrm{g.ml^{-1}}$ (Dammel and Schroeder, 1991).
- Sludge storage resulted in a decrease in floc density, which might be caused by phosphorus release in anaerobic conditions.
- No density changes were observed between sludge samples taken during different phases of an SBR-cycle. Differences would be expected due to the sequential release and uptake of phosphorus. However, the measurement accuracy might have been too low.
- Floc densities before and after flocculation in the Flocunit increased from 1.02 to 1.03 $\mathrm{g.ml^{-1}}$. This might either be caused by the Calcium that was added, or due to restructuring and decrease of the bound water content.

Although the results look promising, a higher resolution is required to investigate small density differences that might have significant effects on settling behaviour. This might be accomplished by using continuous linear gradients, which are, however, rather expensive to make with dedicated lab equipment. Hence, this was not further investigated.

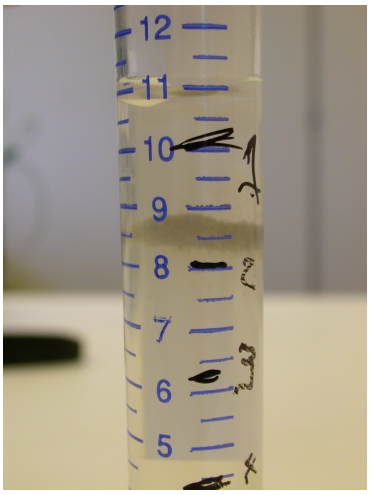

Figure 3.6: Real sample of a floc density measurement based on a Percoll density gradient ranging from 1.01 to 1.05 $\mathrm{g.ml^{-1}}$

3.5 Modelling and simulation platform WEST®

For modelling, simulation and optimisation the modelling and simulation platform WEST (Hemmis NV, Kortrijk, Belgium) is used. WEST is the acronym for *Wastewater treatment plant Engine for Simulation and Training*. It is designed to solve algebraic and differential equations and has mainly been used to simulate wastewater treatment processes.

WEST consists of 2 environments: a modelling environment and an experimentation environment. The former enables the user to create new models from scratch or by using existing models from a modelbase. The different models and process units (depicted as icons) can be linked and configured in a hierarchical graphical editor (HGE). These models are written in the model specification language (MSL), a high-level-object-oriented declarative language. To create new models, the user can write these models in the same language. In either case, the MSL-file is then parsed into low level C-code, which is in its turn compiled to an executable WEST model library (WML-file), which can be loaded into the experimentation environment (Vanhooren et al., 2003). The models used in this dissertation, include summation terms which could not be properly handled by the parser. Therefore, these were written in an external C-file and compiled along using an include statement. A schematic overview of the model creation in WEST is given in Fig. 3.7.

The experimentation environment allows to define and run different experiments with the model like simulation, optimisation, sensitivity analysis, scenario analysis and optimal experimental design (OED). The model created in the modelling environment is loaded and an experiment can be designed by creating plot windows and setting initial parameter values. By default, the experimentation environment is in *simulation mode*. Here, the model can be simulated for a defined time duration and the behaviour can be followed on the graphs. Different simulation algorithms (solvers) are available. In this study, the Runge-Kutta 4th order with adaptive step size (Gerald and Wheatley, 1994) and the CVODE stiff-solver (Cohen and Hindmarsh, 1994) were used for solving the discretised set of population balance equations.

The user can manually change to *optimisation mode*. Here, the model parameters can be estimated using an experimental data set. Optimisations are performed using a least squares or a weighted least squares

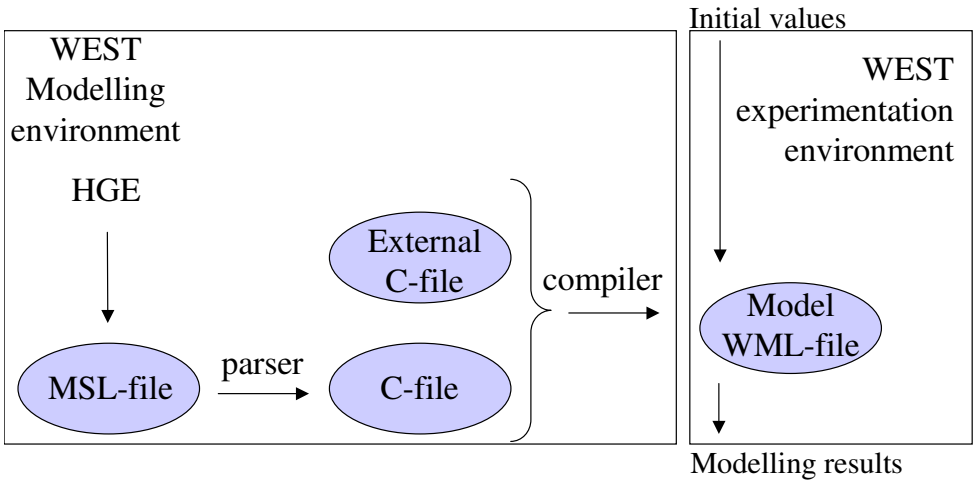

Figure 3.7: Process of creating a WEST model

objective function in order to minimise the difference between data and model predictions (Dochain and Vanrolleghem, 2001). The simplex optimisation algorithm is used to perform the minimisation of the objective function and obtain the best parameter estimates (Nelder and Mead, 1965).

The other tools available in WEST are not discussed since they have not been applied in this work. A screenshot of the experimentation environment is shown in Fig. 3.8.

For this work, the three discretisation algorithms discussed in chapter 2 were implemented in WEST. It would be too exhaustive to include all the code here or in an appendix. Instead, an overview of the structure of the files is given.

In general, three files are needed to compile a model:

- MSL-file
- header-file
- external C-file

3.5.1 MSL-file

This file in which the basis of the model is specified, consists of

- object definitions – An object can be any kind of variable of a predefined type or a user-defined type or class
- class definitions – A class is a generalisation of an object, a user-defined type which can be completely customised in terms of initial value, unit,... They are used to group objects that have the same nature.

Prior to defining the model-class, separate classes for vectors and matrices need to be defined. Intervals and units can be defined separately for every class. In the actual model class, different parts are present:

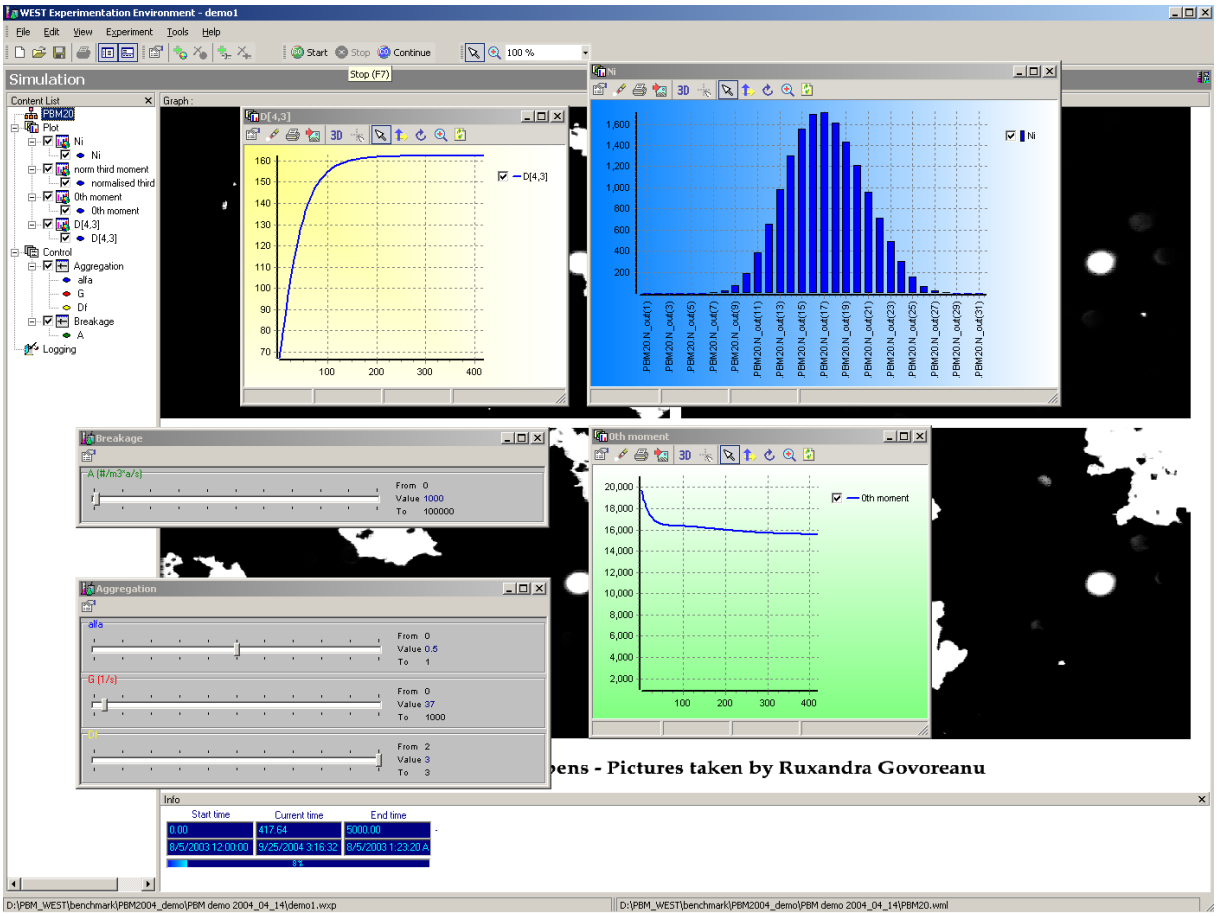

Figure 3.8: Screenshot of the WEST experimentation environment

- comments – The programmer can write some explanation about the model.
- interface – This part contains input and output variables to other submodels.
- parameters – Definition of all model parameters. This definition typically consists of the name of the variable, a description, a default value, an interval of realistic values and the units.
- independent – Contains the independent variables. Typically, this is time.
- state – Definition of all state variables of the model (both derived and algebraic state variables).
- initial – This section allows to assign initial (calculated) values to certain state variables. In this particular application, this section was used to define the grid of the size distribution. The grid definition was implemented in two different ways. Either the grid values (boundary and pivotal volumes) were calculated from a given lower boundary value, or the values were computed elsewhere and read in through a vector of parameters.
- equation – In this section all model equations are defined. Due to some limitations of the MSL language, not all model equations could be implemented here. A first limitation is the poor handling of vectors and matrices as all elements of vectors or matrices are treated as separate variables. This becomes a limiting factor when the number of classes of the model is increased since a lot of

vectors and matrices increase exponentially in size. This results in very large C++ files that can no longer be handled by the C++ compiler. A second limitation is that indices of control loops cannot be used in nested control structures (e.g. a SUMOVER statement within a FOR-loop). These are necessary given the model structure and the solution algorithms. Therefore, it was decided to use an external C-file for computation of certain matrices (to limit the size of the C++ file created from MSL) and for the implementation of the solution methods, and then use function calls in MSL to use them.

3.5.2 header-file

This file is needed to declare the functions that are called from MSL and that are defined in the external C-file. It consists of the function name followed by the arguments it needs when it is called.

3.5.3 external C-file

This file contains all external function definitions. It can be divided into two main parts:

- function definitions of solution algorithms – Here, the different solution algorithms are implemented. They typically consist of 4 functions: aggregation birth/death and breakage birth/death. The functions need arguments concerning the grid and the kernels that are used. For the latter, several options are available. The kernels can be calculated in the MSL-file and the values passed on with the argument list of the function call. Alternatively, they can be calculated in separate functions in this file, which is computed every time it is called or which is dynamically allocated (calculated once per time step). When calculating kernel values in the external file, all states and parameter values required need to be passed on as arguments in the function call.
- function definitions of kernels – These can be used when kernels are not computed in the MSL-code (e.g. when larger numbers of grid classes are used). To easily use and swap between different kernel structures within a model without having to recompile it over and over, kernels can be implemented as a master function that receives a parameter as argument that can be used in a case-structure. Every case then calls a different kernel function. This can be done for all kernels that need to be computed.

CHAPTER 4

Comparison of different discretised solution methods of PBMs

4.1 Abstract

In order to solve the population balance equation (PBE), a solution method needs to be chosen [1]. In this PhD-study, it was decided to use discretisation techniques for solving the PBE. There were 2 reasons for this:

- It was proven elsewhere that discretisation techniques give rise to acceptable calculation times, which is important when the model is to be used in parameter estimation or process control studies or in combination with Computational Fluid Dynamics (CFD).
- The algorithms are quite straightforward to implement and were compatible with the modelling and simulation environment WEST that was used in this study.

Once this decision is made, one needs to decide which of the discretisation algorithm from literature will be used. In this chapter it was investigated which discretisation algorithm is most suitable for solving a PBM including aggregation and/or breakage using different initial conditions as an additional degree of freedom. Important properties of a method are:

- ease of implementation
- flexibility
- accuracy
- computational performance
- stability and pittfalls

Three discretisation techniques were taken from literature and investigated:

[1] Published at Nopens, I., Beheydt, D., Vanrolleghem, P.A., 2005. Comparison and pitfalls of different discretised solution methods for population balance models: a simulation study. Comp. Chem. Eng., 29(2), 367-377.

- method of Hounslow (Hounslow et al., 1988)
- the fixed pivot technique (Kumar and Ramkrishna, 1996a)
- the moving pivot technique (Kumar and Ramkrishna, 1996b)

The three methods have already been described in section 2.5.3 and this will not be repeated here. This chapter is structured as follows. First the model structure (aggregation and breakage kernels) that was used is shortly introduced. Next, practical details of the simulation study are given and, finally, the simulation results are discussed followed by some conclusions.

4.2 The population balance model

4.2.1 Applied model equation

Instead of approaching the biomass as a lumped biophase, which is common practice in wastewater modelling, sludge can also be viewed as a segregated population of individual flocs. This approach implies that floc properties, in our case floc size, are no longer average values but distributions. Models that allow the description of dynamical changes in property distributions are better known as Population Balance Models (PBMs). The general format of a one-dimensional PBM (describing just 1 distributed property) looks like (Hulburt and Katz, 1964; Ramkrishna, 2000):

$$\frac{\partial n\left(x,t\right)}{\partial t}+\frac{\partial}{\partial X}\left(\dot{X}\left(x,t\right)n\left(x,t\right)\right)=h\left(x,t\right) \tag{4.1}$$

where x is the floc size expressed as volume, $n(x,t)$ is the number-based floc size distribution (FSD), $\dot{X}$(x,t) is the time derivative of the floc size and $h(x,t)$ the net generation rate of x-sized flocs. Hence, eq. 4.1 describes the time evolution of the number-based FSD. $\dot{X}(x,t)$ can be interpreted as the biomass growth rate. Since the model will be used to describe rather short flocculation experiments (max. 2h), it can be assumed that no significant growth occurs, allowing to omit the second term on the left-hand side of eq. 4.1. This simplification is justified since no substrate is available in the settler and, hence, growth can only occur using lysed cell material which is determined by the decay rate b_h. In activated sludge systems, this first order rate is approx. 0.05 d^{-1} (Gujer et al., 2000), resulting in a biomass reduction of less than 0.5% during a 2 hour experiment, which is considered to be negligible.

Hence, for this type of process eq. 4.1 is reduced to

$$\frac{\partial n\left(x,t\right)}{\partial t}=h\left(x,t\right) \tag{4.2}$$

$h(x,t)$ accounts for discontinuous aggregation/breakage processes. It describes the creation or birth and the disappearance or death of flocs of a certain size x during an infinitesimal time interval dt. Since both aggregation and breakage can give rise to birth and death of flocs, h(x,t) consists of 4 processes: aggregation birth (AB), aggregation death (AD), breakage birth (BB) and breakage death (BD). This is illustrated in eq. 4.3:

$$\begin{aligned} h\left(x,t\right) &= h\left(x,t\right)_{agg}+h\left(x,t\right)_{break} \\ &= h\left(x,t\right)_{AB}-h\left(x,t\right)_{AD}+h\left(x,t\right)_{BB}-h\left(x,t\right)_{BD} \end{aligned} \tag{4.3}$$

A Smoluchowski type *aggregation model* was used (Thomas et al., 1999; Ramkrishna, 2000):

$$h\left(x,t\right)_{agg} = \frac{1}{2}\int_0^x \alpha\beta\left(x-x',x'\right) n\left(x-x',t\right) n\left(x',t\right) dx' \\ - n\left(x,t\right)\int_0^\infty \alpha\beta\left(x,x'\right) n\left(x',t\right) dx' \quad (4.4)$$

where $\beta(x,x')(L^3.T^{-1})$ is the collision frequency for particles of volume *x* and *x'* and α (-) is the collision efficiency. The former describes the transport of particles toward one another, whereas the latter describes the probability that these collisions lead to aggregation taking into account short-range forces like van der Waals attraction, charge repulsion and hydrodynamic interaction.

Breakage models typically look like (Ramkrishna, 2000):

$$h\left(x,t\right)_{break} = \int_x^\infty n\left(x',t\right) S\left(x'\right) v(x')\Gamma\left(x,x'\right) dx' - n\left(x,t\right) S\left(x\right) \quad (4.5)$$

where $S\left(x\right)$ is the breakage rate of particles of size $x\left(s^{-1}\right)$, $v(x')$ the average number of particles resulting from a breakage event and $\Gamma(x,x')$ the breakage distribution function.

4.2.2 Model structure - aggregation/breakage kernel definitions

Throughout this work, several aggregation and breakage functions, also referred to as 'kernels' will be used. For the simulation studies of chapters 4, 5 and 7 basic kernels were used, which will be described here shortly. Only chapter 8 also uses other kernels. These will be explicitly defined there.

An orthokinetic kernel $\beta(x-x',x)$ was borrowed from Spicer and Pratsinis (1996a):

$$\beta\left(x-x',x\right) = 0.31\,\bar{G}\left[\left(x-x'\right)^{\frac{1}{3}} + x^{\frac{1}{3}}\right]^3 \quad (4.6)$$

in which

$$\bar{G} = \left(\frac{\bar{\epsilon}}{\nu}\right)^{\frac{1}{2}} \quad (4.7)$$

is the average velocity gradient which can be measured and, hence, is explicitly known.

α was chosen to be a constant between 0 and 1. In the latter case ($\alpha = 1$), all collisions are considered to be successful. The collision efficiency is often used as a fitting parameter in calibration studies. Other aggregation efficiency expressions are available in literature (Adler, 1981a; Kusters et al., 1997; Ducoste, 2002) but are not considered here since this was not the goal of the work in this chapter. Some of them will be used in chapter 8.

$S\left(x\right)$ was assumed to be a power law (Spicer and Pratsinis, 1996b):

$$S\left(x\right) = Ax^a \quad (4.8)$$

where *a* is a constant chosen to be equal to $1/3$ and *A* is the breakage rate coefficient $\left(L^{-1}.T^{-1}\right)$. It is fixed in simulation studies, but is typically used as fitting parameter in calibration studies. Binary breakage into equally sized daughters is assumed

$$v(x')\Gamma\left(x,x'\right) = 2\delta\left(x-\frac{x'}{2}\right) \quad (4.9)$$

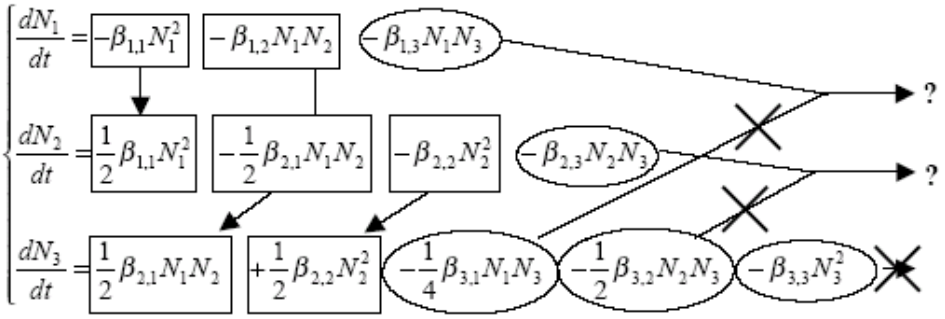

Figure 4.1: Illustration of the importance of correctly chosen boundary conditions of the Hounslow equations

Other, more complex breakage functions can be found in literature (Konno et al., 1983; Kramer and Clark, 1999; Vanni, 2000; Ducoste, 2002) but were not considered in this particular study focusing on solution methods. Some of them will be used in chapter 8.

4.3 Practical details of the simulation study

The three different discretisation algorithms that were described in section 2.5.3, all conserving both numbers and mass, were implemented in the modelling and simulation platform WEST (Hemmis NV, Belgium).

The Hounslow algorithm is quite straightforward to implement. However, one should be cautious to set the boundary conditions properly to avoid mass leaks. At the breakage end, the breakage rate S for the lower boundary class should be explicitly set to 0. The same goes for the aggregation death term of the upper boundary class. An important consequence is that the summation in the final term of eq. 2.29 should only take into account j-values up to the one but last class (and not the upper boundary class) in order to avoid a mass leak. This is illustrated in Fig. 4.1 for a simple grid of 3 classes. In order to avoid a mass leak from the upper boundary class (i.e. class 3) the 3 negative terms should be set to 0 since they cannot be born elsewhere as the resulting particle is larger than the largest possible size. However, the circled terms in the top 2 equations are the complementary terms of the collisions that result in particles outside the particle range, and, hence, these should also be put to 0 to avoid mass loss. It concerns all collisions with particles from the upper boundary class.

The implementation of the fixed pivot algorithm is a more tedious task and, here too, one should be cautious to set the boundary conditions properly. Particles should always be born (through either aggregation or breakage) between the smallest and largest pivot, pivots being representative points of a class where the particles in the interval are concentrated at. This means that some aggregation and breakage events must be ignored even though they would result in particles within the particle range.

The moving pivot is relatively easy to implement. There is, however, a subtle difference in boundary conditions since all particles born within the complete particle range can be taken into account. Hence, the covered range is between v_0 and v_M rather than between x_0 and x_{M-1} as illustrated in Fig. 4.2. This might best be illustrated using a simple numerical example. Say, the lower boundary v_0 equals

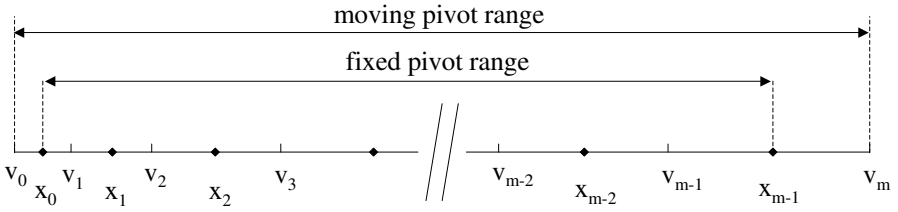

Figure 4.2: Illustration of the subtle difference in grid range between the fixed and moving pivot technique

$1\,\mu\mathrm{m}^3$. When using a geometric grid with factor 2 and 5 classes, this means that the class bounds are respectively 1,2,4,8,16 and 32. If the arithmetic mean is used to determine the pivots, these will respectively be 1.5;3;6;12 and 24. When the fixed pivot (or the Hounslow algorithm) is used, flocs can have values between the lower and upper pivot, i.e. in the interval $1.5 - 24$. All mechanisms that form flocs outside this interval will be prohibited by the algorithm. When using the moving pivot, the entire size range $1 - 32$ is allowed for flocs to be formed, which allows more aggregation or breakage events to occur. Note that the part of the range that is lost becomes larger in the case of a geometric grid when more classes are added at the large size end of the grid.

Another practical, numerical, issue is the fact that none of the classes should be or become 0 since this would imply a division by 0 in eq. 2.50. Therefore, a lower limit of 1E-13 was adopted in initial conditions (also for the other algorithms). The value was chosen in order to not add significant mass to the system.

With regard to an appropriate choice of grid, 2 things have to be born in mind: the type of grid and its coarseness. Several types of grids exist like linear grids, where a fixed amount of volume is added to define a class sequence, and geometric grids, where volumes are multiplied by a constant factor to define the class sequence. The choice of type must be inspired by the span of the particle size range. If a broad range is needed, linear grids become less attractive as the number of classes needed to describe the entire range will blow up, making the model computationally inefficient. Since the model will be used for a pretty large range, it was therefore decided to focus on geometric grids. A second aspect, next to the grid type, is its coarseness. The latter brings us back to the discussion on restoration of inconsistency (see section 2.5.3) that was induced by discretisation and, hence, reflects on the accuracy of the method. A factor of 2 is frequently being used in practice, merely inspired by physical reasoning. Indeed, when 2 particles of the same volume aggregate, they will form a particle that has double the volume.

For the application at hand the lower boundary of the entire size range was chosen to be $0.6\mu m$. The class boundary values were calculated based on volume and using a geometric factor of either 1.6, 2.0 or 2.4. The pivotal volumes were calculated as the arithmetic mean of the class boundary volumes. The pivotal diameters were calculated from the pivotal volumes assuming sphericity. The final class of which the pivotal diameter is smaller than $800\mu m$ is chosen to be the upper boundary class. This resulted in respectively 25, 31 and 46 classes for the different geometric factors.

A fixed total particle volume density of 1.82E-8m^3m^{-3} was chosen arbitrarily (= 100 particles in the upper boundary class in the case of a geometric factor of 2.0). The different initial conditions for the geometric case with factor 2 are summarised in Table 4.1.

All initial conditions were defined for the case of a geometric factor of 2.0 and then recalculated for the

Table 4.1: Overview of different initial conditions that were used

initial condition	type of dispersion	size range (μm^3)
1	monodisperion	8.89E-14
2	monodispersion	8.69E-17
3	uniform polydisperion	1.70E-19 – 1.82E-10
4	uniform polydisperion	1.70E-19 – 8.69E-17
5	uniform polydisperion	3.56E-13 – 1.82E-10
6	uniform polydisperion	1.74E-16 – 1.78E-13

other cases (geometric factors of 1.6 and 2.4) conserving both numbers and mass. This transformation is not always possible and depends on the relative location of the initial pivots of the boundary classes of both grids (problems only occur when particles are present in boundary classes, i.e. init3, init4 and init5). This can be illustrated by a simple example. Say a number of particles is present in the lower boundary class of a grid with geometric factor 2. If one wants to use a grid with geometric factor 2.4, one cannot redistribute these particles among the adjoining pivots since there is only one adjoining pivot (the volume of the particles to be redistributed is smaller than the volume of the smallest pivot of the 2.4 grid). In that case one cannot conserve 2 properties. These problems only occur with conversions to grids with geometric factor 2.4 (init3, 4 and 5).

The simulations were performed for three cases: (1) pure aggregation, (2) pure breakage and (3) combined aggregation/breakage. In the pure aggregation case, arbitrary parameter values were chosen to be $\alpha = 1, \bar{G} = 100\, s^{-1}, A = 0\, cm^{-1}s^{-1}$. For the pure breakage case, parameter values were chosen to be $\alpha = 0, \bar{G} = 100\, s^{-1}, A = 1E4\, cm^{-1}s^{-1}$. Finally, for the combined aggregation/breakage case, parameter values were chosen to be $\alpha = 0.2, \bar{G} = 100\, s^{-1}, A = 1E4\, cm^{-1}s^{-1}$. Note that these values are not based on real-life values, but were chosen in order to obtain relatively fast simulations to reach steady state. All simulations were performed on a Pentium IV-2.8GHz machine using the CVODE stiff solver (Cohen and Hindmarsh, 1994), unless otherwise stated. As default settings, the absolute tolerance was chosen to be 0 and the relative tolerance to be 0.005. The Adams linear multistep method and functional iteration method were used.

The simulation results are presented either as cumulative oversize number density (CON), cumulative undersize number density (CUN), cumulative oversize volume density (COV) or cumulative undersize volume density (CUV):

$$CON\,(v,t) = \int_v^{\infty} n\left(v',t\right) dv' \tag{4.10}$$

$$CUN\,(v,t) = \int_v^{0} n\left(v',t\right) dv' \tag{4.11}$$

$$COV\,(v,t) = \int_v^{\infty} n\left(v',t\right) v' dv' \tag{4.12}$$

$$CUV\,(v,t) = \int_v^{0} n\left(v',t\right) v' dv' \tag{4.13}$$

4.4 Simulation study results

4.4.1 The pure aggregation case

For a pure aggregation process, one expects all particles to move into the upper boundary class at *steady state* (SS). SS is defined to be reached when 99.99% of the particle volume is present in the upper boundary class and the number of particles in all other classes has dropped below 1. The simulation times (sim. time) for the different cases were chosen in order to make sure the SS was reached. Results of the pure aggregation case for the Hounslow method, the fixed pivot and the moving pivot are summarised in respectively Table 4.2, 4.3 and 4.4. Here, the computation time (comp. time) is the physical time needed by the computer to finish the simulation. The simulation time needed to reach SS (sim. time to SS) is that part of the simulation time which is needed to reach SS. In all cases the Hounslow method reaches SS without mass losses. However, the simulation time needed to reach SS is different for the different initial conditions. They seem to be dependent on the initial degree of aggregation of the system. The computation time is very low and seems to be independent of the initial condition. It should be noted that these results were obtained by using the correct boundary conditions. When the last summation in eq. 2.29 is performed up to the upper boundary class, mass losses between 40 and 60% were observed.

The fixed pivot reaches SS for all cases using 31 classes. The simulation times required to reach steady state are the same as the ones observed using the Hounslow method and, hence, again depend on the initial condition. The computation times needed to perform the simulations are, however, significantly larger, but still acceptable. Unlike the Hounslow algorithm, the computation time seems to be dependent on the initial condition. The difference is probably due to the fact that quite some if-clauses are present in the fixed pivot algorithm whereas these are directly integrated in the Hounslow equations.

In the cases using 25 classes the simulation time to reach SS is somewhat larger (but in the same order of magnitude), which might be explained by the fact that the pivotal volume of the upper boundary class is somewhat larger compared to the 31 classes grid. The computation time is somewhat smaller compared to the cases using 31 classes (lower amount of equations to solve) and seems to be independent of the simulation time.

The cases with 46 classes did not reach the SS as defined above. However, after a certain simulation time, the system reaches another SS, with some particles being trapped in the one but last class. In order to distinguish this state from a normal SS, it was called a *pseudo steady state* (PSS), meaning that a steady state has been reached, but not all particles have reached the theoretically expected upper boundary class. This situation occurs when the system evolves into a state where no longer valid collisions are possible

Table 4.2: Overview of results for the pure aggregation case using the Hounslow algorithm

init	classes	sim. time (s)	comp. time (s)	SS/PSS	sim. time to SS (s)
1	31	1.0E+4	1	SS	8.0E+3
2	31	3.0E+6	1	SS	2.7E+6
3	31	1.0E+5	1	SS	8.1E+4
4	31	1.0E+9	2	SS	3.0E+8
5	31	1.1E+3	1	SS	1.1E+3
6	31	1.0E+6	1	SS	8.4E+5

Table 4.3: Overview of results for the pure aggregation case using the fixed pivot algorithm

init	classes	sim. time (s)	comp. time (s)	SS/PSS	sim. time to SS (s)
1	25	1.0E+4	4	SS	8.2E+3
	31	1.0E+4	6	SS	8.0E+3
	46	3.0E+3	174	PSS	3.0E+3
2	25	3.0E+6	4	SS	2.9E+6
	31	3.0E+6	13	SS	2.7E+6
	46	3.0E+3	61	PSS	3.0E+3
3	31	1.0E+5	7	SS	8.1E+4
	46	1.0E+3	174	PSS	1.0E+3
4	31	1.0E+9	20	SS	3.0E+8
	46	1.0E+4	182	PSS	1.0E+4
5	31	1.1E+3	1	SS	1.1E+3
	46	1.0E+3	138	PSS	1.0E+3
6	25	1.0E+6	3	SS	9.0E+5
	31	1.0E+6	6	SS	8.4E+5
	46	4.0E+3	169	PSS	4.0E+3

between particles of the one but last class and any other particle in the system. This invalidity is due to the fact that the sum of volumes of the colliding particles exceeds the volume of the upper boundary class pivot. Since aggregation is the only working mechanism here, there is no possibility for these particles to escape from their state and, hence, they are trapped in the one but last class. This phenomenon is illustrated in Fig. 4.3. The PSS can only occur when geometric grids with factors smaller than 2 are used. Indeed, in the case of a geometric grid with factor 2, the particles of the one but last class can always aggregate with themselves, still producing particles that have a valid volume. This is illustrated in Fig. 4.4.

The simulation times needed to reach the PSS are substantially shorter compared to the cases using 25 and 31 classes and, therefore, the total simulation times were adjusted accordingly. The PSS's were somewhat different for the different initial conditions, i.e. the number of particles that are trapped are different. Especially when particles are initially present in the last but one class (init3 and init5), a considerably larger amount of particles is trapped. Although simulation times were substantially shorter, calculation times were larger for the cases using 46 classes due to the increased number of equations that needs to be solved.

The moving pivot reaches SS for all cases using 31 classes. The simulation times to reach SS are, however, substantially smaller compared to the ones that were needed in the Hounslow and fixed pivot cases. For example, to reach a state where 99.99% of the volume is present in the upper class takes 8200 s for init1 using either the Hounslow and fixed pivot algorithms, whereas for the moving pivot SS is reached in 1000s. This is caused by the subtle difference in valid size range for particle formation between the different methods, i.e. the range between the smallest and largest pivot for Hounslow and the fixed pivot versus the entire size range from the lower boundary up to the upper boundary of the system for the moving pivot. In the moving pivot case, a lot of aggregations are allowed that have to be ignored in the other two cases. For example, collisions with particles from the upper class are not ignored as long as the resulting particle's volume does not exceed the upper system boundary. Evidence of this

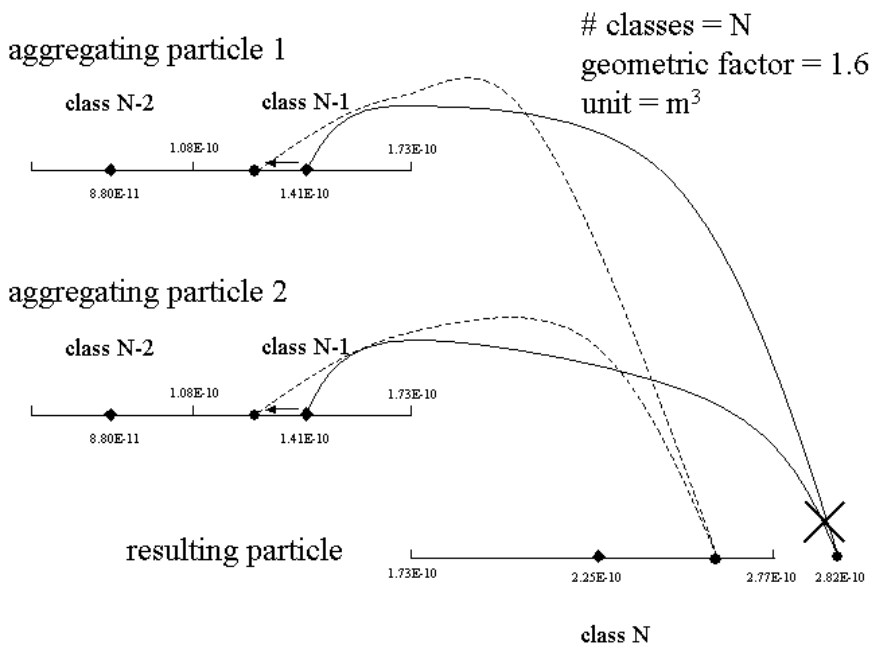

Figure 4.3: Illustration of the pseudo steady state that occurs with the fixed/moving pivot using a geometric factor of 1.6

can also be found in the fact that the pivot of the upper boundary class moves towards the upper system boundary in all simulated cases. The fact that the fixed pivot (and the Hounslow algorithm) slows down the simulation seems to be in disagreement with the findings of Kumar and Ramkrishna (1996b), who found a slower moving front when using the moving pivot. However, they only compared the methods when the front had not yet reached the upper classes of the system. Indeed, in some cases where the upper classes are initially empty, the front indeed moves faster for the fixed and Hounslow algorithm. Once the upper classes get filled with particles, however, the abovementioned findings are observed, and the moving pivot will reach SS faster. Although simulation times to reach SS are substantially smaller, increased calculation times are required. This is most probably caused by the fact that twice as many equations need to be solved. The calculation time dependency on the initial condition is also much more pronounced. This is caused by the extremely small values of the pivots combined with extreme initial conditions, forcing the solver to take very small steps to avoid numerical errors. Especially when empty classes are initially present and get filled by a number of particles, one needs to force the solver to take small steps to force the pivots to stay within the class bounds. These small steps also cause the calculation time to increase, which is definitely a drawback of the method.

Similar results were found for the cases using 25 classes. The calculation times are substantially smaller due to the smaller set of equations that needs to be solved. No clear dependency on the initial condition was observed.

The cases using 46 classes again showed PSS, which can be explained in the same way as for the fixed pivot case. Again, the number of particles trapped in the one but last class was different for the different initial conditions. It is very much governed by the movement of the pivots of the 2 upper classes. One

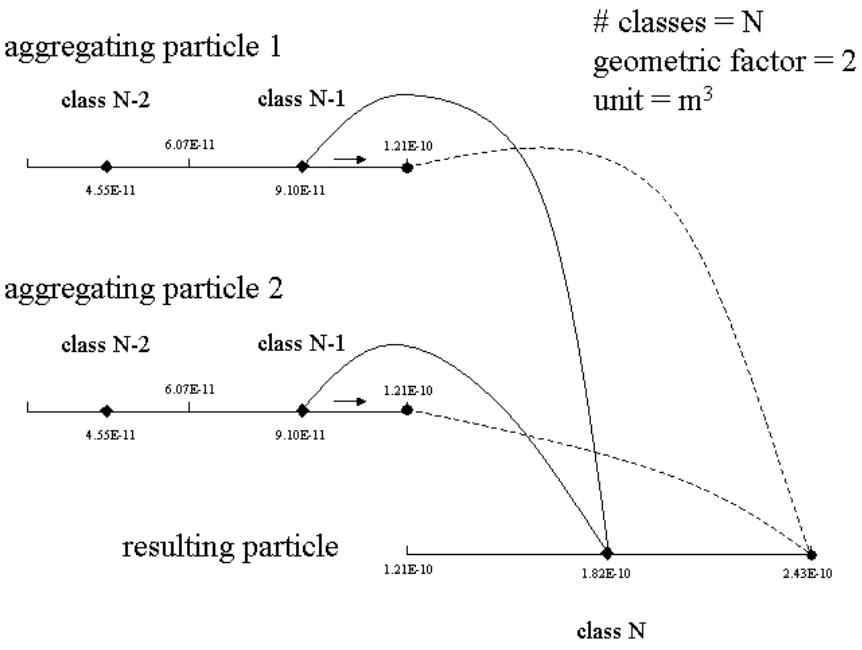

Figure 4.4: Illustration that a pseudo steady state can never occur for a fixed/moving pivot using a geometric factor of 2.0

Table 4.4: Overview of results for the pure aggregation case using the moving pivot algorithm for a simulation time of 1000s

init	classes	comp. time (s)	SS/PSS	sim. time to SS (s)
1	25	14	SS	1000
	31	20	SS	1000
	46	52	PSS	1000
2	25	781	SS	1000
	31	1745	SS	1000
	46	4293	PSS	1000
3	31	14	SS	1000
	46	44	PSS	90
4	31	279933	SS	1000
	46	706719	PSS	1000
5	31	15	SS	1000
	46	44	PSS	230
6	25	20	SS	1000
	31	18	SS	1000
	46	49	PSS	1000

way for the particles of the one but last class to escape is when the value of the pivot would drop below half of that of the upper boundary. However, this did not happen in any of the cases. The number of particles that eventually gets trapped will be determined by the number of particles present in the classes just below the one but last class. Also, the decrease of particles in these classes is highly influenced by the movement of the pivot of the upper boundary class. When the latter remains rather small, collisions with these particles will still be valid and will result in a fast depletion of the class, making them unavailable for collisions with particles from the one but last class, causing these to get trapped. The calculation times are again higher compared to the fixed pivot and really blow up in extreme cases.

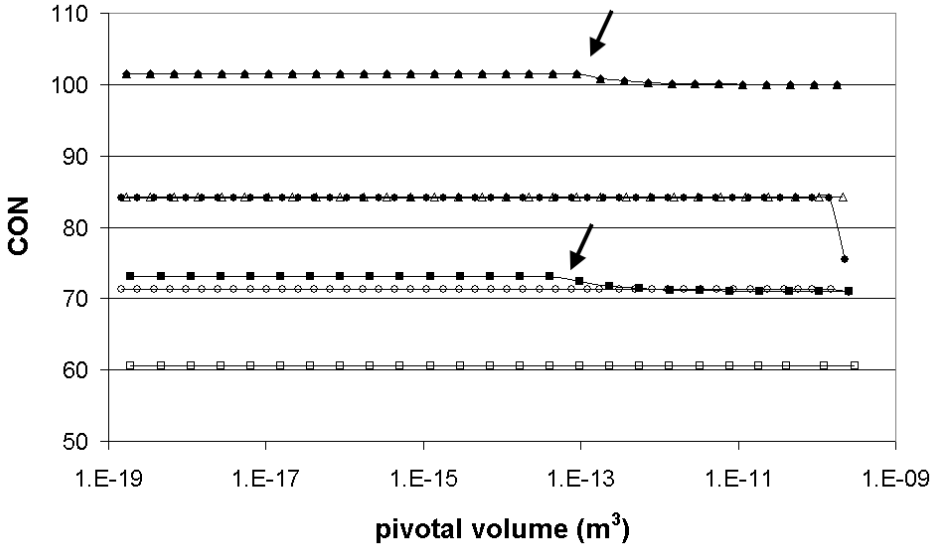

Figure 4.5: CON(v,t) for init1 for the pure aggregation case: Hounslow (♦), fixed 25 (■), fixed 31 (▲), fixed 46 (●), moving 25 (□), moving 31 (△) and moving 46 (○)

Fig. 4.5 shows the CON(v,t) for the different grid densities and solution techniques for init1 at SS/PSS. Due to the difference in pivotal volume of the upper boundary class for the different grids, the total number of particles (N_{tot}) is of course different. Adopting the case with geometric factor 2 (31 classes) as reference, N_{tot} will be smaller than 100 for upper boundary pivotal volumes that are larger than the reference pivotal volume.

The Hounslow and the fixed pivot methods using 31 classes exhibit exactly the same behaviour (coinciding CON-curves). At the time of assumed SS, there are still some particles that have not reached the upper boundary class, which is also the case for the fixed pivot using 25 classes (indicated by the arrows). In all other cases the particles have reached the upper boundary class, except for the fixed pivot, where one can clearly observe the PSS, and the moving pivot using 46 classes (less clear). Fig. 4.6 shows that the total volume is conserved for all cases. Here too, for the cases using 46 classes the PSS can be observed. All other initial conditions yield similar results (not shown).

To conclude, pure aggregation processes are best simulated using a moving pivot technique in combination with a grid using a geometric factor of 2 or higher. Hounslow and the fixed pivot slow down the aggregation rate due to the smaller allowed particle range. Hence, the numerical solution significantly affects the model outcome. Moreover, when using a finer grid (46 classes), particle entrapment in the one but last class occurs resulting in a PSS for these two methods. A coarser grid (25 classes)

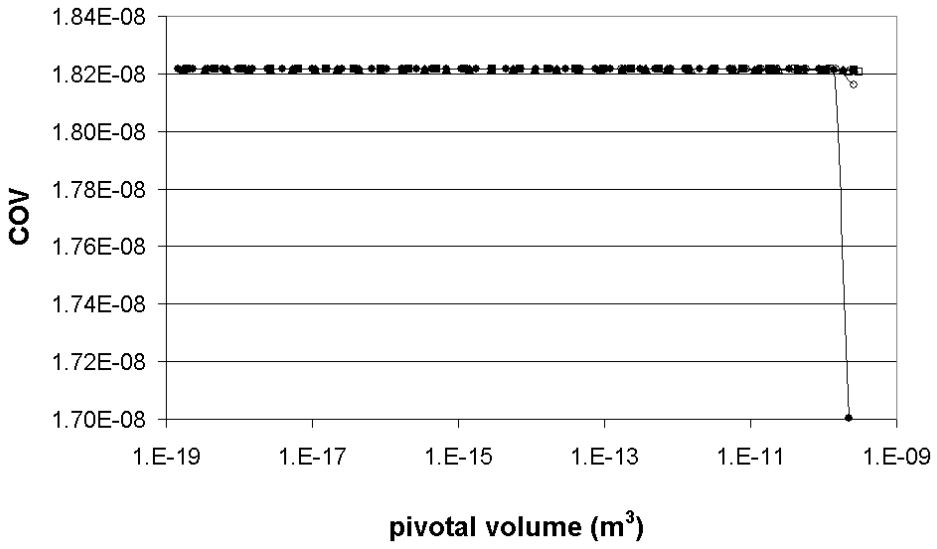

Figure 4.6: COV(v,t) for init1 for the pure aggregation case: Hounslow (♦), fixed 25 (■), fixed 31 (▲), fixed 46 (●), moving 25 (□), moving 31 (△) and moving 46 (○)

sometimes results in a significantly faster calculation time, but is, on the other hand, less accurate. The choice is, therefore, governed by the initial condition and the goal of the simulation work (i.e. parameter estimation, control, combination with CFD,...).

4.4.2 The pure breakage case

For a pure breakage process (in this work binary into equally sized daughters), one would expect all particles to move into the lower boundary class at SS. Hence, SS is defined to be reached when all particles are present in the lower boundary class and the number of particles in the second class has dropped below 0.1. As above, the total simulation times for the different cases were chosen larger then the time needed to reach the defined SS. Results of the pure breakage case for the fixed pivot and the moving pivot are summarised in respectively Table 4.5 and 4.6. The Hounslow case was not considered since the equations were only developed for pure aggregation.

The fixed pivot method using 31 classes reaches SS in all cases without mass losses. However, the simulation time needed to reach SS is slightly different for the different initial conditions. They seem to be dependent on the initial degree of aggregation of the system. Calculation speed is rather low compared to the pure aggregation case and seems also to be dependent on the initial condition.

Using a coarser grid (25 classes) increases the required time to reach SS. The reason for this is quite obvious and is related to the type of breakage that was used (binary into equally sized daughters). When a particle of class i breaks, it will produce 2 particles of class i-1 when a geometric grid with factor 2 is used. No reallocation of particles is needed since the particles that are born always coincide with an existing pivot. However, this is not the case when a coarser grid is used. A particle of class i that breaks up will produce particles somewhere in between the pivots of class i and i-1, implying that they will be partly reallocated to class i, which slows down the breakage process. Again, the model output is sensitive

Table 4.5: Overview of results for the pure breakage case using the fixed pivot algorithm and a simulaton time of 6000s

init	classes	comp. time (s)	SS/PSS	sim. time to SS (s)
1	25	577	SS	6000
	31	1217	SS	4900
	46	17184	PSS	4800
2	25	589	SS	6000
	31	1222	SS	4800
	46	19725	PSS	4700
3	31	1544	SS	4900
	46	4339	PSS	4800
4	31	1214	SS	4700
	46	3692	PSS	4700
5	31	8693	SS	4800
	46	4377	PSS	4800
6	25	575	SS	6000
	31	1216	SS	4800
	46	3847	PSS	4800

to the numerical method which is unacceptable. The calculation times are again lower due to the lower number of equations. Here too, they are dependent on the initial condition.

When using a finer grid (46 classes) the phenomenon of particle entrapment again occurs, resulting in a PSS. The reasoning is exactly the same as in the aggregation case, but now occurs at the lower end of the particle range. The PSS was defined to be reached when the number of particles in the third class drops below 0.1. Simulation times required for reaching PSS are in the same order of magnitude as the ones for 31 classes. Calculation times are again higher due to the increased number of equations to be solved simultaneously. They are dependent on the initial condition.

The moving pivot using 31 classes yields exactly the same result as the fixed pivot for 31 classes. This is caused by the specific type of breakage that is used (i.e. binary breakage). Hence, the simulation times to SS are the same. However, the calculation speed is faster compared to the fixed pivot, which seems odd since twice as many equations need to be solved. The reason for this is unclear. A dependency on the initial condition is also observed.

When coarsening the grid for the moving pivot technique, the CVODE-solver experiences problems due to the fact that it attempts to reduce the step size to levels where convergence is no longer found. Other solvers with adaptive step size failed too. In the end the simulation was performed using a Runge Kutta 4^{th} order solver (RK4) using a small step size (1E-4), resulting in long calculation times (several days), which is not the intention of the discretised methods under study. Therefore, the simulations were not completed and it is recommended not to use the moving pivot with a coarse grid for this breakage problem.

Using finer grids combined with the moving pivot also resulted in problems with the CVODE-solver in some cases. Changing solver settings nor using a different solver allowed to solve the numerical problems. For the same reason mentioned before, the simulations with the RK4 solver were not completed.

Table 4.6: Overview of results for the pure breakage case using the moving pivot algorithm and a simulation time of 6000s (empty lines indicate slow calculations or numerical problems)

init	classes	comp. time (s)	SS/PSS	sim. time to SS (s)
1	25	–	–	–
	31	350	SS	4800
	46	–	–	–
2	25	–	–	–
	31	204	SS	4800
	46	–	–	–
3	31	256	SS	4900
	46	778	PSS	4800
4	31	201	SS	4700
	46	615	PSS	4500
5	31	257	SS	4900
	46	–	–	–
6	25	–	–	–
	31	202	SS	4800
	46	–	–	–

In the cases where it did work, PSS's were observed and calculation times were larger compared to the fixed pivot using 31 classes, due to the increased number of equations.

Fig. 4.7 shows the CUN(v,t) for the different grids and solution techniques for init1 at SS (note that no results are shown for the moving pivot using 25 and 46 classes due to the numerical problems). The difference in pivotal volume of the lower boundary class for the different cases causes the total number of particles (N_{tot}) to be different. However, the fixed and moving pivot with 31 classes yield exactly the same result, obviously caused by the binary breakage into equally sized daughters in combination with a geometric factor of 2. The fixed pivot with a fine grid exhibits particle entrapment.

Fig. 4.8 shows that volume is conserved and is exactly the same for all cases. Again, one can observe the fixed pivot with 46 classes suffering from particle entrapment.

All other initial conditions yielded similar results (not shown).

In conclusion, the pure binary breakage process into equally sized daughters is best solved using a geometric grid with factor 2. The solution method does not really matter since all result in exactly the same solution in exactly the same simulated time. However, the moving pivot algorithm needs the least calculation time.

4.4.3 The combined aggregation/breakage case

The steady state that develops in combined aggregation/breakage cases is solely dependent on the model parameters and was shown to be independent of the initial condition when the total volume in the system is constant (Chen et al., 1990). For this case the Hounslow equations were accompanied with breakage equations, similar to those used by the fixed pivot, but less general. Results of the combined case for the

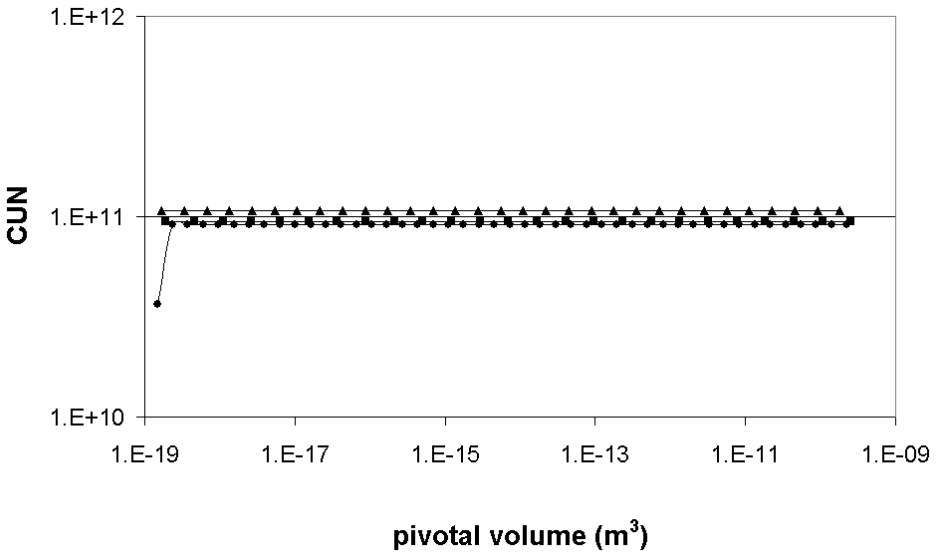

Figure 4.7: CUN(v,t) for init1 for the pure breakage case: fixed 25 (■), fixed 31 (▲), fixed 46 (•) and moving 31 (△)

Hounslow method, the fixed pivot and the moving pivot are summarised in respectively Table 4.7, 4.8 and 4.9.

The Hounslow method results in exactly the same SS for all cases. The simulation time to SS is slightly variable, but the calculation times are similar and very fast.

The fixed pivot using 31 classes yields the same results as the Hounslow method in terms of SS and simulation time needed to reach SS. The calculation time is, however, significantly larger and depends on the initial conditions. This larger calculation time is partly caused by the difference in aggregation equations, but also by the more general implementation of the breakage equations compared to the Hounslow method.

Coarsening the grid results in a slightly different SS, especially in the tail accuracy (Fig. 4.9 and Fig. 4.10). Simulated number concentrations in both the upper and lower tail are higher. The simulation time

Table 4.7: Overview of results for the combined case using the Hounslow algorithm and a simulation time of 50s

init	classes	comp. time (s)	sim. time to SS (s)
1	31	11	220
2	31	11	290
3	31	11	240
4	31	12	280
5	31	11	250
6	31	11	250

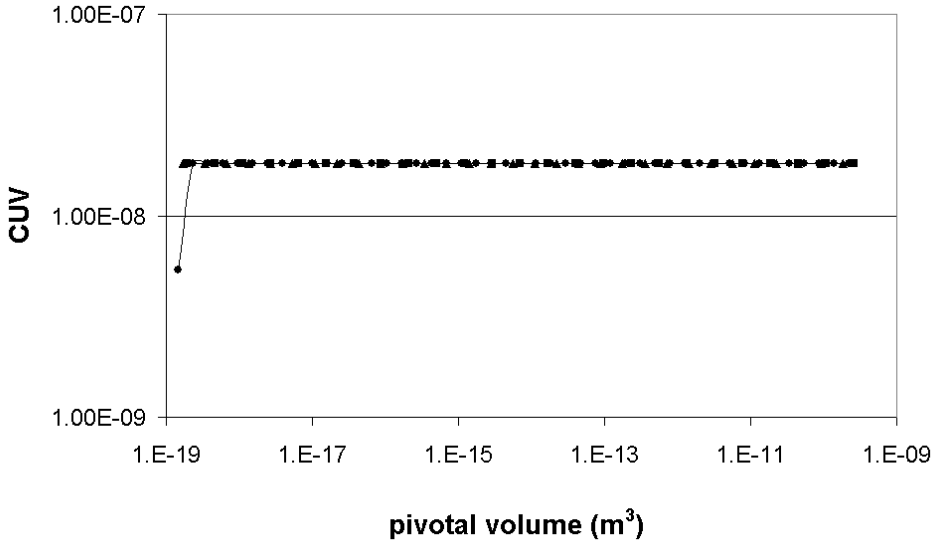

Figure 4.8: CUV(v,t) for init1 for the pure breakage case: fixed 25 (■), fixed 31 (▲), fixed 46 (●) and moving 31 (△)

Table 4.8: Overview of results for the combined case using the fixed pivot algorithm and a simulation time of 50s (all reach a normal SS)

init	classes	comp. time (s)	sim. time to SS (s)
1	25	60	220
	31	753	220
	46	519	220
2	25	62	290
	31	148	290
	46	579	290
3	31	143	240
	46	523	240
4	31	146	280
	46	534	280
5	31	145	250
	46	541	250
6	25	60	250
	31	142	250
	46	533	250

Table 4.9: Overview of results for the combined case using the moving pivot algorithm and a simulation time of 50s (all reach a normal SS)

init	classes	comp. time (s)	sim. time to SS (s)
1	25	–	–
	31	96	220
	46	2159	220
2	25	2969	290
	31	129	290
	46	35820	290
3	31	96	240
	46	1389	240
4	31	205	280
	46	–	–
5	31	87	250
	46	868	250
6	25	2955	250
	31	92	250
	46	2133	250

to reach SS is similar. Calculation times are smaller due to the smaller number of equations. Refinement of the grid also results in a slightly different SS in the tails. Simulated number concentrations are now lower in the upper tail, whereas they are still higher in the lower tail. Simulation times are similar and calculation times larger.

The moving pivot using 31 classes yields similar results in the lower tail as the Hounslow and fixed pivot with 31 classes, but predicts smaller number concentrations in the upper tail (Fig. 4.9 and Fig. 4.10). These findings were also reported by Kumar and Ramkrishna (1996b), who concluded that the moving pivot algorithm is more accurate even for coarse grids. Indeed, one observes that using the fixed pivot with finer grids results in solutions that move towards the moving pivot solution. This difference in accuracy was proved to become important when performing parameter estimations, since the different methods resulted in significantly different parameter estimates for exactly the same model (see chapter 7). The simulation times needed to reach SS are similar, whereas calculation speed is higher compared to the fixed pivot but lower compared to the Hounslow algorithm. Hence, the question to the user is whether the increased accuracy justifies the increased calculation time. For a single simulation the answer is yes, but for an optimisation requiring 300 runs, the answer might not be so straightforward.

Coarsening the grid resulted in problems with the CVODE solver for init1. In the cases where it was possible to perform the simulation, no significant difference in solution was observed. However, the calculation time increased significantly, which is rather contradictory since the number of equations to be solved is smaller. An explanation for this was not found.

Refining the grid resulted in similar SS and required the same simulation times. However, the accuracy is not significantly improved by refining the grid and the calculation time increases significantly. Moreover, empty classes appear in the distribution due to the specific pivot movement as is indicated by the arrows in Fig. 4.10 and will be more thoroughly discussed in chapter 5. When pivot x_i becomes smaller than twice the value of the boundary of the underlying class v_{i-1}, particles break into class $i-2$ instead of

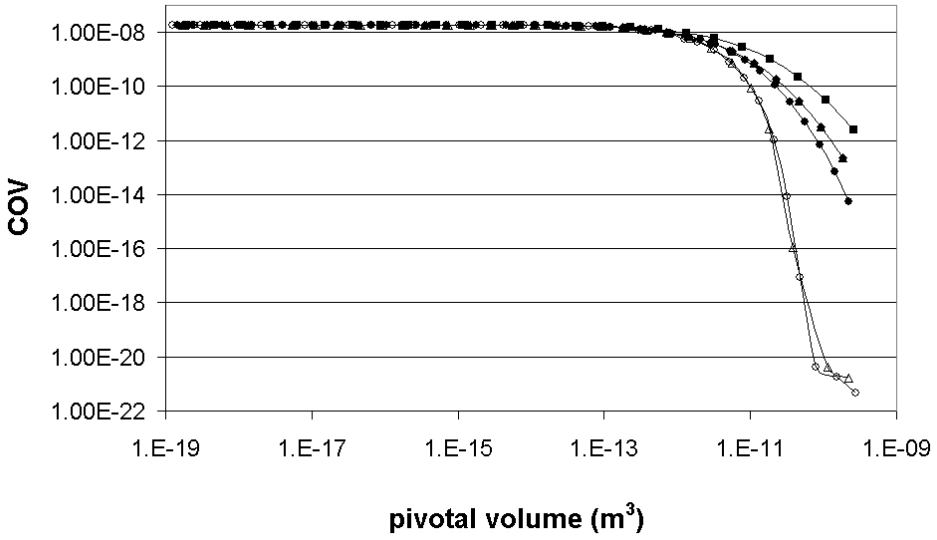

Figure 4.9: COV(v,t) for init1 for the combined case: Hounslow (⧫), fixed 25 (■), fixed 31 (▲), fixed 46 (●), moving 31 (△) and moving 46 (○)

class $i-1$. For as yet unclear reasons, init4 resulted in very long calculation times and could not be completed.

When comparing the different initial conditions, it was observed that the fixed pivot with 31 classes yields exactly the same steady state distribution, independent of the initial distribution. Moreover, the movement of the pivots and the steady state distributions when using the moving pivot with 31 classes are also independent of the investigated initial conditions.

In conclusion, the moving pivot with a geometric factor of 2 seems to be the most accurate solution method for the combined aggregation/breakage case. However, the goal of the study will determine whether the increased accuracy justifies the increased calculation time.

4.5 Conclusions

Three different solution methods for solving a PBE based on discretisation (the Hounslow method, the fixed pivot and the moving pivot) were compared for three different processes (pure aggregation, pure breakage and combined aggregation/breakage) using 6 different initial conditions with a fixed total system volume.

For pure aggregation, the moving pivot with a geometric factor of 2 turned out to be the best solution method. The Hounslow method and the fixed pivot slowed down the aggregation rate due to the fact that some aggregations are (mathematically) not allowed. In other words, the numerical technique influences the model output, which is unacceptable. When using a finer grid, both the fixed and moving pivot suffered from particle entrapment in the one but last class. A coarser grid (25 classes) sometimes resulted in a significantly faster calculation time, but was, on the other hand, less accurate. The choice is, therefore, governed by the initial condition and the goal of the simulation work (i.e. parameter estimation, control,

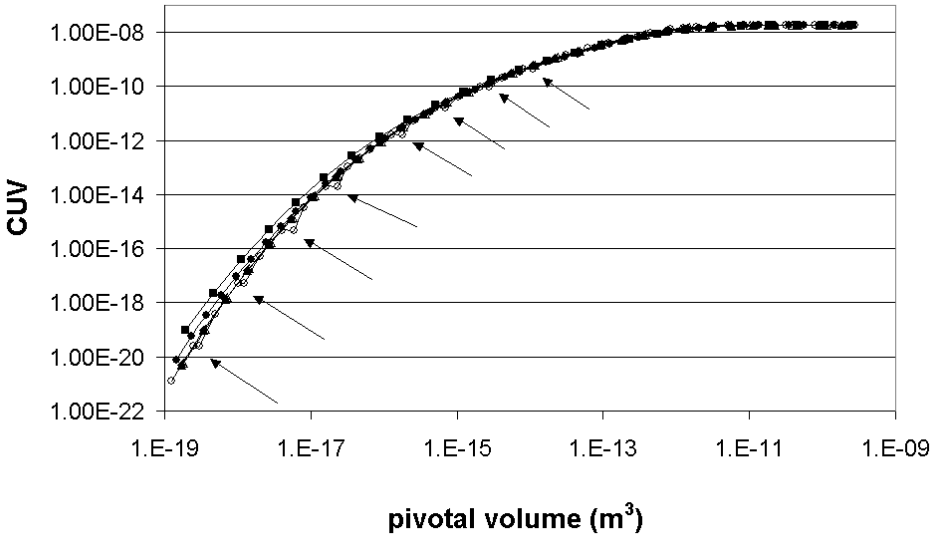

Figure 4.10: CUV(v,t) for init1 for the combined case: Hounslow (⧫), fixed 25 (■), fixed 31 (▲), fixed 46 (●), moving 31 (△) and moving 46 (○)

combined with CFD,...).

The pure binary breakage process into equally sized daughters is best solved using a geometric grid with factor 2. Coarser grids resulted in slower breakage for the fixed pivot case and in numerical difficulties in the moving pivot case, whereas finer grids gave rise to particle entrapment. The fixed and moving pivot resulted in exactly the same solution in exactly the same simulation time. However, the moving pivot algorithm needs the least calculation time and might, therefore, be preferred.

The moving pivot with a geometric factor of 2 is the most accurate solution method for the combined aggregation/breakage case. The Hounslow and fixed pivot method resulted in a less accurate approximation of the steady state solution, although Hounslow's algorithm performed the simulation faster. Refining the grid using the fixed pivot resulted in an improvement of the accuracy, but it still is worse compared to the moving pivot's accuracy. In the end, the goal of the study (including the desired accuracy) will determine whether the increased accuracy justifies the increased calculation time.

CHAPTER 5

Discretising a population balance model with equally sized breakage using the moving pivot technique

5.1 Abstract

This chapter deals with a problem that was first observed when the moving pivot technique was applied with a geometric grid (with factors smaller than 2) to solve a PBM with binary breakage into equally sized daughters (see chapter 4). It demonstrates, explains and provides a solution to this general problem of equally sized breakage that surfaced when this (too) simple kernel was applied to activated sludge flocculation.

5.2 The population balance model

The applied model equation and kernel structure for aggregation and breakage are the same as those defined in section 4.2 and will not be repeated here. Attention is drawn to the special type of breakage distribution function that was used: binary breakage into equally sized daughters. This can be expressed as:

$$v(x')\Gamma\left(x, x'\right) = 2\delta\left(x - \frac{x'}{2}\right) \tag{5.1}$$

The specific problem arises when this model is solved using the moving pivot technique and a geometric grid with a factor s smaller than 2.

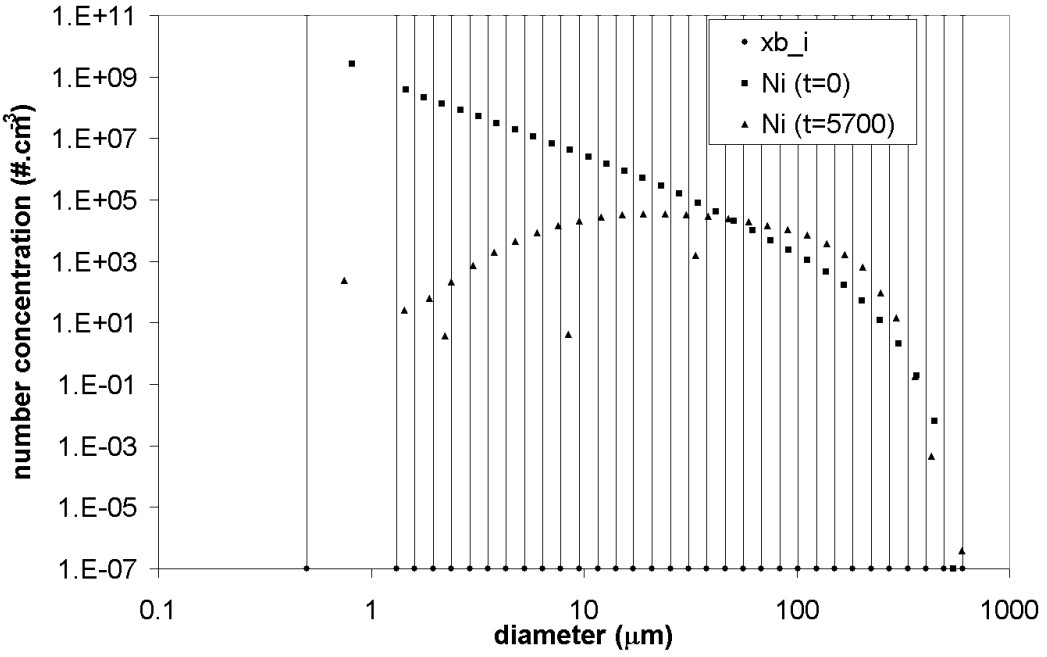

Figure 5.1: Initial and final number distribution after solving the PBM with 32 classes using the moving pivot discretisation technique (geometric grid with factor s=1.8)

5.3 Results and discussion

The discretisation grid used here was taken from the default output of one of the sizing devices used in this work, i.e. a Malvern Mastersizer E (Malvern, UK). The instrument-defined grid of the raw data was geometric with a factor s=1.8 (volume-based) and contained 32 classes. A PBM with 32 classes using the same grid as the instrument was implemented in the modelling and simulation platform WEST (Hemmis NV, Belgium) and solved using the moving pivot technique. The initial pivots were chosen to be the geometric mean of the size class boundaries $\mathrm{x_{bi}}$ (similar to the grid definition of the Mastersizer). It should be noted that the first class did not meet the geometric grid as defined earlier. This was, however, not within our power since the raw data of the experiment were not available. It does not harm the conclusions of this chapter though.

The initial condition was taken from the experiment of Biggs (2000) performed at $\bar{\mathrm{G}} = 19.4\,\mathrm{s}^{-1}$. Parameter values were chosen to be A=226 $\mathrm{m}^{-1}\mathrm{s}^{-1}$ and $\alpha = 0.0152$. Again, these have no real-life meaning and were chosen to demonstrate the behaviour.

When performing simulations, discontinuities in the size distribution were observed, as illustrated in Fig. 5.1 (classes 4, 11 and 18) even though no discontinuities were present in the initial distribution. After 5700s, clearly the pivots in all size classes have moved from their initial position and 3 classes (4, 11 and 18) contain a lower number of flocs than the neighbouring classes. Noteworthy is the fact that the pivots in the upper adjoining classes (5, 12 and 19) have all moved to and almost collapse with the lower boundary of the class ($\mathrm{x_{b5}}$, $\mathrm{x_{b12}}$ and $\mathrm{x_{b19}}$). In the quest for an explanation of the irregularities, focus will be on class 11 (findings for classes 4 and 18 are similar and will not be discussed in depth).

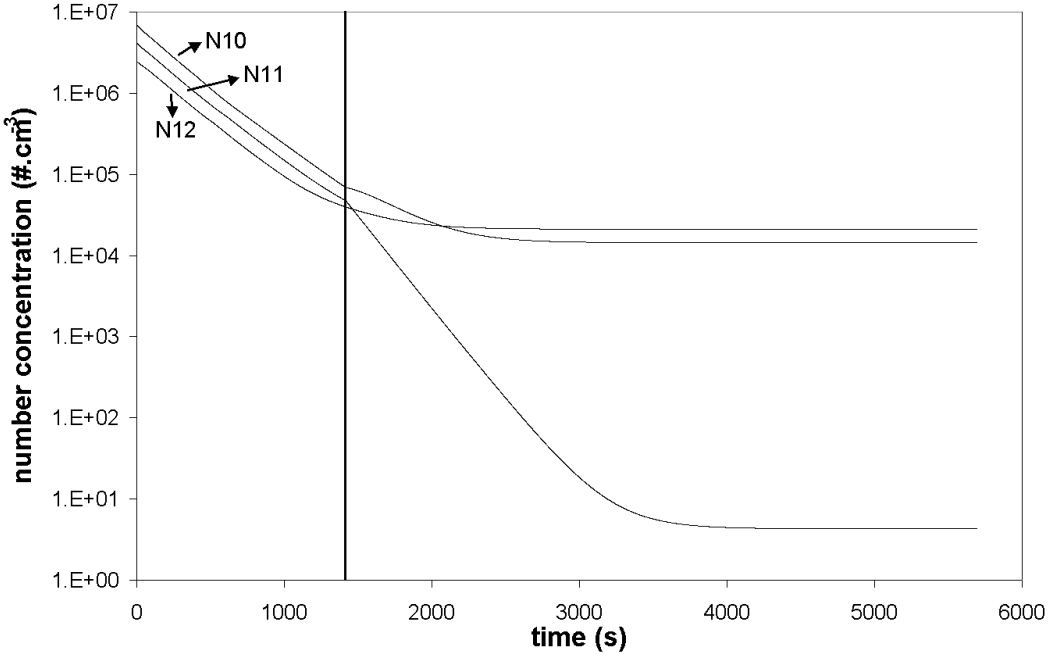

Figure 5.2: Simulated time evolutions of N_{10-12}

The time evolution of the number of flocs in classes 10, 11 and 12 (N_{10-12}) and their pivots (x_{10-12}) are shown in Fig. 5.2 and Fig. 5.3 respectively. It can be observed that around t=1418 s the slope of N_{10} suddenly becomes less steep, whereas the slope of N_{11} becomes steeper. At the same time instant, the pivot of class 10 (x_{10}) suddenly increases and the pivot of class 11 (x_{11}) stops decreasing. Also noteworthy, the pivot of class 12 (x_{12}) decreases and ends up close to its lower class boundary ($\mathrm{x}_{\mathrm{b}12}$). At t=1418 s, the value of x_{12} is 4.92e-16 m^3, exactly the double of the lower boundary of class 11 ($\mathrm{x}_{\mathrm{b}11}$). After t=1418 s, x_{12} further decreases which leads to the particular behaviour that particles that break up from class 12 will no longer end up in the adjoining class 11, but in class 10 since a geometric grid with a factor 1.8 was used. This explains the sudden decrease in slope of N_{11} and the increase in slope of N_{10}. It also explains why the pivot values x_{10} and x_{11} change the way they do. Since flocs are no longer formed in the lower part of class 11, the pivot x_{11} is no longer forced to reduce its value. On the contrary, it now starts increasing because only particles larger than the pivot are formed through aggregation. Pivot x_{10} increases as well since suddenly particles are formed with a size close to the upper boundary of its size class ($\mathrm{x}_{\mathrm{b}11}$). To confirm this behaviour leading to the observed irregularities in the size distribution, the time evolution of the breakage birth terms of classes 10-12 (BB_{10-12}) was investigated too (Fig. 5.4). At t=1418 s BB_{11} was found to drop from 142 to 0, whereas BB_{10} increased from 140 to 282, exactly recovering all the particles breaking from class 12.

In summary, simulating an aggregation-breakage system in which breakage is binary into equally sized daughters combined with the moving pivot technique and a geometric factor s smaller than 2 leads to discontinuities. Indeed, when lowering the number of classes of the PBM from 32 to 28, which corresponds to s=2 (volume-based), the irregularities no longer occur (Fig. 5.5). Even if a pivot drops to the value of the lower boundary of the class, flocs will still break up into the lower adjoining class. From the above it is concluded that it is essential to use a geometric grid with s at least equal to 2 when using the moving pivot technique to solve a PBM with binary breakage into equally sized daughters.

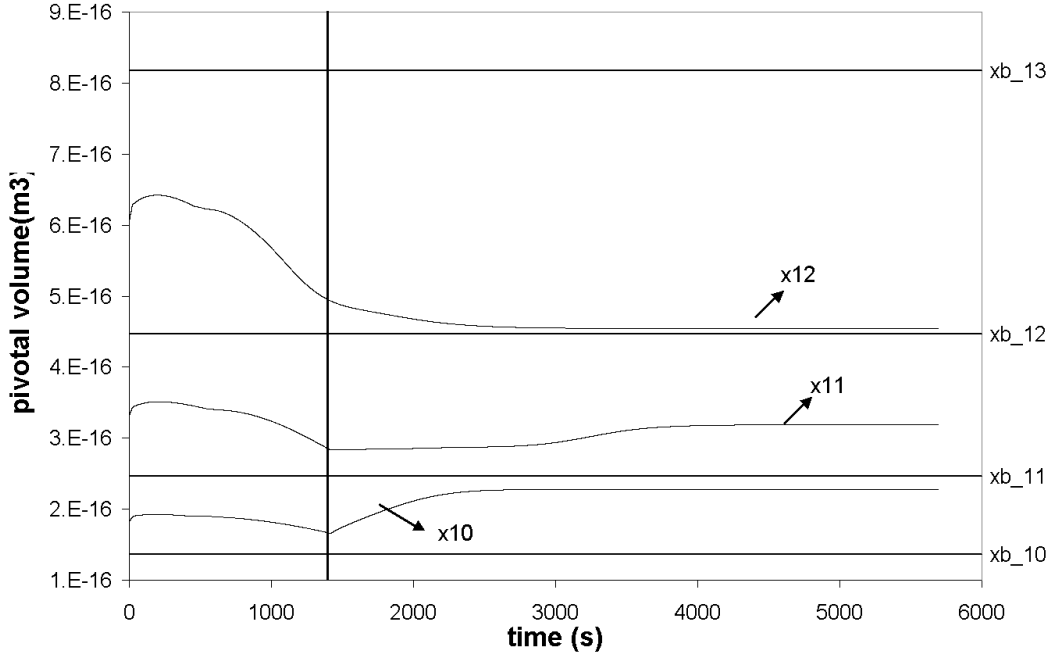

Figure 5.3: Simulated time evolutions of x_{10-12}

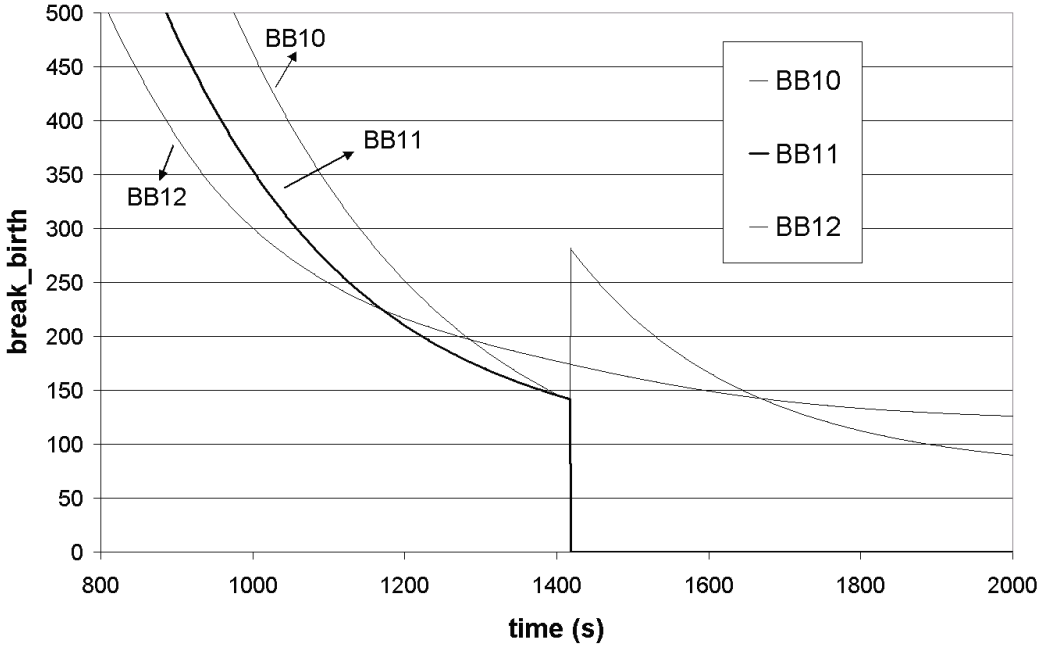

Figure 5.4: Simulated time evolution of breakage birth terms of classes 10-12

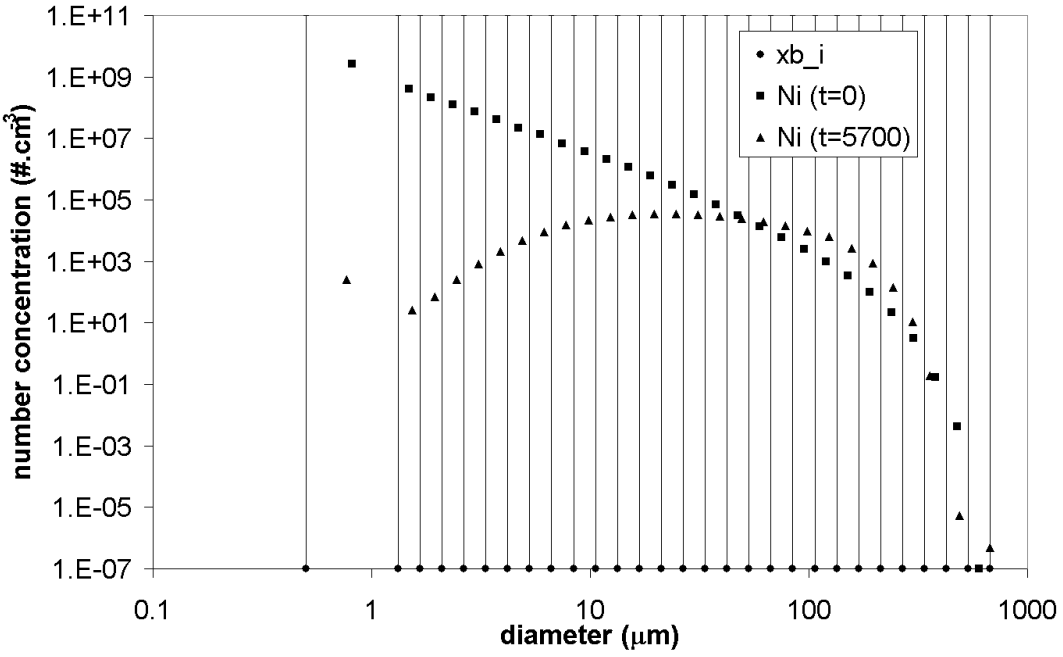

Figure 5.5: Initial and final number distribution after solving the PBM with 28 classes using the moving pivot discretisation technique (geometric grid with factor s=2)

This severely limits the freedom of grid choice and forces one to adapt the sizing device output grid by changing the software settings prior to the measurement (if possible).

This reasoning can be extended to any equally sized breakage kernel given by

$$v(x')\Gamma\left(x,x'\right)=\eta\delta\left(x-\frac{x'}{\eta}\right) \tag{5.2}$$

where η is a constant and $\delta(\mathrm{x})$ is the Dirac function. To avoid the aforementioned problem, the following general rule can be adopted

$$s \geq \eta \tag{5.3}$$

For increasing values of η this means that increasingly coarser grids are required for the moving pivot technique, substantially deteriorating the accuracy of the method. Alternatively, one could give up using geometric grids and use linear grids instead, but this is not trivial when large size ranges must be covered since it will severely increase the number of size classes and, hence, equations, thus, increasing the computational load.

5.4 Conclusions

It was shown that a PBM with equally sized breakage into η daughters that is solved using the moving pivot technique using a geometric grid with a factor $\mathrm{s} < \eta$ introduces discontinuities in the distribution. The reason for this is that certain pivots decrease below a certain value (but still within the size class) resulting in the phenomenon that particles that break up no longer appear in the lower adjoining class,

but one class below. This causes discontinuous changes in both the number concentration and the pivots of these classes. It is, therefore, essential to use a geometric grid with $\mathrm{s} \geq \eta$ when using the moving pivot technique to solve a PBM with breakage into equally sized daughters. This severely limits the freedom of grid choice and, consequently, the output of the sizing device should be adapted. For large values of η the accuracy of the method might be affected by the coarseness of the grid.

CHAPTER 6

Experimental data analysis of flocculation experiments

In this work, two sets of data are considered. A first data set was borrowed from Biggs (2000) whereas a second one was obtained using the experimental set-up that was described in section 3.3. The focus of this chapter will be on the evolution of the distributions rather than a summarising parameter such as e.g. D[4,3] on which Biggs (2000) and Govoreanu (2004) focused in their respective work. It will be investigated whether useful information is lost when discarding the distributions by summarising them in one variable. Especially the connection with the Kolmogorov scale will be investigated.

6.1 Experimental data set from Biggs (2000)

Biggs (2000) was the first to obtain on-line experimental data of activated sludge flocculation. The experimental set-up and procedures that were used are briefly described here.

A 1 L vessel was filled with a diluted activated sludge sample, which was operated under certain controlled conditions (shear rate and Ca-addition). Prior to the experiments, the sludge flocs were sonicated in order to deflocculate them into single cells ($1\,10^{-6}\,\mathrm{m}$) and microcolonies of about $1\,10^{-5}\,\mathrm{m}$. The sonication time was chosen in a way not to cause significant cell lysis. The sludge was then allowed to reflocculate under certain specific conditions of mixing intensity and calcium addition and was circulated through the sample dispersion unit of a Malvern Mastersizer E (Malvern, UK) in order to obtain on-line quantitative information about floc structure, floc size distribution (FSD) and their derived equivalent diameters. The measurement technique is based on forward laser light diffraction and has been used by other researchers (Wilén and Balmér, 1999; Guan et al., 1998; Waite, 1999a; Biggs and Lant, 2000; Spicer and Pratsinis, 1996b; Govoreanu et al., 2003). The sludge flocs are brought in a laser beam where they cause forward scattering of the incoming light. Small particles will scatter the light in the large angle range, whereas large particles scatter the light in the small angle range. Hence, a heterogeneous particle

population, as is the case for activated sludge, will result in a diffraction pattern. This light intensity pattern is measured by a number of detectors located at different angles from the incident laser beam. An optical model (i.e. Fraunhofer model) is then used to transform the diffraction pattern into a FSD. The latter is presented as a volume percentage (vol%) distribution (i.e. the percentage of total solids volume in every size class), but other descriptive parameters can be derived from it such as different moments and weighted diameters. An often used weighted diameter is the mass mean diameter (also termed D[4,3]) defined as the ratio of the fourth and third moment of the distribution:

$$D[4,3] = \frac{\int_0^\infty f_N(x)x^4}{\int_0^\infty f_N(x)x^3} \approx \frac{\sum_{i=1}^N \Delta f_N(x_i)x_i^4}{\sum_{i=1}^N \Delta f_N(x_i)x_i^3} \tag{6.1}$$

where x and $\mathrm{x_i}$ represent the floc size and the floc size in class i respectively. $\Delta \mathrm{f_N(x_i)}$ represents the number fraction in size class i (=$\mathrm{N_i}/\sum \mathrm{N_i}$).

The main advantage of this technique is its on-line applicability. Drawbacks of the laser diffraction method are: (1) the assumption of sphericity of particles in the optical model, and (2) the required dilution step ($< 0.2 \mathrm{kg.m^{-3}}$) to avoid multiple scattering since this is not accounted for by the optical model. The latter is checked by means of the obscuration level, which should be inside a certain range for the measurement to be reliable. In order not to disturb the sample to be measured by, for instance, a change in ionic strength, filtered effluent ($4.5\,10^{-7}\,\mathrm{m}$) should be used for dilution purposes (Mikkelsen et al., 1996; Govoreanu et al., 2001). The flow rate to the flow-through cell was determined in a way to minimise shear effects and pump pulsation influences and to avoid settling in the tubes (to approximate isokinetic sampling). A flow rate of $3\,10^{-3}\,\mathrm{kg.s^{-1}}$ was selected (Biggs and Lant, 2000).

6.1.1 Experiments using different shear rates

A first experimental data set that was borrowed consists of 4 distinct experiments applying different shear intensities, reported as average velocity gradient $\bar{\mathrm{G}}$ (for definition, see Eq. 2.57). The values that were applied are 19.4, 37, 113 and $346\,\mathrm{s^{-1}}$. The available data sets consist of time evolutions of vol% distributions. The latter express the percentage of total floc volume that is present in the different size classes. The grid is the default Malvern grid and is geometric with a volume-based factor s of 1.8 (i.e. $\mathrm{v_{i+1}} = 1.8\,\mathrm{v_i}$).

The D[4,3] or mass mean diameter (i.e. the fourth moment of the distribution divided by the third moment) is often used as a summarising variable of the distribution. The time evolution of the D[4,3] of the experiments conducted at different shear rates are shown in Fig. 6.1. It is revealed that the mass mean diameter initially increases quite fast, obviously due to the fact that aggregation is dominant over breakage (flocs were broken by sonication). Eventually, a steady state is reached (although a small positive slope still persists). Lower shear rates result in higher steady state mass mean diameters.

However, based on the mass mean diameter as a summarising parameter, it is difficult to judge which particle classes are most affected by the changes in mixing intensity. In that respect, it is better to investigate the entire distribution as such, i.e. the time evolutions of the vol% in the different size classes. The latter are depicted in Fig. 6.2 for the case of $\bar{\mathrm{G}} = 19.4\,\mathrm{s^{-1}}$.

The size classes are indicated in terms of the size class diameter (in $\mu\mathrm{m}$). The Kolmogorov microscale near the impeller was determined to be $127\,\mu\mathrm{m}$, assuming that the local energy dissipation is 10 times that of the average energy dissipation (Dr. Nandishkor Nere, personal communication). For this determination, the reader is referred to Table 2.4. This seems to be a good estimate, since the largest volume

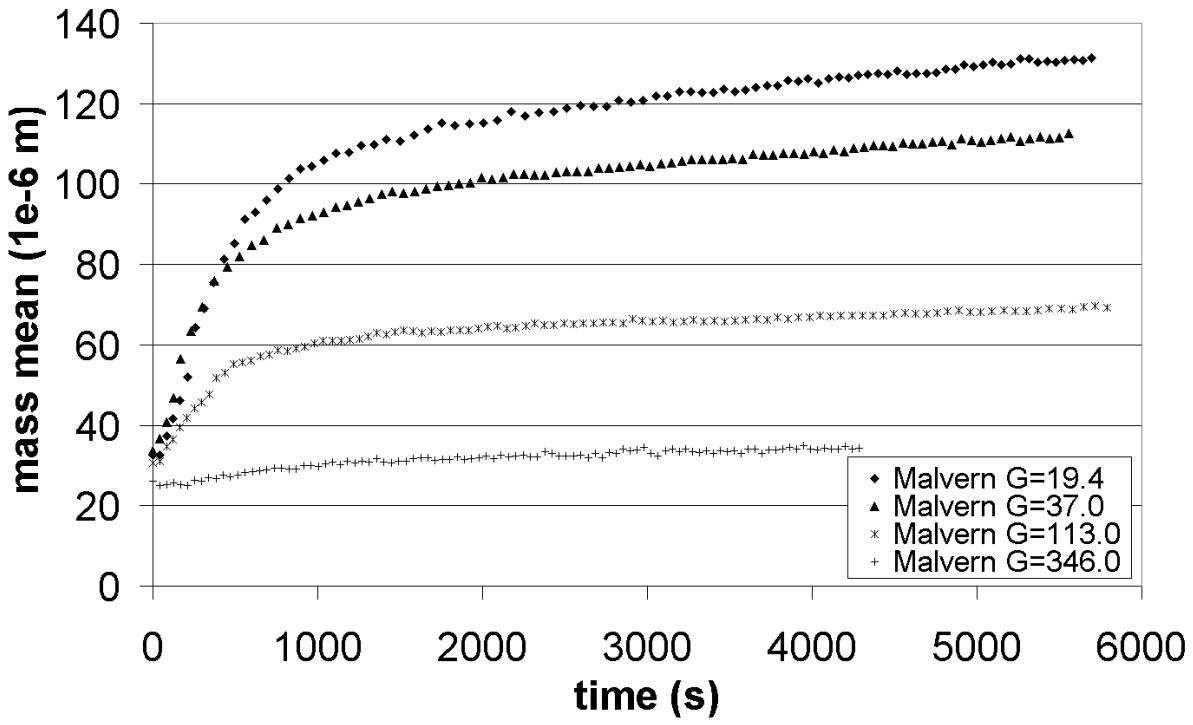

Figure 6.1: Time evolutions of D[4,3] for the experiments at different shear intensities

fractions are found for floc size classes in that neighbourhood (112-136 μm). Concerning the shape of the time evolutions, 3 cases can be distinguished:

1. size classes larger than the Kolmogorov microscale are continuously increasing and tend to reach an equilibrium (this is similar to the D[4,3] evolution confirming its dependence on large particle size classes)
2. size classes smaller than the Kolmogorov microscale tend to grow and reach a maximum after which they drop again to an equilibrium
3. the smallest classes don't exhibit peak behaviour and just drop to reach an equilibrium

From case 1 it could be argued that breakup does not occur to a large extent. If it would, a significant volume decrease of the particles larger than the Kolmogorov scale would be expected, which is definitely not the case. The leveling off to an equilibrium can either be explained by aggregation becoming slower or breakage gaining more importance. Most probably the latter is true, since it is unlikely that aggregation would stop as a lot of small particles are still present in the system (small in volume but large in numbers). Steady state is, however, not yet completely reached as was also observed from the D[4,3] analysis.

The peaks appearing in case 2 (size classes smaller than the Kolmogorov microscale) are caused by large amounts of aggregation of flocs smaller than these size classes, whereas flocs from these classes aggregate at a slower rate (i.e. aggregation birth outnumbers aggregation death). In other words more flocs are formed than the number that disappears through aggregation. Breakage does not need to be considered here since it can be argued that hardly any breakage of larger flocs is occurring (i.e. no

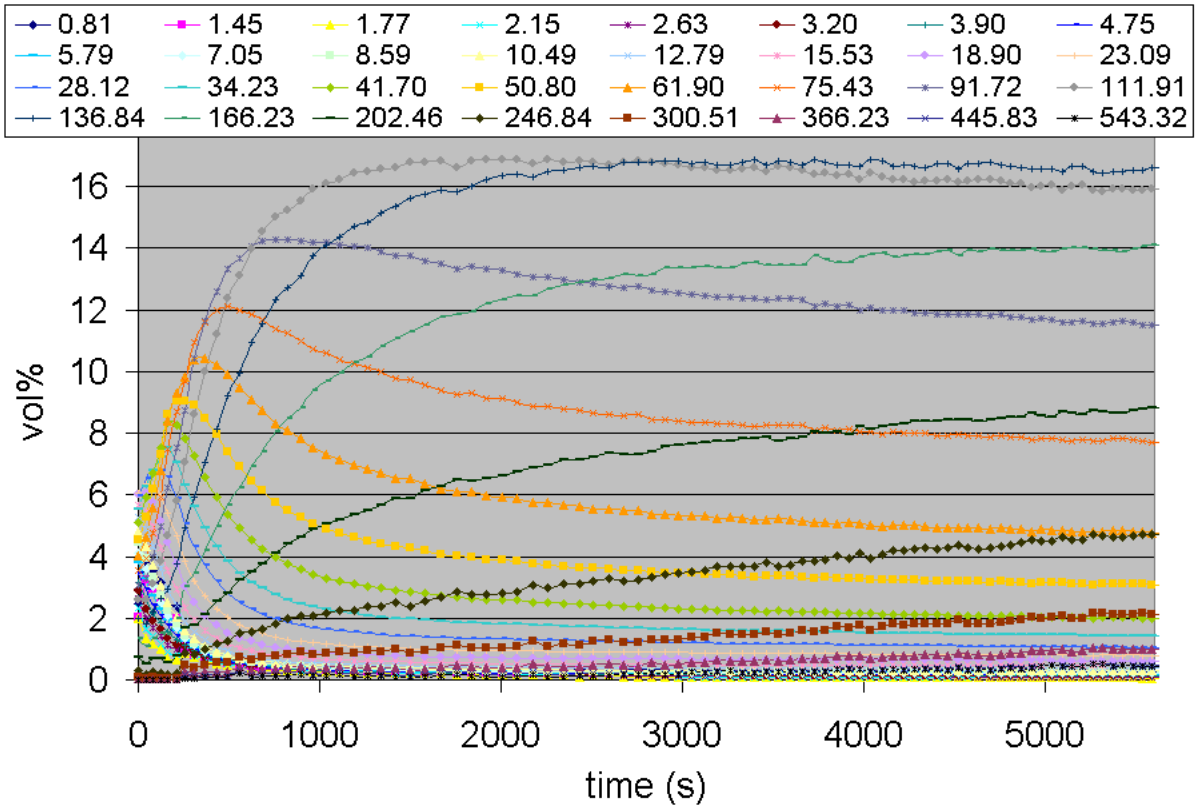

Figure 6.2: Time evolutions of vol% in the different size classes for the experiment at an average shear rate of $19.4\,\mathrm{s}^{-1}$

breakage birth). Moreover, flocs smaller than the Kolmogorov microscale do not break since they are smaller than the smallest eddy scale. This supports the hypothesis. The decrease after the peak can be explained by a similar, but opposite reasoning: more flocs aggregate out of the size class than flocs are formed through aggregation of smaller flocs. Hence, the observed evolution can be regarded as a 'front' of flocs moving through the size space, which is also confirmed by the fact that the peaks appear at a later time instant for larger size classes.

The really small classes (case 3) do not exhibit the peak behaviour meaning that they are solely aggregating into larger flocs and are only formed to a lesser extent from smaller size classes (i.e. aggregation death outnumbers aggregation birth). The peak behaviour is absent for floc size classes smaller than $19\,\mu\mathrm{m}$.

Similar observations were found for the other average shear rates. Results are given in Appendix C.

6.1.2 Experiment with step changes in shear rate

A second data set that is borrowed from Biggs (2000) consists of one experiment in which, after initial sonication, several step changes in shear rate $\bar{\mathrm{G}}$ were applied ($19.4\,\mathrm{s}^{-1} \rightarrow 113\,\mathrm{s}^{-1} \rightarrow 19.4\,\mathrm{s}^{-1} \rightarrow 113\,\mathrm{s}^{-1}$). D[4,3]-evolution versus time for this experiment is shown in Fig. 6.3. In the first part (-4000 – 0 s) the sonicated sludge is allowed to reflocculate at an average shear rate of $19.4\,\mathrm{s}^{-1}$ (similar to section 6.1.1).

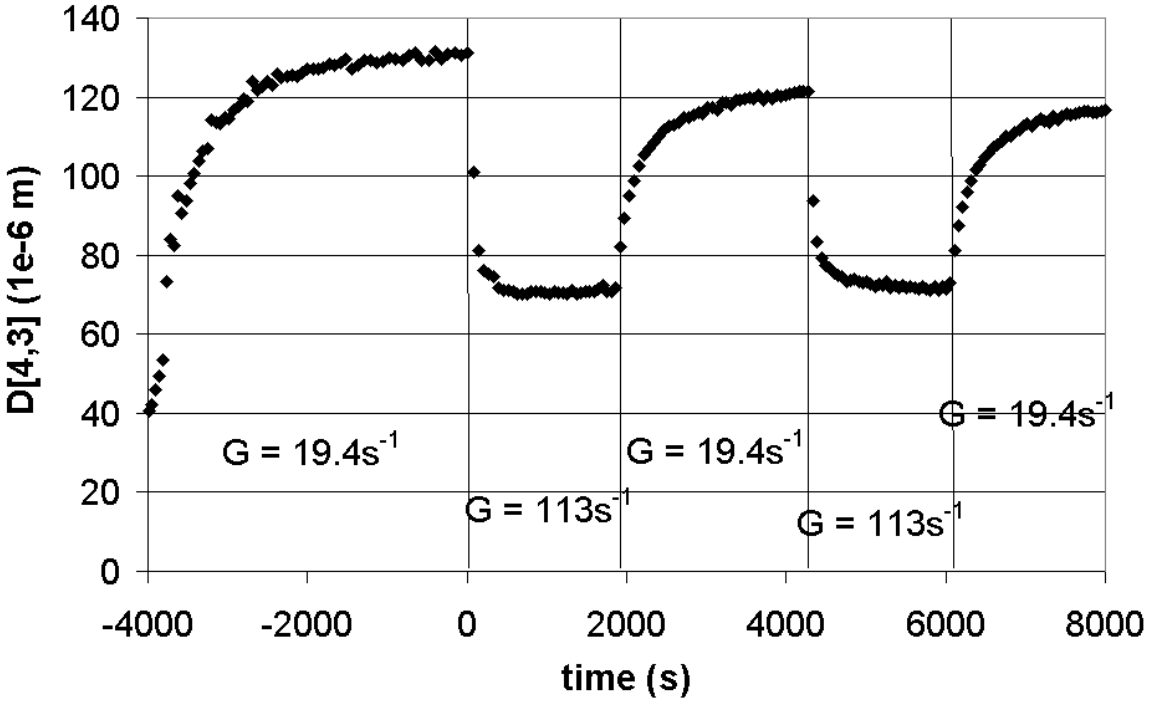

Figure 6.3: Time evolutions of D[4,3] for the experiment with step changes in average shear rate

At time 0, the shear rate is increased to $113\,\mathrm{s}^{-1}$, forcing the D[4,3] to decrease from 130 to 70 μm. Note, however, that the initial value was 40 μm, and, hence, that increased shear does not have the same effect as sonication. The latter questions the use of sonication at lab-scale to study the activated sludge flocculation mechanism. Around t=2000 s, the average shear rate is again decreased to $19.4\,\mathrm{s}^{-1}$, allowing reflocculation. A lower steady state value is observed (120 instead of 130 μm, which is most probably related to the difference in initial condition of the 2 different flocculation experiments (break-up via either sonication or shear). Around t=4000, the shear rate is again increased to $113\,\mathrm{s}^{-1}$. The D[4,3] decreases and reaches approximately the same value as before (i.e. 70 μm). Note that it takes somewhat longer to reach steady state, which might be caused by a difference in floc strength. Finally, the shear rate is decreased again to $19.4\,\mathrm{s}^{-1}$. An even lower steady state D[4,3]-value is observed, which is claimed to be caused by irreversible flocculation dynamics (Biggs, 2000).

The evolutions of the vol% are depicted in Fig. 6.4. The first part (-4000 – 0 s) exhibits the same behaviour as in the previous experiment at shear rate $19.4\,\mathrm{s}^{-1}$ (see section 6.1.1) and will not be discussed again. For the second part (0 – 2000 s, $\bar{\mathrm{G}}$ increased to $113\,\mathrm{s}^{-1}$), the following observations can be made:

1. Small floc size classes (up to 9 μm) first increase (some noise occurs) after which a slight decrease (by 0.01-0.05%) is observed. The increase is due to breakage of larger particles, whereas the decrease can only be due to increased aggregation (i.e. higher number of collisions).

2. Floc sizes between 10 – 60 μm exhibit an increase reaching a steady state. The increase is most probably caused by breakup of larger flocs.

3. Floc size classes between 75 – 90 μm show a pronounced maximum. This means that for these

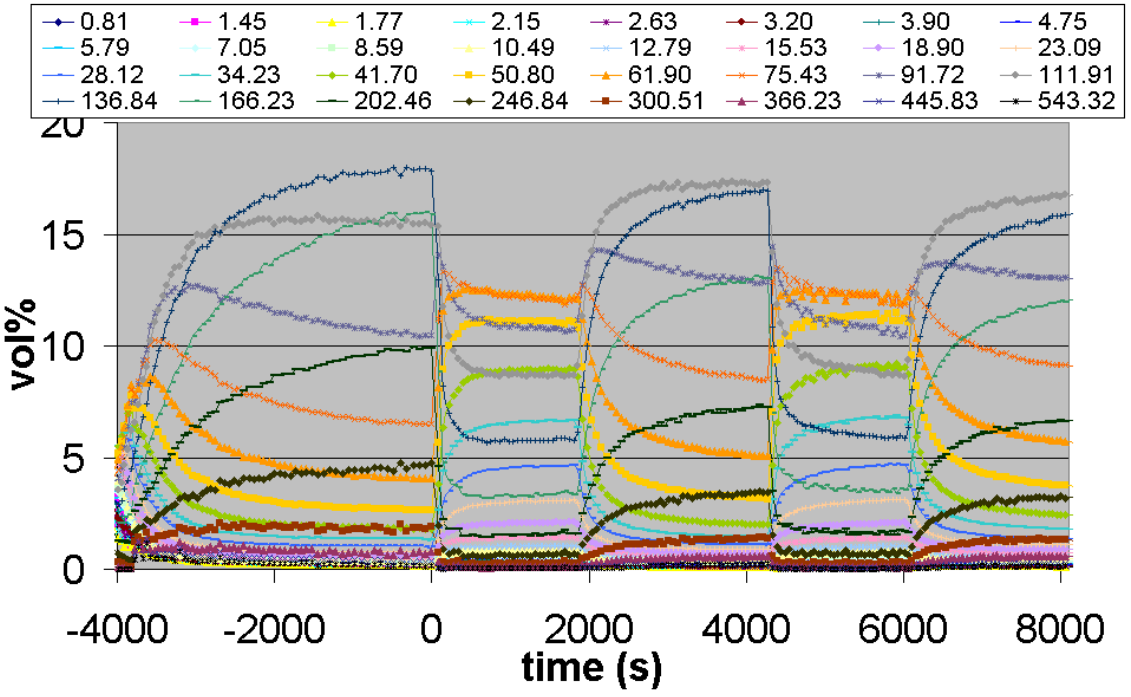

Figure 6.4: Time evolutions of vol% in different size classes for the experiment with step changes in shear rate

classes the rate of formation due to breakage of larger flocs is the initial driving force, resulting in an increase. The decrease is, however, due to their own breakup exceeding the amount of flocs formed from breakup of larger flocs and cannot be due to aggregation (since all larger classes keep decreasing in volume). Also these classes have the highest vol%. This means that the Kolmogorov-scale has clearly decreased to a value around 60 – 75 μm, which is about the same as was found in the aggregation experiment using the same mixing intensity.

4. All floc size classes larger than 90 μm exhibit a decrease due to breakage.

In the third part (2000 – 4000 s, $\bar{G}$ decreased to 19.4 s^{-1}), the following observations can be made:

1. The initial vol% of the smallest classes (0.81 – 10 μm) is substantially lower (ca. 5 times) compared to the first part, which is clearly caused by the difference in approach for breakage (sonication versus increased shear). A decrease to similar end values is observed for these size classes, meaning that they are aggregating out of these classes to the same extent, clearly depending on the shear intensity.

2. For classes between 12 – 60 μm, no maximum peaks were observed as was the case in part 1. Instead, an immediate decrease is observed to end values which are comparable to the first part. This is probably due to the smaller amount of particles available in the smallest classes and, hence, the lower aggregation rate. The system is initially in a higher state of flocculation (i.e. the front is located at a higher floc size).

3. Flocs of 75 – 91 μm do exhibit a peak as observed in the first part, but end up at steady state values that are substantially higher compared to the first part. In part 1, this decrease was governed by a

higher amount of flocs aggregating out of the class compared to the amount of flocs aggregating into the class. The smaller decrease observed here would mean that either more particles are aggregating into the class or less particles are aggregating out of the class compared to what happened in the first part. The former is unlikely since less small particles are available.

4. Flocs of about $111\,\mu\mathrm{m}$ now have the largest vol%, also substantially higher than in the first part. This suggestes that the flocs are more compact.

5. All larger classes exhibit an increase to a steady state, which values are, however, smaller compared to the first part.

The differences in observed steady states explain why the D[4,3] reaches a lower steady state value. Although the boundary classes of the distribution reach similar steady state values, the classes around the Kolmogorov microscale show substantial shifts. Probably, the initial lower amount of small particles is the reason for this.

Despite the fact that the initial condition was different compared to the second part, part 4 (4000 – 6000 s, $\bar{\mathrm{G}}$ increased to $113\,\mathrm{s}^{-1}$) exhibits almost exactly the same steady state values. Size classes smaller than the Kolmogorov scale increased to a new steady state, whereas larger classes decreased to the new steady state. No maxima occur in the transient part for any of the classes. All changes can be addressed to increased breakage.

Finally, in part 5 (6000 – 8000 s, $\bar{\mathrm{G}}$ decreased to $19.4\,\mathrm{s}^{-1}$), similar trends are observed as in part 3. The classes just above the Kolmogorov scale exhibit some lower steady state values, whereas the opposite is true for classes smaller than the microscale of turbulence. Again, no maxima occur in the transient part for any of the classes.

An important thing to note is that all these quantitative observations from the vol-% evolutions are lost when only considering the D[4,3]-evolution. With regard to finding the right kernels for the PBM, this additional information is very useful.

6.2 Experimental results from Flocunit

In order to quantify the influence of different physico-chemical parameters on (de)flocculation dynamics, an experimental design was developed for the Flocunit which was described earlier (section 3.3). Five relevant factors were retained from a list of potential influencing factors via pre-screening experiments:

1. temperature (5 - 10 - 15 - 20 - 25 °C)
2. shear rate (15 - 28 - 55 - 105 - 200 s^{-1})
3. dissolved oxygen (0 - 1 - 2 - 3 - 4 $\mathrm{mg.L}^{-1}$)
4. sludge concentration (0.1 - 0.25 - 0.63 - 1.59 - 4 $\mathrm{g.L}^{-1}$)
5. calcium addition (0 - 6 - 12 - 18 - 24 $\mathrm{meq.L}^{-1}$)

The design resulted in a total of 36 experiments (one-half fractional factorial design, augmented with an axial design and 10 central points), which are shown in Table 6.1. More details concerning the design can be found in Govoreanu (2004). The values that are indicated along with the factors are those that were used in the experimental design.

The temperature values that were chosen are typical values for regions with a moderate climate (e.g. western Europe). Shear rate values were chosen logarithmically between the minimum value needed to keep the sludge in suspension and the maximum value allowed by the mixing device (torque meter).These values are in accordance with typical values encountered in wastewater treatment plants (Tchobanoglous et al., 2003). Dissolved oxygen values were chosen to mimic a variety of environments ranging from anaerobic, over oxygen limiting environments, up to normal values found in wastewater treatment plants. Sludge concentration values were chosen from very dilute up to normal values encountered in treatment plants. Since the sludge-producing SBR was fed with rather low Ca^{2+}-concentrations, rather high values were chosen in order to obtain a variety of monovalent to divalent cation ratios.

In what follows a brief overview of effects of the individual factors on the sludge flocculation process is given. The main difference with the discussion in Govoreanu (2004) is that, next to the mass mean diameter, the underlying distributions are discussed too. For every factor 3 levels are compared: the minimum and maximum axial design points and the central design point. The latter is characterised by the following values: T= 15°C, G= 55 s^{-1}, DO= 2 $\mathrm{mg.L}^{-1}$, X= 0.63 $\mathrm{g.L}^{-1}$ and $\mathrm{Ca}^{2+} = 12\,\mathrm{meq.L}^{-1}$. Prior to each experiment, the sludge sample was subjected to identical *'standard'* conditions for a period of 10 minutes. These conditions were chosen to be those at the center point except that no Ca^{2+} was added. Then, the factor values for the experiment are imposed and measurements are collected for another 10 minutes. Finally, the Ca is added. This approach is different from the one used by Biggs (2000) where sonication was applied prior to all experiments. The expected transients are, therefore, expected to be less pronounced, since experiments do not start from a sludge in a deflocculated state.

In this study, in the Flocunit set-up described in section 3.3 a second sizing device was used next to the Malvern, i.e. the CIS-100 (Ankersmid, Belgium). Unlike the Malvern, the CIS-100 measures number concentrations by counting particles of certain size (time of transition method). Note that a small difference in particle count might have a larger effect on volume-based variables when these few particles happen to be large in size. Similarly, the total number of particles will hardly be affected by a small shift in the large size classes as only few particles are typically found in these classes. This should be taken into account when interpreting the results.

Table 6.1: Overview of the experimental conditions imposed in the Flocunit according to the fractional factorial design (Govoreanu, 2004)

#	T (°C)	G (s^{-1})	DO ($mg.L^{-1}$)	X ($g.L^{-1}$)	Ca ($meq.L^{-1}$)
1	15	55	2	0.63	12
2	15	200	2	0.63	12
3	10	28	1	0.25	18
4	10	105	3	1.59	6
5	10	28	3	0.25	6
6	15	55	2	0.63	12
7	10	105	1	1.59	18
8	25	55	2	0.63	12
9	15	55	2	0.63	12
10	15	55	2	0.63	12
11	15	55	2	0.63	12
12	15	55	2	0.1	12
13	15	55	2	4	12
14	15	55	4	0.63	12
15	20	28	1	0.25	6
16	20	28	1	1.59	18
17	20	28	3	0.25	18
18	15	55	2	0.63	12
19	20	105	3	1.59	18
20	10	28	1	1.59	6
21	15	55	2	0.63	12
22	15	55	2	0.63	0
23	20	105	3	0.25	6
24	15	15	2	0.63	12
25	10	105	3	0.25	18
26	15	55	2	0.63	12
27	15	55	2	0.63	24
28	15	55	2	0.63	12
29	20	105	1	1.59	6
30	20	28	3	1.59	6
31	15	55	2	0.63	12
32	5	55	2	0.63	12
33	10	28	3	1.59	18
34	15	55	2	0.63	12
35	20	105	1	0.25	18
36	10	105	1	0.25	6

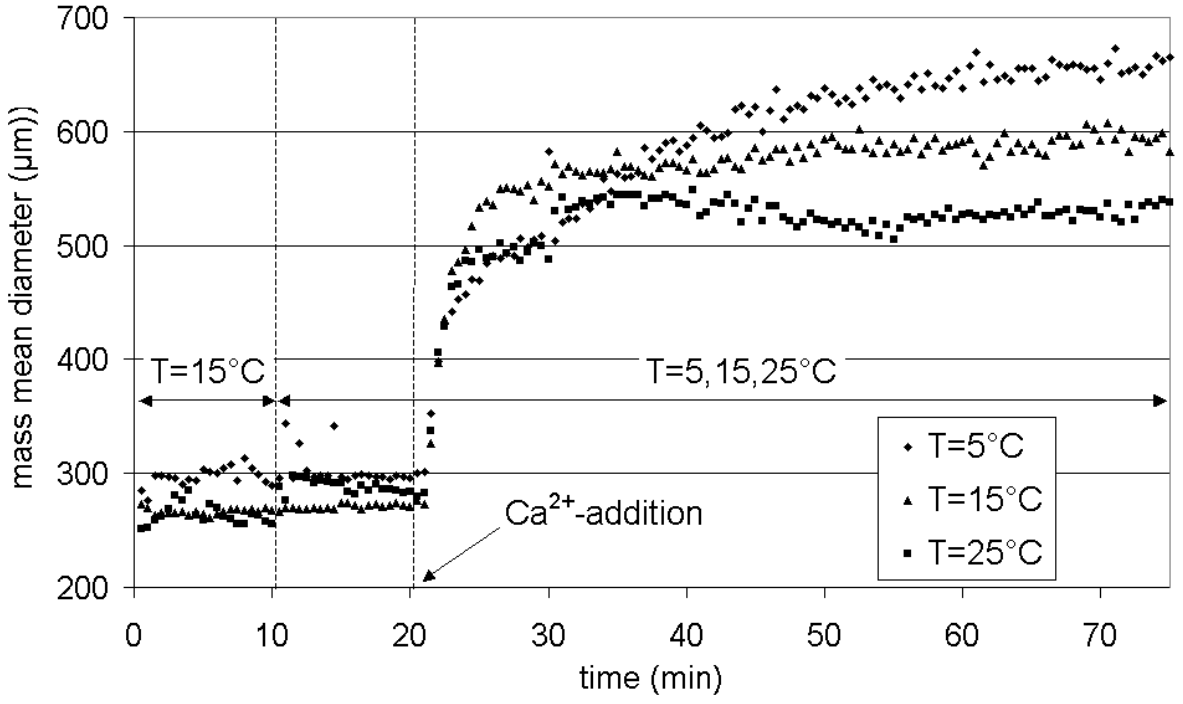

Figure 6.5: Temperature influence on the mass mean diameter measured by the Malvern Mastersizer

The following sections have a common structure. First, the time evolution of the D[4,3] is given and discussed. Then, the underlying distributions produced by the Malvern Mastersizer (Malvern, UK) are analysed. Finally, the time evolution of the total number of flocs (N_{tot}) given by the CIS-100 (Ankersmid, Belgium) is investigated.

6.2.1 Temperature

D[4,3]

To investigate the influence of temperature, experiments were analysed for the design axial points (5 and 25 °C) and the center point (15 °C). The other operational conditions were kept constant at the center point values, which have been described earlier. Results of the mass mean diameter (D[4,3]) versus time for different temperatures recorded by the Malvern Mastersizer are given in Fig. 6.5.

Compared to the data of section 6.1, the results are in general more noisy. The reason for this could be (1) the difference in flocculation reactor volume (5 L instead of 1 L) which might enhance the inhomogeneity and (2) the sampling procedure (no recirculation was used here). However, when discarding this noise, the same general trends can be observed. Note that the differences in reactor configuration were necessary for enabling the additional measurements of temperature, DO, turbidity, conductivity and pH. In what follows, only the general trends will be discussed, i.e. the noise will be ignored.

During the first 20 minutes of the experiments (i.e. prior to Ca-addition) no significant variations in mass mean diameter were observed. When, after 10 minutes, temperature was lowered to 5 °C, the mass mean

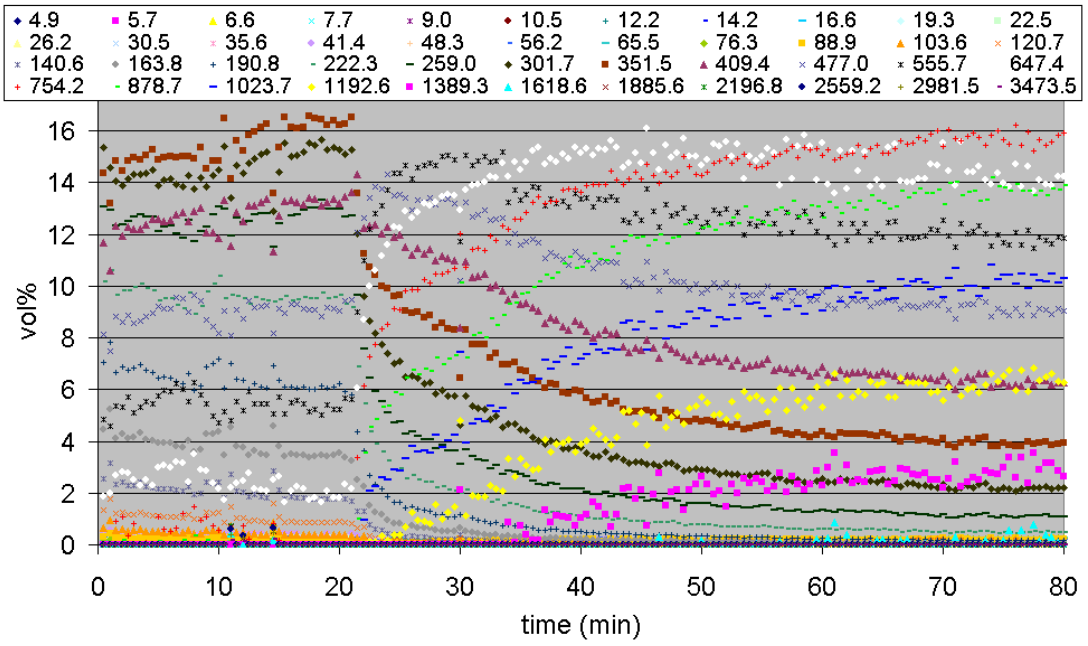

Figure 6.6: Time evolutions of vol% in different size classes measured by the Malvern Mastersizer for T=5 °C

diameter was not affected. On the other hand, increasing the temperature to 25 °C resulted in an increase of mass mean diameter (though it should be noted that approximately 1 hour was needed to change the temperature setpoint). As expected, not changing the temperature did not enhance any changes either. When Ca^{2+} was added, different behaviour was observed at different temperatures. At low temperature (5 °C), the time needed to reach steady state is rather large (about 40 minutes) despite the fast initial response to Ca^{2+}-addition. A steady state mass mean diameter of 650 μm was reached. At high temperature (25 °C), a fast increase is observed, followed by a small decrease reaching a steady state value of about 525 μm, significantly lower than at low temperature. A separate experiment without Ca^{2+}-addition confirmed the flocculating behaviour at low temperature and the deflocculating behaviour at higher temperature (Govoreanu, 2004). The reason for these rather short-term effects is either the viscosity changes that are imposed by the temperature difference or the physico-chemical properties of the flocs, especially the production and physico-chemical properties of exopolymeric substances (EPS). The biological activity will be influenced too, which might have an indirect effect on the aforementioned physico-chemical floc properties. At intermediate temperature (T=15 °C), the mass mean diameter remains constant during the first 20 minutes and increases to a value of about 575 μm, intermediate between the low and high temperature steady state values, when Ca^{2+} is added.

Volume percentage distributions

The evolutions of the vol% measured by the Malvern Mastersizer for $T = 5$°C are depicted in Fig. 6.6. In the first part of the experiment (0-20 min, prior to Ca^{2+}-addition), the different size classes are rather stable (apart from some measurement noise), although some small shifts toward higher floc sizes can be observed when the temperature is decreased after 10 minutes. Flocs of about 350 μm are most abundant

during this stage of the experiment, suggesting that this would be the Kolmogorov scale. However, when applying the same rule as in section 6.1 for the relation between the Kolmogorov scale and the average shear rate (i.e. calculate the scale of turbulence at 10 times the average energy dissipation), it would mean that the average shear rate would be $2.6\,\mathrm{s}^{-1}$, clearly different from the one used in the experiment, i.e. $55\,\mathrm{s}^{-1}$. This might have several causes. A first possibility is that different shear distributions (or flow patterns) are present in both vessels. This might be caused by the presence of other obstacles in the reactor (i.e. probes and sampling tube), different mixing blade designs and different volumes (1 versus 5L) as was shown by Ducoste and Clark (1998a). Relating the most abundant floc size to the average shear intensity would mean that the local shear intensity was 45 times smaller than the average value. The relationship between average and local shear intensities is mainly depending on the ratio of the volumes that are exposed to certain shear intensities (or in other words the flocs residence times in each of the 'compartments') and the absolute difference between the maximal and minimal shear intensity throughout the reactor. The larger volume of the reactor and the different flow pattern could, therefore, justify the aforementioned relationship (i.e. factor 45). The second possible cause is that in the conducted experiments flocs larger than the Kolmogorov scale are strong enough to withstand the forces that work upon them and can persist. However, floc strength is difficult to quantify. Further research is required to further study this potential cause.

After Ca^{2+}-addition, many classes need a long time (up to 1 hour) to reach their new equilibrium. Three different types of behaviour can be distinguished:

1. Size classes up to 400 $\mu\mathrm{m}$ tend to decrease, which can be explained by the increased aggregation rate.

2. Size classes from 450 up to 650 $\mu\mathrm{m}$ exhibit an increase to a maximum followed by a decrease to a steady state value. The maximum is attained by an increased formation of these flocs, which is governed by the increased aggregation rate of smaller flocs. The decrease is caused by the increased aggregation rate of flocs in the class under consideration. It can again be seen as a front of flocs moving along the size axis.

3. Size classes ranging from 650 up to 1400 $\mu\mathrm{m}$ significantly increase. Here, an increased formation is again followed by an increased aggregation out of the class, but this effect is balanced out by an increased breakage of larger flocs.

Flocs of about 750 $\mu\mathrm{m}$ become most abundant. Since the average shear intensity was controlled at the same value, it is clear that the size of the most abundant floc size is not necessarily related to the Kolmogorov scale. The Ca-addition clearly increases the strength of the flocs, allowing them to withstand the forces they are exposed to. One should, therefore, be careful when calculating Kolmogorov-scales from distributions.

The evolutions of the vol% measured by the Malvern Mastersizer for $T = 25°\mathrm{C}$ are depicted in Fig. 6.7. The different size classes are noisy in the first part of the experiment, but no trends can be observed. Most abundant flocs appear around 300 $\mu\mathrm{m}$, which is different from the experiment at T=5 °C, despite the 'standard' conditions that were applied. A possible explanation might be the history of the flocs in terms of strength (or resistance to stress) and compactness. After Ca^{2+}-addition, a new equilibrium sets in much faster compared to the low temperature experiment. Only 2 different types of behaviour are observed: flocs smaller than 400 $\mu\mathrm{m}$ decrease to a new equilibrium, whereas flocs larger than 400 $\mu\mathrm{m}$ increase to a new equilibrium. The absence of maxima in certain classes can be explained by the much faster aggregation rate that is observed. Classes simply don't have the time to build up large numbers as

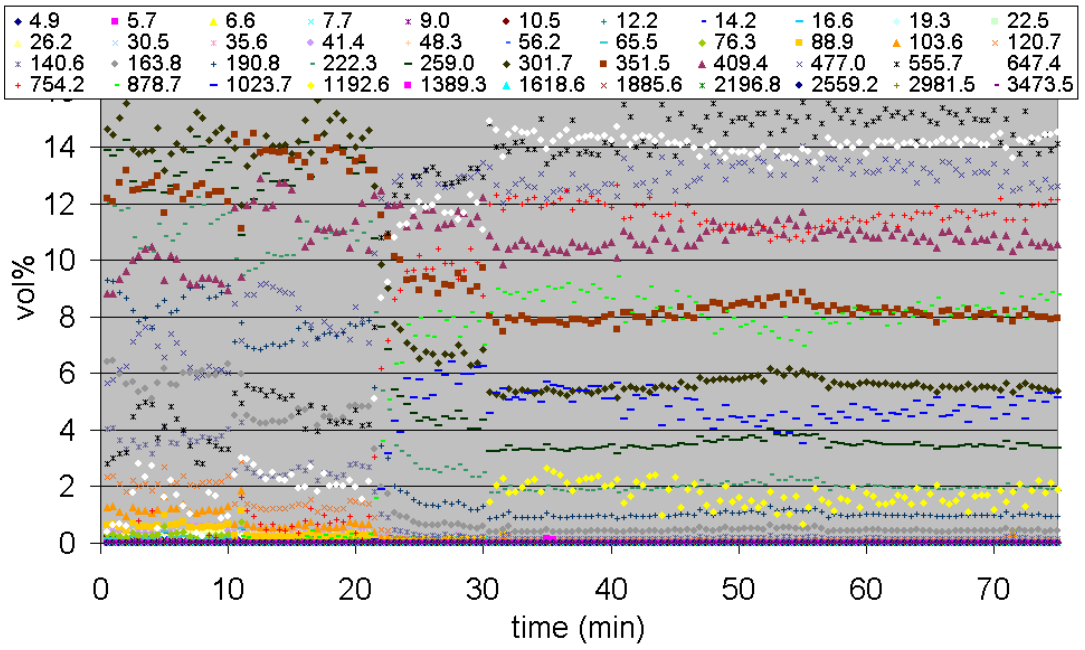

Figure 6.7: Time evolutions of vol% in different size classes measured by the Malvern Mastersizer for T=25 °C

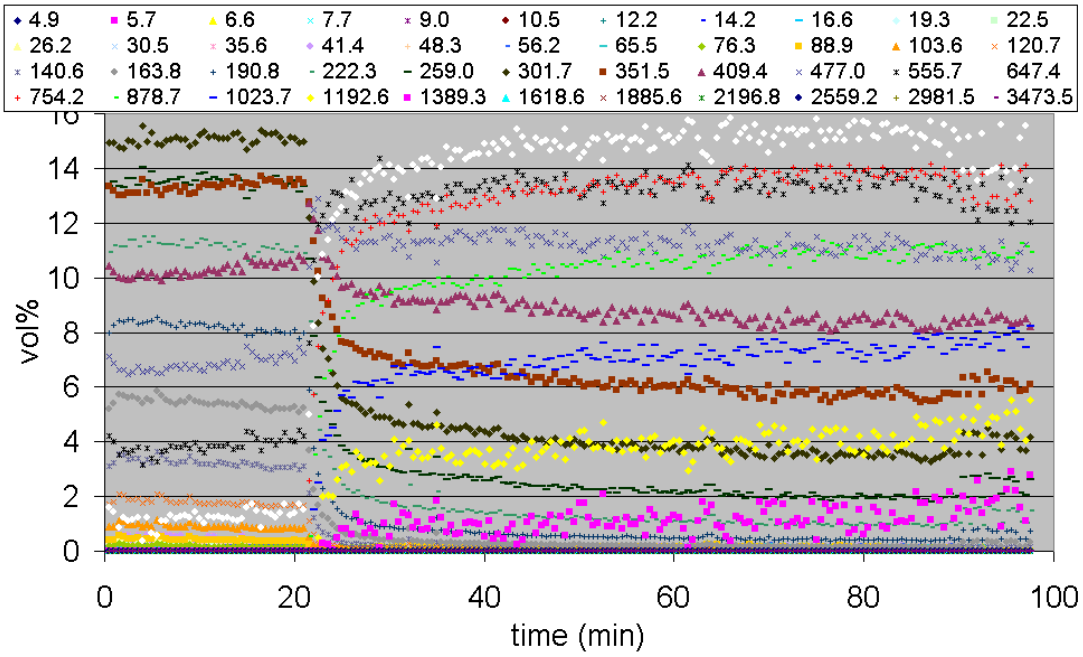

Figure 6.8: Time evolutions of vol% in different size classes measured by the Malvern mastersizer for T=15 °C

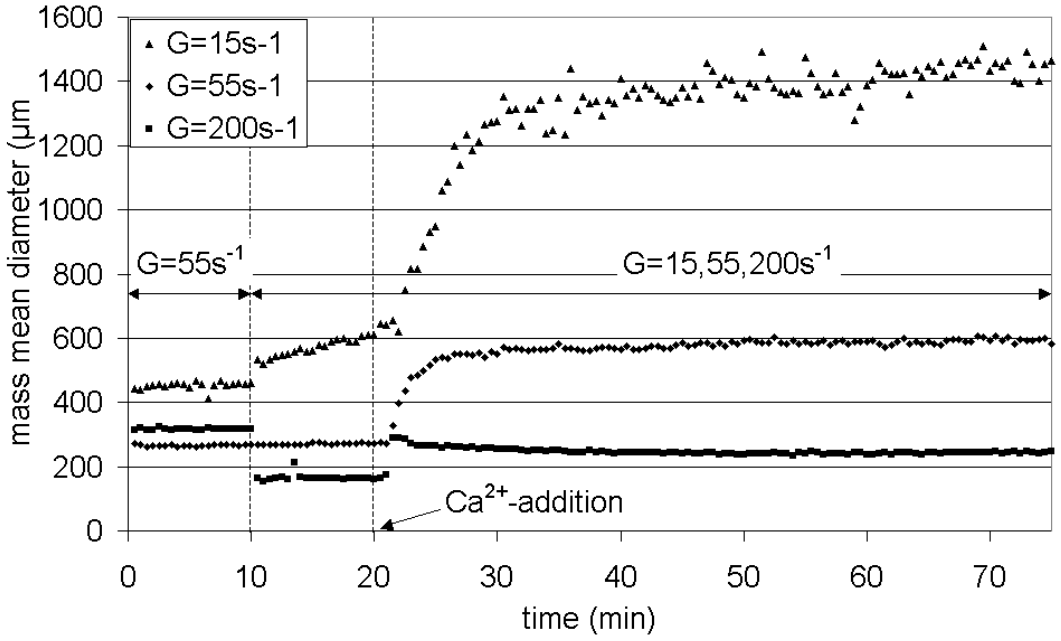

Figure 6.9: Shear rate influence on the mass mean diameter measured by the Malvern Mastersizer

they immediately aggregate out of that class again. Most abundant flocs are now about 600 μm, which is significantly lower compared to the low temperature case. As explained before, one possible explanation could be a difference in floc strength governed by changes in viscosity or EPS-properties due to different temperature. Hence, one could conclude that stronger flocs are formed at lower temperature.

The evolutions of the vol% measured by the Malvern Mastersizer for T=15 °C are depicted in Fig. 6.8. The first 20 minutes of the experiment are less prone to noise. No significant changes are taking place. 300 μm sized flocs are most abundant. Note again the difference compared to the experiments at T=5 °C and T=25 °C respectively. When Ca^{2+} is added, size classes smaller than 400 μm decrease, whereas those ranging from 400 up to 1400 μm increase significantly. No maxima occur, probably because of the same reasons as in the previous case. The most abundant size class is 650 μm.

6.2.2 Shear rate

D[4,3]

To investigate the influence of shear rate, the shear intensity was set to the nominal experimental value for 10 minutes prior to Ca^{2+}-addition. Results of the mass mean diameter (D[4,3]) for different shear rates recorded by the Malvern Mastersizer are given in Fig.6.9.

At G=200 s^{-1}, an immediate (<30s, i.e. the sampling rate) drop in mass mean diameter is observed, which is partly restored when Ca^{2+} is added. However, the fast response and the time needed for 1 measurement does not allow to capture the dynamics. From a dynamic modeller's point of view, this type of experimental data is not very useful.

Volume percentage distributions

The evolutions of the vol% measured by the Malvern Mastersizer are depicted in Fig. 6.10. In the first 10 minutes of the experiment ($\bar{\mathrm{G}} = 55\,\mathrm{s}^{-1}$), a rather constant size distribution is observed with dominating particle sizes of around 350 μm. The Kolmogorov scale calculated for this G (based on 10 times the average energy dissipation rate rule) is 76 μm, which is clearly lower. Apparently, the relation between maximum diameter and Kolmogorov scale that was found for the data sets in section 6.1 is not valid here. As argued before, this could be due to the different configuration and volume of the vessel and the differences in floc strength or a combination of those factors.

When the average velocity gradient is increased to $200\,\mathrm{s}^{-1}$, the most abundant floc size is observed at 190 μm. At this average velocity gradient, the Kolmogorov scale was calculated to be in the neighbourhood of 40 μm, which is again much smaller for the same reasoning as mentioned earlier. All flocs larger than 260 μm show a decrease in vol%, whereas these of flocs between roughly 40 and 200 μm increased significantly. This clearly proves that large flocs are broken into smaller ones. The changes in the different size classes are as abrupt as the change in D[4,3]. However, initially some noise occurs without any clear pattern.

When 12 meq Ca^{2+} is added, the most abundant floc size again increases rapidly to 260-300 μm. The only explanation for this can be an increase in floc strength, since the configuration is not changed throughout the experiment (assuming that the shear rate control to correct for the decrease in volume does not significantly change the velocity gradient distribution). Using a similar reasoning as in the previous paragraph, one can prove that aggregation occurs (smaller particles leave the system, larger ones are born).

At G=$15\,\mathrm{s}^{-1}$, a linear increase in mass mean diameter is observed. However, this increase is much slower compared to the decrease observed at G=$200\,\mathrm{s}^{-1}$. After the Ca^{2+}-addition, a further, much steeper increase is observed, finally reaching a new equilibrium. The evolutions of the vol% measured by the Malvern Mastersizer are depicted in Fig. 6.11. In the first part, a rather constant size distribution can be observed (apart from some noise). As expected, a larger dominating particle size compared to the previous experiment (at G=$200\,\mathrm{s}^{-1}$) sets in, i.e. 470 μm. This suggests that the floc strength is different, because all operational parameters are exactly the same except for the sludge sample, which was taken on 2 different days and might have been slightly different in terms of filament content and ionic strength, two factors affecting the floc strength.

When the average velocity gradient is decreased to $15\,\mathrm{s}^{-1}$, volume fractions of floc sizes ranging from roughly 200 to 600 μm decrease, whereas these of particles between 650 and 1400 μm increase. This clearly proves that aggregation occurred. The changes in the different size classes are not discontinuous, but have a smoother nature compared to the G=$200\,\mathrm{s}^{-1}$ case.

When adding 12 meq Ca^{2+}, the most abundant floc size increases to around 1500 μm. The trend that was observed in the previous paragraph persists, i.e. aggregation continues until a new dynamic equilibrium is reached. Apart from one class, none exhibit a peak. This is due to the 'gentle' aggregation making the front move very slow, not causing any overshoots. This is in contrast with the sonication experiments discussed before, where a large driving force is available due to the large amount of small particles present.

The intermediate case (G=$55\,\mathrm{s}^{-1}$) was discussed earlier (this case is the same as the intermediate T-case). The evolutions of the vol% measured by the Malvern Mastersizer are depicted in Fig. 6.8. Intermediate results are found with regard to response rate and most abundant floc size after Ca^{2+}-addition.

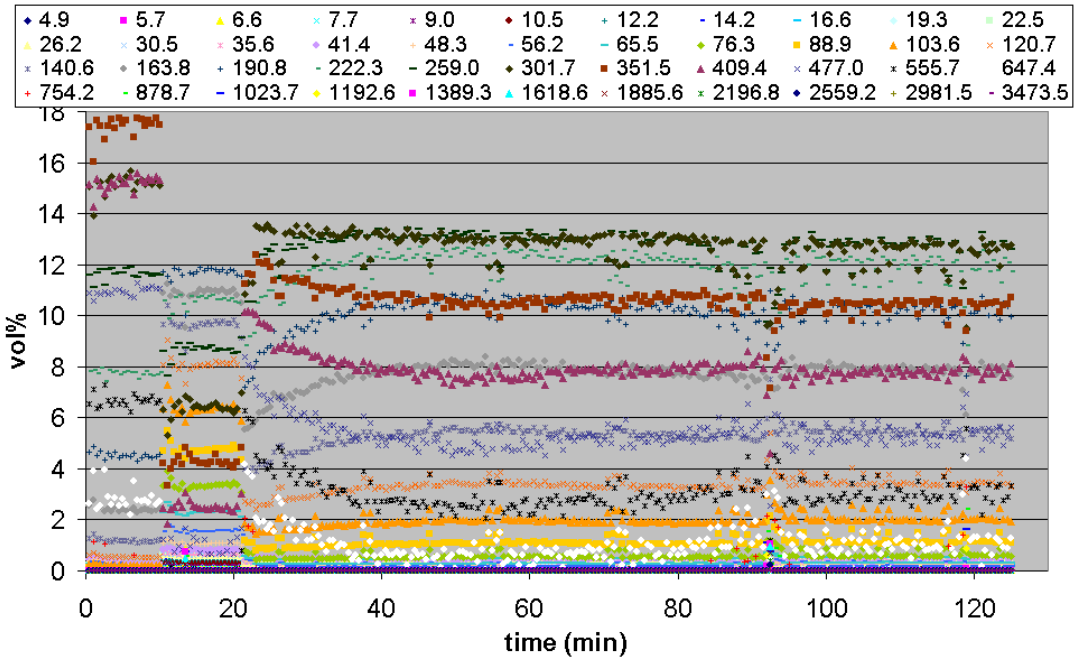

Figure 6.10: Time evolutions of vol% in different size classes measured by the Malvern Mastersizer for G=200 s^{-1}

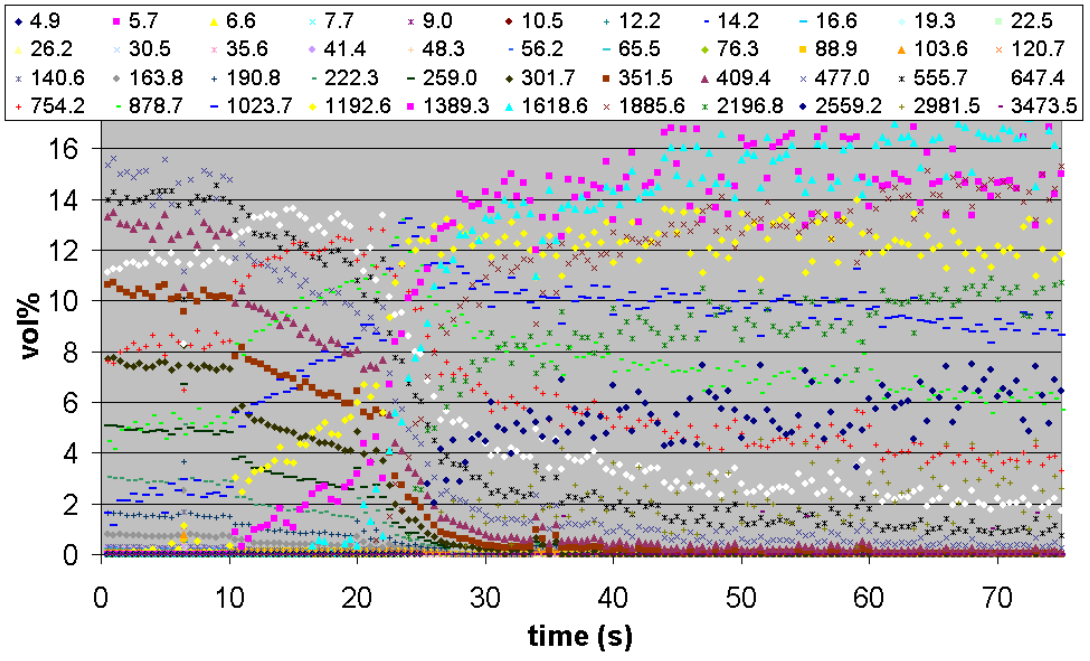

Figure 6.11: Time evolutions of vol% in different size classes measured by the Malvern Mastersizer for G=15 s^{-1}

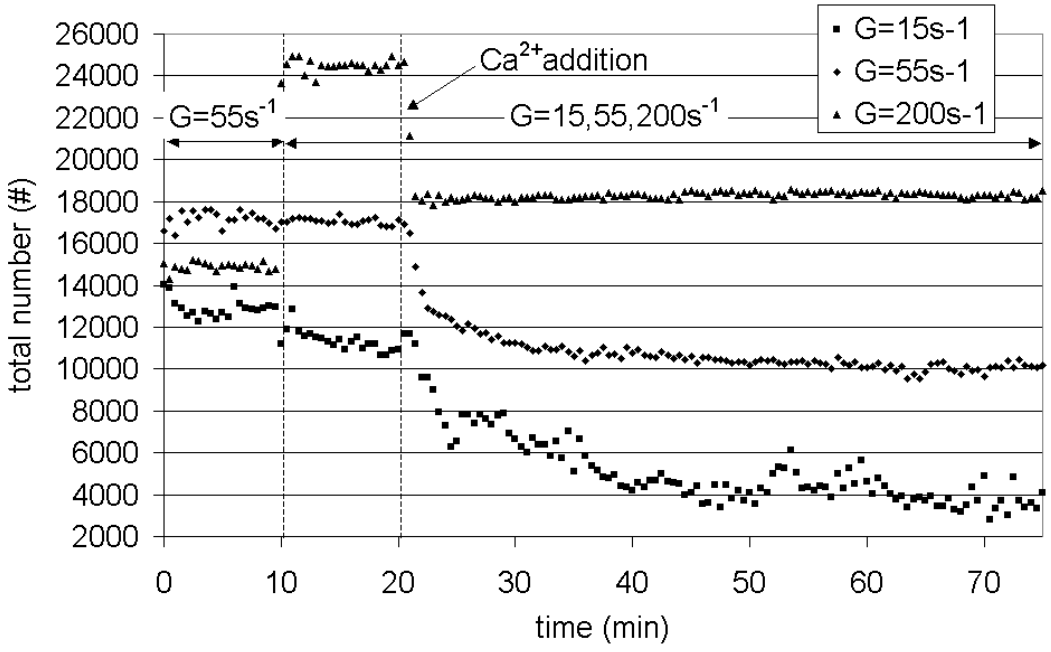

Figure 6.12: Shear rate influence on the total number of flocs measured by the CIS-100

Number distributions

Results of the total number of flocs (N_{tot}) for different shear rates recorded by the CIS-100 (time of transition method) are given in Fig.6.12.

At G=200 s^{-1}, a significant increase in N_{tot} is observed. Obviously, this is caused by breakage since the total floc mass did not change. Ca^{2+}-addition caused N_{tot} to decrease again, governed by aggregation, although the equilibrium sets in at a different level compared to the initial level. These qualitative findings are similar to the ones obtained by the laser diffraction device.

For the G=15 s^{-1} experiment, one notices that N_{tot} is initially lower, again suggesting that stronger flocs are present in the system. Indeed, a lower N_{tot} implies larger flocs in the system (the mass is distributed over a lower number of flocs), and these are subjected to the same shear stress as in the previous experiment (i.e. G=55 s^{-1}). Hence, they need to be structurally stronger to withstand these forces. When decreasing the average velocity gradient, N_{tot} decreases linearly suggesting that aggregation is occurring, again similar to the observations made with the laser diffraction device. Adding Ca^{2+} results in a further decrease in N_{tot}.

At G=55 s^{-1}, a higher initial N_{tot} is observed, confirming the weaker nature of the flocs, which was observed in the Malvern measurements as well. This level remains constant until Ca^{2+} was added, the latter causing N_{tot} to decrease. This implies that aggregation takes place.

The evolution of the number of flocs per class versus time are extremely noisy, not allowing any trend to be deduced from them (not shown). These data can, therefore, not be used for model calibration.

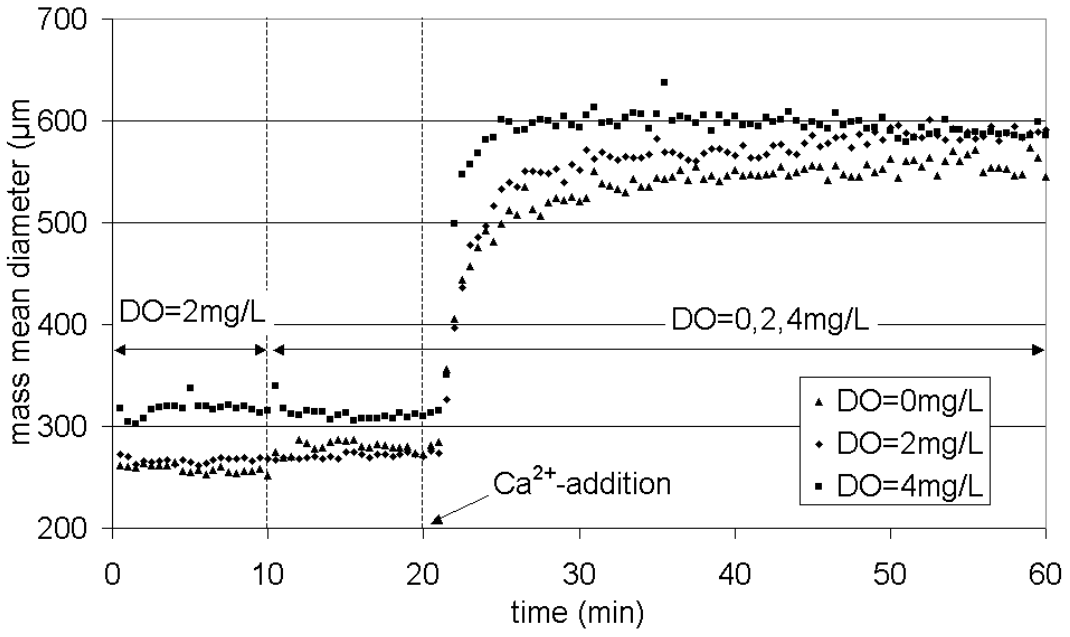

Figure 6.13: Dissolved oxygen concentration influence on the mass mean diameter measured by the Malvern Mastersizer

6.2.3 Dissolved oxygen

D[4,3]

To investigate the influence of the dissolved oxygen concentration, experiments were performed for the design axial points (0 and 4 $\mathrm{mg.L^{-1}}$) and the center point (2 $\mathrm{mg.L^{-1}}$). Noteworthy is that it took almost an hour to change the DO-setpoint to 0 $\mathrm{mg.L^{-1}}$. The other operational conditions were kept constant at the center point values, which have been described earlier. Results of the mass mean diameter (D[4,3]) for different sludge concentrations recorded by the Malvern Mastersizer are given in Fig. 6.13. Note that all observations cannot be due to additional shear, as bubbleless aeration was applied.

Again, differences in mass mean diameter during the first 10 minutes between the three experiments were observed. Changing the DO to the respective nominal set-points resulted in no changes for increasing DO, whereas an increase was observed when imposing anaerobic conditions. This is not in accordance with Wilén and Balmér (1999), who did not observe any short-term effect of DO, and observed a floc deterioration after long-term anaerobic conditions. After $\mathrm{Ca^{2+}}$-addition, flocculation occurred in all cases. However, responses are faster and the steady state is somewhat higher for higher DO-concentrations.

Volume percentage distributions

The evolutions of the vol% measured by the Malvern Mastersizer for $DO = 4\,mg.L^{-1}$ are depicted in Fig. 6.14.

The distribution is quite stable during the first 20 minutes. Apparently, the rise in DO did not alter the

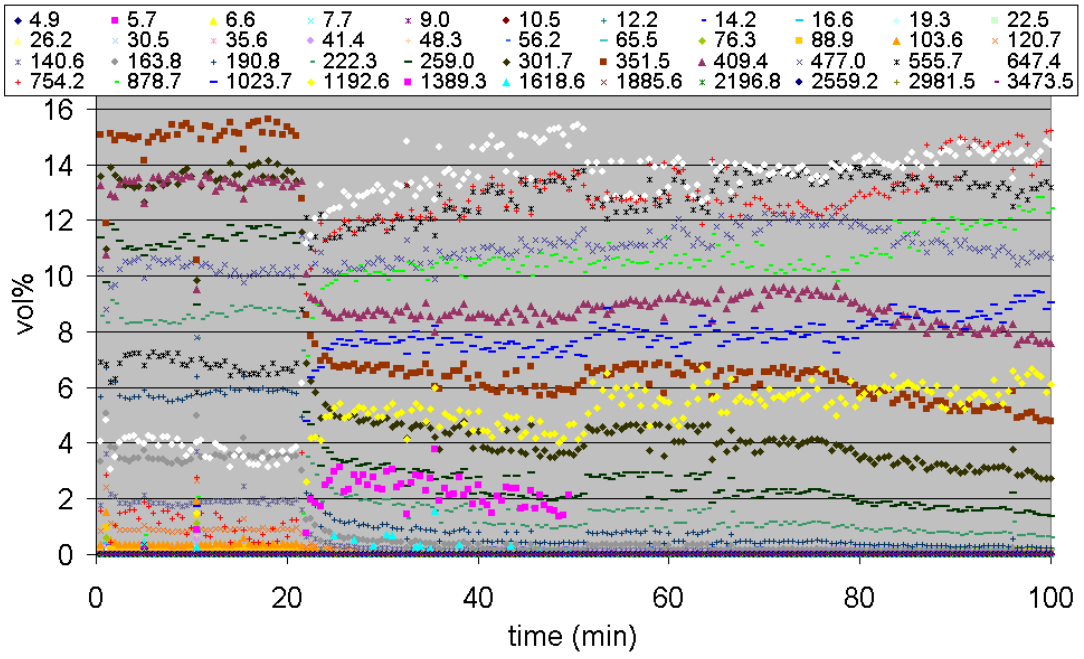

Figure 6.14: Time evolutions of vol% in different size classes measured by the Malvern Mastersizer for DO=4 $\mathrm{mg.L^{-1}}$

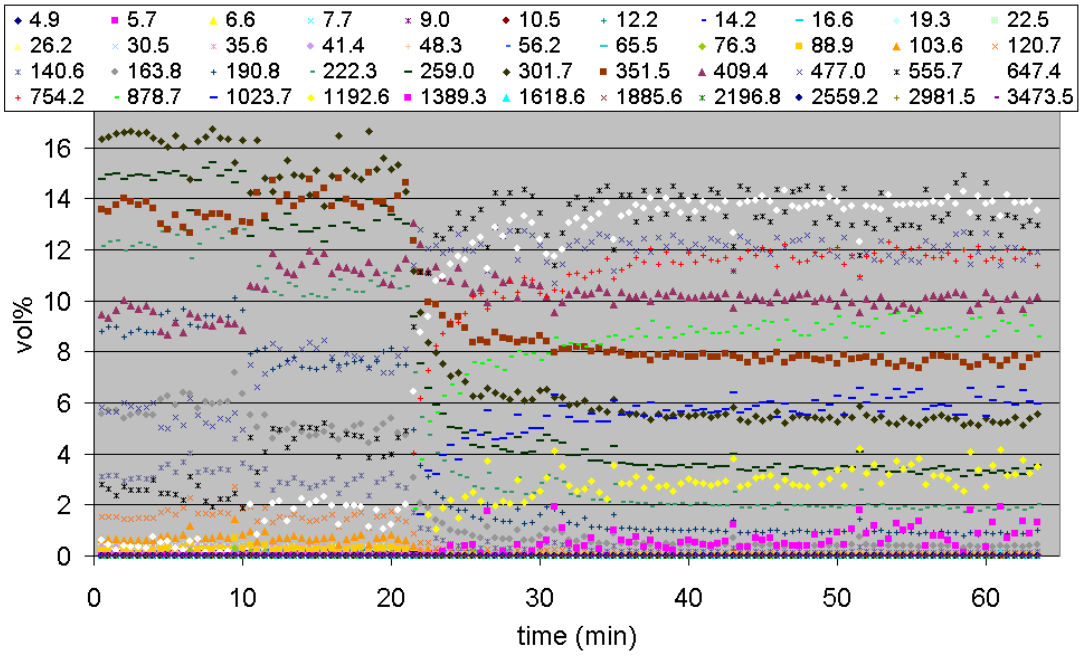

Figure 6.15: Time evolutions of vol% in different size classes measured by the Malvern Mastersizer for DO=0 $\mathrm{mg.L^{-1}}$

distribution in the short-term. The most abudant flocs have a size of 350 μm. Ca^{2+}-addition caused fast changes in several size classes. Flocs smaller than 480 μm decrease, whereas the ones ranging from 500-1200 μm increase. Most abundant flocs now have a size of 700 μm. No overshoots occur, again suggesting that 'gentle' aggregation is taking place.

The evolutions of the vol% measured by the Malvern Mastersizer for $DO = 0\, mg.L^{-1}$ are depicted in Fig. 6.15. During the first 10 minutes, a quite stable distribution is observed. Most abundant flocs have a diameter of 300 μm. After imposing anaerobic conditions, some shifts in the distribution toward larger flocs can be noticed (the discontinuity is due to the fact that it about one hour to impose anaerobic conditions; during this period no measurements were performed). After adding Ca^{2+}, a flocculating trend is observed. However, the response is slower compared to the high DO case. Flocs smaller than 450 μm decrease, whereas those ranging from 450 up to 1400 μm increase without any peaks occurring. Most abundant flocs are about 600 μm in size.

The evolutions of the vol% measured by the Malvern Mastersizer for $DO = 2\, mg.L^{-1}$ were already shown in Fig. 6.8. Results are intermediate compared to the ones at other DO-concentrations.

6.2.4 Sludge concentration

D[4,3]

To investigate the influence of the sludge concentration, experiments were performed for the design axial points (0.1 and 4 $g.L^{-1}$) and the center point (0.63 $g.L^{-1}$). The other operational conditions were kept constant at the center point values, which have been described earlier. Results of the mass mean diameter (D[4,3]) for different sludge concentrations recorded by the Malvern Mastersizer are given in Fig. 6.16.

Prior to the Ca^{2+}-addition, the mass mean diameter is slightly different for the different sludge concentrations. Here, one would expect a larger mean diameter for higher concentrations because the collision rate is higher and, hence, the possibility to form larger flocs is larger. On the other hand, differences in floc strength might also be partly responsible as was discussed in 6.2.2. This explains why the mass mean diameter for $X = 4\, g.L^{-1}$ is larger than that for $X = 0.63\, g.L^{-1}$. At the lowest sludge concentration a decreasing trend is observed, which might be explained by an irreversible breakup of flocs due to the low probability of collisions. It should be noted that at this concentration the sludge was recirculated instead of diluted in-line.

When adding Ca^{2+}, the effect of the different collision probabilities (caused by sludge concentration) can clearly be observed. Higher sludge concentrations reach higher equilibrium mass mean diameters.

Volume percentage distributions

The evolutions of the vol% measured by the Malvern Mastersizer for $X = 4\, g.L^{-1}$ are depicted in Fig. 6.17. Apart from some noise, the distribution is rather stable in the first 20 minutes. The most abundant particle size is observed around 400 μm, which is again significantly larger than the Kolmogorov scale. After Ca^{2+}-addition, the volume of flocs ranging from roughly 550 to 1600 μm significantly increases, whereas those of flocs roughly between 90 and 480 μm significantly decreased and no peaks are observed. Obviously, this is due to aggregation caused by the Ca^{2+}-addition. Flocs of around 700 μm now become the most abundant.

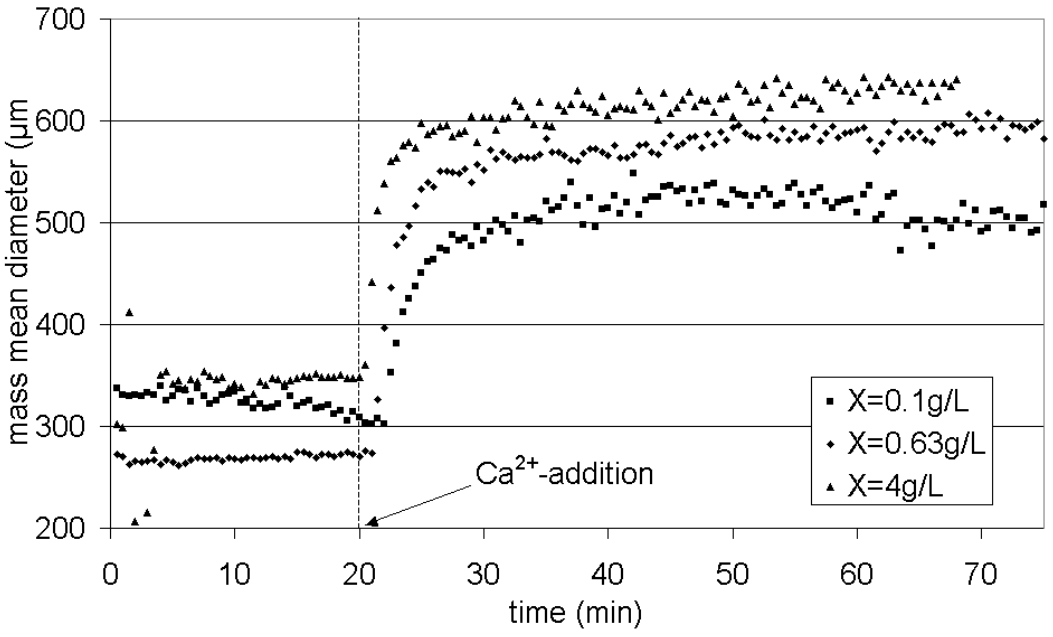

Figure 6.16: Sludge concentration influence on the mass mean diameter measured by the Malvern Mastersizer

The evolutions of the vol% measured by the Malvern Mastersizer for $X = 0.1\,g.L^{-1}$ are depicted in Fig. 6.18. The distribution is not very stable during the first 20 minutes. It is more noisy, probably caused by the low concentration (less flocs are analysed). The most abundant size class is again roughly $400\,\mu\mathrm{m}$. Size classes between 220 and $550\,\mu\mathrm{m}$ show decreasing vol%, whereas classes smaller than $220\,\mu\mathrm{m}$ increase. Some slow breakage seems to be taking place. Interesting to note is that size classes larger than $550\,\mu\mathrm{m}$ do not decrease (but are very noisy). The impose dilution might be an explanation for the increased noise levels due to lower particle counts. When adding Ca^{2+}, size classes smaller than $400\,\mu\mathrm{m}$ decrease, whereas those ranging from 400 up to $1200\,\mu\mathrm{m}$ increase. Flocs of around $600\,\mu\mathrm{m}$ now become the most abundant. Despite the increase in size, it is smaller compared to the increase found at higher sludge concentrations.

The evolutions of the vol% measured by the Malvern Mastersizer for $X = 0.63\,g.L^{-1}$ was already shown in Fig. 6.8. Results are intermediate compared to the ones at other sludge concentrations.

Number distributions

Results of the total number of flocs (N_{tot}) for different sludge concentrations recorded by the CIS-100 (time of transition method) are given in Fig. 6.19. Note that N_{tot} has a similar order of magnitude for the different cases during the initial 20 minutes, which is caused by the same sample dilution prior to the measurement. Differences here can be either caused by slight differences in effective concentration at measurement or stem from a different aggregation state. The former is unlikely since the dilution step was standardised.

For $X = 0.1\,g.L^{-1}$, N_{tot} increases during the first 20 minutes, confirming the decrease in vol% and,

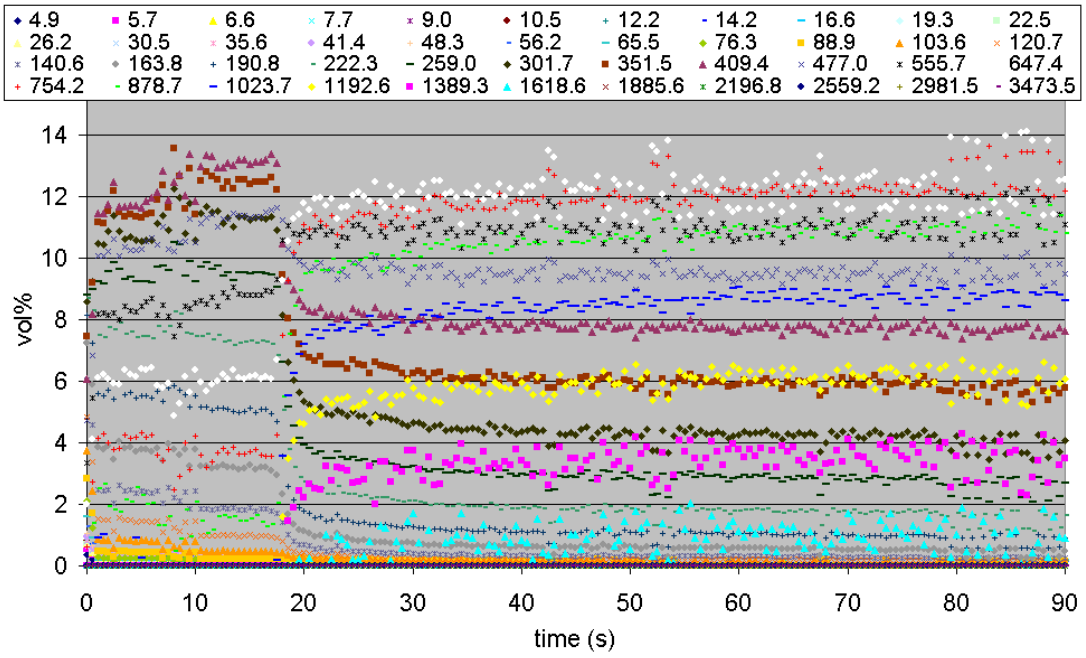

Figure 6.17: Time evolutions of vol% in different size classes measured by the Malvern Mastersizer for X=4 $\mathrm{g.L^{-1}}$

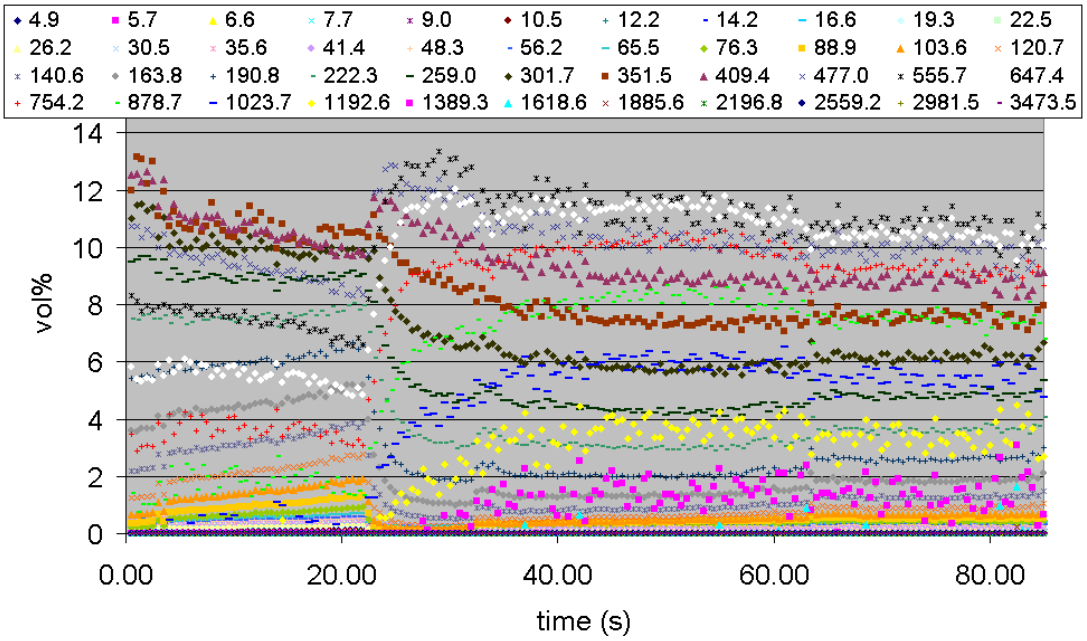

Figure 6.18: Time evolutions of vol% in different size classes measured by the Malvern Mastersizer for X=0.1 $\mathrm{g.L^{-1}}$

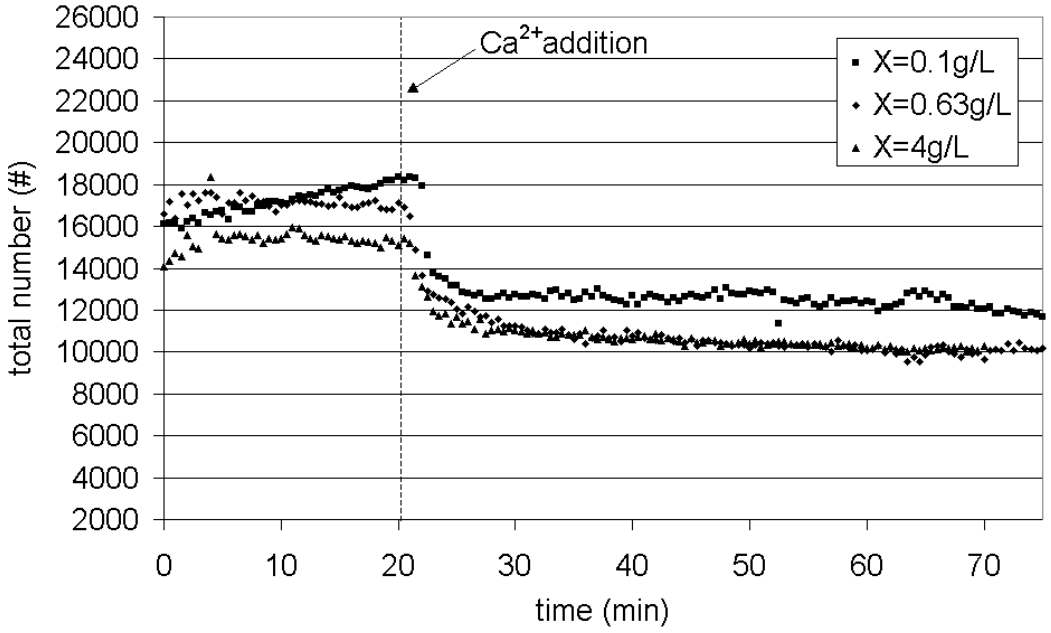

Figure 6.19: Sludge concentration influence on the total number of flocs measured by the CIS-100

thus, the slow breakage that was observed earlier with the Malvern. After adding Ca^{2+}, N_{tot} decreased to reach a steady state.

In case $X = 4\,g.L^{-1}$, a constant, but smaller N_{tot} was observed during the first 20 minutes, again suggesting that the floc strength is slightly different in both experiments, although the lower sludge dilution might also have an effect here. Ca^{2+}-addition resulted in a decrease of N_{tot}. The steady state that was reached, however, is smaller compared to the low concentration case. This confirms the qualitative conclusion that a higher degree of flocculation has been reached in this more concentrated suspension.

The intermediate case ($X = 0.61\,g.L^{-1}$) was already discussed before (section 6.2.1). The steady state N_{tot} is, however, not very different from the high concentration case. This is caused by the fact that number concentrations rather than volumes are used. A difference of a few hundred flocs might not show a large difference in a number-based graph, whereas this is more emphasised in a volume-based plot (see Fig. 6.16).

6.2.5 Calcium addition

D[4,3]

To investigate the influence of Ca^{2+}, experiments were performed for the design axial points (0 and $24\,\mathrm{meq.L}^{-1}$) and the center point ($12\,\mathrm{meq.L}^{-1}$). The other operational conditions were kept constant at the center point values, which have been described earlier. Results of the mass mean diameter (D[4,3]) for different Ca^{2+}-additions recorded by the Malvern Mastersizer are given in Fig. 6.20. It should be noted that the sludge from the SBR was low on Ca^{2+} due to the use of softened water for influent make-up. This might have emphasised the observed Ca^{2+}-effects (Govoreanu, 2004).

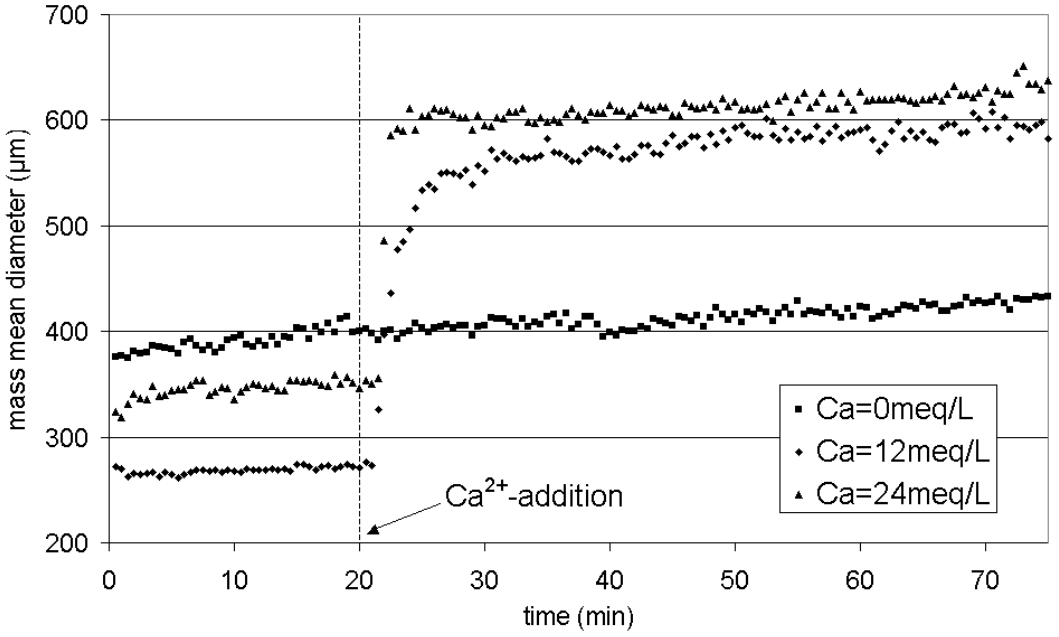

Figure 6.20: Calcium addition influence on the mass mean diameter measured by the Malvern Mastersizer

Again, it can be observed that the mass mean diameter is different during the first 20 minutes of the different experiments, suggesting a difference in floc strength between the different sludge samples. The Ca^{2+}-addition resulted in an increase in mass mean diameter, reaching steady state values. The latter were larger for higher amounts of Ca^{2+} added, although the observed difference was not very large taking into account that the Ca^{2+}-dosage was doubled. Also, the response was significantly faster for higher concentrations added. Still, however, a slight background increase is observed in both cases at steady state. The blank case (no Ca^{2+}-addition) showed this slightly increasing trend of the mass mean diameter throughout the entire duration of the experiment. This trend is, therefore, most probably not related to Ca-addition.

Volume percentage distributions

The evolutions of the vol% measured by the Malvern Mastersizer for a Ca^{2+}-addition of $24\,meq.L^{-1}$ are depicted in Fig. 6.21. During the first 20 minutes of the experiment, flocs of around 350-400 $\mu\mathrm{m}$ are the most abundant. Ca^{2+}-addition caused a sudden jump in the different size classes. Size classes smaller than 500 $\mu\mathrm{m}$ show a decrease, whereas the ones ranging from 500-1400 $\mu\mathrm{m}$ exhibit a significant increase. The most abundant flocs have a size of about 700 $\mu\mathrm{m}$.

The evolutions of the vol% measured by the Malvern Mastersizer for a Ca^{2+}-addition of $0\,meq.L^{-1}$ are depicted in Fig. 6.22. Although the conditions during the experiment do not alter, some evolution of the different size classes can be observed. Size classes smaller than, say, 450 $\mu\mathrm{m}$ tend to slightly decrease, whereas those ranging from 450 up to 1000 $\mu\mathrm{m}$ slightly increase. A possible explanation could be that flocs are reorganised and tend to get stronger, enabling them to withstand the same shear forces imposed by the mixing.

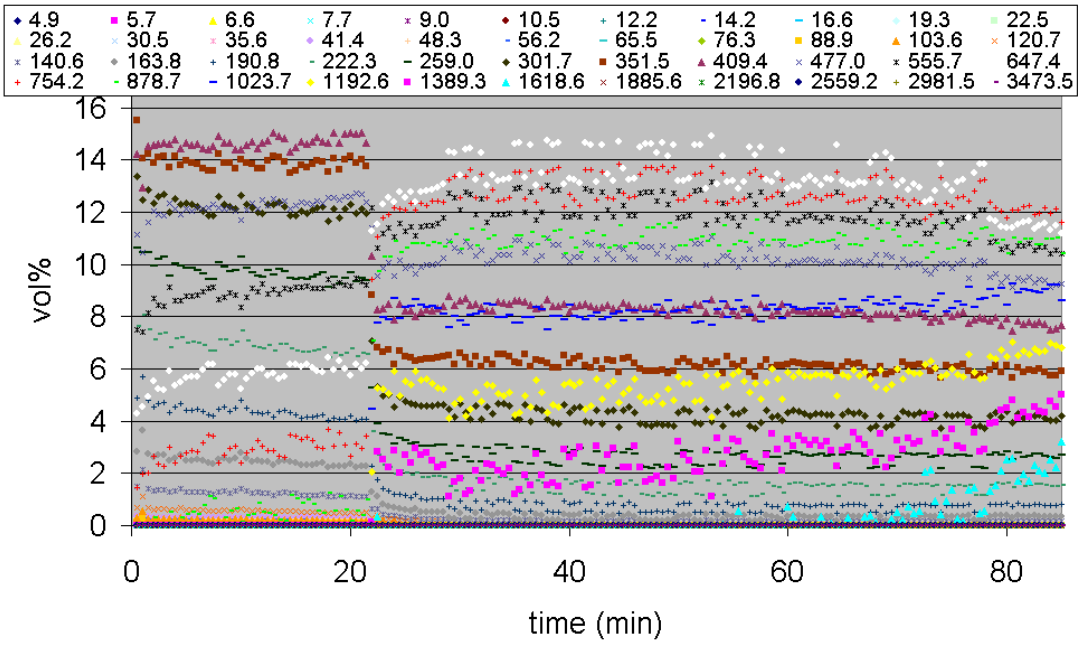

Figure 6.21: Time evolutions of vol% in different size classes measured by the Malvern Mastersizer for a Ca^{2+}-addition of $24\,meq.L^{-1}$

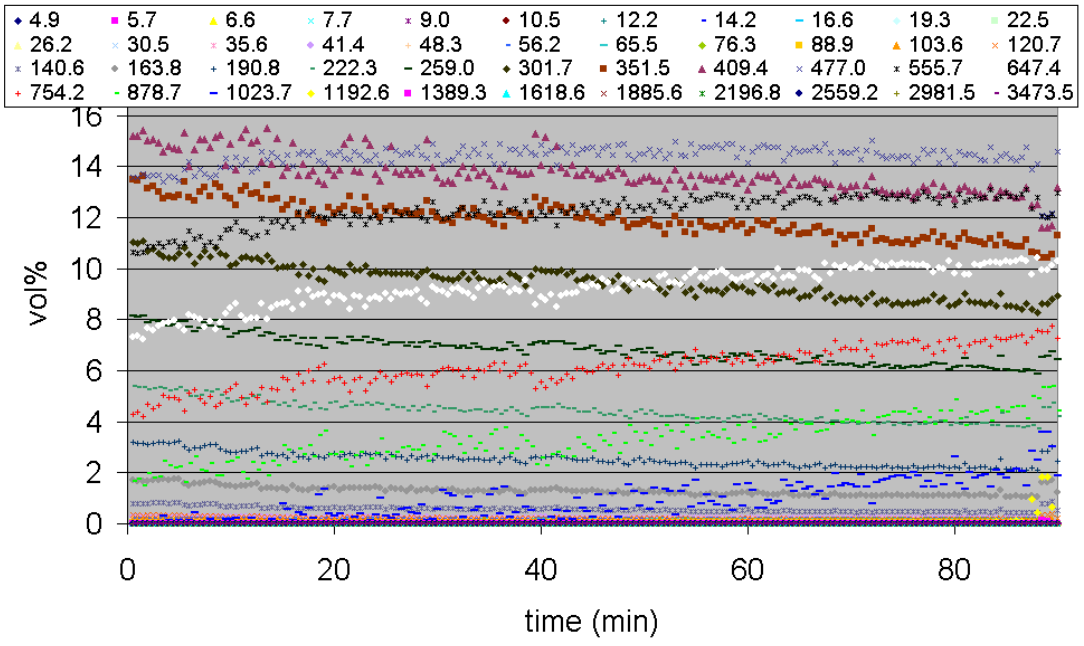

Figure 6.22: Time evolutions of vol% in different size classes measured by the Malvern Mastersizer for a Ca^{2+}-addition of $0\,meq.L^{-1}$

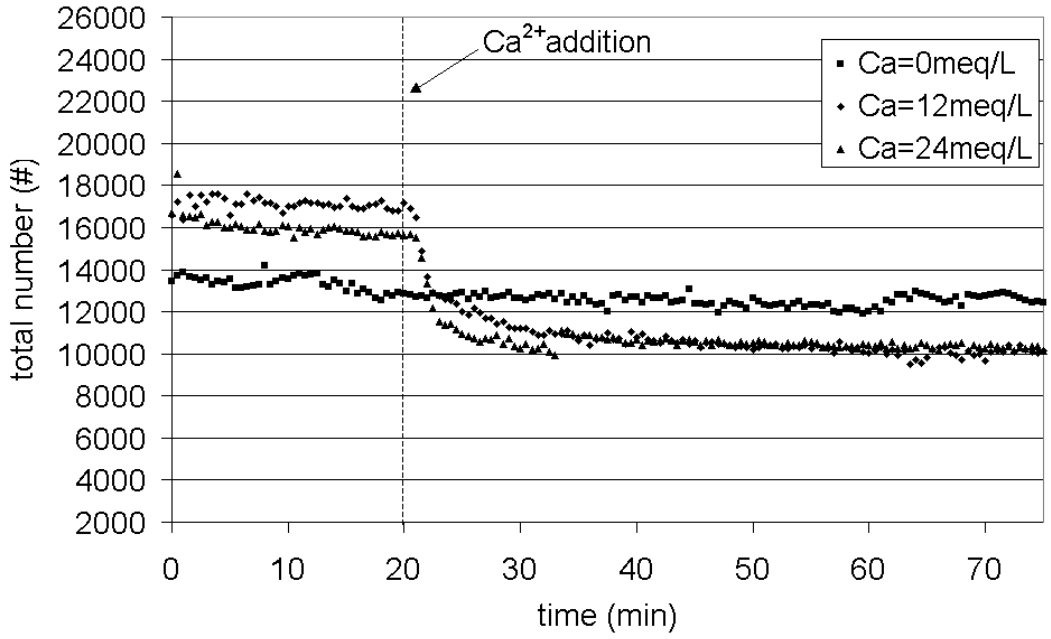

Figure 6.23: Ca^{2+}-addition influence on the total number of flocs measured by the CIS-100

The intermediate case (Ca^{2+}-addition of $12\,meq.L^{-1}$) was already discussed before (section 6.2.1). The response rate of the changes in the different size classes is smaller compared to the higher dosage case. The most abundant floc size is also somewhat smaller.

Number distributions

Results of the total number of flocs (N_{tot}) for different Ca^{2+}-additions recorded by the CIS-100 (time of transition method) are given in Fig. 6.23.

Similar observations as in the sludge concentration case were made. N_{tot} is different during the first 20 minutes for the three experiments. The trends observed in the Malvern results are again confirmed. Ca^{2+}-addition caused N_{tot} to decrease. The rate at which this happened is higher for the larger dosage of Ca^{2+}. Also, N_{tot} at steady state is not very much different for different dosages.

6.3 Concluding remarks

Distributions contain a lot of information which is lost when a summarising parameter like e.g. D[4,3] is used. From the experiments using different shear rates, it can be concluded that different size classes exhibit different behaviour depending on how their size relates to the Kolmogorov microscale of turbulence. Larger size classes increase toward an equilibrium, smaller classes reach a maximum and decrease to reach a steady state, whereas the smallest classes do not exhibit a peak behaviour. The peak behaviour was, however, not observed in the cases where 'gentle' aggregation occurred (i.e. aggregation from a non-sonicated sludge). It was reasoned that no breakage occurred prior to the onset of steady state. Fur-

Table 6.2: Kolmogorov-scales and most abundant floc sizes for all Flocunit experiments (prior to Ca-addition)

experiment	$\bar{G}\ s^{-1}$	η (μm) 10-fold rule	η (μm) from $\bar{G}$	most abundant floc size (μm)
center point	55	76	135	300
Low T	55	76	135	350
High T	55	76	135	300
Low G	15	146	259	350
High G	200	40	70	190
Low DO	55	76	135	300
High DO	55	76	135	350
Low X	55	76	135	400
High X	55	76	135	400
Low Ca	55	76	135	450
High Ca	55	76	135	350-400

thermore, the estimate of the Kolmogorov scale by using the 10-fold of the average energy dissipation seemed to be a good assumption for the experimental data of Biggs (2000), whereas this assumption was not found to hold for in the experiments using the Flocunit. This is illustrated in Table 6.2 that presents the calculated Kolmogorov-scales η (based on the 10-fold average energy dissipation rule of thumb) and the most abundant floc sizes for all Flocunit experiments prior to Ca-addition. The fact that the rule is not applicable in the Flocunit experiments is possibly caused by the different reactor configuration (probes are obstacles and have a 'baffle' function). The only way to verify this would be to build a CFD-model of both reactors and calculate the differences in energy dissipation rate distributions.

The experiment with the step changes in average shear rate showed similar results when solely looking at a summarising parameter. However, (de)flocculation behaviour is clearly different when looking at the complete distributions. A comparison of the reflocculation after sonication and increased shear rate, showed that the initial number of small particles is much larger in the former case. Whereas all classes smaller than the Kolmogorov scale exhibited a peak in the sonication pre-treatment case, this was not true for the increased shear rate case. Also, the size class exhibiting the largest vol% was somewhat smaller, suggesting more compact flocs. This leads to an important conclusion: sonication prior to the experiment seems to induce a different kind of flocculation compared to break-up through shear as a pre-treatment. Moreover, sonication is not happening in practice (whereas shear rate changes do) and is thus not representative for the flocculation occurring in a full-scale treatment plant. Lab-scale studies should, therefore, not apply sonication in order to elucidate the activated sludge flocculation behaviour.

Experiments performed in the Flocunit showed more measurement noise than the experiments performed by Biggs (2000). This may be related to the reactor configuration (different volume and many obstacles), reactor volume and the sampling procedure, which was not based on recirculation. However, when discarding the noise, the main trends could still be evaluated.

The 'standard' initial part of all experiments in the design could not prevent that distributions were different. This is probably caused by a different flocculation history which induced sludges of different strengths. Also, the previously used empirical relationship between average shear intensity and Kolmogorov scale appeared not to be valid here. This was reasoned to be caused by differences in reactor configuration and differences in floc strength (resistance to stress). Another empirical relationship may be valid for this reactor configuration.

The conclusions drawn from the CIS-100 measurements in terms of total number of flocs are the same as those obtained from the Malvern measurements. However, the CIS-100 number distributions were found to be too noisy to be used for model calibration.

Basically, the conclusions that are drawn based on the evolution of the mass mean diameter or from the complete distributions are the same. However, many details, e.g. moving of fronts, most abundant floc size and floc size classes that are affected by changes in operational conditions, are lost when summarising parameters such as D[4,3] are used. Distributional data are very useful when investigating model structure and calibrating a model (see chapter 7). Indeed, many distributions can exhibit a similar mass mean diameter, and, hence, many models can describe these data without capturing what is really happening. This doesn't mean that summarising parameters are useless. On the contrary, they are very useful for getting a first impression of the dynamics of a process.

The effects of the different factors that were investigated in the experimental design can be summarised as follows:

- Flocs are not disturbed when temperature is lowered. However, some immediate flocculation occurs when temperature is increased. Addition of calcium results in stronger flocs at lower temperatures.
- Shear has an important effect on the activated sludge flocculation. High shear destroys flocs and shifts distributions toward smaller sizes. Low shear allows larger flocs to be present in the system and exhibits slower dynamics. The addition of calcium confirms the hypothesis of floc strength playing an important role. Even at high shear a partial reflocculation was observed after Ca-addition. From a modeller's point of view, the dynamics at high shear cannot be investigated since the measurement frequency with the available set-up was too low to capture the fast flocculation dynamics.
- Changes in DO did not have an immediate effect (even though it took some time to change set-points). Though no short-term changes were observed for an increase in DO, imposing anaerobic conditions resulted in a shift toward larger floc sizes. This is in disagreement with Wilén and Balmér (1999), who did not observe short-term effects and found floc deterioration in the long-term. Ca-addition leads to stronger flocs when the DO-concentration is higher. DO-effects could be determined independent of shear since bubbleless aeration was used.
- At low sludge concentration, a slow deflocculation can be observed, caused by the smaller collision probability. This can also be observed when Ca is added. The largest sludge concentration results in the largest floc size.
- Ca-addition results in extensive flocculation (partly caused by the Ca-deficient sludge that was used). However, the results clearly show that the degree of flocculation is not proportional to the amount of Ca added. A slow background flocculation was observed when no Calcium was added.

CHAPTER 7

From experimental flocculation data to a calibrated population balance model

7.1 Abstract

Fitting a model to an experimental data set is often referred to as *model calibration*. In this procedure, optimal values of the model parameters are determined that result in the best description of the experimental data. [1]

In the case of combining a population balance model with the experimental data sets shown in chapter 6, some additional issues need to be addressed/solved like

- influence of solution technique
- grid transformation
- measurement errors
- fitting variable

In this chapter, a new comprehensive calibration methodology is developed allowing to calibrate a population balance model using experimental data. The chapter is organised as follows. First the nature of the experimental data is discussed along with the numerical methods that were used. Then, the methodology is proposed and discussed, ending with some concluding remarks.

[1] Nopens, I., Vanrolleghem, P.A., 2005. PBM and activated sludge flocculation: from experimental data to calibrated model. AIChE Journal, in press.

7.2 The population balance model

Details of the model equation and the kernel structures that were used in this chapter for developing the calibration methodology are the same as those described in section 4.2 and will not be explicitly repeated here.

7.3 Experimental set-up and numerical methods

The experimental data used in this part of the study were obtained from Biggs and Lant (2000) who were the first researchers to study the influence of mixing intensity and calcium addition on flocculation kinetics on-line. The experimental data that were used in this chapter are described in section 6.1.1 and appendix C.

In order to solve the PBM, two different discretisation techniques were used: the fixed pivot (Kumar and Ramkrishna, 1996a) and the moving pivot technique (Kumar and Ramkrishna, 1996b). Both allow a free choice of grid. In this discretised size range only particles of these pivotal sizes exist. However, aggregation and/or breakage processes give rise to particles of other, non-existing sizes. The fixed pivot technique redistributes these particles to the adjoining pivots. The number of pivots to which the particles are redistributed determines the number of properties that can be conserved by the algorithm. Typically, it is chosen to redistribute mass and numbers to the 2 adjoining pivots, and, hence, both these can be conserved. In the moving pivot algorithm, the pivot is allowed to move within the boundaries of the class it represents. This is a more accurate algorithm, but it requires additional equations to describe the movement of the pivots. For a more detailed explanation, the reader is referred to section 2.5.3 or to literature (Kumar and Ramkrishna, 1996a,b). Both algorithms were implemented in the modelling and simulation software platform WEST (Hemmis NV, Belgium).

Optimisations were conducted using either a least squares (LS) or a weighted least squares (WLS) method for a simultaneous fit of several variables (Dochain and Vanrolleghem, 2001):

$$LS: \quad J(\theta) = \sum_{j=1}^{m} \sum_{i=1}^{N_j} \left(y_{i,j} - \hat{y}_{i,j}(\theta)\right)^2 \tag{7.1}$$

$$WLS: \quad J(\theta) = \sum_{j=1}^{m} \sum_{i=1}^{N_j} \frac{1}{\sigma_i^2} \left(y_{i,j} - \hat{y}_{i,j}(\theta)\right)^2 \tag{7.2}$$

where $J(\theta)$ is the sum of squared errors (SSE) or objective function, $y_{i,j}$ is the measured variable, $\hat{y}_{i,j}(\theta)$ is the model prediction using parameter set θ, m is the number of experimental data sets, N_j is the number of experimental data points of experiment j and σ_i is the measurement error (which inverse is often used as a weight to express the accuracy of the measurement).

The simplex optimisation algorithm (Nelder and Mead, 1965) was used to minimise $\mathrm{J}(\theta)$.

7.4 Calibration methodology

Parameter estimation is a difficult task as it is highly dependent on the model structure, the number of parameters to be estimated and both the quality and quantity of the experimental data. It was decided

to estimate two parameters in total: one parameter in the aggregation part of the model (α) and another one in the breakage part of the model (A). This choice was justified for the D[4,3] by means of a sensitivity analysis that showed that both parameters were sensitive in a different part of the experiment. For the volume and number concentrations, justification can be found in the qualitative discussion of the experimental data in chapter 6, where it was concluded that in the dynamic part of the experiment, pure aggregation or breakage could be assumed. Hence, this dynamic part can be used to fit one parameter, whereas the dynamic equilibrium (i.e. steady state) will then fix the remaining parameter.

The goal of this chapter is to introduce a new comprehensive calibration methodology for PBM using experimentally collected flocculation data. It discusses problems that arise during a calibration procedure and will influence the results, such as (1) the choice of solution method (in this case discretisation methods were used), (2) data transformations that are necessary in order to be able to solve the discretised set of equations (3) measurement errors and (4) the choice of fitting variable.

7.4.1 Solution method

When calibrating a model using experimental data, it is important to use a relatively fast solution method (e.g. discretisation techniques) since many simulations might be needed before the optimum model parameters are found. In their work, Thill et al. (2001) used the discretisation technique of Hounslow et al. (1988), which is exactly the same as the fixed pivot technique when using a geometric grid with factor 2 (e.g.$1, 2, 4, 8, 10^{-18}\,\mathrm{m}^3$) and conserving both numbers (0th moment) and mass (3rd moment) during the discretisation procedure. Kumar and Ramkrishna (1996b), however, compared this fixed pivot technique with an analytical solution for a simple PBM and found that it suffers from overpredictions of numbers when large gradients are present in the distribution. To deal with this, they introduced an alternative technique, the moving pivot, and showed that this technique gave a much better prediction of the analytical solution, even for a coarse grid. To confirm this improved accuracy in this study, the PBM was solved with both techniques, fixed and moving pivot, using the same parameter set ($\alpha = 6.5\,10^{-3}$ and $\mathrm{A} = 201.5\,\mathrm{m}^{-1}\mathrm{s}^{-1}$). The simulation results are represented as cumulative oversize number density (CON)

$$CON\,(x,t) = \int_x^\infty f_N\left(x',t\right)dx' \tag{7.3}$$

in order to emphasise the predictions of the large floc size tail and the 0th moment (= total number of particles in the system) of the distribution in one single plot. It can be seen that the predictions of the fixed pivot starting from the same initial distribution (Fig. 7.1) indeed yield a lower 0th moment (= total number of flocs) and a larger number of flocs in bigger size classes (Fig. 7.2) at t=2000s, suggesting that the aggregation has occurred faster compared to the moving pivot.

Also, the model as solved with the different solution techniques, was fitted to one of the experimental D[4,3] data sets of Biggs and Lant (2000) using the LS objective function (eq. 7.2). The resulting parameter values along with the ones found by Biggs and Lant (2000) are given in Table 7.1. It can be observed that the estimate of parameter α is much lower when the fixed pivot is used since the technique inherently speeds up the aggregation as was observed in chapter 4. In order to fit the same data set, the aggregation parameter α must be decreased (by 50%), leading to erroneous parameter estimates. The difference in A is less pronounced. The results are also somewhat different compared to the ones found by Biggs and Lant (2000). The latter is due to a different data transformation (see next section).

Corroborating the conclusions of chapter 4 on discretised solution techniques and those of Kumar and Ramkrishna (1996b), it is therefore advisable to use the moving pivot to solve the PBM in order to obtain

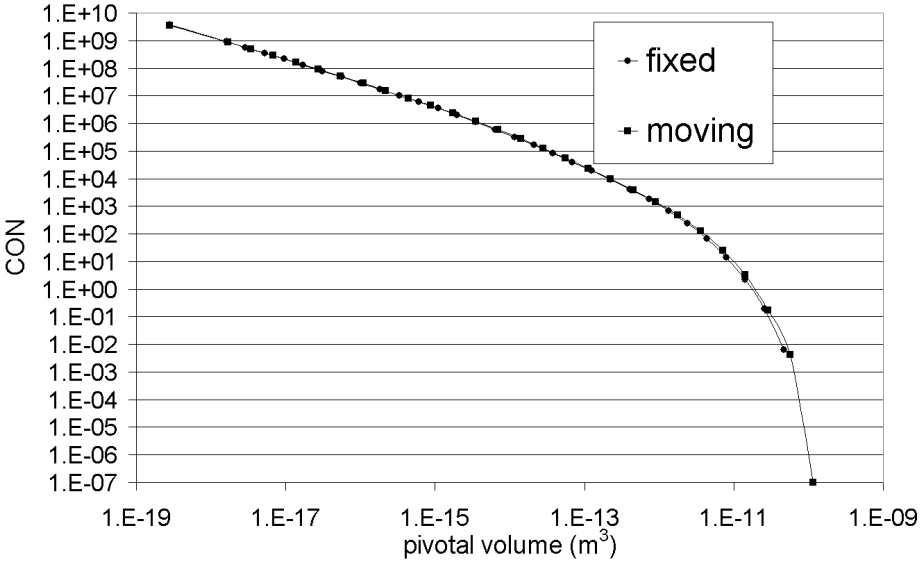

Figure 7.1: Comparison of fixed and moving pivot initial conditions (t=0 s)

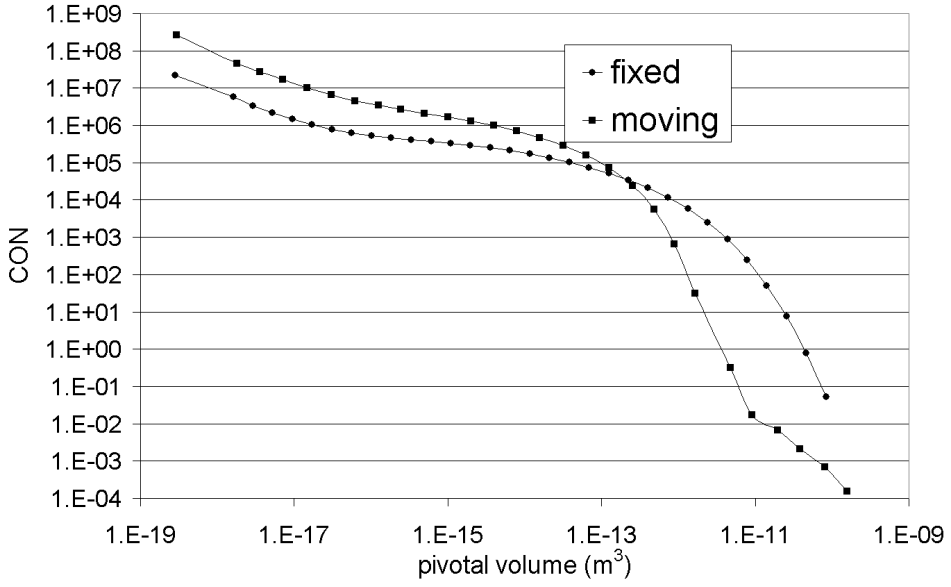

Figure 7.2: Comparison of fixed and moving pivot solutions at t=2000s of a PBM with the same parameters ($\alpha = 0.0065$, A=202 $\mathrm{m}^{-1}\mathrm{s}^{-1}$)

Table 7.1: Parameter estimates of fit on D[4,3] using fixed and moving pivot on the same data set ($\mathrm{G} = 19.4\,\mathrm{s}^{-1}$, see section 6.1.1). The parameters found by Biggs and Lant (2000) for the same data set (but different transformation) are given as well.

method	$\alpha(-)$	$\mathrm{A}(\mathrm{m}^{-1}\mathrm{s}^{-1})$
fixed	6.48E-3	202
moving	1.36E-2	195
Biggs and Lant (2000)	4.95E-4	230

accurate estimates of α and A. As was proven here, the accuracy of the solution technique can have a significant impact on the parameter estimates. Since these model parameters express physical quantities, these biases can lead to unrealistic interpretations when comparing them to values obtained in other studies, which significantly decreases the power of the model.

7.4.2 Data transformation

Every transformation of experimentally collected data will unavoidably introduce some error and should be minimised. In some cases, however, transformations cannot be avoided due to incompatibility of the model and the experimental data. This is the case here: The raw output of the Mastersizer is a vol% distribution for a given grid, based on which the number distribution and some summarising parameters can be calculated. On the other hand, the model is formulated on a number basis and uses a different grid. This gives rise to 2 incompatabilities that need to be sorted out:

- recalculation of the experimental Malvern data is required to make them compatible with the model grid (geometric with factor 2)
- a volume-to-number conversion is needed to obtain an initial distribution to feed the model

Biggs and Lant (2000) fitted log-normal distributions to the original raw vol% distributions, inspired by findings in literature (Li and Ganczarczyk, 1991). The fits were claimed to be good based on high correlation coefficients (R^2 of about 0.92), although clear deviations could be observed near the tails of the distribution. This is illustrated in Fig. 7.3 by comparing the raw cumulative vol% distribution and the one calculated from the number distribution of Biggs and Lant (2000). Subsequently, these log-normal fits were used to interpolate volume fractions along the entire floc size range. After this interpolation step, the volume distribution was transformed into a number distribution assuming the particles to be spherical.

Hence, fitting the log-normal distributions as intermediate step introduced large errors in the number distributions, even though high values of R^2 were obtained. Indeed, small deviations between the log-normal distribution and the experimental data blow up when number distributions are calculated. Biggs (2000) reported this as a shift in D[4,3] between that calculated from the raw data and the one calculated from the transformed number distribution (Fig. 7.4). Such differences are unacceptable and therefore an alternative method is required. Parameter estimates found by Biggs and Lant (2000) after fitting the model to this transformed D[4,3] data set are reported in Table 7.1 and clearly reflect the introduced transformation errors.

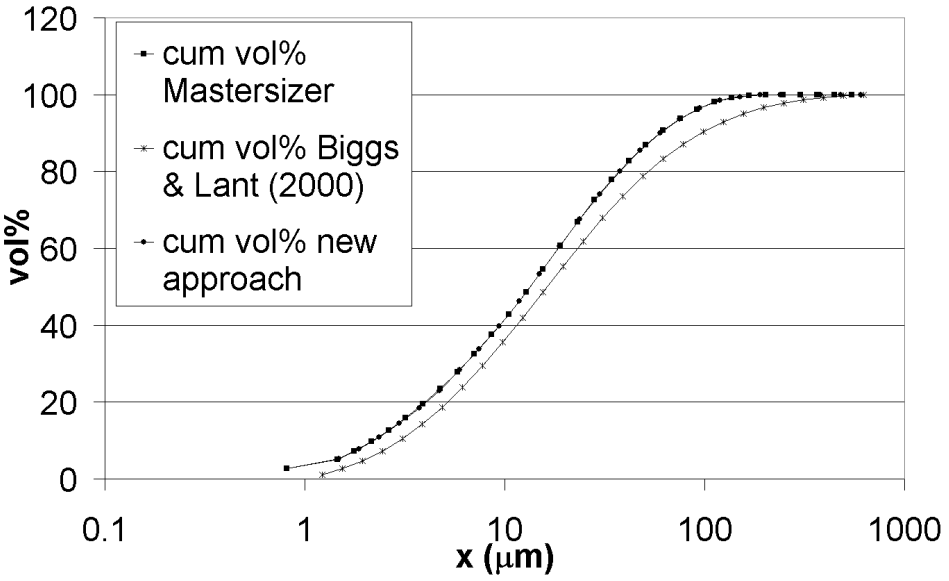

Figure 7.3: Comparison of original and recalculated cumulative volume percentage

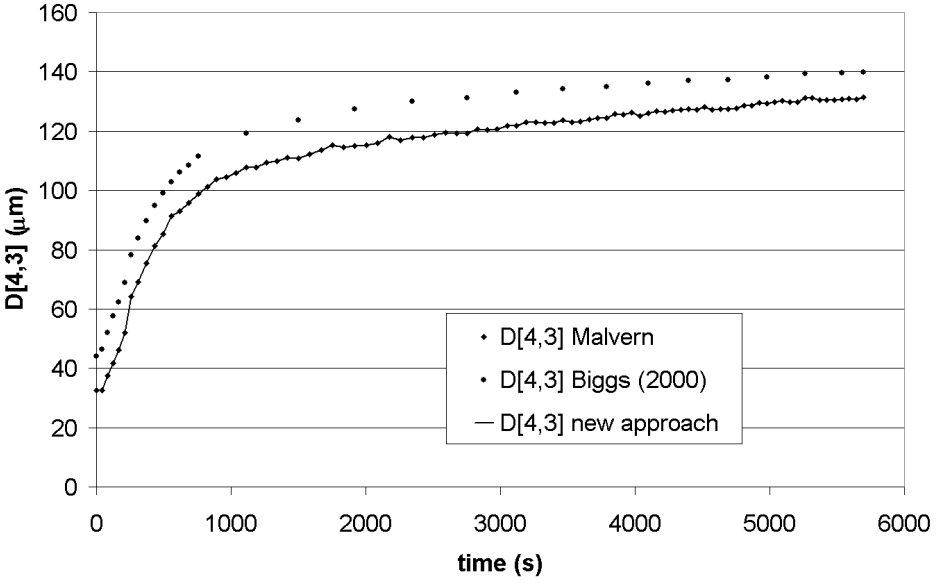

Figure 7.4: Difference between D[4,3] evolution based on (1) raw Mastersizer, (2) the recalculated number distribution of Biggs (2000) and (3) the new approach

As an alternative approach to deal with the difference in discretisation grid, a cumulative vol% distribution is first calculated from the raw distribution. The latter is then interpolated at the pivots of the new grid resulting in a cumulative distribution in the new grid, allowing the recalculation of the volume percentage distribution. Fig. 7.3 and 7.4 show that this transformation does not alter the raw data.

Second, the incompatibility between the experimental vol% distributions and the number-based model needs to be solved. One could argue the need for this transformation and use a volume-based model. However, this has two disadvantages: (1) it was illustrated before that fitting on volumes is dangerous because the tails often are under- or overpredicted, introducing severe errors; (2) the interpretation of the model is less clear when using a volume-based model. Instead of a number of particles $\mathrm{N_i}$ colliding with a number of particles $\mathrm{N_j}$, a volume of particles $\mathrm{v_i}$ will collide with a volume of particles $\mathrm{v_j}$, which is clearly more abstract and no longer compatible with Smoluchowski's law for aggregation.

The experimental data are expressed as vol%, i.e. the ratio between the floc volume in class i ($\mathrm{V_i}$) and the total floc volume of all classes ($\mathrm{V_f}$), $\mathrm{V_i/V_f}$. The model, on the other hand, is expressed in number concentrations or the ratio between the number of particles of class i ($\mathrm{N_i}$) and the total sample volume ($\mathrm{V_T}$), $\mathrm{N_i/V_T}$. To convert $\mathrm{V_i}$ into $\mathrm{N_i}$, the total floc volume fraction $\mathrm{V_f/V_T}$ is needed.

Kinnear (2002) derived a ratio (C) between the liquid and solid mass ($\mathrm{m_l}, \mathrm{m_s}$) within a sludge floc, based on the heterogeneous floc model and the densities of liquid (ρ_l), flocs (ρ_f) and dry solids (ρ_s):

$$C = \frac{m_l}{m_s} = \frac{\rho_l(\rho_s - \rho_l)}{\rho_s(\rho_f - \rho_l)} \tag{7.4}$$

Assuming that a floc consists of solids and interstitial bound water, a mass balance can be written as:

$$m_f = m_s + m_l \tag{7.5}$$

Combining eq. 7.4 and 7.5 yields:

$$m_f = m_s(1 + C) \tag{7.6}$$

Assuming constant densities for flocs and solids and dividing by the total sample volume $\mathrm{V_T}$, one can rewrite eq. 7.6:

$$\frac{\rho_f V_f}{V_T} = \frac{\rho_s V_s}{V_T}(1 + C) \tag{7.7}$$

The factor outside the parenthesis on the right hand side of eq. 7.7 is in fact the Mixed Liquor Suspended Solids (MLSS) referred to as X. This yields the following expression for the total volume of flocs:

$$\frac{V_f}{V_T} = \frac{(1 + C)}{\rho_f} X \tag{7.8}$$

where X is the MLSS ($\mathrm{kg.m^{-3}}$). Eq. 7.8 allows the calculation of the total floc volume fraction by using the measurements of MLSS and the floc, liquid and dry solids densities. The former is a routine measurement in wastewater treatment, whereas the latter can be obtained by means of density-gradient pycnometry (Kinnear, 2002; Dammel and Schroeder, 1991). Literature values for ρ_f range from 1010-1090 $\mathrm{kg.m^{-3}}$, whereas ρ_s ranges from 1200-1800 $\mathrm{kg.m^{-3}}$. As an example, the total floc volume fraction for a sludge with $\mathrm{X} = 3\,\mathrm{kg.m^{-3}}$ and ρ_f, ρ_l, and ρ_s respectively equal to 1040, 1000 and 1400 $\mathrm{kg.m^{-3}}$ was found to be 2.14%. An overview of total floc volume fractions in different ranges of ρ_f and ρ_s and

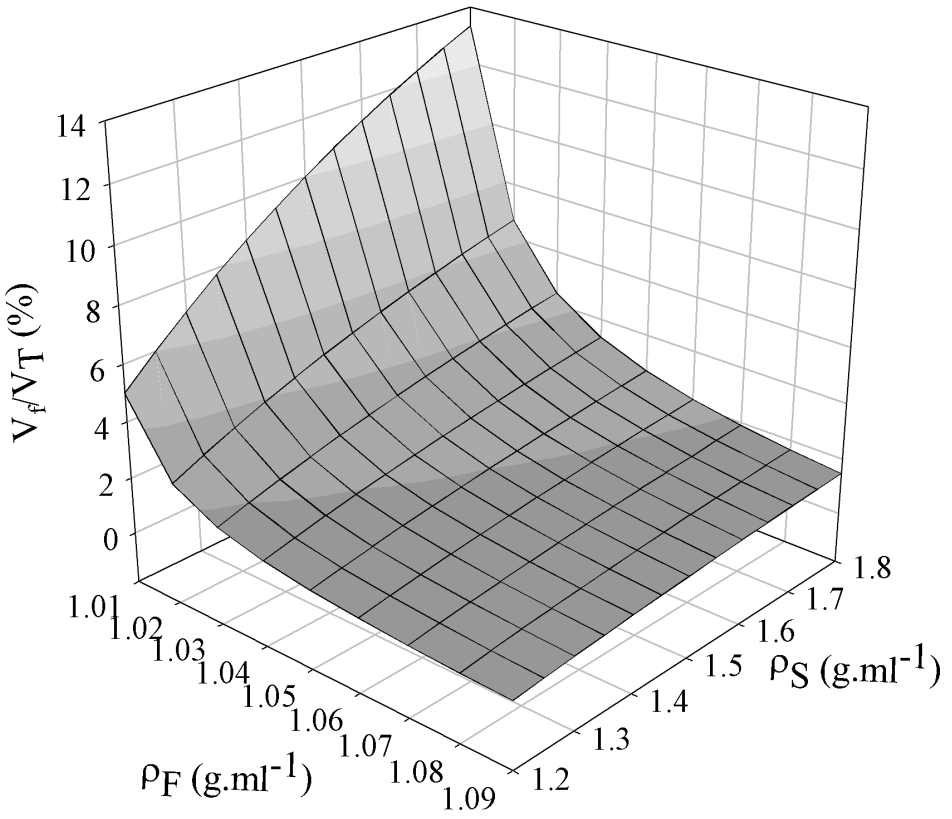

Figure 7.5: Total floc volume fractions as function of floc and dry solids densities ($\mathrm{X} = 3\,\mathrm{g.L}^{-1}$)

for $\mathrm{X} = 3\mathrm{kg.m}^{-3}$ is given in Fig. 7.5. For a fixed ρ_f, the total floc volume increases when ρ_s increases. Heavier particles will cause the floc to contain more water in order to conserve the floc density, causing the floc to be more voluminous. For a fixed ρ_s, the total floc volume increases when ρ_f decreases. The latter could be expected since a floc with a smaller density (but equal solid density) needs to contain more water and, hence, will be more voluminous.

At this stage, the volume concentration and, hence, the number concentration can be calculated assuming the flocs to be spherical:

$$\frac{N_i}{V_T} = \left(\frac{6}{\pi d_i^3}\right) \frac{V_i}{V_f} \frac{V_f}{V_T} \tag{7.9}$$

where $\mathrm{d_i}$ is the diameter of a particle in size class i.

The D[4,3] based on this new distribution exactly matches the one reported by the Mastersizer based on the raw volume percentage distribution (Fig. 7.4). The parameter estimates reported in Table 7.1 for the fixed and moving pivot were obtained using this new conversion. Comparing them with the values found by Biggs and Lant (2000), it can be concluded that the new data conversion results in different parameters. Especially the value of α is significantly higher and seems to be more realistic than the low

value reported by Biggs and Lant (2000). This lower value can be explained by the fact that the system is, initially, in a more flocculated state and apparently does not require the same degree of flocculation to reach steady state (i.e. smaller α).

7.4.3 Measurement error

As mentioned before, measurement errors can be used in the WLS optimisation procedure to account for the uncertainty of experimental data. Practically, this means that the discrepancies between model calculations and data with a high degree of uncertainty are less accounted for in the calculation of the WLS compared to data that have a lower degree of uncertainty.

In their work, Biggs and Lant (2000) only used the mass mean diameter (D[4,3]) as fitting variable. The measurement error was determined by repeated measurement of D[4,3] at steady state. However, a background slope had to be subtracted since no real steady state could be reached. Since the error was assumed to be the same throughout the entire experiment, there was no need for a WLS and a normal LS was used. However, the measurement error value was used to calculate uncertainty intervals for the measurements in order to check whether the model prediction was inside these intervals.

In this work, also number distributions were used as fitting variables. Since the measurement error is not the same for different size classes (which can be understood from the procedure used to derive the distribution from the raw scattering data, see section 2.6) it is of interest to determine measurement errors for each size class. A similar approach as was used for the D[4,3], i.e. using a repetition of measurements during a pseudo steady state, cannot be applied here since the background flocculation cannot be quantified for each single size class $\mathrm{N_i}$. However, since every FSD produced by the Mastersizer is determined by using a large number of measurements (or sweeps), one can assume every Mastersizer measurement to be a *counting* of particles in each size class $\mathrm{N_i}$. Based on this assumption, every single measurement of $\mathrm{N_i}$ can be assumed to be multinomial distributed (Agresti, 1990). The variance of such a multinomial distribution represents the measurement error and can be calculated as follows (Agresti, 1990):

$$\sigma^2(N_i) = N_i \left(1 - \frac{N_i}{N}\right) \tag{7.10}$$

where N is the total number of particles measured. This approach allows determination of the measurement errors for all size classes Ni from one single measurement.

7.4.4 Choice of fitting variable

Two data sets were adopted from Biggs and Lant (2000) and used to calibrate the PBM. They contain data of flocculation experiments at different mixing intensities represented by the average velocity gradient $\bar{\mathrm{G}}$ (19.4 and 37.0 s^{-1}). The new approach based on the constant volume concentration was used for the conversion of raw vol% distributions to number distributions (using $\mathrm{X} = 3\,\mathrm{kg.m}^{-3}$, $\rho_\mathrm{l} = 1000\mathrm{kg.m}^{-3}$, $\rho_\mathrm{f} = 1040\mathrm{kg.m}^{-3}$, $\rho_\mathrm{s} = 1700\mathrm{kg.m}^{-3}$). The PBM was fitted to 4 different sets of fitting variables using the entire range of experimental data: (1) volume percentage distributions, (2) D[4,3], (3) number distributions and (4) weighted number distributions. The parameter estimates of all optimisations are summarised in Table 7.2. Results of the predictions (for $\bar{\mathrm{G}} = 19.4\mathrm{s}^{-1}$) of both the volume percentage distribution and the number distribution after a simulated time of 1920s are given in Fig. 7.6 and 7.8 for the four cases. Similar results were found for $\bar{\mathrm{G}} = 37.0\mathrm{s}^{-1}$ (not shown). From the parameter estimates and the predictions of both the volume percentage and number distribution, it can be seen that the choice

Table 7.2: Optimisation results of fits on vol%, D[4,3], N_i and weighted N_i

$\bar{G}(s^{-1})$	fitting variable	$\alpha(-)$	$A(m^{-1}s^{-1})$	$J(\theta)$
19.4	vol%	1.21E-2	166	1336
	D[4,3]	1.36E-2	195	2712
	N_i	7.30E-3	12	1.6E+19
	weighted N_i	7.80E-3	12	2.64E+10
37.0	vol%	8.30E-3	260	1926
	D[4,3]	8.10E-3	260	1958
	N_i	9.80E-3	32	1.47E+19
	weighted N_i	7.80E-3	18	3.76E+10

of fitting variable is critical. Both fits show on the other hand that the model is not flexible enough and that the structure of the kernels needs to be investigated. This will be the focus of the next chapter.

Fit on vol%/D[4,3]

At first sight, fitting on the volume percentage distribution yields a fairly good result for the volume percentage distribution (Fig. 7.6). However, when zooming in on the tails of the distribution, it seems that both the lower and upper tail are underpredicted (Fig. 7.7). The reason for this is merely the fact that the frequencies in these classes are low and will have a smaller contribution to the objective function ($J(\theta)$) in the LS optimisation. For the application under study, the lower tail is of primary interest since flocs with these diameters will usually end up in the effluent of the treatment plant. When looking at the vol%-fitted model prediction of the number distribution (Fig. 7.8), similar conclusions can be drawn, but they are much more pronounced. The model tries to predict the middle classes better compared to the lower and larger size classes. Here, underpredictions by a factor 10-15 occur in the classes with sizes up to $1\,10^{-5}\,m$. Parameter estimates are such that both aggregation and breakage rates are high. In that case, all particles end up in the middle of the size range.

Since the D[4,3] is calculated based on the third and fourth moment of the distribution, it is volume-related. When fitting the model to D[4,3], it can therefore be expected to give similar results as the ones found when fitting on the volume percentage distribution. This expectation was confirmed (Fig. 7.6 and 7.8). However, the underprediction of the lower end classes is even more severe (15-30 times) (Fig. 7.7). Parameter estimates are somewhat higher than the ones found when fitting on volume percentages (Table 7.2). Another noteworthy observation is that the discretised solution technique that was used here and by Biggs and Lant (2000) only conserves numbers (0th moment) and mass (3rd moment). To calculate the D[4,3], the prediction of the 4th moment is needed, which is not at all guaranteed to be conserved. This is another argument why D[4,3] should not be used as a fitting variable (unless the 4th moment is explicitly conserved by the solution algorithm.

Fit on N_i / weighted N_i

When fitting on N_i, the prediction of the volume percentage distribution is bad. However, when looking at Fig. 7.8, one can see that the predictions of the lower size tail are better compared to fitting on either the

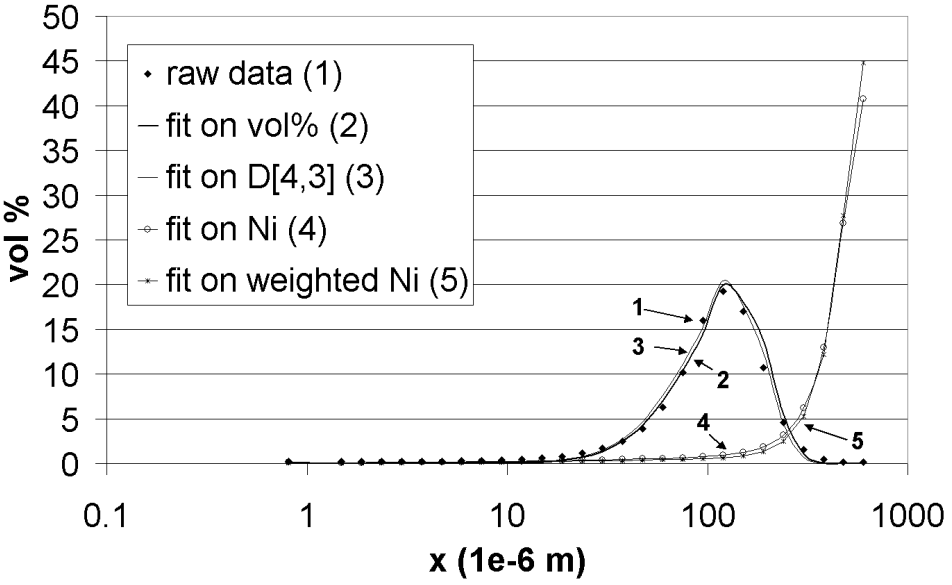

Figure 7.6: Comparison of model predictions of the volume percentage distribution at t=1920s after the model was fitted to different fitting variables

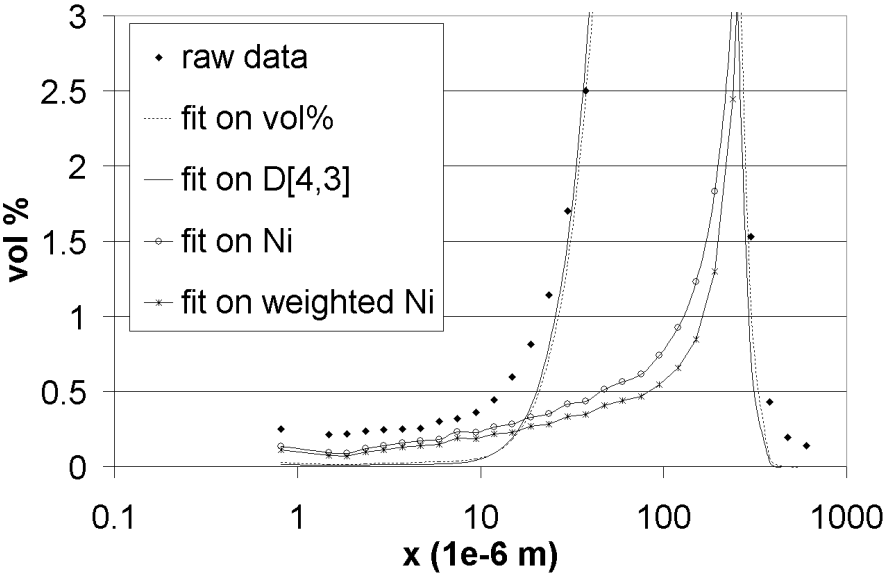

Figure 7.7: Zooming in on the small particle tail model predictions at 1920s after the model was fitted to different fitting variables

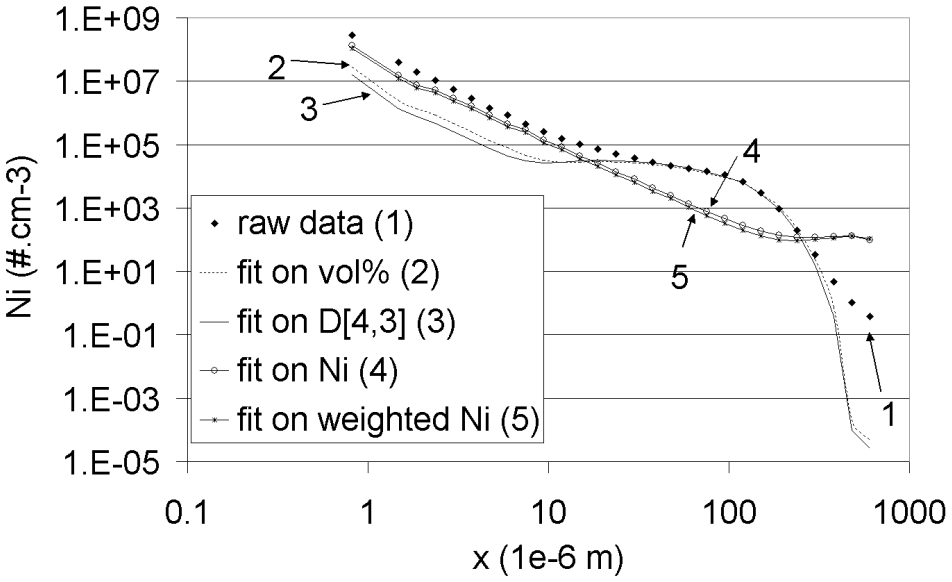

Figure 7.8: Comparison of model predictions of the number distribution at t=1920s after the model was fitted to different fitting variables

volume percentage distribution or D[4,3]. Looking at the prediction of the number distribution, similar observations can be made. Underprediction factors of the lower tail now range between 1.5 and 2.5, which is still rather high, but already much better compared to fits on the volume percentage distribution or D[4,3]. The reason for this is the fact that when fitting to numbers, the absolute number of flocs in every class will determine which classes will contribute most to the $\mathrm{J}(\theta)$. Since a lot of flocs are present at the lower end of the size range, these classes will be focused upon during the calibration. In order to do so, the parameter estimates are decreased by the optimisation algorithm. This means that both aggregation and breakage occur at slower rates. In the application at hand, gravitational solid-liquid separation, one is mainly interested in the small flocs that will not settle. This means that a better prediction of the small size classes is needed. In this regard, it is better to fit the current model to the number distribution instead of the volume distribution since it gives a better prediction of the classes of interest. It should, however, be noted that this can be different for other applications with different targets. The prediction of the number distribution is, however, still not good, due to a lack of model flexibility. The model needs improvement by using more appropriate aggregation and breakage kernels. However, the strategy that one would follow (i.e. altering the different kernels for aggregation and breakage) might be quite different depending on the fitting variable that was used.

Finally, when fitting on weighted $\mathrm{N_i}$ using the multinomial approach to calculate the weights, similar results as the fits on $\mathrm{N_i}$ were found. However, since the calculated measurement errors are positively correlated with the absolute numbers in the size classes, they will be larger for classes containing large numbers of particles and, hence, their weights will be smaller. This results in lower predictions of both volume percentages and numbers in the lower and middle range. Underpredictions of the lower end size classes range between 2-3.3. Only the parameter estimate for α is somewhat higher, resulting in somewhat faster aggregation. This is due to the fact that the contribution of the lower end class prediction to the $\mathrm{J}(\theta)$ is reduced since these measurements are less certain, whereas the contribution of larger classes to the $\mathrm{J}(\theta)$ has increased.

7.5 Conclusions

A new comprehensive methodology was presented that deals with problems that arise when calibrating a PBM using experimental data collected on-line during flocculation. Four issues were discussed: (1) choice of solution method, (2) data transformation, (3) measurement errors and (4) choice of fitting variable(s).

It was shown that the fixed pivot solution method overpredicts both the 0th moment and the number of flocs in the large size class range in agreement with findings by Kumar and Ramkrishna (1996b), leading to a severe underprediction of the aggregation parameter a (50%). Therefore, it is advised to use the moving pivot technique to solve the PBM.

Data transformation is needed to ensure compatibility between experimental data and the model. The calculation of the volume percentage distribution in the model grid was accomplished by means of calculating the cumulative volume percentage distribution and interpolating at the pivots of the model grid. A new approach for volume to number conversion based on a fixed total floc volume was presented. The total floc volume could be calculated from the sludge concentration (X) and the densities of liquid (ρ_l), solids (ρ_s) and flocs (ρ_f). The technique conserved the D[4,3] of the original distribution.

Unlike the measurement error of the D[4,3], which could be derived from a repetitive measurement at pseudo steady state (correcting for the background slope), the measurement errors for different size classes of the measured distributions were determined by assuming the distribution to be multinomial. In this case the observed variance can be used as a measure of the error.

Finally, the PBM was fitted to 4 different fitting variables: (1) volume percentage distribution, (2) D[4,3], (3) number distribution and (4) weighted number distribution. Fitting on volume based variables (vol%, D[4,3]) resulted in good predictions of the volume percentage distribution. However, both tails of the distribution are severely underpredicted. The predictions of the number distribution showed a similar result, but more pronounced with underpredictions in the lower end up to a factor 10-30. Parameter estimates correspond with quite high rates, forcing the particles to move to the middle part of the size range. Moreover, it should also be noted that the 4th moment which is used to calculate the D[4,3] is not conserved by the discretised solution technique. Fitting on number related variables (N_i, weighted N_i) resulted in bad overall predictions of the volume percentage distribution, but the underpredictions at the lower end tail were found to be smaller. Again, more pronounced results were found for the predictions of the number distribution. Underpredictions of the lower end size classes ranged between 1.5-3.3. Parameter estimates correspond to lower aggregation/breakage rates. For the application at hand, gravitational solid-liquid separation, it is advised to optimise the model by means of the number distribution and not volume distribution, noting that this might be different for other applications.

CHAPTER 8

The "'quest"' for kernel structures for floc breakage/aggregation

An early effort to model the activated sludge flocculation process was performed by Parker et al. (1972) with the aim to describe changes in settling characteristics. The proposed model describes the changes in supernatant primary particles (turbidity measurements) after settling and was validated by Wahlberg et al. (1994). Floc aggregation and break-up appeared to be key processes that occur simultaneously. However, the Parker model does not allow overall modelling of the settler, since it only provides information concerning primary particles in the supernatant, determining effluent suspended solids. A population balance model is capable of tracking substantially more size classes and can, therefore, be used for predicting settling behaviour too. Before this step can be taken though, the model structure needs to be identified. This will be the goal of this and the next chapter.[1]

8.1 The population balance model

The model equation that was used in this chapter is the same as that defined in section 4.2 and will not be repeated here.

8.2 Aggregation and breakage kernels

In order to make the described PBM operational, expressions for the collision efficiency $\alpha(x, x')$, the collision frequency $\beta(x, x')$, the breakage rate $S(x)$ and the breakage distribution function $\Gamma(x, x')$ are

[1]Nopens, I., Koegst, T., Vanrolleghem, P.A., 2004. Comparison of different aggregation and breakage kernels for PBMs of the activated sludge flocculation process. In: Proceedings 2nd International Conference on Population Balance Modelling. Valencia, Spain, May 5-7, 2004.

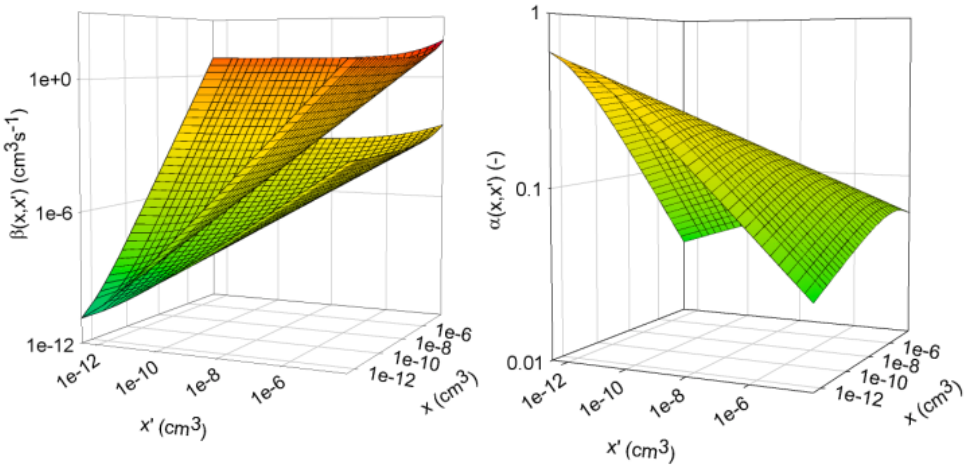

Figure 8.1: Shape of the collision frequency kernel for $Df = 3$ (lower surface) and $Df = 2$ (upper surface) (left) and the collision efficiency for the size-dependent expression of Adler (1981a) (right)

required.

8.2.1 Aggregation

Camp and Stein (1943) assumed simple shear flow within the smallest eddies of turbulence and proposed the following expression for $\beta(x, x')$:

$$\beta(x, x') = \frac{4}{3}\bar{G}(R_x + R_{x'})^3 \tag{8.1}$$

where $\bar{G}$ is the average velocity gradient (defined earlier in section 4.2, ν the kinematic viscosity and $\bar{\epsilon}$ the average turbulent energy dissipation rate. R_x and $R_{x'}$ represent the collision radii of the colliding particles. When assuming the flocs to be impermeable solid spheres, the collision radius equals the floc radius and eq. 8.1 can be rewritten as (Spicer and Pratsinis, 1996b):

$$\beta(x, x') = \frac{\bar{G}}{\pi}\left(x^{\frac{1}{3}} + x'^{\frac{1}{3}}\right)^3 \tag{8.2}$$

However, when the flocs are assumed to have a fractal structure, eq. 8.1 can be rewritten as (Lee et al., 2000):

$$\beta(x, x') = \frac{\bar{G}}{\pi}x_0^{1-\frac{3}{Df}}\left(x^{\frac{1}{Df}} + x'^{\frac{1}{Df}}\right)^3 \tag{8.3}$$

where Df represents the fractal dimension and x_0 the size of the 'primary floc' expressed as volume, which is assumed to be one bacterial cell and corresponds to the smallest size measurable by the sizing device ($2.8\,10^{-13}\,cm^3$). Note that eq. 8.3 reduces to eq. 8.2 for $Df = 3$. Fractal particles ($Df < 3$) will collide more frequently than solid particles (Df = 3) because the collision radius of fractal aggregates increases faster than for aggregates of constant density (Kusters et al., 1997). This is illustrated in Fig. 8.1 (left) for $\bar{G} = 19.4\,s^{-1}$. In this study, both eq. 8.2 and eq. 8.3 were used.

The collision efficiency $\alpha(x, x')$ can be chosen as a constant in the interval $\{0, 1\}$ expressing the fraction of collisions that are successful. In this way, the collision efficiency actually corrects for factors that are

not considered in the collision frequency, like electrostatic repulsion, hydrodynamic interaction and van Der Waals attraction, which modify the trajectories of the colliding flocs. Hydrodynamic interaction arises from distortion of the fluid flow and tends to inhibit collisions. In literature, expressions for α are present which take into account the aforementioned forces. Adler (1981a) suggested an expression based on the flow number (term between square brackets), representing the ratio of hydrodynamic shear forces to van Der Waals forces between colliding impermeable porous flocs:

$$\alpha_{x,x'} = \alpha_0 \left[\left(\frac{18\mu \left(x^{1/3} + x'^{1/3} \right)^3 G}{32 A_{ham}} \right) \left(\frac{1}{x_0 \left(\frac{1}{x^{1/3}} + \frac{1}{x'^{1/3}} \right)} \right) \right]^{-0.18} \tag{8.4}$$

where μ represents the dynamic viscosity and A_{ham} the Hamaker constant ($A_{ham} = 3.10^{-17}\, J$). An example of the shape of the surface is given in Fig. 8.1 (right) for G = 19.4 s^{-1} and $\alpha_0 = 1$. It can be observed that collisions between larger particles are less efficient since larger flow distortion will be induced. Also, homogeneous collisions (between similar-sized particles) have a higher probability to be successful.

However, when the flocs are considered to be permeable, implying that liquid can flow through the flocs, the hydrodynamic forces will be far less pronounced than the ones predicted in eq. 2.64 resulting in enhanced collision efficiencies. Kusters et al. (1997) tackled this problem by introducing the shell-core model (SCM) concept, which approximates the floc as a spherical body with an impermeable core and a completely permeable shell. The resulting expression of $\alpha\left(x, x'\right)$ is similar to eq. 2.64, but uses the hydrodynamic radius $(R_{H,x})$, which is based on the floc permeability, instead of the floc size (x). For details, the reader is referred to Kusters et al. (1997). In this study, similar to the studies of Kusters et al. (1997) and Ducoste (2002), the SCM concept was only used for similar-sized flocs (with $\frac{x}{x'} > 0.2$). Dissimilar sized collisions were described by eq. 8.4.

8.2.2 Breakage

The breakage kernel is often considered to be a power law (Ramkrishna, 2000):

$$S\left(x\right) = Ax^a \tag{8.5}$$

where a and A are constants. Spicer and Pratsinis (1996b) successfully used an a-value of 1/3 to describe the breakup of inorganic flocs at different levels of shear. Therefore, this value was used throughout this study, unless otherwise mentioned. The shape of the breakage kernel for different values of A and a is shown in Fig. 8.2.

Ducoste (2002) used a modified version of the breakage frequency expression proposed by Kusters (1991), which incorporates the level of shear turbulence:

$$S\left(x\right) = \left(\frac{4}{15\pi} \right)^{1/2} \left(\frac{K_i \bar{\epsilon}}{\nu} \right) exp\left(\frac{-C_1}{x K_i \bar{\epsilon}} \right) \tag{8.6}$$

where K_i represents the ratio of the average energy dissipation rate $\bar{\epsilon}$ and the local energy dissipation rate ϵ, and C_1 is a constant. The exponential function expresses the probability that a critical velocity gradient occurs that will cause the floc to break. The shape of this breakage kernel is also shown in Fig. 8.2.

For simplicity, binary breakage into equally sized daughter particles was assumed, which was described in section 4.2.

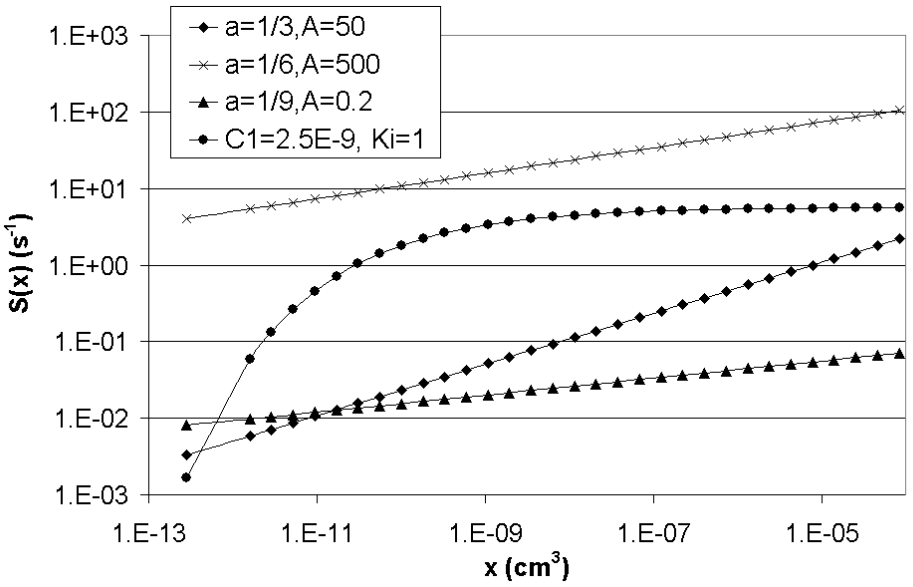

Figure 8.2: Shape of the breakage frequency for eq. 4.8 and eq. 8.6 (model parameters are given in the legend)

8.3 Materials and methods

The experimental data that were used in this chapter are described in section 6.1.1 and appendix C.

Unfortunately, the raw scattering data of the experiments were no longer available. This forced us to use a similar methodology as Biggs and Lant (2000) based on the vol% distributions. This is bound to introduce some error, since the optical model assumes sphericity of the flocs. Since the mass mean diameter is based on higher moments (3rd and 4th), it is considered to be biased towards more accurate prediction of larger flocs. In the application at hand, however, we are mostly interested in the number of small flocs, since these are not settling well and finally end up in the effluent of the treatment plant. Therefore, D[4,3] is not considered a good summarising parameter for our goal. What should be used instead? Govoreanu et al. (2004) suggested to minimise the manipulation of data from particle size analysers. The Malvern device outputs vol% distributions. However, one needs to be careful when fitting on vol% distributions using a non-weighted least squares algorithm. The algorithm will try to predict the classes with the largest absolute volumes best since their squared errors will be large. Since small particles have small volumes, they typically represent small absolute values in vol% distributions. Hence, relatively larger discrepancies will be allowed by the fitting algorithm and, therefore, large errors can occur when calculating these predicted volumes back to number concentrations.

It was, therefore, opted to use number distributions as fitting variable for the PBM. The method for data-conversion from the Malvern vol% distribution into the number distribution was somewhat different from the one used by Biggs and Lant (2000) and is described in 7. Summarized, this method first calculates the total floc volume of the system using 3 densities (liquid, solid and floc) and the biomass concentration (which was approx. 3 g/L) using the heterogeneous floc model concept, which assumes the floc to consist of solids and interstitial water. With this total floc volume, the volume per size class and, therefore, the number of particles in that class can be calculated.

Table 8.1: Overview of different models used in this study

#	agg. efficiency	agg. frequency	break. frequency
1	constant	eq. 8.2	eq. 8.5
2	constant	eq. 8.3	eq. 8.5
3	eq. 8.4	eq. 8.2	eq. 8.5
4	eq. 2.64	eq. 8.3	eq. 8.6

Eq. 4.1 was discretised into i classes producing a set of differential equations in N_i. These represent the number concentration of size class i and were solved in the modelling and simulation software platform WEST (Hemmis NV, Belgium) using the fixed pivot discretisation algorithm conserving numbers and mass (Kumar and Ramkrishna, 1996a) in combination with the grid provided by the Malvern device (geometric with factor 1.8 resulting in 32 classes). Note that the number and mass conservation (which is typically chosen for discretised solution methods) puts another constraint on the choice of fitting variable. Using D[4,3], as was done by Biggs and Lant (2000), can not be justified since the 4th moment is not conserved by the solution method. As discussed earlier, number distributions were chosen as fitting variable in this study, and this approach is therefore not suffering from a potential bias.

Optimisations were conducted using a least squares (LS) method (Dochain and Vanrolleghem, 2001):

$$LS: \quad J(\theta) = \sum_{j=1}^{m} \sum_{i=1}^{P_j} \left(y_{i,j} - \hat{y}_{i,j}(\theta)\right)^2 \tag{8.7}$$

where $J(\theta)$ is the objective function, here the sum of squared errors (SSE) or objective function, $y_{i,j}$ is the measured variable, $\hat{y}_{i,j}(\theta)$ is the model prediction using parameter set θ, m is the number of experimental data sets, P_j is the number of experimental data points of experiment j.

Four different models were investigated in this study by combining different aggregation and breakage kernels that were discussed earlier. They are summarised in Table 8.1. For each model two parameters were estimated, one for aggregation and one for breakage. Therefore, models can be evaluated directly on this fitting performance, since their complexity (expressed by the number of estimated parameters, Dochain and Vanrolleghem (2001)) is identical.

8.4 Simulation results of model 1

Model 1 was fitted to two data sets of Biggs and Lant (2000) ($\bar{G} = 19.4$ and $37.0\,s^{-1}$ respectively) using the LS method. The experimental data for $\bar{G} = 19.4$ are shown in Fig. 8.3 at 8 of the 87 measured moments in time (data for $37.0\,s^{-1}$ looks similar and is not shown). It can be clearly seen that the number concentration of flocs smaller than 1E-7 cm^3 decreases, whereas larger flocs increase in number. Most of the dynamics occur during the first 1000 s of the experiment, although one cannot claim that a steady-state has set in yet at the end of the experiment.

The optimal simulation results for model 1 (a=1/3) and $\bar{G} = 19.4$ are given in Fig. 8.4 for 4 time instants (to not overload the figure). The best fit results are summarised in Table 8.2 together with the 95% confidence intervals of the parameter estimates (i.e. the probability that the true parameter values are contained by this interval is 95%). Similar results were obtained for the $37.0\,s^{-1}$ case (not shown).

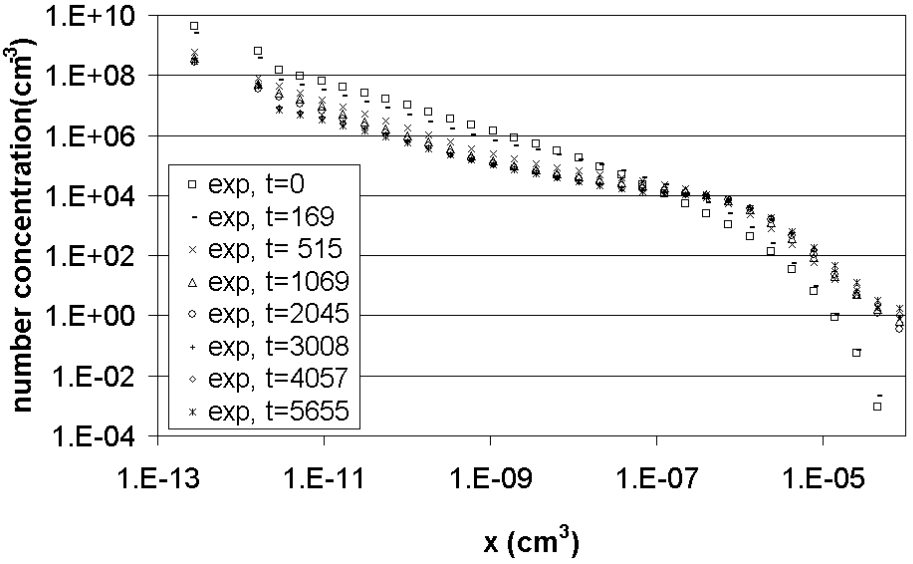

Figure 8.3: Experimental data for $\bar{G} = 19.4\, s^{-1}$

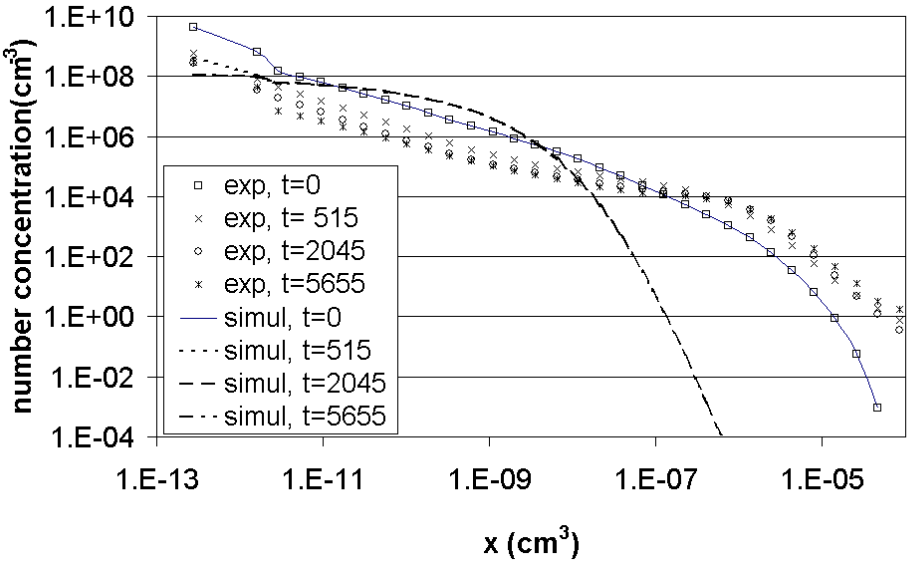

Figure 8.4: Best fit simulation results for $\bar{G} = 19.4\, s^{-1}$ using model 1 (a=1/3). Note that most dynamics occur in the first 2000s, resulting in collapsing distributions after that time instant.

Table 8.2: Summary of fitting results and 95% confidence intervals for model 1

	$\bar{G}$=19.4			$\bar{G}$=37.0		
a (-)	α (-)	A $\left(m^{-3a}s^{-1}\right)$	$J\,(\theta)$	α (-)	A $\left(m^{-3a}s^{-1}\right)$	$J\,(\theta)$
1/3	0.0181 ± 0.0004	3736 ± 95	$5.02.10^{18}$	0.0121 ± 0.0004	5245 ± 189	$8.27.10^{18}$
1/6	0.0245 ± 0.0004	8.98 ± 0.15	$2.31.10^{18}$	0.0164 ± 0.0004	12.43 ± 0.30	$3.58.10^{18}$
1/9	0.0291 ± 0.0004	1.37 ± 0.02	$2.12.10^{18}$	0.0200 ± 0.0004	1.91 ± 0.04	$2.96.10^{18}$

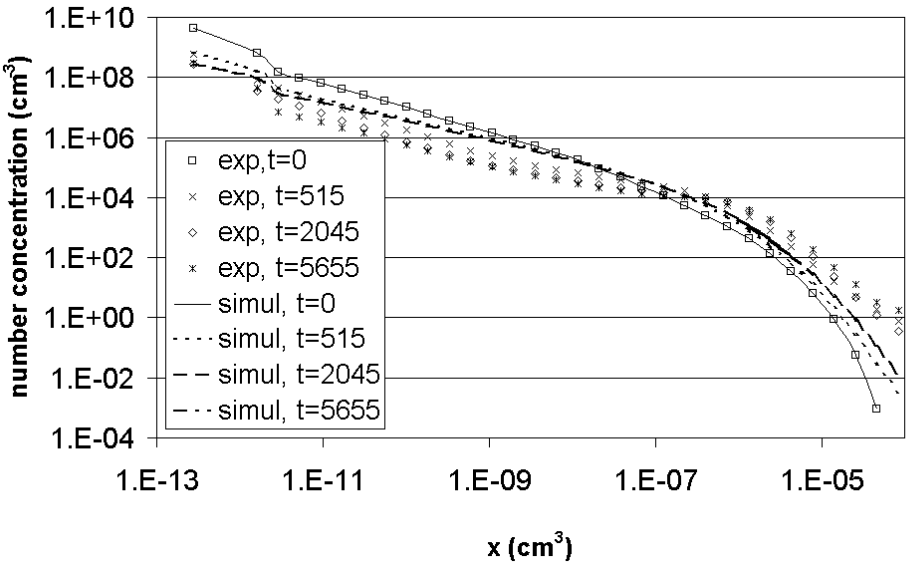

Figure 8.5: Best fit simulation results for $\bar{G} = 19.4\, s^{-1}$ using model 1 and a=1/9

From Fig. 8.4, it can be observed that (1) the primary particles are underpredicted, (2) flocs up to $1.10^{-8}\, cm^3$ are overpredicted and (3) larger flocs are again underpredicted. This behaviour sets in during the first 500 s and remains like that for the rest of the simulation. It should be noted that errors in the small size classes are relatively larger than in larger particle classes, caused by the focus on the number concentration. This makes the optimisation procedure questionable since focus will be on trying to decrease errors of classes with high number concentrations, thereby neglecting classes with smaller number concentrations. This weakness of the optimisation approach may be solved by using a weighted least squares method, but this was not further investigated at this stage.

Since too much breakup appears to occur for large particles, it was tried to alter this behaviour by changing exponent a in eq. 8.5 to smaller values (1/6 and 1/9 respectively, see Fig. 8.2). Optimal parameter estimates are given in Table 8.2 and show, next to a smaller objective function value, a higher estimate of α and a lower estimate of A. The optimal simulation is shown in Fig. 8.5 revealing that the model prediction improved significantly. Decreasing the exponent of the breakage frequency had a positive effect. However, similar, but less pronounced effects as in the a=1/3 case can still be observed. Estimating both parameters in the breakage frequency kernel (A and a) showed to be highly dependent on the intitial parameter values and resulted in highly correlated parameter estimates, suggesting identifiability problems (Dochain and Vanrolleghem, 2001).

An interesting aspect to note here is the fact that the model is not able to predict the bump that builds up (around $x = 1.10^{-7}\, cm^3$) in the experimental data after the initial stages of aggregation. The model always predicts a monotonous decrease of the number distribution for increasing particle volume, whereas the experimental data show a decrease for the smaller particle classes, followed by a kind of plateau for the middle-large sized particles and ending with a decrease of large sized particles.

Table 8.3: Summary of fitting results and 95% confidence intervals for model 2 (n.a. means low parameter confidence due to ill-conditioned covariance matrix)

$\bar{G}\,s^{-1}$	Df (-)	α (-)	A $\left(m^{-1}s^{-1}\right)$	$J\left(\theta\right)$
19.4	2.2	$0.0004 \pm n.a.$	$1669 \pm n.a.$	$7.90.10^{18}$
37.0	2.3	0.00065 ± 0.00008	2681 ± 314	$9.09.10^{18}$

8.5 Simulation results of model 2

Model 2 differs from model 1 (a=1/3) only with respect to the aggregation frequency kernel which is now dependent on the fractal dimension (Df). Df values were heuristically chosen to be 2.2 and 2.3 since they could not be derived directly from the experimental data (raw scattering data were not available). The larger Df-value for the experiment at higher shear is inspired by observations in literature (Gregory, 1997). Best fit results for model 2 are summarised in Table 8.3. The confidence of some parameter estimates is poor due to an ill-conditioned covariance matrix (confidence interval indicated as n.a.). The simulation result for the best fit parameter set is given in Fig. 8.6. Similar results were obtained for the $37.0\,s^{-1}$ case (not shown).

Results show that no severe underprediction of the large size classes occurs (as was the case for model 1 with a=1/3). This is due to the increased formation of larger flocs governed by the Df-dependence of $\beta(x, x')$. Also the optimal breakage rate A is lower. The lower value of α compared to model 1 is necessary to limit the extent of aggregation. Still, model 2 is not capable of predicting the plateau that occurs in the experimental data and severely underpredicts the small size classes, suggesting that the aggregation rate is too high for these flocs. It is not unthinkable that small flocs are more compact (thus, higher Df) leading to slower aggregation rates. It would be interesting to repeat the optimisation for size-dependent Df.

Lowering the exponent a of the breakage function was not considered here since it has a similar effect as the introduction of Df on the aggregation side. If one would do the exercise, the optimal a-value would be largely determined by the choice of Df. On the other hand, it is thought that model 2 is intrinsically more correct since it has been shown that sludge flocs have a fractal nature (Gregory, 1997) and this is not considered in model 1. However, model 2 performs worse than model 1 (with a=1/9), mainly caused by the underestimation of small size classes.

8.6 Simulation results of model 3

Model 3 differs from model 1 in terms of a size-dependent aggregation efficiency rather than a constant efficiency, which should allow to more realistically account for hydrodynamic and van Der Waals forces. Optimisation results for model 3 are summarised in Table 8.4. Simulation results for the best fit parameter set are shown in Fig. 8.7. Similar results were obtained for the $37.0\,s^{-1}$ case (not shown).

Qualitatively, the results are similar to the ones found for model 1. Severe underprediction of the large size classes is caused by the fact that the modified size-dependent aggregation efficiency makes it even more difficult for large flocs to form (due to larger hydrodynamic forces acting upon them). The optimisation algorithm, therefore, lowers the breakage rate A, causing a large decrease (and underestimation) of flocs in the small size ranges. The latter needs to be limited since the errors on the small size classes

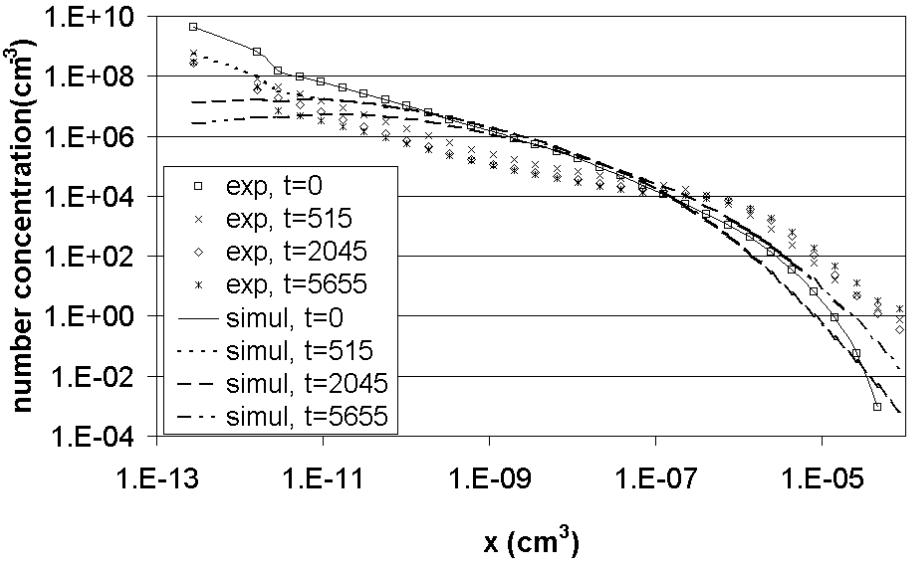

Figure 8.6: Best fit simulation results for $\bar{G}$=19.4 s^{-1} using model 2

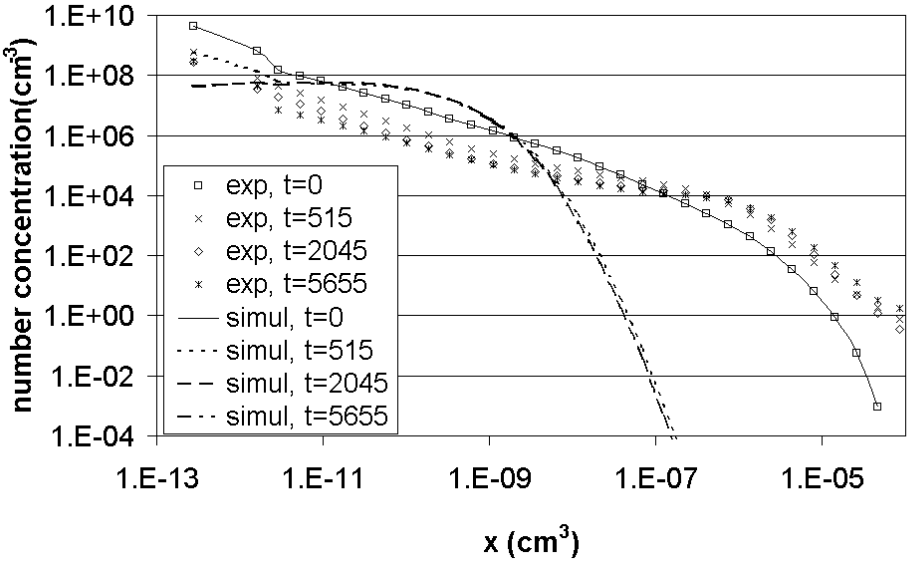

Figure 8.7: Best fit simulation results for $\bar{G} = 19.4\, s^{-1}$ using model 3

contribute strongly to the LS objective function (eq. 8.7). Even when the introduction of the external forces in the expression of the aggregation efficiency may seem acceptable, it seems to have an opposite effect on the simulation result. Note that the estimate of α_0 is quite large and will result in α-values larger than unity in some cases. This suggests that $\beta(x, x')$ is too low and α needs to compensate for this (Thomas et al., 1999). A combination with the Df-based aggregation frequency could correct for this, but was not investigated at this stage.

8.7 Simulation results of model 4

Model 4 differs from model 1 with respect to 3 expressions. It uses the permeable porous floc aggregation efficiency instead of a constant, it incorporates Df in the aggregation frequency and it uses the breakage frequency expression based on turbulent shear. Best fit results for model 4 are summarised in Table 8.5. The parameter estimates themselves are not reliable due to an ill-conditioned covariance matrix (indicated as n.a.). The simulation results for the best fit parameter set are shown in Fig. 8.8. Similar results were obtained for the $37.0\,s^{-1}$ case (not shown).

A severe underprediction of the large particle size classes can be observed as well as an overprediction of the middle size classes. An immediate drop of the lower size classes occurs, which might be explained by the low amount of breakage events producing these flocs and high α-values. Since many new expressions have been inserted in the different kernels, it is difficult to extract from the model prediction which kernel feature is responsible for this rather strange behaviour. To extract this, a more step-wise approach of kernel implementation should be followed starting from an easy structure that is relatively well understood.

8.8 Conclusions

This study tried to fit a PBM with different literature-reported kernels for aggregation and breakage reported in literature to on-line experimental activated sludge flocculation data. Model 1 resulted in severe underpredictions of large size classes, overpredictions of middle size classes and underprediction of primary particles when using a least squares model fitting procedure. The model performance could be improved significantly by lowering the power (a) of the breakage frequency. Unfortunately, the optimal value of a is difficult to obtain due to practical identifiability problems. Model 2 showed that introducing the fractal dimension Df has an effect similar to the lowering of the power (a) of the breakage frequency. It is, in principle, thought to be a better approach since activated sludge flocs are known to have a fractal structure. However, in terms of fitting performance, model 1 with a=1/9 performed better. Probably, Df is not a fixed value over the entire size range. Model 3 also severely underpredicted the large size classes, overpredicted the middle size classes and underpredicted primary particles. Despite the fact that the knowledge introduced with model 3 seems logical, it seems to have a contradictory effect on the

Table 8.4: Summary of fitting results and 95% confidence intervals for model 3

$\bar{G}\,s^{-1}$	α_0 (-)	A $\left(m^{-1}s^{-1}\right)$	$J\,(\theta)$
19.4	8.53 ± 0.21	1842 ± 119	$7.73.10^{18}$
37.0	6.17 ± 0.25	2922 ± 178	$9.09.10^{18}$

Table 8.5: Summary of fitting results and 95% confidence intervals for model 4 (n.a. means low parameter confidence due to ill-conditioned covariance matrix)

$\bar{G}\, s^{-1}$	α_0 (-)	C1 (-)	$J(\theta)$
19.4	$0.74 \pm n.a.$	$3.7E-8 \pm n.a.$	$8.44.10^{18}$
37.0	$0.85 \pm n.a.$	$1.35E-7 \pm n.a.$	$1.53.10^{19}$

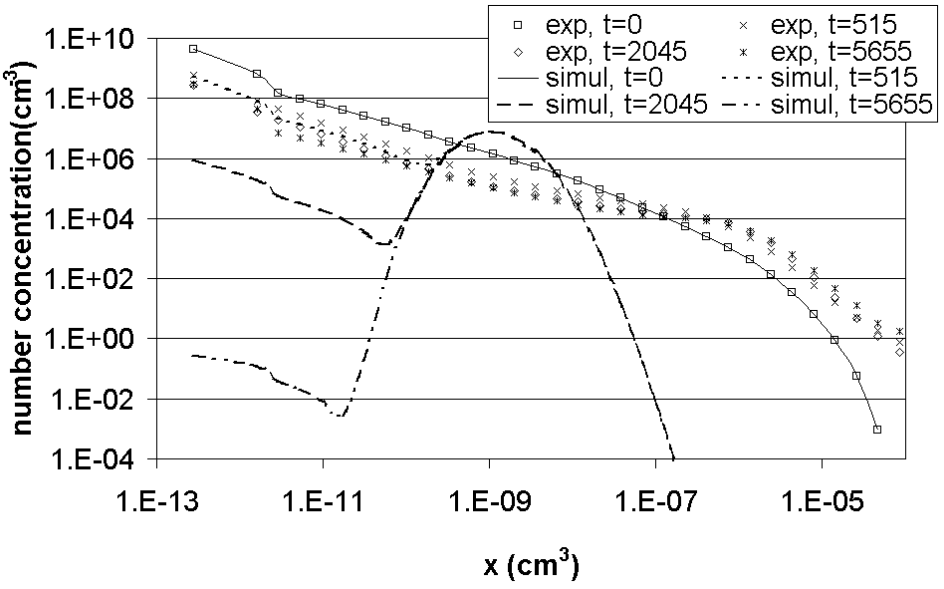

Figure 8.8: Best fit simulation results for $\bar{G} = 19.4\, s^{-1}$using model 4

simulation results and requires higher collision frequencies. These might be obtained by introducing Df to replace the exponent in the aggregation kernel. Model 4 resulted in poor predictions. The exact reason for this should be further investigated.

To conclude, none of the tested models using existing kernels from literature was able to predict the evolution of the number distribution accurately. However, the performed study allows to track the weaknesses of the kernels with regard to the experimental data and improve them with this knowledge. Consequently, further work is needed and in the next chapter an alternative approach to find better kernel structures is adopted in which the inverse problem is solved and possible self-similarity behaviour of the experimental data is exploited (Wright and Ramkrishna, 1992; Sathyagal et al., 1995). Another path to be investigated is to step down from the approach with binary breakage into equally sized daughter particles and use a more realistic daughter size distribution.

CHAPTER 9

Similarity analysis of experimental flocculation data

An alternative way to get a grip on the different kernel structures for aggregation and breakage is through solving the inverse problem, which is schematically given in Fig. 9.1. The first step checks whether the experimental data exhibit self-similar behaviour, as this simplifies the solution of the inverse problem considerably and will be investigated in this chapter. All other steps will be dealt with in the chapter 11.

9.1 Investigation of self-similarity of experimental data

This section is organised as follows. First self-similar behaviour was sought for the experiments where the activated sludge was sonicated and then allowed to flocculate at different shear intensities. Then, self-similar behaviour of the experimental data set where alternating shear intensities were applied is investigated.

9.1.1 Sonicated sludge flocculated at different shear intensities

In order to investigate self-similar behaviour of an experimental data set, a similarity analysis needs to be conducted. Different similarity analysis procedures exist for pure aggregation, pure breakage and the combined case. The thorough analysis of the distribution data set in section 6.1.1 allows to conclude that pure aggregation is a valid assumption and, hence, the similarity analysis for pure aggregation can be investigated. This again proves the usefulness of the thorough analysis of the distributions performed in chapter 6. The idea behind the similarity analysis is to look for a collapsing solution in the dynamic part of the experimental data as explained below.

Practically, this means that a scaling function $\mathrm{h(t)}$ given by the ratio of two successive integral moments

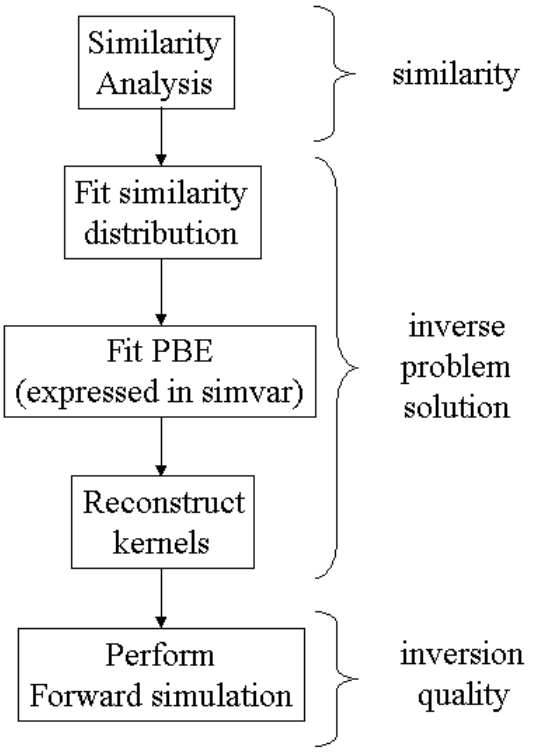

Figure 9.1: Schematic overview of the steps related to the inverse problem solution

μ of the number density function $\mathrm{f_1(x,t)}$

$$h(t) = \frac{\mu_{k+1}(t)}{\mu_k(t)} = \frac{\int_0^\infty x^{k+1} f_1(x,t)dx}{\int_0^\infty x^k f_1(x,t)dx} \tag{9.1}$$

is computed and used to rescale the particle volume into the similarity variable

$$\eta \equiv \frac{x}{h(t)} \tag{9.2}$$

Since the cumulative distribution F(x,t) is itself a candidate for the self-similar solution, this distribution is rescaled and a k-value is looked for that makes all distributions collapse onto one single distribution, the self-similar distribution. The process of determining k proceeds through trial and error.

The initial evolution of the cumulative distribution is given in Fig. 9.2 (note that the first measurements have been omitted). From Fig. 9.2, it can be clearly observed that the floc size distribution is evolving in time toward a larger size range. Fig. 9.3 is directly derived from Fig. 9.2 by determining the values of x as a function of time for different fixed values of F. Through rescaling x to the similarity variable η, it is tried to obtain lines that are parallel to the time axis. This means that every fixed value of F corresponds to a value of the similarity variable η. When choosing a k-value of 0 in Eq. 9.1, the similarity variable versus time plot at fixed F values becomes like Fig. 9.4. From Fig. 9.4, it can be seen that the evolutions are not parallel with the time axis. Hence, this k-value will also not give rise to a collapsed cumulative distribution as is confirmed in Fig. 9.5, which shows the rescaled cumulative

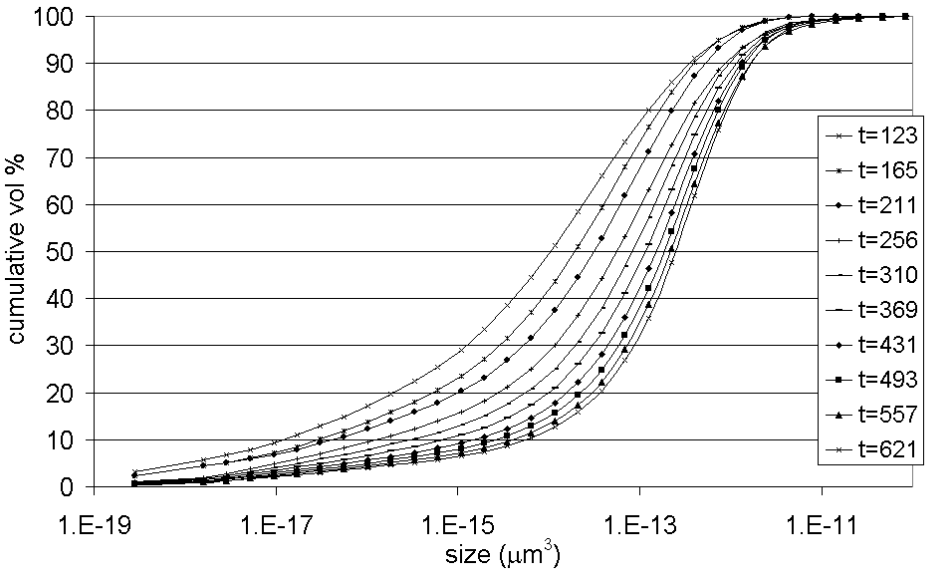

Figure 9.2: Time evolution of the cumulative distribution for the flocculation experiment at a shear intensity of $\bar{\mathrm{G}} = 19.4\,\mathrm{s}^{-1}$

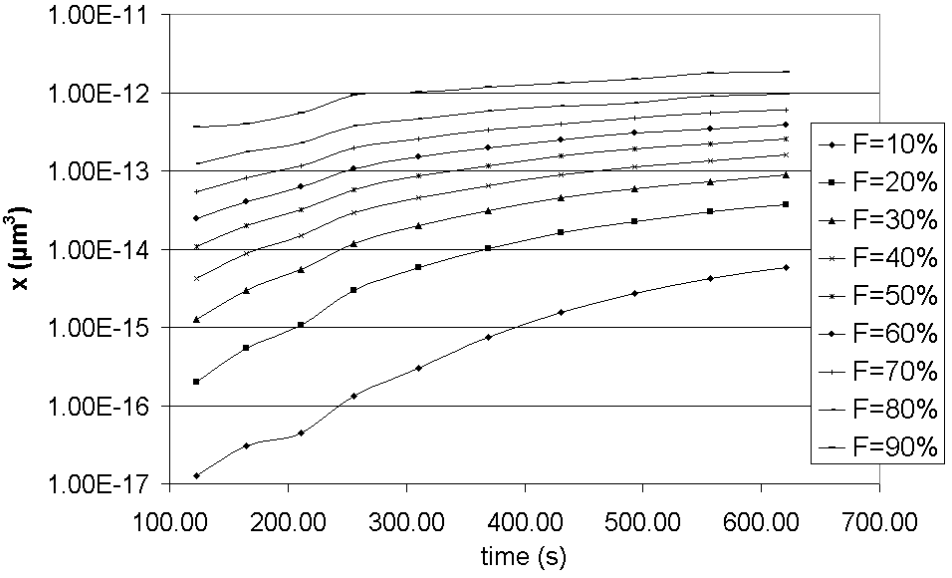

Figure 9.3: Volume x versus time for different fixed values of F

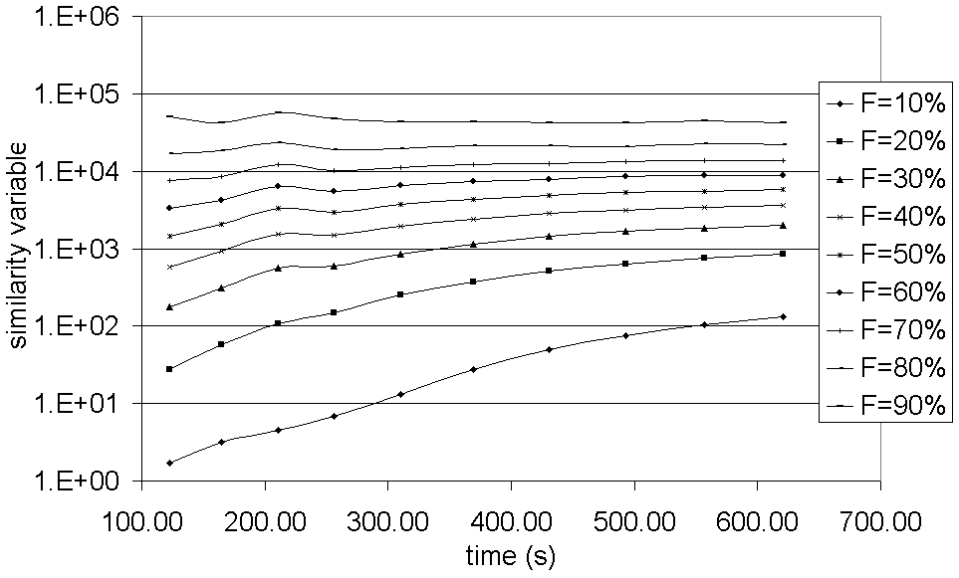

Figure 9.4: Similarity variable η versus time for different fixed values of F for k=0

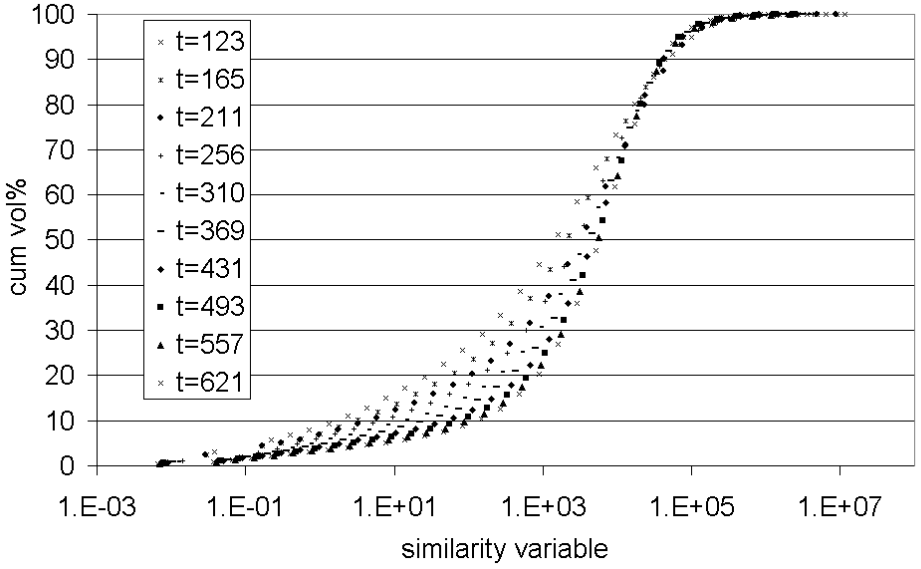

Figure 9.5: Cumulative distributions versus the similarity variable η for k=0

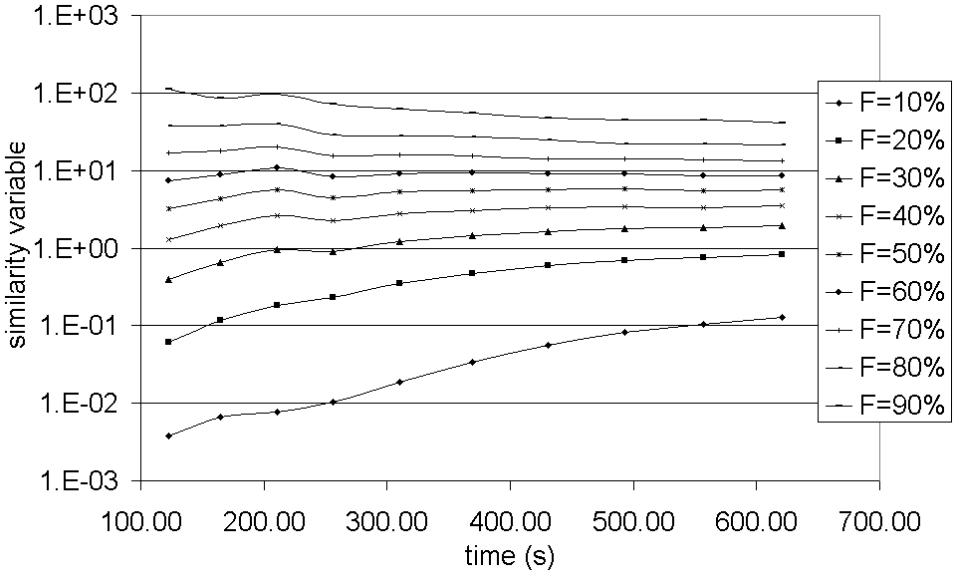

Figure 9.6: Similarity variable η versus time for different fixed values of F for k=0.534

distributions. However, when comparing Fig. 9.2 and 9.5, one can observe a decrease in variance between the cumulative distributions in time, obviously caused by the rescaling that was performed. So, it might be that a value of k exists that will make all distributions collapse.

In order to find this k-value for which the cumulative distributions collapse (if it exists), a trial and error procedure is required. Alternatively, it can be tried to solve this problem mathematically through minimisation of the variance of all similarity variables (one for each fixed value of F) at the different fixed values of F. In order to do so, one could sum all similarity variable variances and minimise this sum. However, since the absolute values of the similarity variables vary quite a lot, it is better to rescale all similarity variable distributions to not favour any of the variances to be minimised. This can be done by subtracting the mean and dividing through the mean. Let Y be the similarity variable at a given fixed value of F. This can be rescaled to Y' as follows

$$Y' = \frac{Y - \mu(Y)}{\mu(Y)} \tag{9.3}$$

Y' will now be distributed about a mean of 0 and exhibit a certain variance $\sigma^2(\mathrm{Y}')$. One can now minimise the sum of these variances by allowing k to alter.

Doing so results in an *optimal* k-value of 0.534. It was confirmed by trial and error that this is indeed the optimal value. The similarity variable versus time plot and the cumaltive distributions as function of the similarity variable are depicted in Fig. 9.6 and 9.7 respectively. From Fig. 9.6 and 9.7, it can be observed that still quite a lot of variance in the similarity variables at fixed F-values is left and, hence, that no true collapse of the cumulative distributions occurs. This means that the data set does not exhibit this kind of similarity.

Similar observations were found for the data sets obtained at other shear intensities.

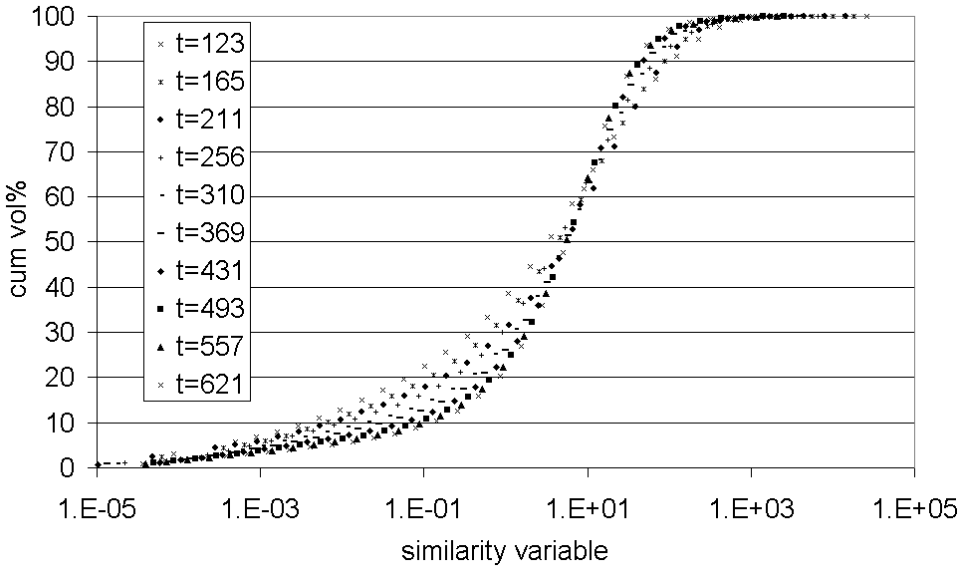

Figure 9.7: Cumulative distributions versus the similarity variable η for k=0.534

9.1.2 Non-sonicated sludge at alternating shear intensities

Analogous similarity analyses were performed for the experiment where alternating shear intensities were applied. It should be noted that the main difference with the previously investigated experiments is the fact that the sludge does not flocculate from an initially sonicated sludge, but rather from a sludge that was deflocculated through increased shear intensity. Also, the alternating nature of the experiment allows to investigate the flocculation or purely aggregation part, as well the deflocculation or the purely breakage part. Again, the thorough analysis of section 6.1.2 supports the assumption of both pure aggregation and pure breakage, which is a necessary requirement. For reasons of clarity, first aggregation is investigated.

Flocculation by means of decreased shear intensity

The experimental data set that is investigated here is taken from the experiment where the sludge was alternatingly exposed to different shear intensities. Moreover, the subset was taken when the sludge was exposed to a lowered shear intensity ($\bar{\mathrm{G}} = 19.4\,\mathrm{s}^{-1}$) for the second time, meaning it flocculated from a non-sonicated state, which is more realistic.

The initial evolution of the cumulative distribution is given in Fig. 9.8 (note that the first measurements have been omitted).

From Fig. 9.8 it can be observed that the initial distribution is situated at larger sizes compared to the one obtained after sonication (Fig. 9.2). Again, only the initial dynamic distributions are taken into account since only for these pure aggregation can be assumed, and, hence, a pure aggregation similarity analysis applied. The optimal k-value was found to be -0.35 and the rescaled cumulative distributions are given in Fig. 9.9, showing a nice collapse of all distributions. Hence, for this particular case, a similarity distribution is found, which is shown in Fig. 9.10.

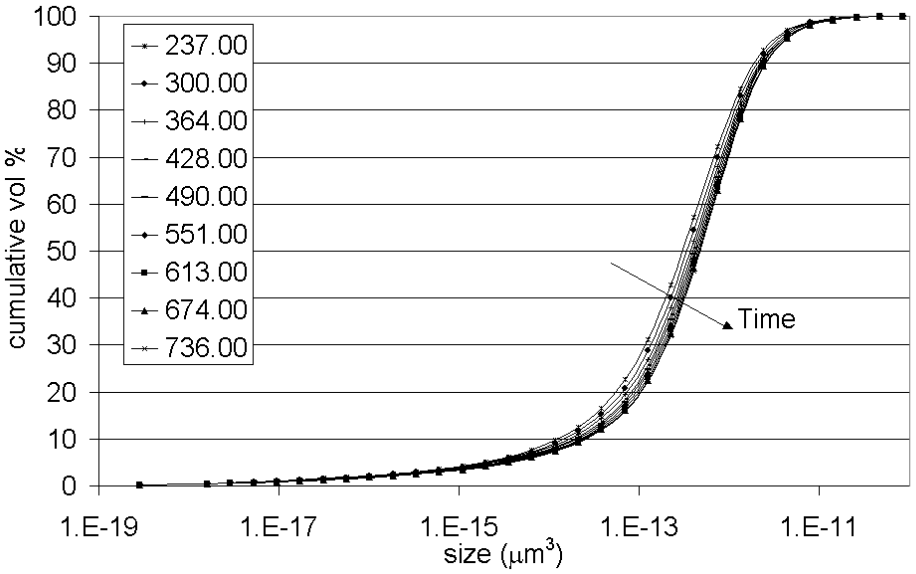

Figure 9.8: Time evolution of the cumulative distribution for the flocculation experiment at a shear intensity of $\bar{\mathrm{G}} = 19.4\,\mathrm{s}^{-1}$ starting from a deflocculated sludge through increased shear intensity

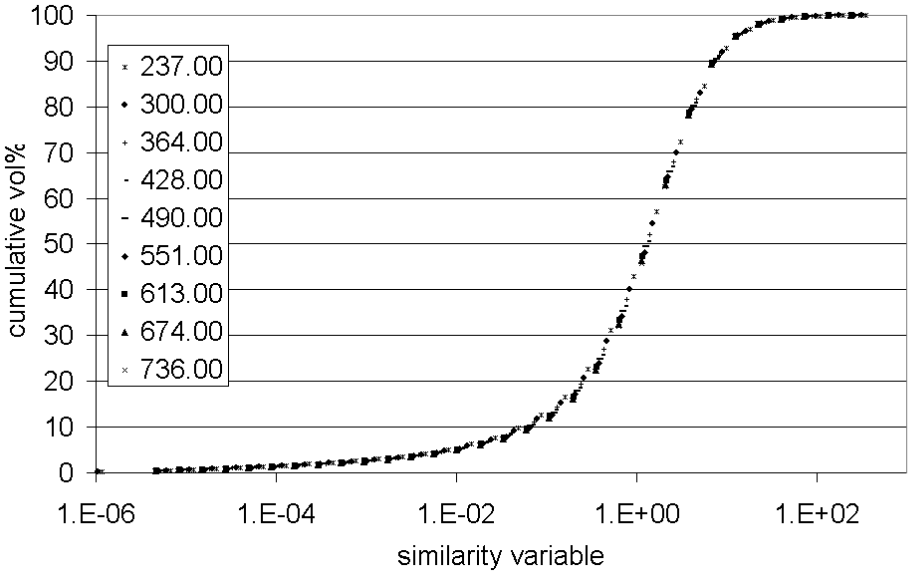

Figure 9.9: Cumulative distributions versus the similarity variable η for k=-0.35

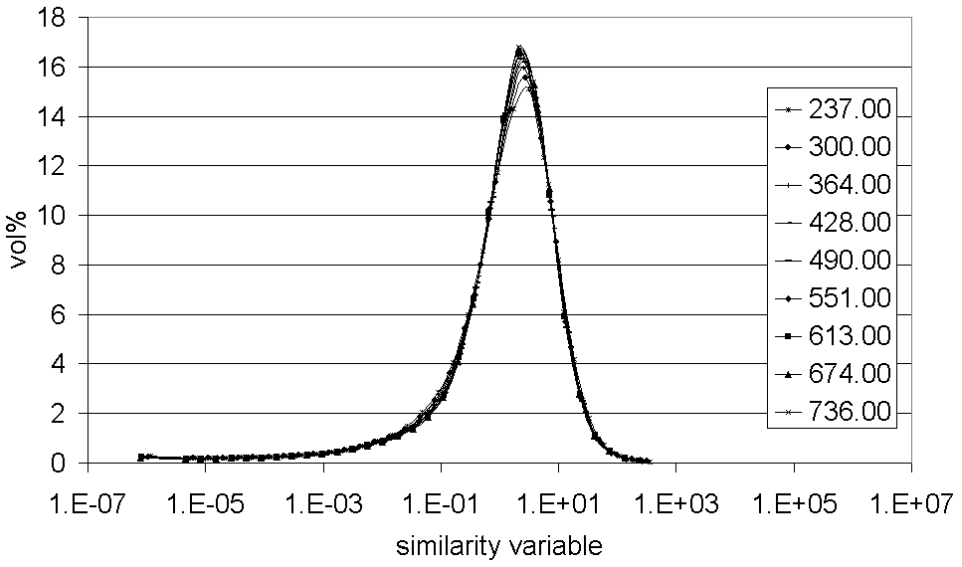

Figure 9.10: Floc size distributions versus the similarity variable η for k=-0.35

In the same experiment, another increase and decrease of shear intensity was performed. For the subset where the shear intensity was decreased again, a similarity distribution was found too (k=-0.3).

The fact that this similarity did not exist for the case where sonication was applied prior to flocculation suggests that a different kind of aggregation is taking place. Since sonication does not occur in the real activated sludge process, it can be concluded that lab experiments studying flocculation starting from a sonicated sludge will not lead to the extraction of the correct flocculation behaviour (i.e. aggregation kernel), and the results obtained cannot be extrapolated to the full-scale case.

Deflocculation by means of increased shear intensity

In this subsection, the parts of the experiment where the shear intensity was increased, are studied. In these cases, the initial evolution of the distribution can be assumed to be caused by pure breakage. Here, a somewhat different similarity analysis, the one for pure breakage, is performed.

Fig. 9.11 shows the initial evolution of the cumulative distributions. It can be observed that a shift towards smaller floc size takes place. The idea is now to look for a proper transformation that makes these curves collapse onto 1 single distribution, the self-similar distribution.

Unlike the aggregation counterpart, the similarity variable cannot be calculated directly from x like in eq. 9.2. Instead, it was shown in literature (Sathyagal et al., 1995) that the transformation $\eta = \mathrm{b(x)t}$ leads to the similarity curve for a variety of functions $\mathrm{b(x)}$ (which are not restricted to power laws only). Although this transformation seems to be impossible due to the fact that $\mathrm{b(x)}$ is unknown, an alternative test has been developed that allows to check for this type of similarity. The latter was described in section 2.5.6. For convenience, the equation that provides the test of the similarity hypothesis is repeated here

$$\frac{d\,ln\,b(x)}{d\,ln\,x} = -\left(\frac{\partial\,ln\,t}{\partial\,ln\,x}\right)_F \tag{9.4}$$

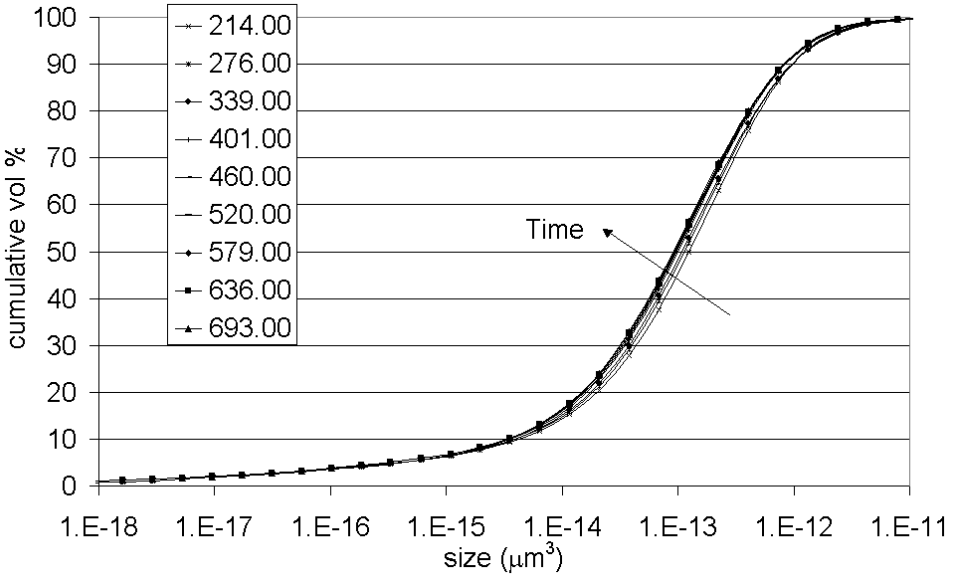

Figure 9.11: Time evolution of the cumulative distribution for the flocculation experiment at a shear intensity of $\bar{\mathrm{G}} = 113\,\mathrm{s}^{-1}$ starting from a flocculated sludge through decreased shear intensity

The test lies in checking that the right-hand-side is independent of F.

The plot of ln(x) versus ln(t) at fixed values of F for the experimental data set is given in Fig. 9.12. In order to confirm the hypothesis, these curves should exhibit the same slopes for the same x-values and different values of F. Several methods have been mentioned in literature that investigate this 'same slope' behaviour. Since the ranges of $\ln(\mathrm{x})$ do not significantly overlap for different fixed values of F, a translation parallel to the $\ln(\mathrm{t})$-axis would not result in a clear conclusion. Instead, curves were fitted to the different data sets (for fixed F-values) and the slopes were plotted as function of $\ln(\mathrm{x})$ (Fig. 9.13). The latter reveals that the slope remains rather constant at a value of about -3.7 over a quite large range of $\ln(\mathrm{x})$. The deviations might be due to measurement errors. This result confirms the similarity hypothesis and, hence, the expression of the breakage rate can be determined up to a constant ($\mathrm{b}(\mathrm{x}_0)$) using the following equation

$$b(x) = b(x_0) exp\left[- \int_{ln\, x_0}^{ln\, x} \left(\frac{\partial\, ln\, t}{\partial\, ln\, x} \right)_{F_1} d\, ln\, x \right] \tag{9.5}$$

and substituting the partial derivative in the right-hand-side by the value of -3.7 that was extracted from the experimental data. Since $\mathrm{b}(\mathrm{x}_0)$ is unknown, the similarity variable is calculated as $\mathrm{b}(\mathrm{x})\,\mathrm{t}/\mathrm{b}(\mathrm{x}_0)$ and used to transform the cumulative distributions. Results of this transformation are shown in Fig. 9.14 for the cumulative distributions and in Fig. 9.15 for the distributions as such.

It can be observed that all distributions collapse onto one single curve, the similarity distribution. The remaining constant in the breakage rate expression and the daughter size distribution now have to be found by solving the inverse problem.

For the second breakage case in this experiment, similar observations were made and a similar value of the power law exponent resulted.

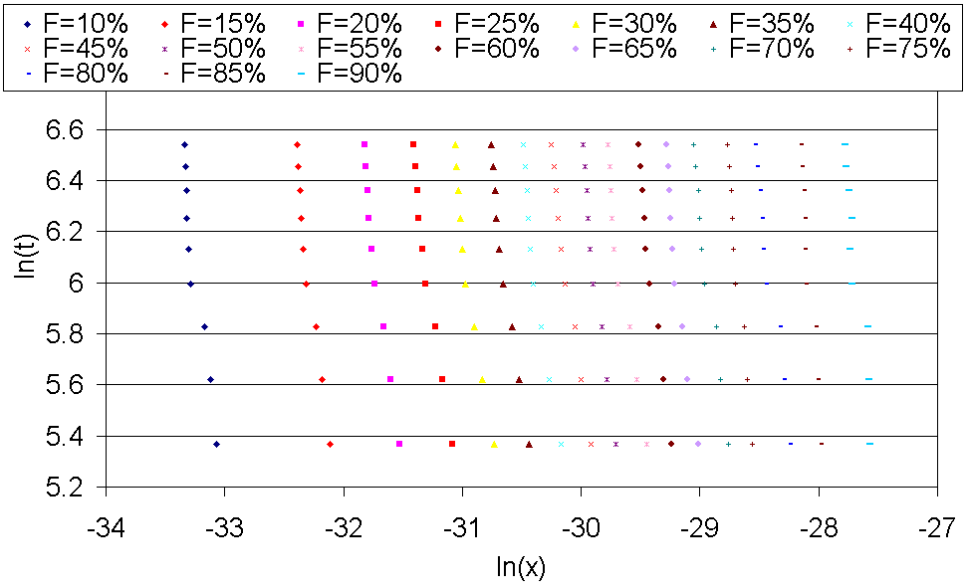

Figure 9.12: Ln(x) versus ln(t) for different fixed values of F

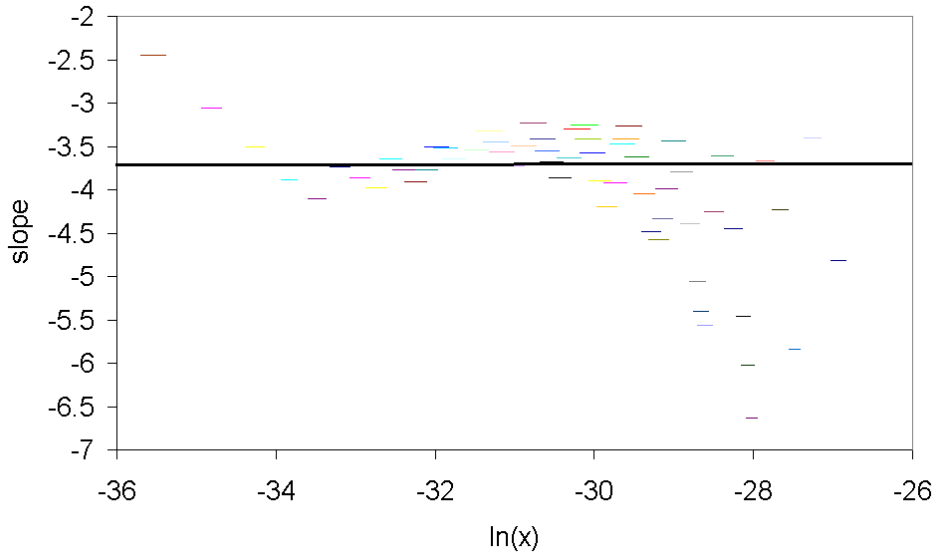

Figure 9.13: Slopes versus ln(x) for different fixed values of F

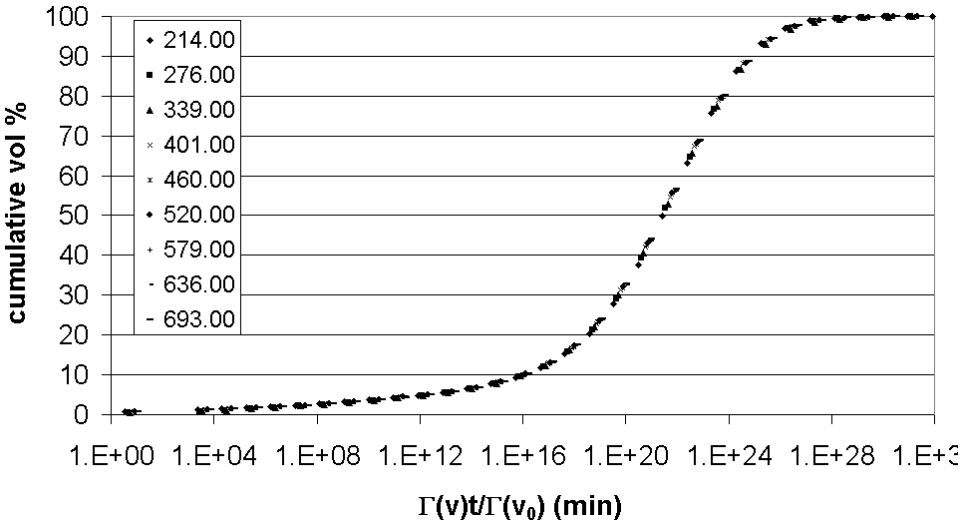

Figure 9.14: Cumulative distributions versus similarity variable $\mathrm{b(x)\,t/b(x_0)}$

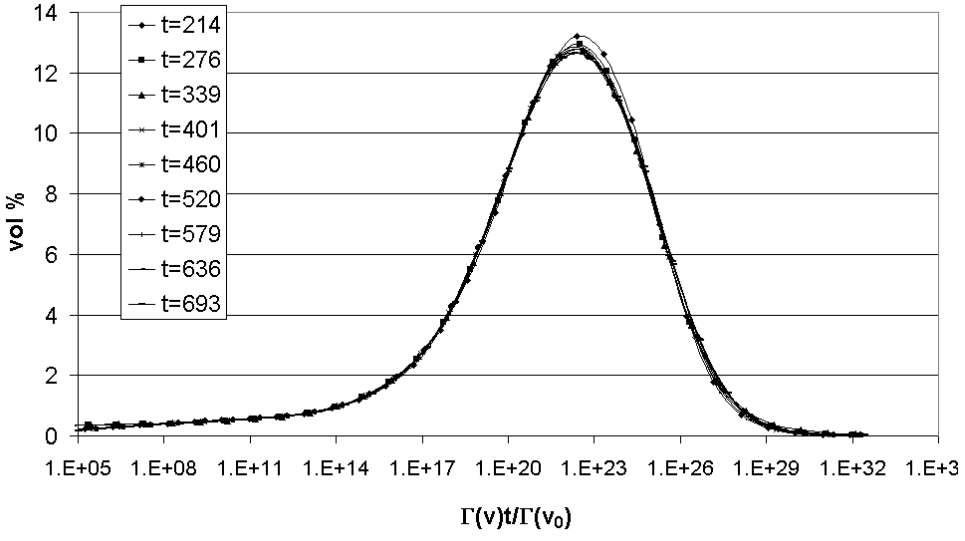

Figure 9.15: Floc size distributions versus similarity variable $\mathrm{b(x)\,t/b(x_0)}$

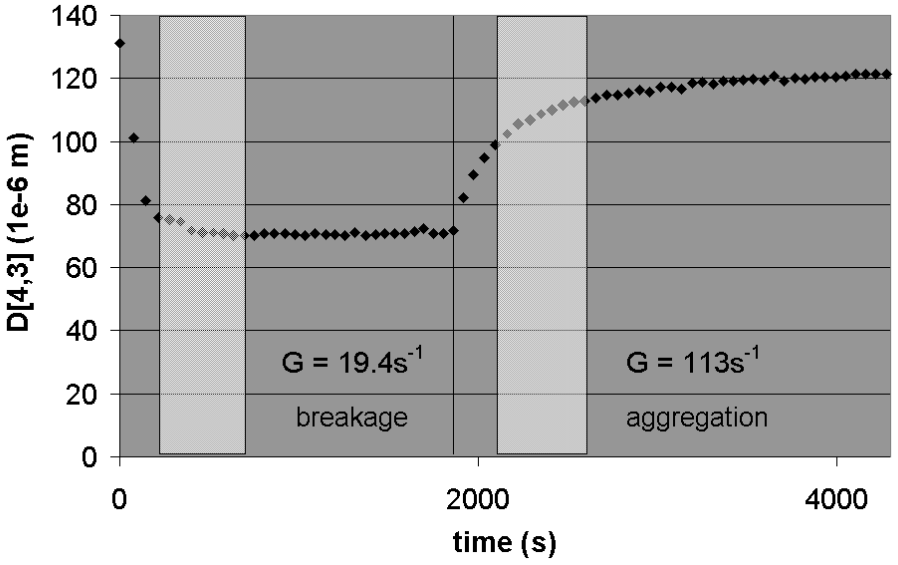

Figure 9.16: Similarity regions that were identified for aggregation and breakage

9.2 Conclusions

In this chapter, experimental data of pure aggregation and pure breakage were checked for self-similar behaviour using techniques reported in literature. The necessary requirements for applicability of these techniques, i.e. that indeed pure aggregation and pure breakage are occurring, could be recovered from the thorough distribution analysis performed in chapter 6.

Experimental aggregation data obtained from a sonicated sludge did not exhibit self-similar behaviour. However, experimental aggregation data from a sludge that was exposed to increased shear did exhibit self-similar behaviour. This confirms the conclusion drawn in chapter 6 stating that the aggregation dynamics induced by sonication are different from those induced by increased shear. The goal of this work was to develop a model that is able to describe activated sludge flocculation as it is occurring in a full-scale treatment plant. Since sonication is not applied there, the dynamics induced by applying it are not of interest to us. Hence, the experimental data used in chapter 8 will no longer be used. Instead, focus should be on the aggregation data obtained without sonication. Therefore, the literature models that were applied in chapter 8, and that were not designed for this type of flocculation, need to be tested using the experimental data without sonication. This will be the subject of the next chapter.

The self-similarity for aggregation was obtained by scaling the particle volume by a function h(t) representing the ratio of two consecutive integral moments, i.e. -0.35 and 0.65. The solution of the inverse problem using the observed self-similarity will be treated in chapter 11.

Although the slopes of ln(t)/ln(v) did not overlap for all fixed values of F, the dynamic experimental breakage distrbutions collapsed when assuming a fixed value for the slope (i.e. -3.7). In the breakage case, a collapse means that the breakage rate can be determined up to a constant. Hence, power law behaviour was found with an exponent of 3.7. Also for this case the solution of the inverse problem using the observed self-similarity will be treated in chapter 11.

For convenience, Fig. 9.16 indicates the regions where similarity was observed for aggregation and breakage respectively. These will be used in chapter refinverse.

CHAPTER 10

Model calibration of non-sonicated reflocculation data

10.1 Introduction

In chapter 8, several models taken from literature were fitted to experimental aggregation datasets of Biggs and Lant (2000). In the previous chapter, in which the similarity of these experimental data was investigated, it was found that the flocculation behaviour in the 'sonication' experiments studied in chapter 8 is different from the flocculation which is observed when a sludge is exposed to a lower degree of shear after a period of high shear. It was concluded that the sonication experiments do not contain the flocculation dynamics that is looked for in this dissertation, i.e. flocculation representative for full-scale treatment plants where zones with different shear rates exist. Therefore, the sonication experiments are discarded and the remainder of the work will focus on the experimental data where flocculation was brought about by a decrease in shear. In this chapter, it will be investigated whether the literature models from chapter 8, that failed for the sonicated experimental data, could possibly describe the data where no sonication was applied.

10.2 Model calibration using non-sonicated experimental data

The model equation and kernel structures are the same as those defined in section 4.2 and will not be explicitly repeated here.

The experimental data set used here combines an aggregation and breakage event, brought about by varying the average velocity gradient as $19.4\,\mathrm{s}^{-1} \rightarrow 113\,\mathrm{s}^{-1} \rightarrow 19.4\,\mathrm{s}^{-1}$. This experiment was described in section 6.1.2. It was opted to use an experiment that sequentially induces aggregation and breakage as it should contain more information about both the aggregation and breakage mechanisms and, hence, allow

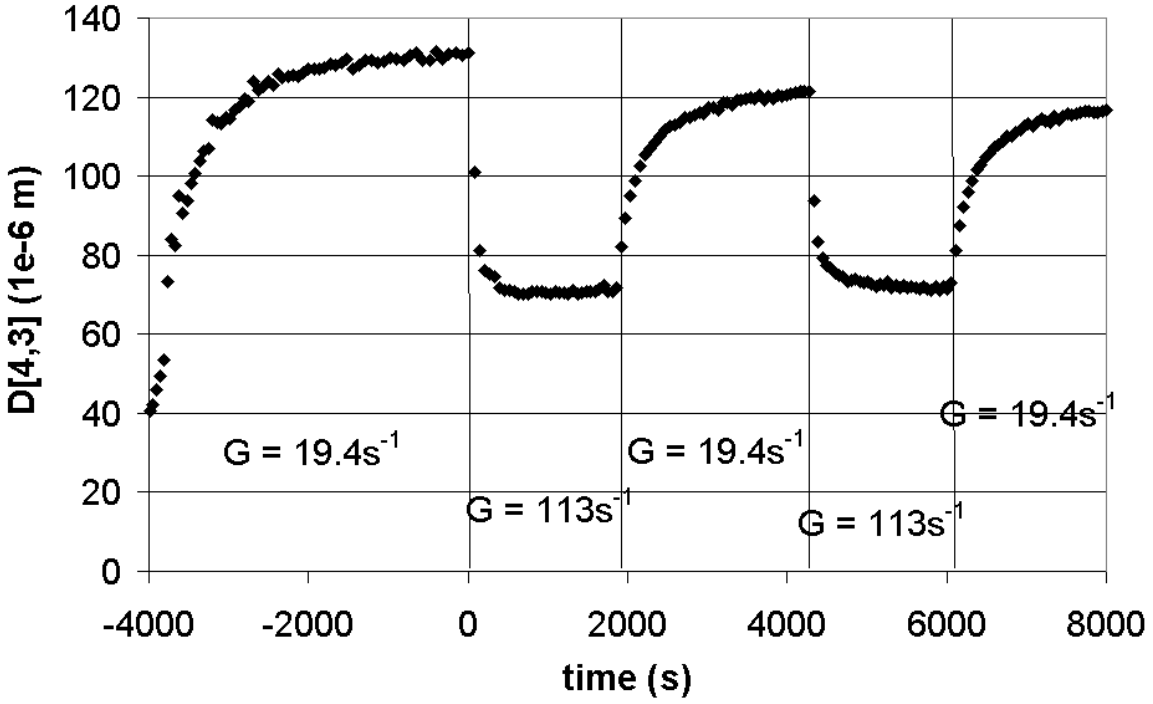

Figure 10.1: Time evolutions of D[4,3] for the experiment with step changes in average shear rate

more accurate parameter predictions. The part from 0 to 4000 s (i.e. one breakage and one aggregation event) was used for parameter estimation. The changes in the average velocity gradient can easily be included in the MSL-code (WEST, Hemmis NV, Kortrijk) by means of a simple if-clause.

First, it was tried to optimise the model by varying one aggregation parameter, i.e. α, and one breakage parameter, i.e. A. However, no acceptable results were found, as the optimal values proposed by the optimisation algorithm changed every time other initial parameter values were adopted. This points to major identifiability problems. Moreover, very large or even negative parameter variances were observed, making the estimation results very doubtful. Before proceeding with other, more complicated models, it was, therefore, decided to investigate the whereabouts of this behaviour. For this, another tool in WEST (Hemmis NV, Kortrijk) proved to be useful, i.e. scenario analysis.

10.3 Scenario analysis for investigation of the parameter space

Scenario analysis is a tool available in WEST that is usually applied to investigate different scenario's of a system, described by a calibrated model, and determine the most optimal one. Every scenario is different in some parameter values and/or initial states. All simulations are performed sequentially without any need for user interaction.

In our case, the tool will be applied with a somewhat different goal. Every 'scenario' represents a combination of parameters α and A, and, hence, one point in the parameter space. In this way, simulations can be performed in all regions of the parameter space. By calculating the sum of squared errors (SSE)

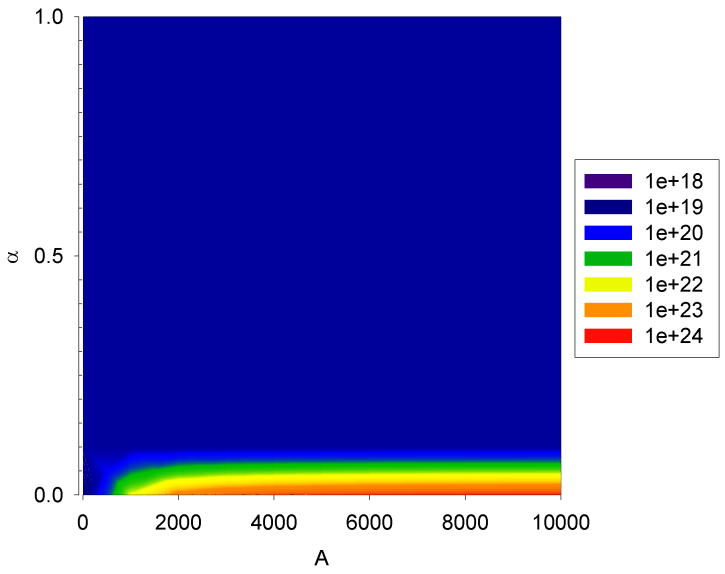

Figure 10.2: Contour plot of the SSE for a wide scan of the parameter space

between simulated data and experimental data, a contour plot can be created that shows where the minimum is located. In order to proceed with the scenario analysis, the parameter space should be discretised in a grid. The coarseness of the grid will determine the number of simulations to be performed. In a first run, a rough discretisation of both parameters was chosen:

- α: 0, 0.1, 0.2, 0.3, 0.4, 0.5, 0.6, 0.7, 0.8, 0.9, 1
- A: 0, 1000, 2000, 3000, 4000, 5000, 6000, 7000, 8000, 9000, 10000

This results in 121 combinations and, hence, an equal number of simulations. The SSE for all parameter combinations were calculated and resulted in a contour plot of the objective function as shown in Fig. 10.2.

It can be observed that most of the parameter space has similar SSE values, which explains why the optimisation algorithm

1. failed to find the global minimum value of the objective function
2. ended up at different 'optimum' parameter combinations for different initial conditions

The worst parameter combinations are those of small α (0-0.1) and moderate to large A (1000-10000). The smallest SSE of the 121 simulations that were performed by the scenario analysis is located in (0,0). Therefore, the region around the origin was investigated with a second scenario analysis using the following, much finer grid in the region of interest:

- α: 0, 0.02, 0.04, 0.06, 0.08
- A: 0, 200, 400, 600, 800

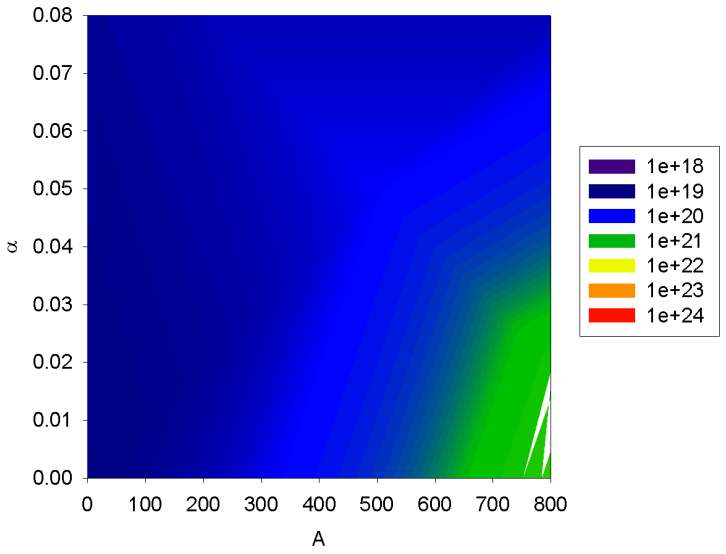

Figure 10.3: Contour plot of the SSE for a focused scan of the parameter space around the origin

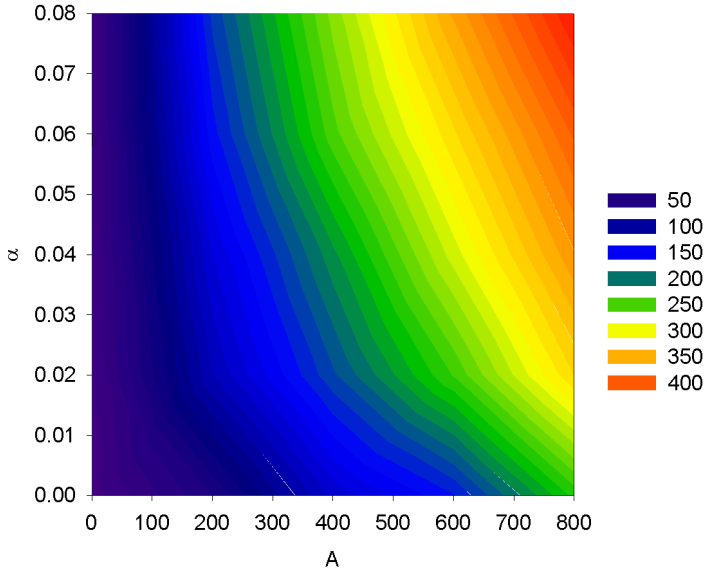

Figure 10.4: Contour plot of the simulation times for parameter combinations around the origin

The resulting contour plot is shown in Fig. 10.3.

Fig. 10.3 reveals the same result as was found in the first scenario analysis run. The minimum is found in the origin. At first sight, this does not make much sense since it means that the best model prediction for the dynamic experimental data is one in which no dynamics occur. This result confirms the conclusion of chapter 8 saying that the model structure (either the aggregation part, the breakage part, or both) is wrong. Only, the method does not tell us where the structural error is located. Since the approach to find an adequate model structure as illustrated here is rather time-consuming and it does not allow us to pin-point the exact problem, it was not further pursued for the other models investigated in chapter 8. They were expected to yield similar results and conclusions.

An interesting observation during the scenario analysis was that the necessary calculation time also varies in the parameter space. One would expect larger simulation times when more dynamics are present in the model or, in other words, when the parameters α and A are large. These large dynamics force the simulation algorithm to decrease its step size substantially, resulting in larger calculation times. This was confirmed by the scenario analysis as shown in Fig. 10.4.

10.4 Conclusions

It was investigated whether the literature models could be calibrated using the experimental data without sonication. However, optimisation resulted in very poor parameter estimates in terms of estimation error. Moreover, the results were not unique since choosing other initial conditions resulted in different optimal parameter estimates. Hence, a clear identifiability problem occurs, even for such simple model structure as evaluated here, i.e. model 1 of chapter 8.

The problem was further investigated by means of scenario analysis, in which simulations at different points in the discretised parameter space were conducted. This revealed that the parameter space does not exhibit a clear minimum, except from that in the origin. However, this minimum suggests that dynamic data would be best described without dynamics in the model, which does not make much sense. This confirms that something is wrong in the model structure, although it cannot be pinpointed in which part of the model the structural error is situated (aggregation, breakage or both). Since the method is rather time consuming, the fitting of the other literature models was not pursued as they were expected to yield similar results.

CHAPTER 11

Solving the inverse problem for aggregation and breakage in activated sludge flocculation

An alternative way to get a grip on the different kernel structures for aggregation and breakage is through solving the inverse problem. The theoretical background to this approach was introduced in 2.5.6 and will not be repeated here. In chapter 9, it was shown that some of the experimental data exhibits self-similar behaviour, which simplifies the solution of the inverse problem considerably. First the pure aggregation case will be investigated, followed by the pure breakage case.

11.1 Solving the inverse aggregation problem

In chapter 9, it was demonstrated that a transformation of the dynamic experimental data into a similarity distribution was possible for the case in which aggregation was initiated from a sludge broken up by increased shear. This presence of similarity can now be used to recover the aggregation kernel from the experimental data. The cumulative vol% versus the similarity variable η for the experimental case that will be used here is given in Fig. 9.9. The region for which similarity was found is indicated in Fig. 9.16. Before actually performing the inversion, the procedure will be elaborated in a bit more detail.

11.1.1 Procedure for inversion of pure aggregation data with self-similar behaviour

The PBE expressed as function of the similarity variable η forms the basis of this exercise. It is reproduced below for convenience.

$$\eta\Phi'(\eta) = \int_0^{\eta} d\eta' \Phi'(\eta') \int_{\eta-\eta'}^{\infty} d\eta'' \frac{\Phi'(\eta'')}{\eta''} \frac{\alpha(\eta', \eta'')}{\langle\alpha\rangle} \tag{11.1}$$

Here, $\frac{\alpha(\eta',\eta'')}{\langle\alpha\rangle}$ is the unknown function that needs to be reconstructed. It represents the scaled aggregation frequency divided by the mean scaled aggregation frequency.

A first issue that should be raised is the fact that eq. 11.1 may be ill-posed, i.e. small uncertainties in $\Phi'(\eta)$ may induce large differences in the extracted $\alpha(\eta',\eta'')$. This can be overcome by using a technique called *Thikonov regularisation* during the inversion process. This can be best understood as follows. Let

$$g = Kb \tag{11.2}$$

be the operator notation of eq. 11.1, where g is the vector representing the left-hand side, b is the unknown vector representing the scaled aggregation frequency $\alpha(\eta',\eta'')$ and K is an integral operator which acts on b. Regularisation is used in the objective function that determines b from this equation, i.e.

$$min \left\|Kb - g\right\|^2 + \lambda_{reg} \left\|b\right\|^2 \tag{11.3}$$

The physical interpretation of regularisation can be explained as follows. As the error in the estimates of g and K increases, the regularisation parameter λ_{reg} must increase. As λ_{reg} increases, the minimisation technique effectively finds solutions b that have smaller norms and, hence, possess smaller fluctuations and are smoother functions.

At this moment, the constrained quadratic minimisation problem can be formulated. The similarity coordinate is discretised into a set of $\{\eta_{\mathrm{i}}\}$ and $\alpha(\eta',\eta'')$ is expanded in terms of basis functions

$$\frac{\alpha(\eta',\eta'')}{\langle\alpha\rangle} = \sum_{j=1}^{n_b} a_j A_j(\eta',\eta'') \tag{11.4}$$

A matrix $\mathrm{X_{i,j}}$ is formulated

$$X_{ij} = \int_0^{\eta_i} d\eta' \Phi'(\eta') \int_{\eta_i-\eta'}^{\infty} d\eta'' \frac{\Phi'(\eta'')}{\eta''} A_j(\eta',\eta'') \tag{11.5}$$

and eq. 11.3 can be rewritten as

$$a^T X^T X a - 2a^T X^T g - g^T g + a^T \lambda_{reg} D a \tag{11.6}$$

which results in the following quadratic minimisation

$$min \ \left(a^T \left(X^T X + \lambda_{reg} D\right) a - 2a^T X^T g\right) \tag{11.7}$$

to obtain the unknown vector a.

The constraints that are used are physical constraints derived from the definition of the aggregation frequency:

1. the aggregation frequency is a symmetric function of its arguments
2. the aggregation frequency is positive everywhere

With regard to the choice of the discretisation points $\{\eta_{\mathrm{i}}\}$, Wright and Ramkrishna (1992) showed that known similarity distributions (of different aggregation frequencies) exhibit the largest variance at small values of the similarity variable η. Hence, a good choice of the discretisation points might be a logarithmic grid from $\eta_{\min}$ to $\eta_{\max}$.

Table 11.1: Structure of the first four Laguerre polynomials

n	$\mathrm{L_n(x)}$
0	1
1	-x+1
2	$\frac{1}{2}\left(\mathrm{x}^2 - 4\mathrm{x} + 2\right)$
3	$\frac{1}{6}\left(-\mathrm{x}^3 + 9\mathrm{x}^2 - 18\mathrm{x} + 6\right)$

An interesting set of basis functions that can be used for this kind of inversion problem are so-called *Laguerre polynomials*. The polynomials are orthonormal in the inner product space

$$\int_0^\infty dx\, e^{-x} \int_0^\infty dy\, e^{-y} f(x,y) g(x,y) \tag{11.8}$$

which means that the matrix D in eq. 11.7 does not need to be calculated. Laguerre polynomials are given by:

$$L_n(x) = \sum_{m=0}^{n} (-1)^m \frac{n!}{(n-m)!m!^2} x^m \tag{11.9}$$

The first four Laguerre polynomials are given in Table 11.1. Orthogonal functions of these polynomials are given by

$$l_n(x,y) = L_i(x) L_j(x) \tag{11.10}$$

where $\mathrm{n} = (\mathrm{i}-1)\mathrm{n_b} + \mathrm{j}$ and $\mathrm{n_b}$ is the number of basis function along one axis.

In order to simplify the matrix equations for the determination of a, as introduced above, a straightforward method is needed for the representation of the similarity distribution $\Phi'(\eta)$ (note that this is the derivative of the cumulative similarity distribution $\Phi(\eta)$). Other advantages of the fitting of the similarity curve lie in the limitation of experimental error and the guarantee that the similarity distribution is continuous. The mathematical expression that is fitted to the distribution should exhibit analogous qualitative and quantitative behaviour of the self similar distributions. A linear combination of γ-distributions exhibits that behaviour, since γ-distributions have the ability to be singular at the origin, but also can show small η-behaviour falling back toward the origin (two different types of behaviour that have been observed in similarity distributions of known aggregation kernels in practice). The expansion of the similarity distribution in terms of γ-distributions is:

$$\Phi'(\eta) = \sum_{k=1}^{n_{term}} A_k \eta^{\alpha_k - 1} exp(-\beta_k \eta) \tag{11.11}$$

where $\mathrm{n_{term}}$ is the number of γ-distributions used in the expansion and $\mathrm{A_k}$, α_k and β_k are parameters of the $\mathrm{k^{th}}\gamma$-distribution.

Since an analytical form is available for $\Phi'(\eta)$, certain simplifications of the matrix equations can be accomplished. Eq. 11.5 can be rewritten as

$$\bar{X}_{ij}(m) = \int_0^{\eta_m} d\eta' \Phi'(\eta') L_i(\eta') \bar{Y}_j(\eta_m - \eta') \tag{11.12}$$

where η_m is a point of discretisation and $\bar{\mathrm{Y}}_\mathrm{j}(\eta_\mathrm{m} - \eta')$ is defined by

$$\bar{Y}_j(\eta_m - \eta') = \int_{\eta_i - \eta'}^{\infty} d\eta'' \frac{\Phi'(\eta'')}{\eta''} L_j(\eta'') \tag{11.13}$$

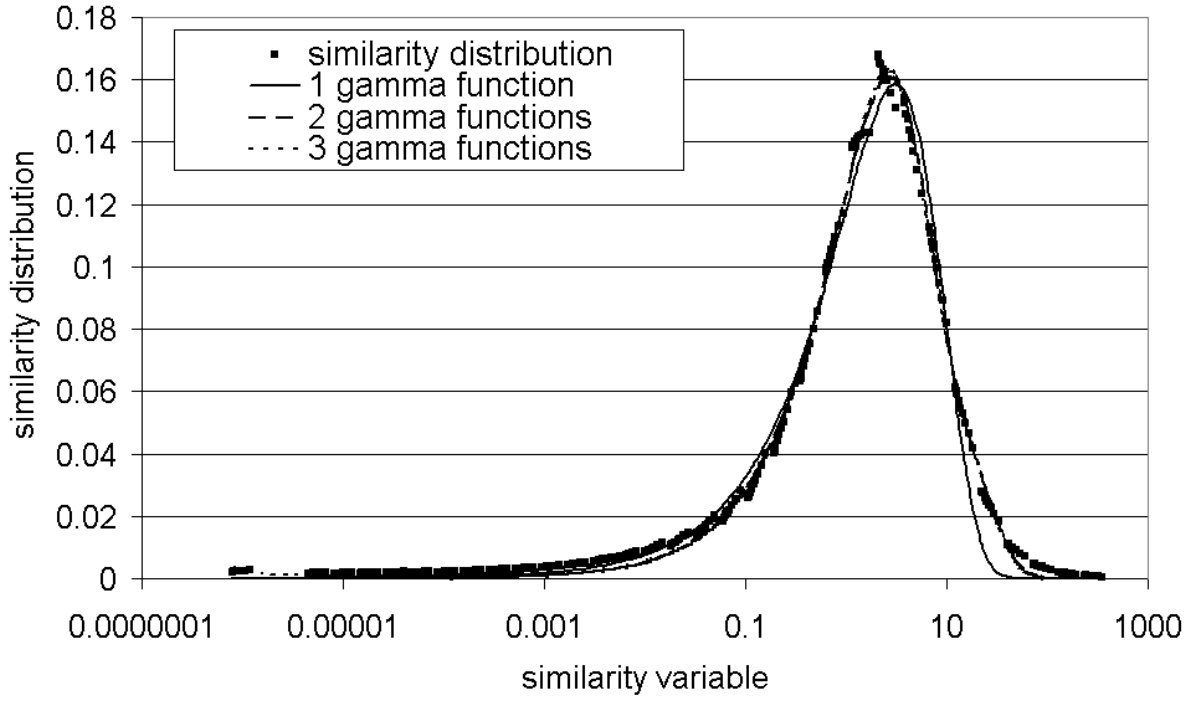

Figure 11.1: Fitting of the similarity distribution $\Phi'(\eta)$ by means of expanded γ-distributions for different values of $\mathrm{n_{term}}$

The analytical form of $\Phi'(\eta)$ and the known form of the Laguerre polynomials can now be exploited to calculate $\bar{\mathrm{Y}}_\mathrm{j}(\eta_\mathrm{m} - \eta')$ semi-analytically (see Appendix B.5)

$$\bar{Y}_j(\eta_m - \eta') = \sum_{k=1}^{n_{term}} A_k \sum_{m=0}^{j-1} (-1)^m \frac{j!}{m!^2(j-m)!} \frac{\gamma_c(\alpha_k + m - 1, \beta_k(\eta_m - \eta')}{\beta^{\alpha_k+m-1}} \tag{11.14}$$

where γ_c is the complementary incomplete γ-function.

A comprehensive, stepwise method was developed to solve this inverse problem using a spreadsheet (e.g. MS Excel, Open Office,...) and Matlab (Mathworks Inc., USA). It is included in Appendix D.1.

11.1.2 Results of inversion for pure aggregation

The method presented in Appendix D.1 was used to solve the inverse problem. First, the range of the similarity variable was discretised. A geometric grid with factor 1.223 was used starting from $\eta_\mathrm{min} = 7.91\mathrm{E} - 7$ and covering the entire range up to $\eta_\mathrm{max} = 352$ with exactly 100 classes.

The continuous function describing/approximating the similarity distribution was obtained using an expansion of γ-functions. In order to perform the fit, the cumulative similarity distribution $\Phi(\eta)$ as shown in Fig. 9.9 was converted into the plain similarity distribution $\Phi'(\eta)$. Also, volume fractions were used instead of vol%. The fit was performed for $\mathrm{n_{term}}$-values of 1, 2 and 3 and the results are shown in Fig. 11.1. The parameter estimates and the sum of squared errors (SSE) are given in Table 11.2. Based

Table 11.2: Fitting results of gamma-expansion of the similarity distribution $\Phi'(\eta)$

n_{term}	SSE	A_1	α_1	β_1	A_2	α_2	β_2	A_3	α_3	β_3
1	9.9E-3	0.15	1.64	0.21	-	-	-	-	-	-
2	2.5E-3	0.16	1.75	0.32	6.2E-3	2.25	0.10	-	-	-
3	1.6E-3	0.12	2.06	0.46	0.05	1.43	0.08	2.67E-9	0.0082	0.11

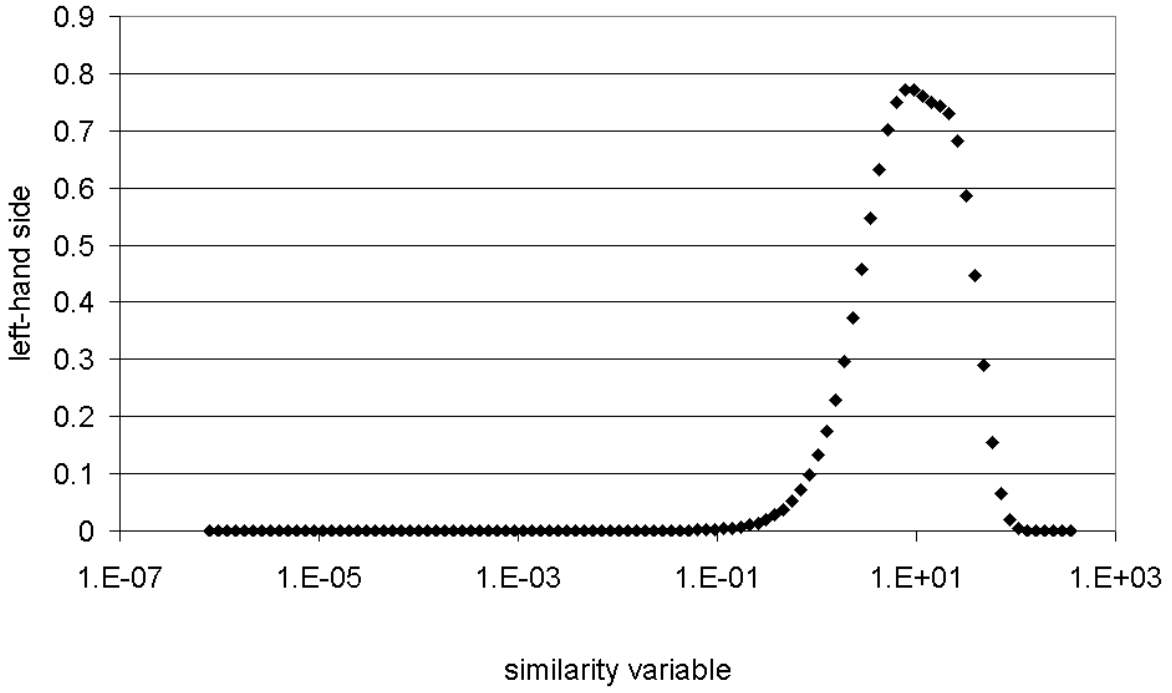

Figure 11.2: Calculated left-hand side of eq. 11.1

on the SSE and the visual inspection, it can be concluded that the expansion using two and three γ-distributions yields the best result. However, adding a third γ-function did not induce significant improvement. Hence, the fitting results from the case using two γ-functions were used in the remainder of the inversion.

At this stage, the left-hand side of eq. 11.1 can be calculated at the discretised η-values. The result is shown in Fig. 11.2.

The goal of inversion is to reproduce this left-hand side with a linear combination of double integrals represented by eq. 11.12. These integrals are evaluated for different combinations of Laguerre polynomials (i.e. inner products $l_{i,j}$) at all discretised η-values. The number of inner products used in the inversion depends on the number of basis functions n_b used per axis. Here, n_b was chosen to be 2,3 or 4, resulting in respectively 4, 9 and 16 inner products. The double integrals for the different inner products are depicted in Fig. 11.3.

A constrained quadratic optimisation procedure is then used to find the coefficients of the linear combination. In other words, the optimal set of coefficients is looked for that, when multiplied with the respective

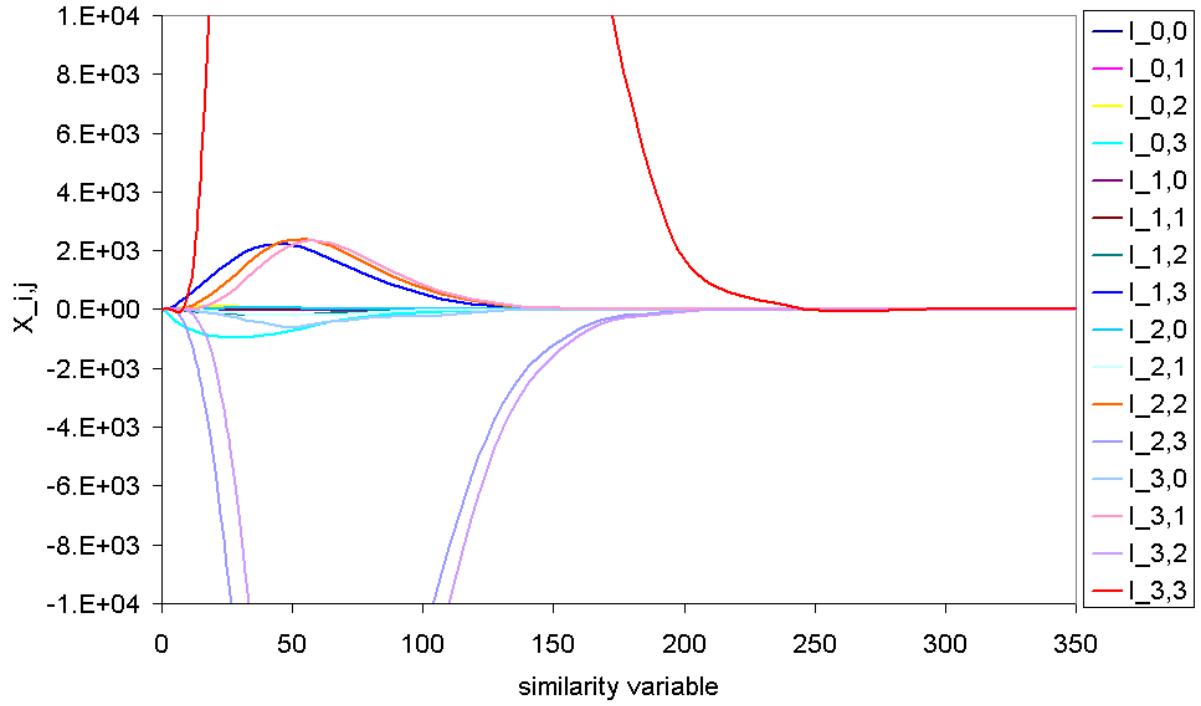

Figure 11.3: Double integrals (eq. 11.12) for different inner products when using a maximum of 4 basis functions ($I_{i,j}$ represents the inner product of the i^{th} and j^{th} Laguerre polynomial)

Table 11.3: Results of constrained quadratic optimisation for different values of $\mathrm{n_b}$ without regularisation

Coefficient	inner product	$\mathrm{n_b} = 2$	$\mathrm{n_b} = 3$	$\mathrm{n_b} = 4$
c1	$\mathrm{I}_{0,0}$	0.1162	0.1216	0.1256
c2	$\mathrm{I}_{0,1}$	-0.0125	-0.0022	-0.0011
c3	$\mathrm{I}_{0,2}$	-	0.0010	0.0017
c4	$\mathrm{I}_{0,3}$	-	-	0.00005
c5	$\mathrm{I}_{1,0}$	-0.0125	-0.0022	-0.0011
c6	$\mathrm{I}_{1,1}$	0.0116	0.0194	-0.00006
c7	$\mathrm{I}_{1,2}$	-	0.0005	-0.0018
c8	$\mathrm{I}_{1,3}$	-	-	-0.00006
c9	$\mathrm{I}_{2,0}$	-	0.0010	0.0017
c10	$\mathrm{I}_{2,1}$	-	0.0005	-0.0018
c11	$\mathrm{I}_{2,2}$	-	0.00001	-0.0003
c12	$\mathrm{I}_{2,3}$	-	-	-0.000008
c13	$\mathrm{I}_{3,0}$	-	-	0.00005
c14	$\mathrm{I}_{3,1}$	-	-	-0.00006
c15	$\mathrm{I}_{3,2}$	-	-	-0.000008
c16	$\mathrm{I}_{3,3}$	-	-	-0.0000002
SSE		0.018	0.012	0.006

inner product (Fig. 11.3) and summed, results in best prediction of the distribution in Fig. 11.2. The results for different values of $\mathrm{n_b}$ and without regularisation are summarised in Table 11.3. The coefficients are somewhat different when using a different number of basis functions. It can be seen that both the symmetry requirements (symmetric off-diagonal elements should be equal) and the positivity requirements were respected. The fits of the right-hand side for different λ_{reg} are shown in Fig. 11.4-11.6 for $\mathrm{n_b}$-values of 2,3 and 4 respectively. The fits seem to be similar. However, when calculating the SSE, it is observed that a higher $\mathrm{n_b}$ yields better accuracy (Table 11.3) which could be expected since the number of degrees of freedom increases when $\mathrm{n_b}$ is increased.

Based on this, it can be concluded that $\mathrm{n_b} = 4$ would be the best choice (note that this was the highest investigated number of basis functions in this study and that further increasing this might even yield better results). However, the forward simulation of the resulting model should confirm this conclusion. It might not be necessary to pursue such high accuracy. The danger of using SSE as only criterion for this choice might be that one starts to fit experimental noise, which is not in our interest.

Regularisation did not affect coefficients values for $\lambda_{\mathrm{reg}} < 1$. For higher values, the fits were found to be worse. The regularisation issue will be further discussed when looking at the kernel structure in the next section.

11.1.3 Kernel structure from inversion

The scaled aggregation kernel $\alpha(\eta', \eta'')/\langle\alpha\rangle$ can be reconstructed using the coefficients found in the previous section (Table 11.3) and the corresponding inner products of the Laguerre polynomials (Table 11.1). They are depicted for $\lambda_{\mathrm{reg}} = 0$ in Fig. 11.7, 11.8 and 11.9 for $\mathrm{n_b}$ equal to 2, 3 and 4 respectively.

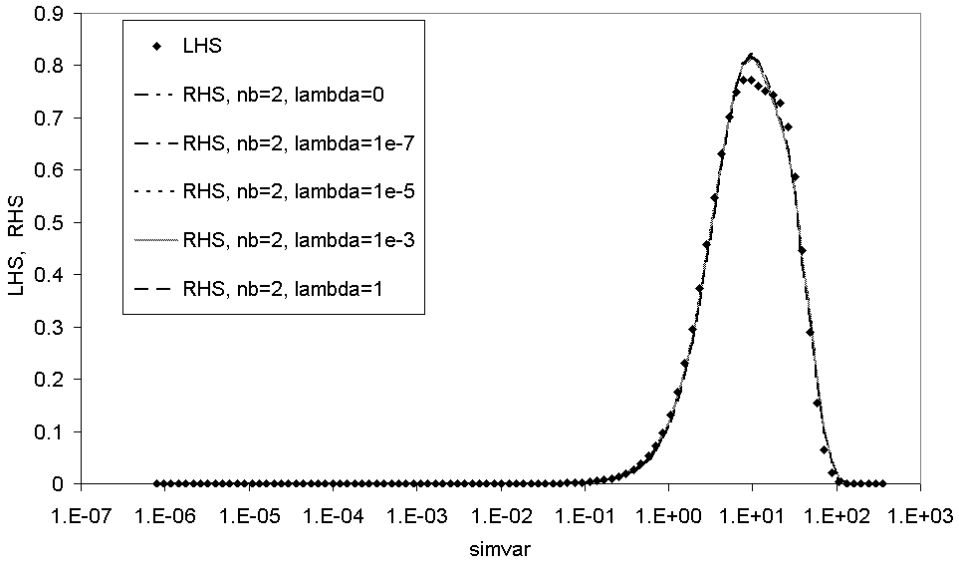

Figure 11.4: Fit of right-hand side to left-hand side for $\mathrm{n_b} = 2$ and different λ_{reg}

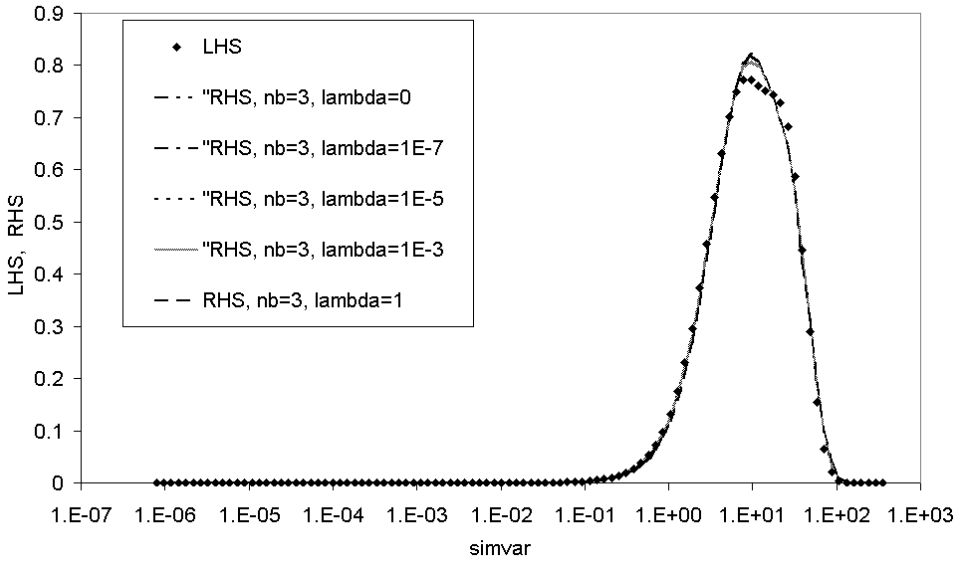

Figure 11.5: Fit of right-hand side to left-hand side for $\mathrm{n_b} = 3$ and different λ_{reg}

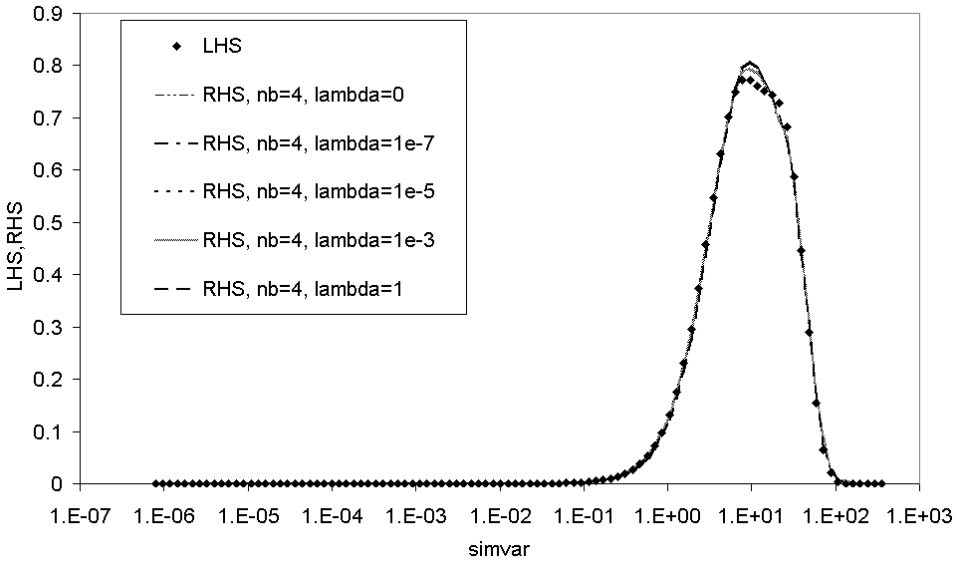

Figure 11.6: Fit of right-hand side to left-hand side for $\mathrm{n_b} = 4$ and different λ_{reg}

When using 2 basis functions ($\mathrm{n_b} = 2$), a monotonic increase in scaled aggregation frequency $\alpha(\eta', \eta'')/\langle\alpha\rangle$ can be observed for increasing (scaled) size of both colliding flocs. The increase is, however, most pronounced for homogeneous collisions. It can also be observed that the requirement of symmetry was fulfilled in the quadratic optimisation. Values of $\alpha(\eta', \eta'')/ < \alpha >$ vary between 0.1 and 105. When increasing λ_{reg} to one, the shape was not affected. However, the range of values changed to 0.08-83.

When using 3 basis functions ($\mathrm{n_b} = 3$), the scaled aggregation frequency $\alpha(\eta', \eta'')/\langle\alpha\rangle$ exhibits completely different behaviour, i.e. a saddle surface is obtained. Increasing the (scaled) size now shows a maximum for intermediate sizes. It was tried to cure this by increasing the regularisation parameter λ_{reg} up to a value of 10 but this was not successful in getting a similar shape as with 2 basis functions (see Fig. 11.10). The reason for this different behaviour is not clear.

When using 4 basis functions ($\mathrm{n_b} = 4$) similar behaviour as in the $\mathrm{n_b} = 2$ case is obtained, i.e. monotonic rising frequencies for increasing (scaled) floc size. However, the frequency values now vary from 0.12-1230, which is a lot higher, and the increase to these large values only starts from intermediate scaled floc sizes, whereas this happened immediately in the $\mathrm{n_b} = 2$ case. The plane obtained in the $\mathrm{n_b} = 2$ case can be regarded as the best approximation of the kernel found here. Increasing λ_{reg} to one does not affect the shape, but again decreases the frequency range (0.08-320).

Unfortunately, no clear conclusion can be drawn from this investigation. The forward simulation, that will be treated in the next section, should enable us to solve the selection issue.

11.1.4 Recovering the unscaled aggregation kernel a(v,v') from the scaled aggregation kernel $\alpha(\eta', \eta'')/ < \alpha >$

Before being able to perform the forward simulation, the unscaled aggregation kernel (i.e. the kernel in terms of volumes instead of similarity variable) needs to be identified. Upon doing this, the equation

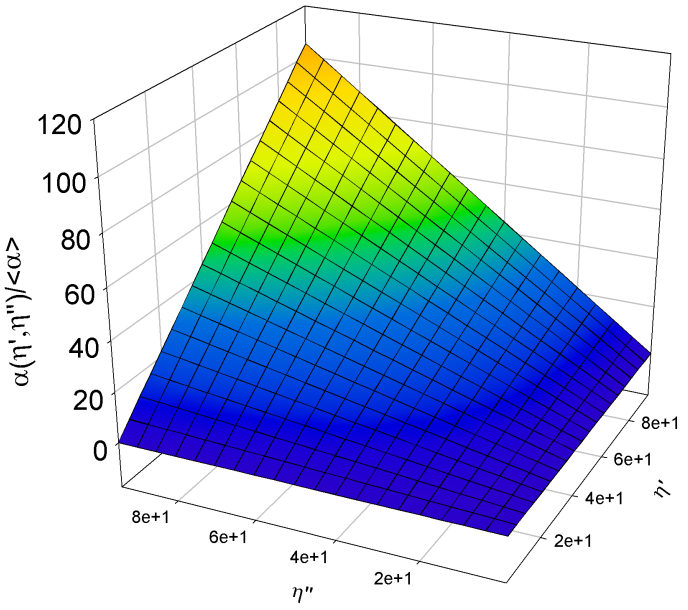

Figure 11.7: Scaled aggregation frequency for $\mathrm{n_b} = 2$ for $\lambda_{\mathrm{reg}} = 0$

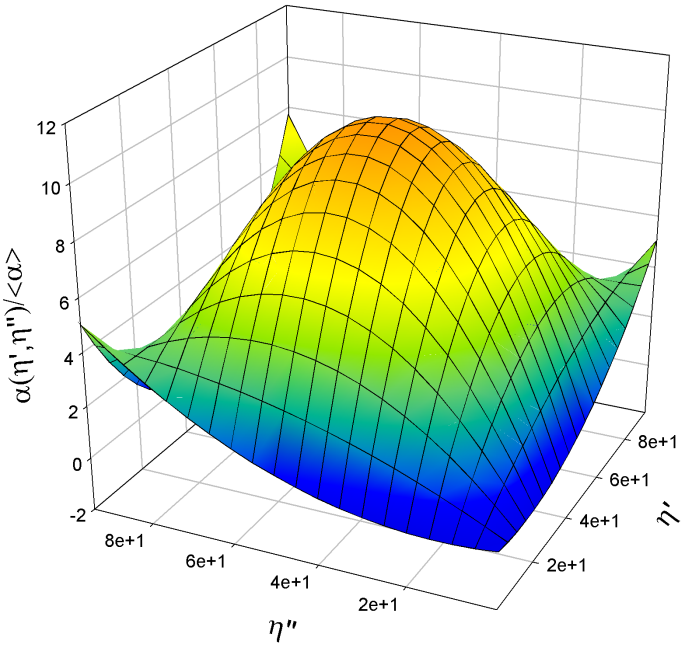

Figure 11.8: Scaled aggregation frequency for $\mathrm{n_b} = 3$ for $\lambda_{\mathrm{reg}} = 0$

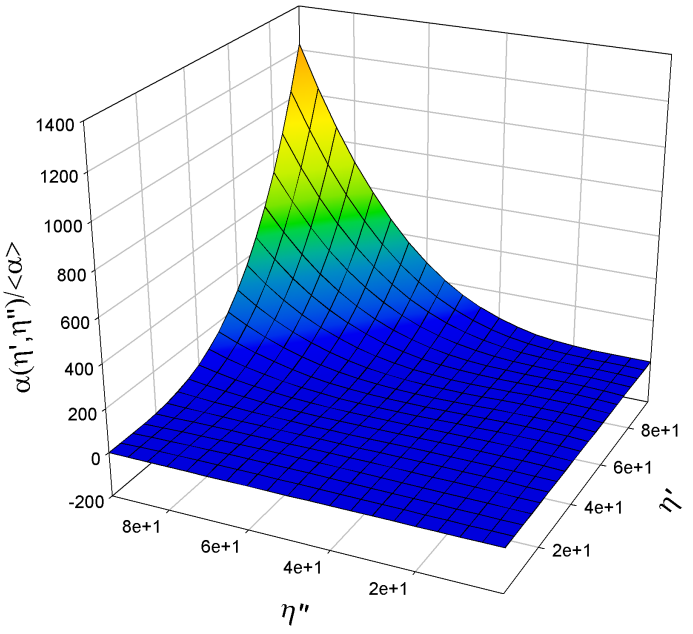

Figure 11.9: Scaled aggregation frequency for $\mathrm{n_b} = 4$ for $\lambda_{\mathrm{reg}} = 0$

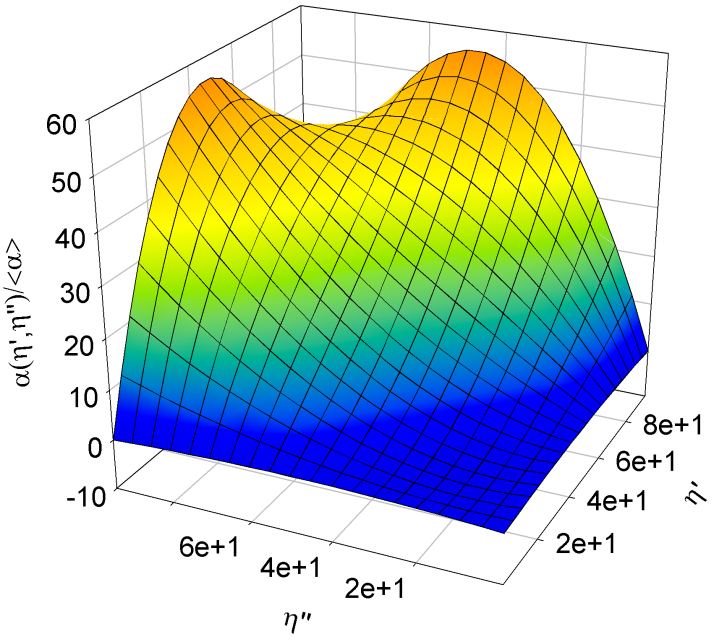

Figure 11.10: Scaled aggregation frequency for $\mathrm{n_b} = 3$ for $\lambda_{\mathrm{reg}} = 10$

describing the relationship between both functions is recalled

$$a(\eta' h(t), \eta'' h(t)) = \alpha(\eta', \eta'') H(h(t)) \tag{11.15}$$

which was a requirement for self-similarity together with

$$h'(t) = cH(h(t)) \tag{11.16}$$

where c turns out to be nothing but $< \alpha >$. In literature, it is often assumed that the aggregation kernel is homogeneous requiring the following

$$a(\tau x, \tau y) = \tau^{\lambda} a(x, y) \qquad \lambda \geq 0 \tag{11.17}$$

and, hence H(t) would be related to h(t) by a simple power law

$$H(h(t)) = h(t)^{\lambda} \tag{11.18}$$

Eq. 11.15 can be rewritten as

$$a(v, v') = \alpha(\eta', \eta'') h(t)^{\lambda} \tag{11.19}$$

From the inversion the expression $\alpha(\eta', \eta'')/ < \alpha >$ is obtained. Hence, $< \alpha >$ and λ need to be determined from the dynamic behaviour of the scaling function h(t) before the unscaled kernel can be obtained.

$< \alpha >$ and λ can be obtained from eq. 11.16 which can be rewritten as

$$h'(t) =< \alpha > h(t)^{\lambda} \tag{11.20}$$

A logarithmic transform of this equation yields

$$log(h'(t)) = log(< \alpha >) + \lambda log(h(t)) \tag{11.21}$$

which allows us to recover $< \alpha >$ and λ from the slope and intercept from a graph plotting log(h'(t)) versus log(h(t)). The dynamic behaviour of h(t) is given in Fig. 11.11. A second order polynomial was fitted to the data in order to enable simple calculation of h'(t) and was found to be

$$h(t) = -2.89E - 19t^2 + 5.12E - 16t + 1.34E - 13 \tag{11.22}$$

The plot of log(h'(t)) versus log(h(t)) is given in Fig. 11.12. This learns that the behaviour is not linear at all. Moreover, a linear fit results in a negative slope, which violates the constraint put on λ in eq. 11.17. This means that the kernel does not meet the criterion of homogeneity and that this approach cannot be used for extracting the unscaled aggregation kernel a(v,v').

Hence, another approach was looked for that does not use the constraint of homogeneity. Combining eq. 11.15 and 11.16 yields

$$a(v, v') = \alpha(\eta', \eta'') H(h(t)) = \frac{\alpha(\eta', \eta'')}{< \alpha >} h'(t) \tag{11.23}$$

The first factor is the scaled frequency function that was extracted through inversion. The derivative was determined earlier from the dynamic behaviour of h(t). A simple multiplication should allow to recover the unscaled aggregation kernel to be used in the forward simulation.

Noteworthy is that the recovered unscaled aggregation kernel is time-dependent (through h'(t)) which is not very common, but has already been reported in literature (Wang and Friedlander, 1967).

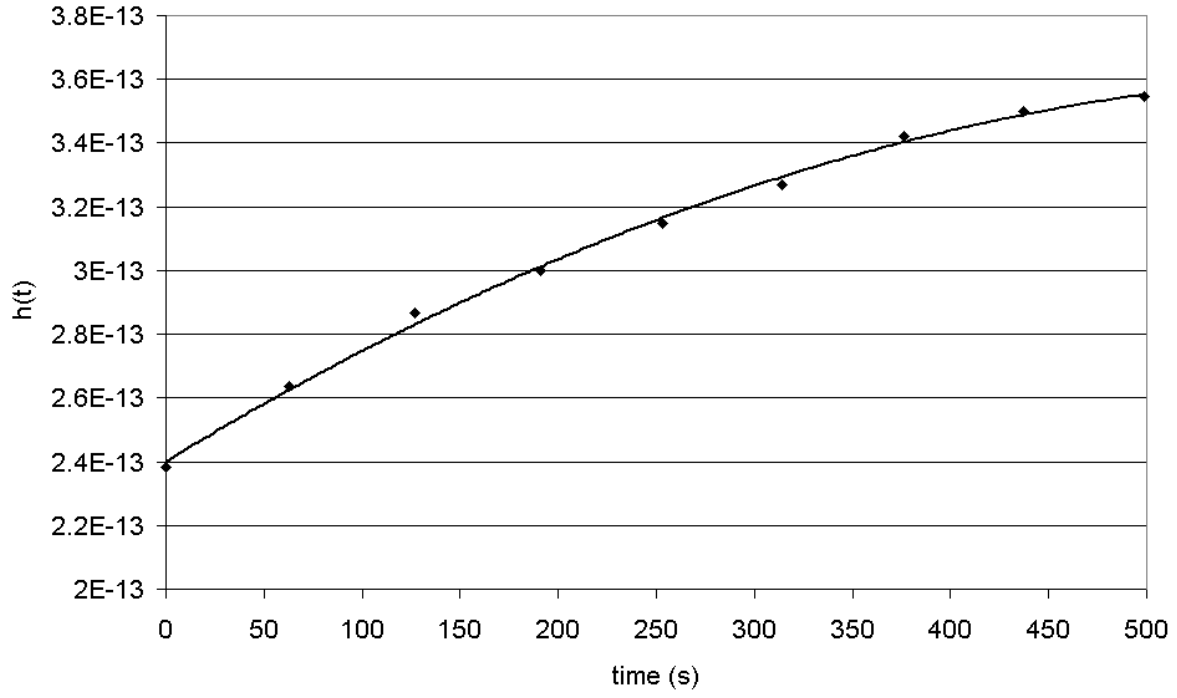

Figure 11.11: Dynamic behaviour of the scaling function h(t)

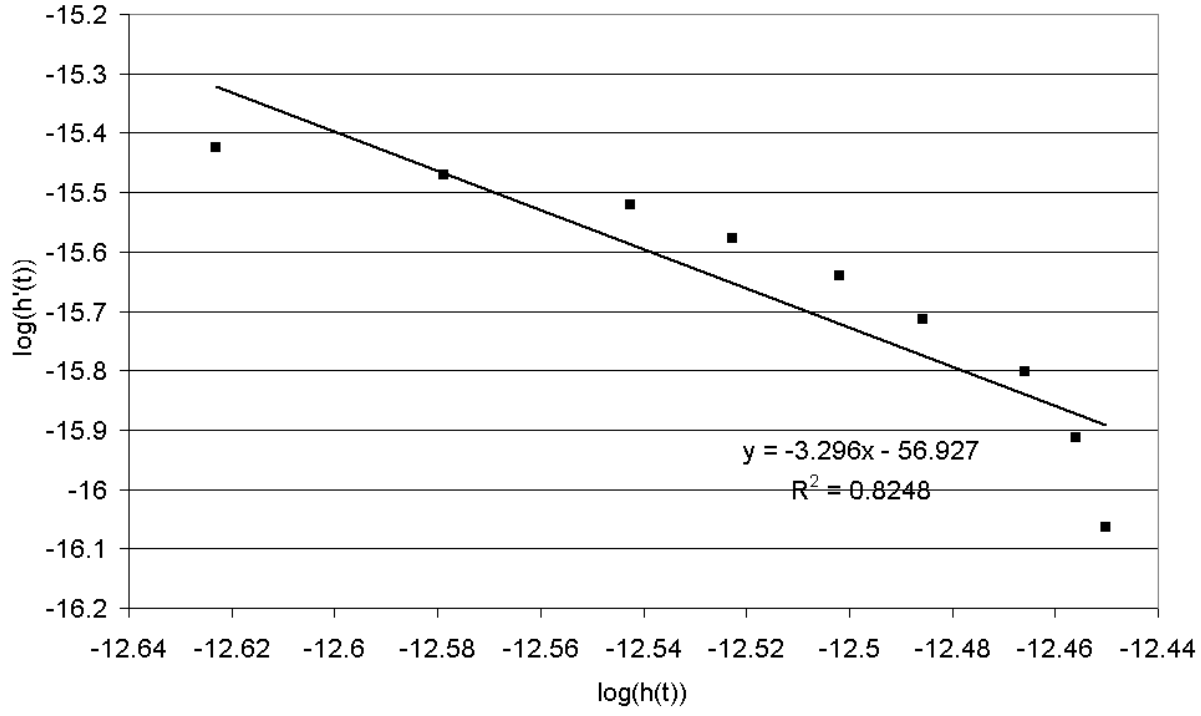

Figure 11.12: Relationship between log(h'(t)) and log(h(t))

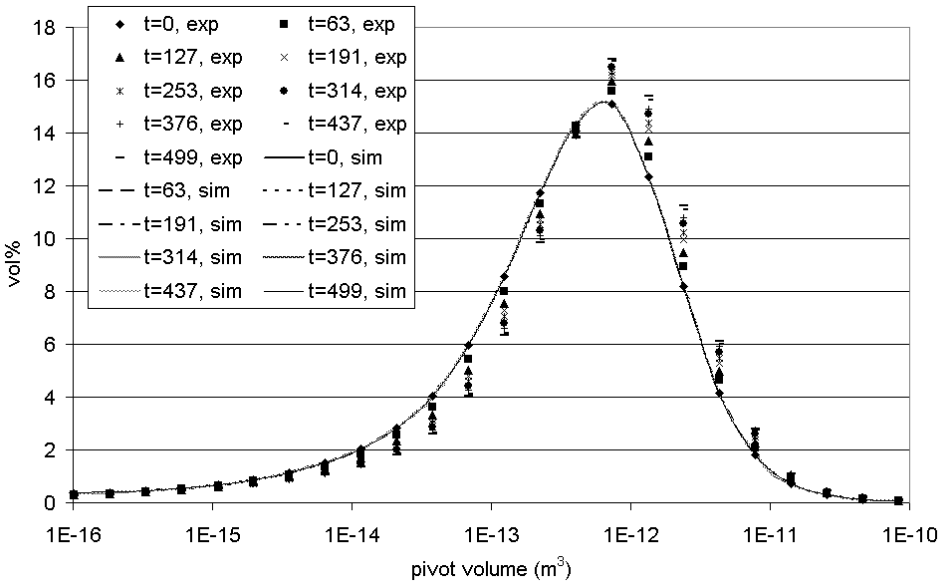

Figure 11.13: Forward simulation using the unscaled aggregation frequency recovered through inversion using 2 basis functions per axis

11.1.5 Forward simulation of volume percentage for pure aggregation

At this stage, the inversion is completed. The correctness of the recovered unscaled aggregation frequency can now be verified by performing the forward simulation using the unscaled aggregation kernel found through inversion. The model should be able to follow the experimental data from which it was extracted. Since the similarity was observed for a certain number of time instances during the reflocculation process and only this dynamic behaviour was used for the extraction of the kernel, the forward simulation is performed for these experimental data. The initial distribution is taken to be the one at the time instant where similarity was first observed.

Two basis functions ($\mathrm{n_b} = 2$) per axis

The forward simulation using the approach outlined in the previous section was performed and the result for $\mathrm{n_b} = 2$ is shown in Fig. 11.13. As can be observed from Fig. 11.13, no (or negligible) aggregation is simulated. It was tried to multiply all aggregation frequencies with a constant factor κ, as this may be lost in the conversion from the scaled to the unscaled frequency (Dr. Nandkishor Nere, personal communication). This improved the results considerably. An optimisation to determine the factor κ was performed and resulted in a value of 502 (SSE=40.52). The resulting forward simulation is given in Fig. 11.14. From Fig. 11.14 it can be seen that the dynamics of the distribution are captured quite well by the model. However, an underestimation of the lower tail and an overestimation of the upper tail is occurring. This might be due to the low number of basis functions that was used, resulting in a kernel that is not accurate enough to capture all details.

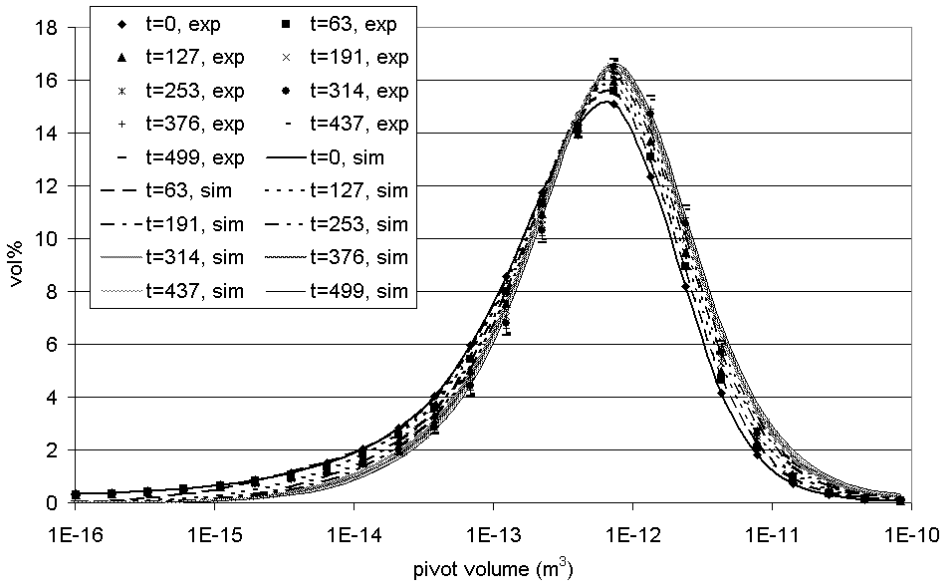

Figure 11.14: Forward simulation using the unscaled aggregation frequency recovered through inversion using 2 basis functions per axis, $\lambda_{\mathrm{reg}} = 0$ and multiplied by a factor 502

Three basis functions ($\mathrm{n_b} = 3$) per axis

When performing the forward simulation for $\mathrm{n_b} = 3$, the same problem that was encountered in the case where $\mathrm{n_b} = 2$, i.e. negligible aggregation was observed. Again, multiplying by a factor κ resulted in a good description of the data. The optimal κ-value was found to be 532 (SSE=75). The results are shown in Fig. 11.15. The peak is somewhat overestimated and the lower tail is underestimated, resulting in somewhat inferior predictions compared to the case where two basis functions were used per axis. This can be seen from the twice as large SSE-value that was calculated for the optimal κ-value. The reason for this probably lies in the different shape of the kernel (see Fig. 11.8).

Therefore, the same procedure was used for the kernel found using a higher regularisation parameter ($\lambda_{\mathrm{reg}} = 1$). These results are shown in Fig. 11.16. The optimal multiplication factor turned out be 477 and an SSE of 35 was found, which is significantly lower than the case where $\lambda_{\mathrm{reg}} = 0$ and even lower than the optimal results found in the case where only two basis functions per axis were used. The main improvements are observed in the prediction of the lower tail. Compared to the $\lambda_{\mathrm{reg}} = 0$ case, the increase of the peak is now underestimated.

Four basis functions ($\mathrm{n_b} = 4$) per axis

When performing the forward simulation for $\mathrm{n_b} = 4$, the same problem surfaced again, i.e. negligible aggregation is taking place. Again, multiplying by a factor κ resulted in a good description of the data. In this case, the optimal κ-value was found to be 395 (SSE=62). The results are shown in Fig. 11.17. The SSE suggests that the prediction is not very good. However, Fig. 11.17 reveals that the upper part of the distributions is captured much better compared to all previous cases. On the other hand, the peak is overestimated and the lower tail is underestimated, explaining why the overall result is not the best.

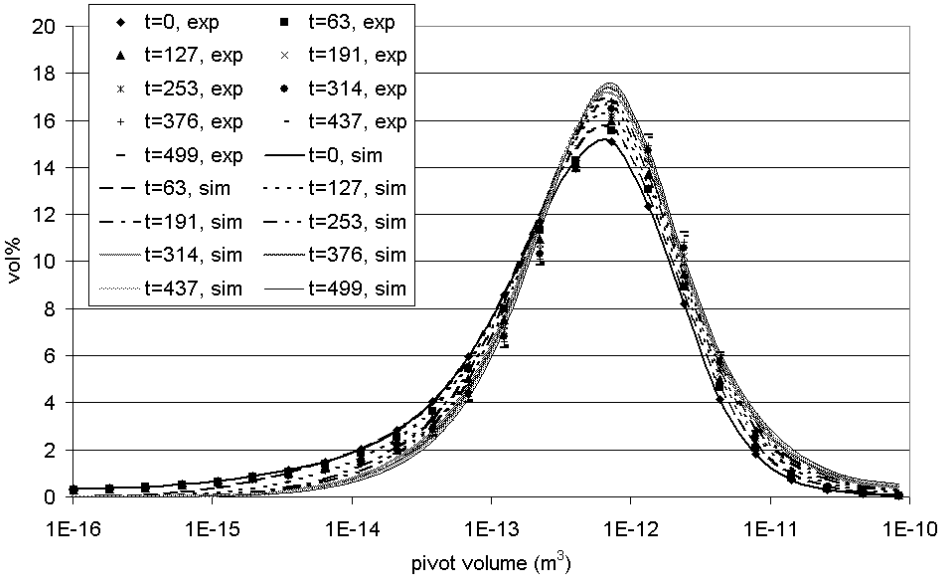

Figure 11.15: Forward simulation using the unscaled aggregation frequency recovered through inversion using 3 basis functions per axis, $\lambda_{\mathrm{reg}} = 0$ and multiplied by a factor 532

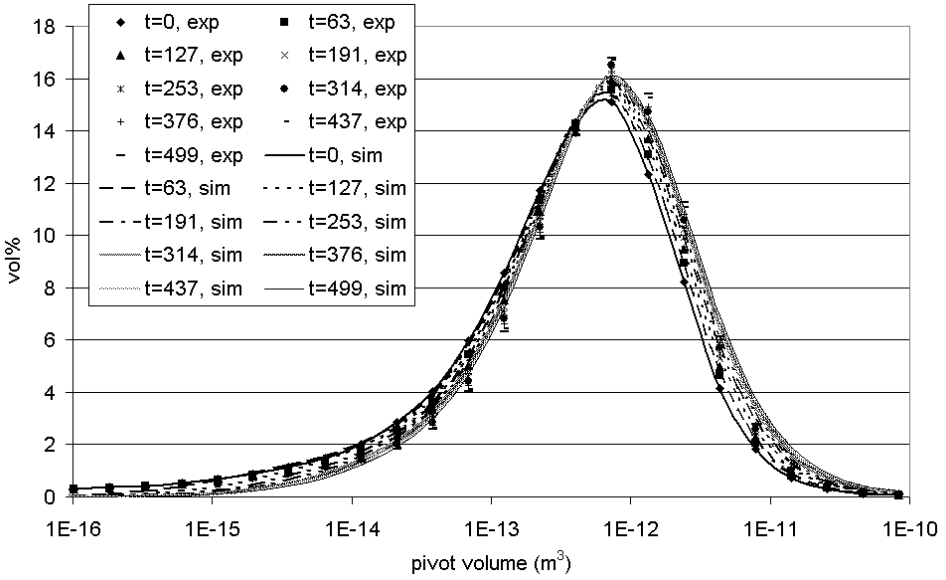

Figure 11.16: Forward simulation using the unscaled aggregation frequency recovered through inversion using 3 basis functions per axis, $\lambda_{\mathrm{reg}} = 1$ and multiplied by a factor 477

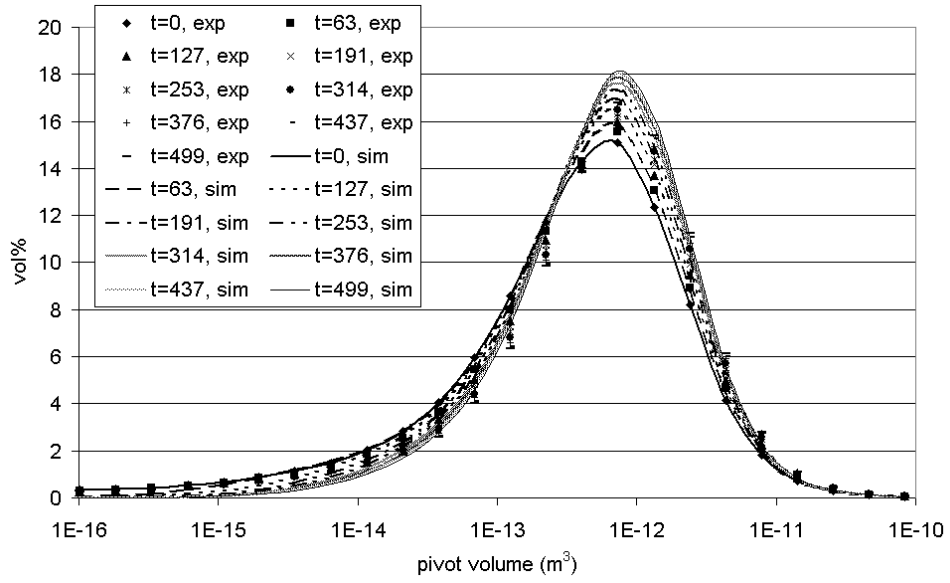

Figure 11.17: Forward simulation using the unscaled aggregation frequency recovered through inversion using 4 basis functions per axis, $\lambda_{\mathrm{reg}} = 0$ and multiplied by a factor 395

Next, the same procedure was followed for the case where $\lambda_{\mathrm{reg}} = 1$. These results are shown in Fig. 11.18. The optimal multiplication factor, that is needed to induce the aggregation behaviour, turned out to be 455 and an SSE of 24.85 was found, which is significantly lower than the case where $\lambda_{\mathrm{reg}} = 0$ and even lower than the optimal results found in all studied cases that used a smaller number of basis functions per axis. The main improvements are observed in the prediction of the upper tail and the peak, which is captured very well. The lower tail is, however, still underestimated.

11.1.6 Forward simulation of the number distribution for pure aggregation

Since the main interest of this work is a good prediction of the small flocs that eventually end up in the effluent, the predicted number distribution was compared with the measured number distribution (using the same transformation procedure described in chapter 8). The results for different numbers of basis functions are shown in Fig. 11.19 ($\mathrm{n_b} = 2$), Fig. 11.20 ($\mathrm{n_b} = 3$) and Fig. 11.21 ($\mathrm{n_b} = 4$). A first thing to note is the fact that the dynamics are almost invisible in the number distributions. The model predictions capture the upper tail extremely well. Moreover, the predictions get better in case more basis functions are used. However, the very obvious failure to capture the lower tail in the volume distributions results in severe underestimations of the lower tail of the number distributions. However, a slight improvement can be noticed when more basis functions are used. Hence, further increasing the number of basis functions might be an option to further improve the prediction of the number distributions. More research is clearly warranted.

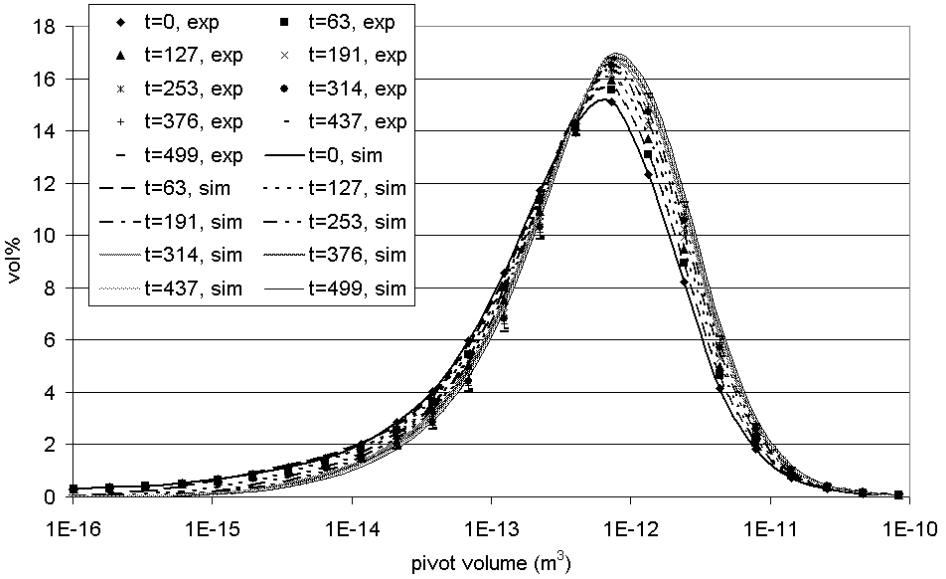

Figure 11.18: Forward simulation using the unscaled aggregation frequency recovered through inversion using 4 basis functions per axis, $\lambda_{\text{reg}} = 1$ and multiplied by a factor 455

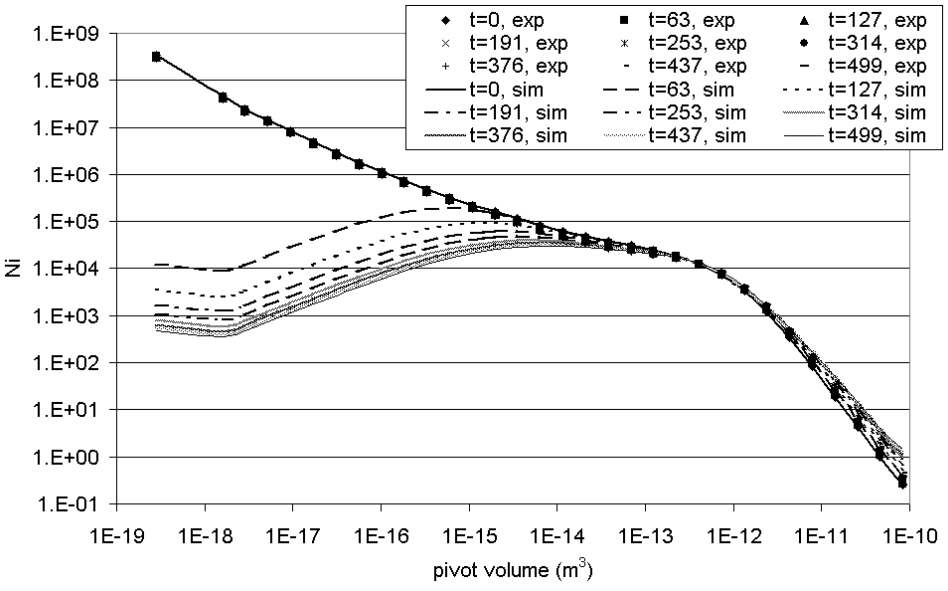

Figure 11.19: Forward simulation of the number distributions using the unscaled aggregation frequency recovered through inversion using 2 basis functions per axis, $\lambda_{\text{reg}} = 0$ and multiplied by a factor 502

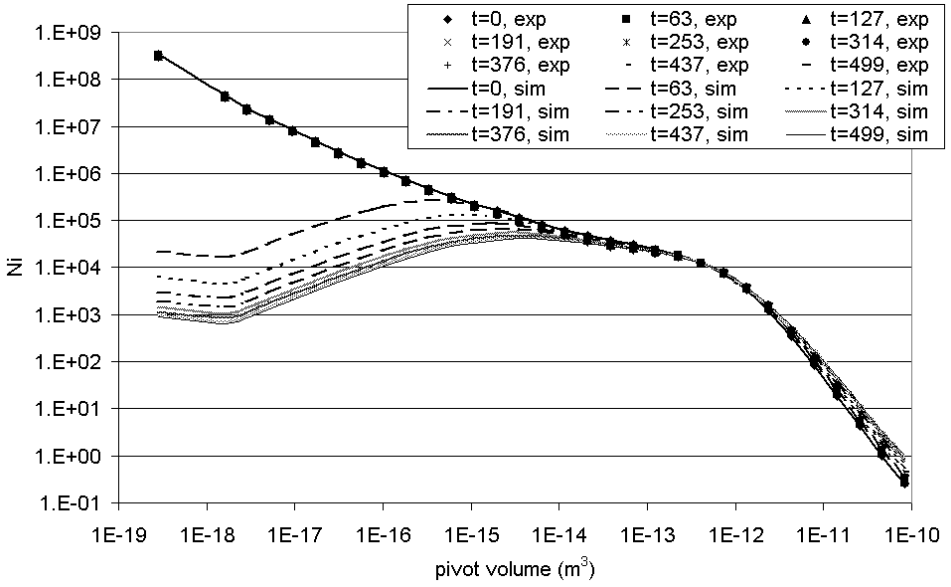

Figure 11.20: Forward simulation of the number distributions using the unscaled aggregation frequency recovered through inversion using 3 basis functions per axis, $\lambda_{\mathrm{reg}} = 1$ and multiplied by a factor 477

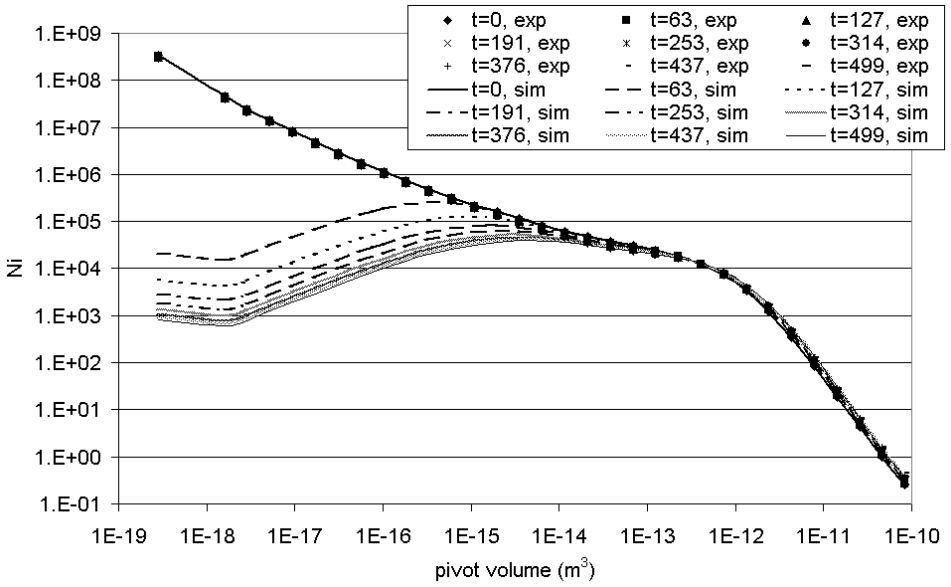

Figure 11.21: Forward simulation of the number distributions using the unscaled aggregation frequency recovered through inversion using 4 basis functions per axis, $\lambda_{\mathrm{reg}} = 1$ and multiplied by a factor 455

11.2 Solving the inverse breakage problem

In chapter 9, it was demonstrated that a transformation of the dynamic experimental data into a similarity distribution was possible for the breakage of a sludge by increased shear. Moreover, the breakage rate expression could be recovered up to a constant. The presence of similarity can now be used to recover the missing constant and the daughter size distribution from the experimental data. Fig. 9.14 shows the cumulative vol% versus the similarity variable η for the experimental case that will be used here. The region for which similarity was found is indicated in Fig. 9.16. Before actually performing the inversion, the procedure will be elaborated in a bit more detail.

11.2.1 Procedure for inversion of pure breakage data with self-similar behaviour

The PBE expressed in function of the similarity variable η forms the basis of this exercise. It is reproduced below for convenience (note that z is used as similarity variable instead of $\hat{z}$ for ease of notation).

$$z\Phi'(z) = \beta \int_0^1 \frac{z^2}{u^3} \Phi' \left(\frac{z}{u}\right) g(u) du \tag{11.24}$$

This equation may also be ill-posed, meaning that small changes in $\mathrm{z}\Phi'(\mathrm{z})$ can cause large differences in the extracted $\beta \mathrm{g}(\mathrm{u})$ function. This can be overcome by using a technique called *Thikonov regularisation* during the inversion process which was discussed earlier (section 11.1.1) and will not be repeated here.

At this moment, the constrained quadratic minimisation problem can be formulated. The similarity coordinate is discretised into a set of $\{\eta_\mathrm{i}\}$ and $\beta \mathrm{g}(\mathrm{u})$ is expanded in terms of basis functions

$$\beta g(u) = \sum_{j=1}^{n_b} a_j G_j(u) \tag{11.25}$$

where $\mathrm{n_b}$ is the number of basis functions and $\mathrm{a} = \{\mathrm{a}_1, \mathrm{a}2, \ldots, \mathrm{a}_{\mathrm{n_b}}\}$ are the coefficients of expansion. Hence, the discrete version of the inverse problem becomes

$$\Phi = Xa \tag{11.26}$$

where X is a matrix whose components are given by

$$X_{ij} = \int_0^1 \frac{\xi_i^2}{u^3} \Phi' \left(\frac{\xi_i}{u}\right) G_j(u) du \tag{11.27}$$

The quadratic minimisation becomes

$$min \left(a^T X^T X a - 2 a^T X^T \Phi\right) \tag{11.28}$$

the solution of which will yield the unknown vector a.

A few constraints need to be taken into account when determining the unknown cumulative daughter distribution function:

1. the function is always positive

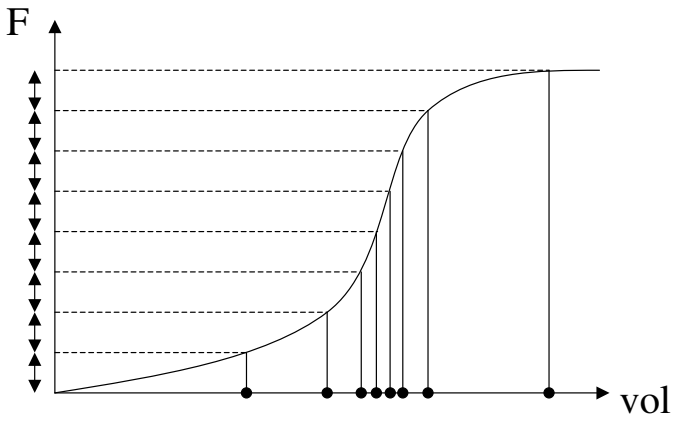

Figure 11.22: Grid determination for obtaining equal areas under the curve

Table 11.4: Structure of the first six Legendre polynomials

n	$G_n(u)$
0	1
1	u
2	$0.5(3u^2 - 1)$
3	$0.5(5u^3 - 3u)$
4	$0.125(35u^4 - 30u^2 + 3)$
5	$0.125(63u^5 - 70u^3 + 15u)$

2. the function is monotonic in its argument

3. at u=1, g(u)=1 and g'(u)=0

The latter constraint allows us to determine the unknown constant β.

According to Sathyagal et al. (1995), the region under the peak of the similarity distribution f'(z) contains the most information. In order to get more points of the discretisation in that region, it is advised to choose intervals such that there are equal areas under the f'(z) curve in each interval (Fig. 11.22).

Problem-specific basis functions that can be used here are modified Jacobi polynomials or Legendre polynomials. The first few functions of the latter are given in Table 11.4.

In order to simplify the matrix equations for the determination of a (eq. 11.28), a straightforward method is needed for the representation of the (cumulative) similarity distribution $\Phi'(\eta)$ or $\Phi(\eta)$). Other advantages of this fitting lie in the elimitation of measurement noise and the guarantee that the similarity distribution is continuous. In the aggregation case, the similarity distribution was expanded in terms of γ-functions. The same procedure was used here.

A comprehensive, stepwise method was developed to solve this inverse problem using a spreadsheet (e.g. MS Excel, Open Office,...) and Matlab (Mathworks Inc., USA). It is included in Appendix D.2.

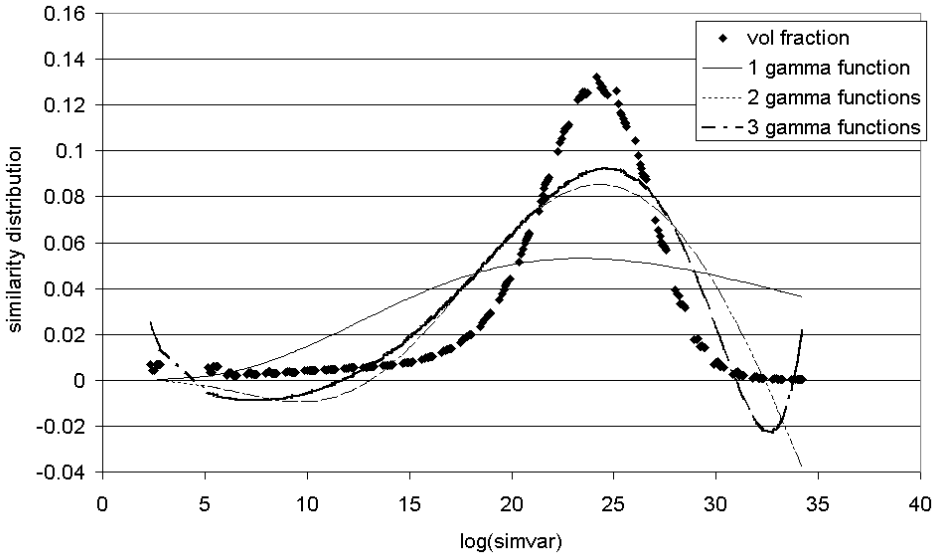

Figure 11.23: Fitting of the similarity distribution $\Phi(\eta)$ by means of γ-functions

11.2.2 Results of inversion for pure breakage

The method presented in Appendix D.2 was used to solve the inverse problem. First, the range of the similarity variable was discretised. A geometric grid with factor 1.171 was used starting from $\eta_{\min} = 1$ and covering the entire range up to $\eta_{\max} = 1.62\mathrm{E} + 34$ with exactly 500 classes.

Next, it was tried to obtain a continuous function for the similarity distribution ($\Phi'(\mathrm{z})$). Sathyagal et al. (1995) used an expansion of γ-functions to do this. However, due to the wide range, a solution for an expansion with γ-functions could not be obtained by the *fminsearch*-function in Matlab (Mathworks Inc, USA). To reduce the range, it was tried to fit to the logarithmic transform of the similarity variable. Here, a solution was found by the search algorithm, but the result clearly showed that γ-functions are not able to capture the similarity distribution. The results are illustrated in Fig. 11.23 for different numbers of γ-functions used in the expansion.

As a relatively easy alternative the cumulative similarity distribution ($\Phi(\mathrm{z})$) was fitted using a Weibul-type sigmoidal curve

$$\Phi(z) = a\left\{1 - exp\left[-\left(\frac{log(z) - x_0 + b(ln2)^{1/c}}{b}\right)^c\right]\right\} \tag{11.29}$$

This yielded a much better fit, as shown in Fig. 11.24. The SSE was 0.053. The parameter estimates are given in Table 11.5.

The availability of a continuous expression for the cumulative similarity distribution $\Phi(\mathrm{z})$ allows to calculate the left-hand side of eq. 11.24. The derivative of $\Phi(\mathrm{z})$ can be explicitly calculated and the previously introduced discretisation (500 classes) was used. The result of $\mathrm{z}\Phi'(\mathrm{z})$ is given in Fig. 11.25.

The goal of inversion is to reproduce this left-hand side with a linear combination of integrals represented by eq. 11.27. These integrals are evaluated for different Legendre polynomials at all discretised z-values

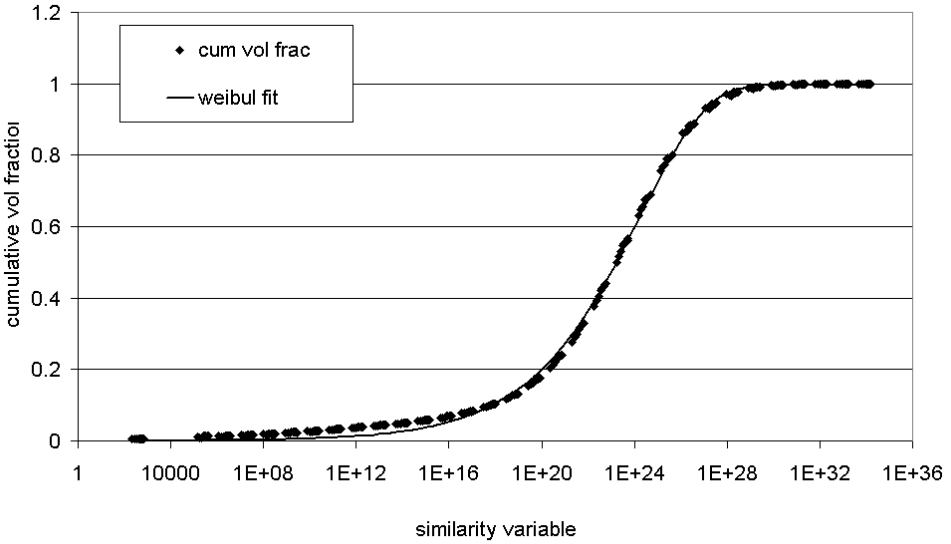

Figure 11.24: Fitting of the cumulative similarity distribution $\Phi'(\eta)$ by means of a Weibul sigmoidal function

Table 11.5: Parameter estimates from the Weibul fit to the cumulative similarity distribution $\Phi(z)$

parameter	value
a	0.9968
b	1.29E+8
c	4.55E+7
x_0	23.21

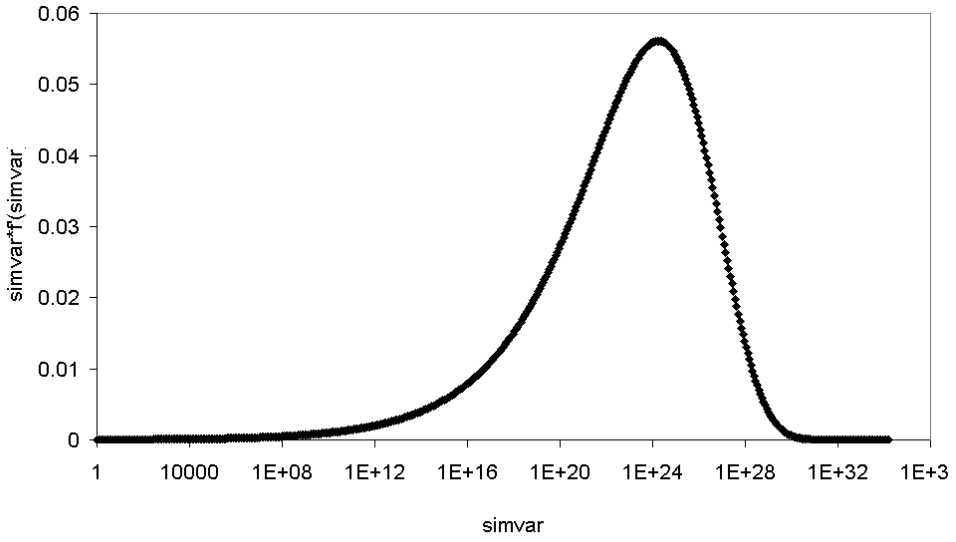

Figure 11.25: Calculated left-hand side of eq. 11.24 using the Weibul fit on the cumulative similarity distribution $\Phi(\mathrm{z})$

using the Weibul fit obtained earlier. The results of the integrals for one, two and three basis functions (i.e. j=0, 1 and 2) are given in Fig. 11.26. From Fig. 11.26, it can be seen that the values of the integrals are very large compared to the values observed in Fig. 11.25. Moreover, the peaks of the integrals occur at different values of the similarity variable. A possible reason for these observations might be the fact that the integrals could not be calculated entirely from lower to upper limit because near the lower boundary, i.e. the origin, the integrand is singular ($1/\mathrm{u}^3$), causing the integral to blow up. The calculations were, therefore performed for a somewhat larger lower limit, i.e. 0.05. This was the lowest value that was accepted by the Matlab-function *quadl* that was used to perform the numerical integration. However, the large absolute values are also induced by the z^2-factor that is present in the integrand. These integrals produced meaningless results for the coefficients of expansion and, hence, did not allow for a good fit of the left-hand side (not shown).

In order to cure the singularity near the origin (i.e. small z), the basis functions need to be modified. The modification is done as follows:

$$\beta g(u) = u \sum_{j=1}^{n_b} a_j G_j(u) \tag{11.30}$$

The integrals to be calculated now become

$$X_{ij} = \int_0^1 \frac{\xi_i^2}{u^3} \Phi' \left(\frac{\xi_i}{u} \right) u G_j(u) du \tag{11.31}$$

which can be further simplified by taking the derivative f'(z/u) with respect to u instead of z/u to solve the problem of singularity

$$X_{ij} = \int_0^1 \frac{\xi_i}{u} \frac{d\Phi \left(\frac{\xi_i}{u} \right)}{du} G_j(u) du \tag{11.32}$$

where the negative sign is assumed to be absorbed in the expansion.

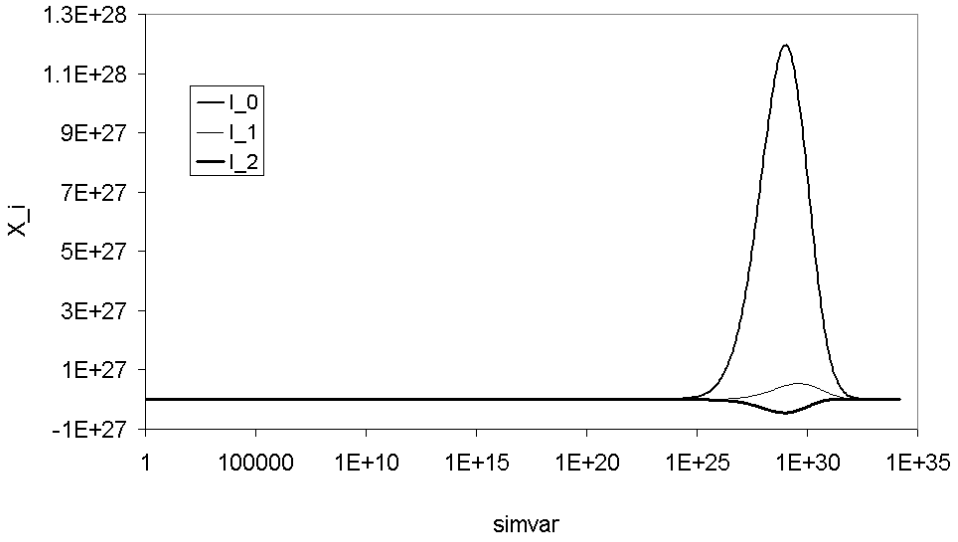

Figure 11.26: Integrals (eq. 11.27) when using 1, 2 and 3 basis functions

When using these integrals, a reasonable fit of the similarity distribution could be obtained (Fig. 11.27). However, the quality of the fit deteriorated when the number of basis functions was increased. Therefore, the remainder of the inversion will be based solely on the fit using two basis functions.

11.2.3 Kernel structure from inversion

The fit with two basis functions resulted in the coefficients of the expansion, being $\mathrm{a}_0 = 3$ and $\mathrm{a}_1 = -1.5$. From these results, the value of the missing constant β in the breakage frequency can be determined immediately. The expansion becomes:

$$\beta g(u) = u(3 - 1.5u) \tag{11.33}$$

Since g(u)=1 for u=1, this results in a value of $\beta = 1.5$. The breakage rate expression therefore becomes:

$$b(x) = 1.5 \left(\frac{x}{x_0} \right)^{3.7} \tag{11.34}$$

where x_0 represents the volume of the primary particle. The breakage rate is plotted on a log-log scale in Fig. 11.28. Due to the large ratio's between the particles and the primary particle and the large exponent (i.e. 3.7), breakage rates become very large for large particles.

Finally, the daughter distribution can be reconstructed from the basis function expansion as (note that the coefficients have been divided by β):

$$g(u) = u(2 - u) \tag{11.35}$$

Since u was defined as the ratio of the breakage rate of a particle with volume x and the breakage rate of a particle with volume x', the cumulative daughter distribution can be written as:

$$G(x|x') = g(\frac{b(x)}{b(x')}) = \frac{b(x)}{b(x')}(2 - \frac{b(x)}{b(x')}) = 2 \left(\frac{x}{x'} \right)^{3.7} - \left(\frac{x}{x'} \right)^{7.4} \tag{11.36}$$

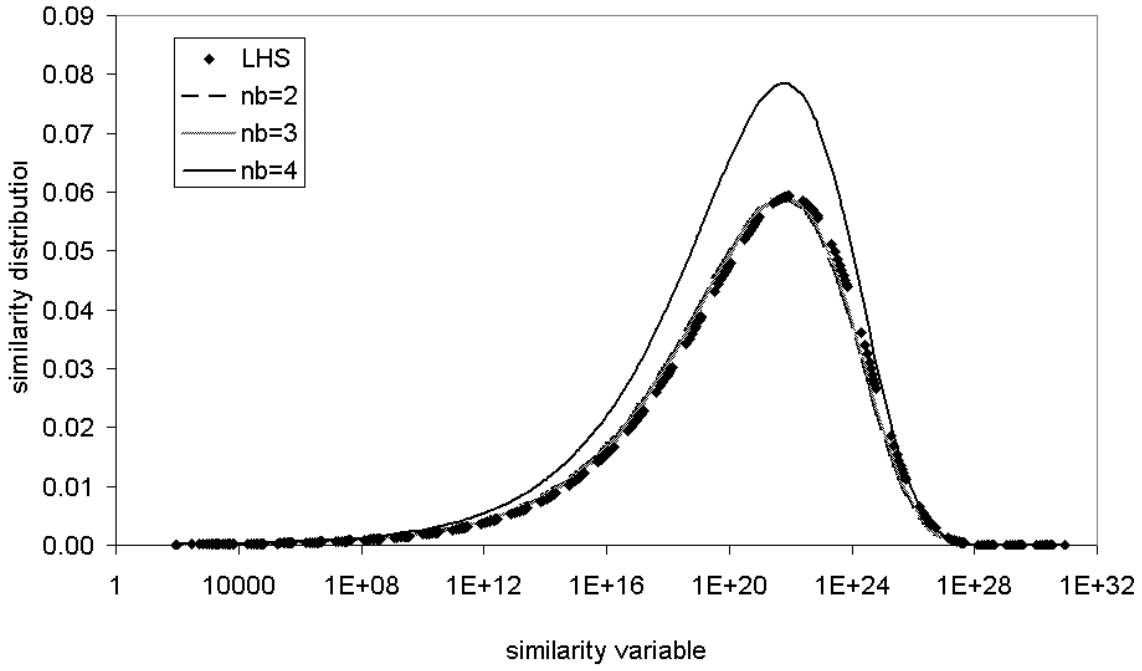

Figure 11.27: Fit of the similarity distribution by using the modified basis functions ($n_b = 2, 3, 4$)

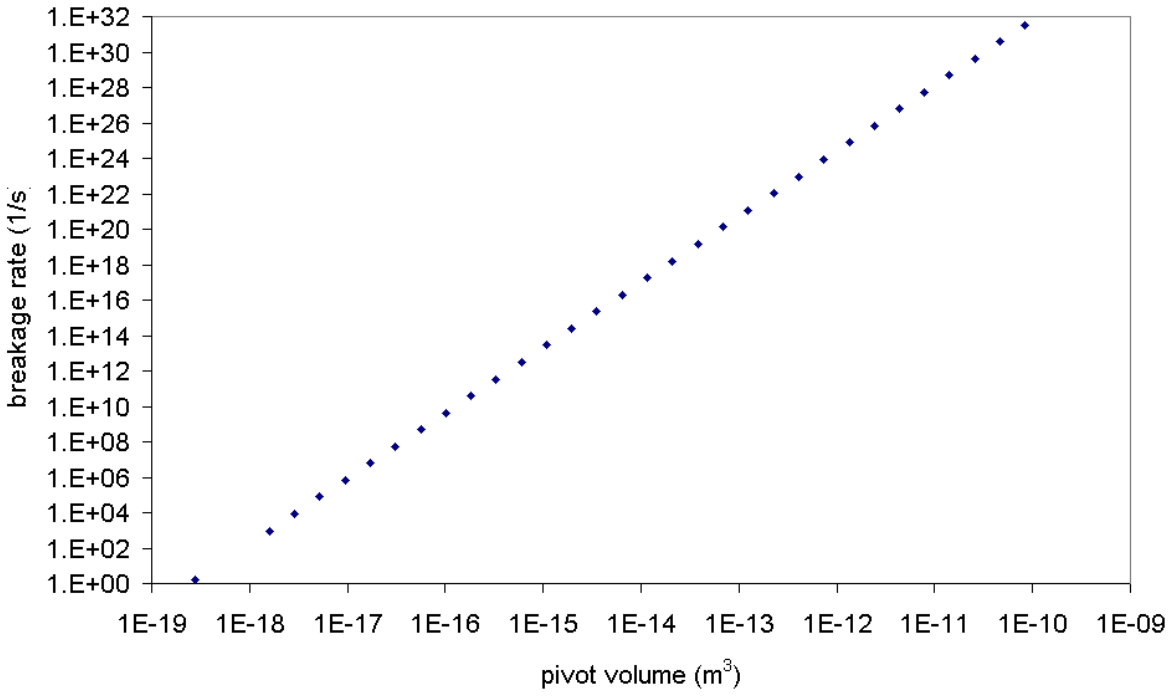

Figure 11.28: Breakage rate found through inversion (log-log scale)

In order to be able to perform the forward simulation, the daughter distribution function $\mathrm{P(x|x')}$ that describes the probability that a particle with mass x is formed from a breakage of a particle with mass x', needs to be determined from the obtained cumulative daughter distribution g(u) (or $\mathrm{G(x|x')}$). The relationship between the cumulative and the plain daughter distributions is given by

$$v(x')P(x|x') = \frac{d(x'G(x|x'))}{dx} \tag{11.37}$$

which was derived from the definition of the (cumulative) volume fraction of broken fragments from breakage of a parent of mass x' that have mass less than x, i.e. $\mathrm{G(x|x')}$

$$G(x|x') = \frac{v(x')}{x'} \int_0^x d\xi \xi P(\xi|x') \tag{11.38}$$

which leads to the expression

$$v(x')P(x|x') = \frac{7.4}{x'^{2.7}} \left(x^{1.7} - \frac{x^{5.4}}{x'^{3.7}} \right) \tag{11.39}$$

which can be plugged in the PBE for pure breakage.

Mass conservation can be checked by calculating the total sum of the volumes of particles that are formed by the breakage event. This quantity is expressed by the following integral

$$\int_0^{x'} xv(x')P(x|x') \tag{11.40}$$

and should be equal to the volume of the breaking particle, i.e. x'. This was the case for the daughter distribution expression that was found (eq. 11.39).

11.2.4 Forward simulation

Finally, the breakage functions were implemented in the PBE and the forward simulation was performed. A first problem that occurred was caused by the high breakage rates that were present at large particle sizes. These induce large derivatives and force the numerical integration algorithm to reduce its step size drastically, which results in very slow calculations. When the breakage functions were implemented as such, the algorithm even did not converge to a solution. Therefore, an extra factor was implemented to reduce the large breakage rates. In this way, it could be checked whether the daughter distribution yields good results. The results of a forward simulation using an additional factor of 1E-30 are shown in Fig. 11.29. The results from the forward simulation do not describe the experimental data that were used to obtain the breakage functions. The difference in breakage rates between small and large particles is too large. From Fig. 11.29 it can be observed that particles in the upper tail have all been broken and resulted in particles of intermediate size. Further study is required to trace the possible cause of this discrepancy. One possibility for future work is to adopt the model structure that was obtained by the inversion and estimate the parameters.

11.3 Conclusions

In this chapter, the inverse problem was solved for both the pure aggregation and the pure breakage experimental data that exhibited self-similar behaviour.

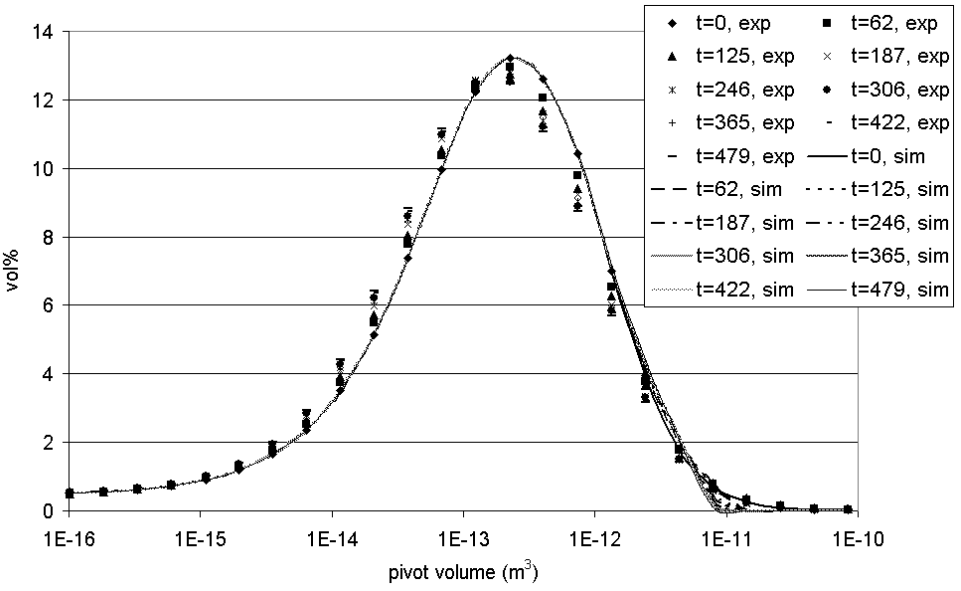

Figure 11.29: Forward simulation of the pure breakage case using the breakage functions obtained through inversion (n_b=2)

In the pure aggregation case, a good fit of the left-hand and the right hand side of the similarity-PBE was obtained. The scaled kernel was recovered using 2, 3 and 4 basis functions per axis respectively. Regularisation only had an influence on the kernel shape when using 3 basis functions. When using 2 basis functions, the frequencies were monotonically rising with scaled volume (i.e. similarity variable), most pronounced for homogeneous particle encounters. Using three basis functions resulted in a saddle surface, which disappeared partly when regularisation was increased. Four basis functions showed similar behaviour as two basis functions, but the increase is steeper for large values of the similarity variable. Also, the aggregation frequencies were found to be higher in absolute value.

When recovering the unscaled kernel, it was found that the kernel was not homogeneous (a negative power was found) and, hence, the recovery was based on the mere multiplication of the scaled kernel by h'(t) which was derived from the dynamics of the scaling variable h(t). This implies that all derived kernels are time-dependent. Once the unscaled kernel was found, it was used in a forward simulation to check the quality of inversion. Most cases captured the dynamic behaviour of the volume percentage distributions quite well, but the kernel values had to be multiplied by a constant factor in order to work. Increasing the regularisation parameter λ_{reg} always improved the prediction. The highest number of basis functions (4) combined with the highest tested regularisation ($\lambda_{\mathrm{reg}} = 1$) was found to give the best prediction, only underestimating the lower tail of the distribution.

Finally, predictions of number distributions were generated with the model and compared with the experimental number distributions. Here, it was noticed that little dynamics occur in the number distribution. The underestimation of the lower tail in the volume percentage distribution causes a severe underestimation of the small floc size classes. Moderate and large floc sizes were predicted very accurately when a large number of basis functions was used. The prediction of the number distribution seems to improve as the number of basis functions increases. Investigating higher values of n_b is, therefore, recommended for future research.

In the pure breakage case, the similarity distribution could not be fitted by means of γ-functions due to the large range of the absolute value of the similarity variable. Even a logarithmic conversion did not result in a good fit. Therefore, the cumulative similarity distribution was fitted using a Weibul expression. This fit was then used to fit the left-hand side and the right-hand side of the similarity-PBE. Unfortunately, problems occurred due to the singularity near the origin and the blow up of the integrand caused by the large values of the similarity variable.

It was tried to cure the latter problem by using modified basis functions which could handle the singularity. Using this approach, a good fit could be obtained. However, increasing the number of basis function resulted in a deterioration of the fit. The constant value of the breakage rate (β) was determined to be 1.5 and, hence, the breakage rate as function of volume was established. However, the breakage rates are very large for larger particles. An expression for the daughter distribution was recovered.

The forward simulation was only conducted for the case with two basis functions because increasing the number of basis functions deteriorated the fit obtained by the expansion. However, the model using the breakage rate and the daughter distribution function recovered from data inversion was not able to describe the experimental data. This is probably caused by the fact that a multiplication factor was necessary to avoid numerical problems (i.e. large derivatives). Future work might comprise of adopting the model structure from inversion and estimate its parameters.

CHAPTER 12

Conclusions and perspectives

The separation step between purified water and the activated sludge flocs still remains a delicate issue in wastewater treatment. Nowadays, the popularity of membrane bioreactors is increasing, despite their higher investment and operational cost. In future it is believed that this more recent technology will outcompete the conventional secondary settling tanks. However, this technology has its operational problems too (e.g. fouling), which should be thoroughly investigated when future application on a wider scale is pursued. On the other hand, some people argue that this membrane technology is partly 'missing its goal' from an engineering point of view since it was designed for high-level separation which is not really the aim in wastewater treatment. During the last decades, a lot of research money was invested in gaining knowledge concerning secondary settling tanks, bringing it to a level where one can guarantee good performance and identify future optimisation paths (a lot of systems are operated in a very conservative way). Stepping away from this conservatism and using the gained knowledge might open doors for alternative uses of the available volume in the secondary settling tank (e.g. biological processes, buffer tank during rain events,...). This would make the technology a lot more attractive and competitive and finally there would be a payback for the years of financial investment in this area.

This illustrates that the evolution of the 'separation market' in wastewater treatment could be significantly influenced by improvements in either technology. The work performed in this dissertation is closely related to this important issue since, as was stated in the introduction and literature review, a better comprehension of secondary settling tank failure and membrane fouling are closely related to the mechanisms of activated sludge flocculation. An improved understanding of the latter would allow its optimisation and, hence, give rise to a significant improvement of the separation step in wastewater treatment technology, either conventional activated sludge systems or membrane bioreactors.

As outlined in the introduction, the focus of this work was to investigate the applicability of a population balance framework for modelling the activated sludge flocculation process and influencing factors. This analysis consists of several separate issues which should be treated in a logical order.

- Investigation of numerical solution methods for solving the population balance equation

- Development of a comprehensive calibration procedure based on typical experimental flocculation data sets
- Model structure identification
- Perform flocculation experiments that investigate different physico-chemical influences on the activated sludge flocculation process
- Calibrate the flocculation model based on these experimental data

This sequence of major steps was reflected in the organisation of this dissertation. In the remainder of this chapter, the main conclusions and perspectives for further research are addressed.

12.1 Numerical solution methods for population balance models

Due to their potential for acceptable calculation times and their compatibility with the simulation environment WEST (Hemmis NV, Belgium)) that was adopted in this work, the search for a suitable solution method was constrained to discretisation techniques only. A simulation study was set up that aimed at evaluating several important issues of a solution method, i.e. ease of implementation, flexibility, accuracy, computational performance and stability and pitfalls. The study investigated three methods from literature: the Hounslow algorithm, the fixed pivot and the moving pivot method. They were applied to solve population balance models for pure aggregation, pure breakage and the combined aggregation/breakage case. Other degrees of freedom in the evaluation were the coarseness of the discretisation grid and the effect of the initial distribution. To the author's knowledge, it was the first time that such a detailed study of a (limited) number of discretisation methods was performed.

It was found that the Hounslow method can be implemented quite easily, although one should be cautious to avoid mass leakages when implementing the boundary conditions. The fixed pivot and the moving pivot are somewhat more tedious to implement and here too the correct implementation of the boundary conditions is important. A subtle difference between the two methods is present in the fact that the mathematical grid range is different.

For the pure aggregation case, it was found that the moving pivot with a geometric factor of 2 yielded the best results. Both the Hounslow and fixed pivot technique suffered from a slowdown in aggregation due to the difference in grid range. Moreover, the observed slowdown was dependent on the initial state of aggregation. This influence of the numerical technique on the simulation results is unacceptable. When using a finer grid, a symptom which was called 'particle entrapment' was detected. It leads to the phenomenon that particles cannot move out of the one but last class, since their volume exceeds the maximum allowed particle size. This behaviour can also be present when using the moving pivot. However, the larger range of allowable particles that is intrinsic to this method makes it less probable. Coarser grids decrease the calculation times, but are found to be less accurate. Hence, the choice of solution method will be a trade-off between accuracy and speed of simulation.

The pure breakage case that was studied involved breakage into equally sized daughter particles. It was found that all grids using a geometric grid using a factor s=2 are superior to tackle this problem. All solution methods performed equally well. Using coarser grids resulted in numerical problems, necessitating the use of less efficient solvers that increase the calculation time substantially. Consequently, since a fast method is looked for, coarse grids should not be used for this particular type of breakage. Refining

the grid again induced the phenomenon of particle entrapment and is not recommended either. Another pitfall was addressed for the specific case where the moving pivot with a geometric grid with factor $\mathrm{s} < 2$ was used in combination with binary breakage into equally sized daughters, i.e. the appearance of gaps in the distribution. This is caused by a specific movement of the pivots in some particle size classes. This causes particles not to be formed in the lower adjacent size class, but one class lower. This forces partial depletion of particles in this lower adjacent class, resulting in gaps in the distribution. Hence, it can be concluded that binary breakage into equally sized daughters should always be used in combination with a geometric grid with factor $\mathrm{s} \geq 2$. This severely limits the grid choice and might induce an adaptation of the grid of the sizing device by changing the software settings prior to the measurement (if possible). It was shown that the reasoning can be extrapolated to specific breakage cases where η equal particles are formed from one breakage event in combination with the moving pivot method. The geometric grid factor s must then meet the constraint $\mathrm{s} \geq \eta$. This constraint might affect the accuracy of the solution method.

The combined aggregation/breakage case gave rise to differences in accuracy and calculation times. In terms of accuracy, the moving pivot was found to be superior even for coarse grids. Indeed, refining the grid in the fixed pivot case forces the solution to approach that of the moving pivot as was reported in literature too. However, the calculation time needed by the moving pivot was significantly larger, which is definitely a drawback of the method. Hence, the decision on what solution method to use will be case dependent and a trade-off between accuracy and speed of simulation. In the cases studied here, the moving pivot was found to be superior since only a relatively small number of classes was needed to reach an acceptable degree of accuracy.

This investigation of the best solution method was clearly limited by a lot of constraints, an important one being the type of solution methods that were studied. Hence, it should be clearly stated that this work does not claim that discretisation methods are the best solution methods for studying the activated sludge flocculation process using a population balance framework. Rather, feasibility studies in terms of calculation speed and accuracy of other solution methods should be performed when one is to choose a solution method for a problem at hand. This might be a perspective for future research that would support the choice of solution method. The development of a methodology might be appropriate here, since this choice is not evident for people that want to merely apply a population balance model, but do not have the background to judge different solution techniques. The overview given by Ramkrishna (2000) would definitely be a good starting point, but it is already outdated due to the fast developments in the field of population balances.

12.2 Development of a comprehensive calibration procedure based on typical experimental flocculation data sets

When calibrating a population balance model by means of typical dynamic experimental flocculation data, one comes across several issues that call for a solution. Before elaborating on the issue of model structure, it is therefore of interest to properly address the calibration issues. Hence, a comprehensive calibration methodology was developed in this work.

The issues that were dealt with were: data transformation for compatibility between model and experimental data, treating experimental errors and choice of variable to fit the model to.

12.2.1 Data transformation

Data transformation should be avoided as much as possible. However, in some cases it might be needed (i.e. to calculate the initial distribution for the model). It was found that the approach adopted by Biggs (2000) that fitted the dynamic distributions using a log-normal distribution, is not recommended as it introduces large errors in the number distributions. This is caused by the fact that the log-normal distribution cannot capture the tails of the distributions. Hence, an alternative method based on the heterogeneous floc model was presented. This enables the conversion from relative to absolute volumes by means of the sludge concentration, and the water, floc and solids densities.

In order to apply this new approach, the experimental determination of the densities of flocs and solids within the flocs is needed. Therefore, this was also briefly investigated in this work. The solids density can be determined by a method called pyknometry which was adopted from the field of soil science. The method resulted in larger values ($1.60\,\mathrm{g.ml^{-1}}$) than those reported in literature ($1.45\,\mathrm{g.ml^{-1}}$). However, further testing of the method is needed and was beyond the scope of this work. The floc density was determined by using a method based on a linear density gradient of Percoll. The results that were found were comparable to values reported in literature (1.02-$1.06\,\mathrm{g.ml^{-1}}$). However, the method did not allow accurate measurements due to the low resolution of the density gradient. Hence, further development of the method is recommended.

Preliminary testing of the new approach for determination of the number distribution showed that parameter estimates of the aggregation efficiency were indeed more realistic.

12.2.2 Experimental errors

Measurement errors on a summarising variable such as D[4,3] can be easily determined from a repetition of measurements during steady state. However, it should be noted that it might be dangerous to conclude the onset of steady state based on a summarising variable as changes might still be occurring which are not captured by this variable (e.g. changes in small size classes will not be detectable by the volume-based D[4,3]). Another difficulty that has been observed is the 'background' flocculation resulting in a continuous increase in D[4,3]. Determining the errors of the separate classes of a number distribution is, however, a more difficult task. A similar approach as used with the D[4,3] is not applicable since the background flocculation can not be quantified for single particle classes. The method that is proposed here to obtain an estimate of the measurement error is based on the fact that the measurement is a counting of particles. In that respect, the measurement error can be regarded as the variance of a multinomial distribution.

12.2.3 Choice of the variable to which the model is fitted

A final important issue that should be dealt with during calibration is the choice of variable to which the model will be fitted. Four possibilities were compared, i.e. D[4,3], volume percentage, number distributions and weighted number distributions. Fitting to either D[4,3] or volume distribution resulted in good predictions of the volume distributions, although it should be noted that prediction of the tails were rather poor. Predictions of the number distributions using volume-based fitting variables were poor too. Fitting to number distributions resulted in poor predictions of the volume distribution. However, an increased prediction quality of the number distributions was observed.

It was concluded that the choice of fitting variable is, therefore, highly dependent on the goal of the calibration exercise. If one is satisfied with good predictions of the volume distribution, a volume-based variable is recommended. However, since interest here lies in prediction of the number concentration of small particles (that end up in the treatment plant's effluent), fitting on number distributions is more appropriate in this work. At this stage, the discrepancy between the model predictions and the experimental data is blamed on the inadequate model structure. Therefore, this was the next issue that was addressed in this work.

12.3 Model structure identification

The identification of the model structure is considered to be another important step in the process of determining the feasibility of applying a population balance framework to the activated sludge flocculation. Two different approaches can be followed. A first one is to use existing models that were formulated and applied in literature. An alternative approach is to extract the model structure from experimental aggregation and breakage data through a mathematical method called inversion. Both alternatives were investigated in this work.

12.3.1 Approach 1: model structures from literature

According the first approach, a selection of literature models for aggregation and breakage that had been applied to similar inorganic flocculating systems was made. Four models were chosen by combining different kernels for aggregation and breakage incorporating different degrees of complexity and were fitted to the dynamic number distributions of shear-induced flocculation experiments (starting from a sonicated sludge) by means of a least squares method.

The first and most simple model used a constant aggregation efficiency, a shear-based, orthokinetic aggregation frequency and a power law breakage. The model was not able to capture the dynamics of the number distributions. Lowering the exponent of the power law breakage function to 1/9 resulted in a substantial improvement.

The second model applied the concept of fractal dimension in the aggregation frequency. When using a decreased exponent, a similar predictive power was observed as model 1. However, the fractal dimension concept is thought to be more transparent since the concept has been described before for activated sludge. The remaining discrepancy might be decreased by using a size-dependent fractal dimension, which was not studied in this work but is suggested for further research.

Model 3 incorporated a size-dependent aggregation efficiency accounting for hydrodynamic forces and Van der Waals interaction. However, this injection of knowledge did not improve the predictions of the dynamic number distributions. On the contrary, it even seems to have an opposite effect. A suggestion for further research here is to combine this model with the fractal dimension concept introduced in model 2.

Model 4 introduces the porous floc aggregation efficiency, the fractal dimension concept and a breakage rate based on turbulent shear. This model was also unable to capture the dynamics of the number distributions.

Overall, from this 'quest' for an appropriate model structure, it was concluded that it is a time consuming

approach and it did not result in any model that was able to capture the dynamics of the number distributions adequately. A lot of different combinations of model structures for aggregation and breakage are possible, but this would result in a search for a needle in a haystack. Therefore, this approach was put aside after this preliminary run. However, in future research, other model combinations might be further investigated.

12.3.2 Approach 2: solving the inverse problem for aggregation and breakage

The second approach is based on extracting the unknown aggregation and breakage functions directly from the experimental data of aggregation and breakage experiments respectively. This is accomplished by solving the inverse problem. This approach has never been applied to activated sludge flocculation and only a few applications based on experimental data are so far available in literature. The inverse problem is simplified when self-similar behaviour is present in the experimental data. Therefore, a similarity analysis was performed first.

Pure aggregation

In search for similarity for aggregation, a similarity analysis was conducted on the aggregation data set where reflocculation was allowed from a sonicated sludge. The necessary requirements for the applicability of the similarity analysis for pure aggregation, i.e. that breakage can be neglected, could be recovered from a thorough distribution analysis. However, no similarity was found for any scaling based on subsequent integral moments of the distribution. However, other data sets of experiments that initiated reflocculation from a sludge previously exposed to high shear did exhibit self-similar behaviour. Hence, it was concluded that flocculation behaviour is different in both cases. Since sonication is not applied in full-scale treatment plants, it can be concluded that flocculation dynamics from a sonicated sludge are not representative for the dynamic behaviour that is looked for in this research. Hence, the experiments using sonication for destruction of flocs were discarded from this moment on. This is also suggested for any future experimental investigation of activated sludge flocculation.

As a result of this conclusion, the first approach for determination of model structure had to be repeated by using the data of the experiments where shear instead of sonication was used for floc destruction. Investigating model 1, however, showed that the optimisation algorithm was very sensitive to the initial parameter values and, moreover, the variance of the parameter estimates was very large or could not be calculated due to identifiability problems. This makes these predictions very doubtful. In order to track the reason for this failure, a screening of the objective function in the entire parameter space was conducted by means of a scenario analysis. The analysis of the parameter space resulted in the finding that a large part of the parameter space is a plateau exhibiting similar objective values, which explains the sensitivity of the parameter estimates to the initial parameter values. Moreover, the best fit was found for parameters in the origin, meaning that no dynamics would be required for predicting a dynamic dataset, which is clearly a contradictory result. Since these problems were already encountered for the most simple model (model 1), the more complex models were not further investigated as they are expected to yield similar results. However, this might be the subject of further efforts.

The presence of similarity allows for a simplified solution of the inverse problem. In this work, a stepwise procedure for solving the inverse problem for aggregation using a combination of a worksheet and some simple scripting in Matlab (Mathworks Inc., USA) was developed. The similarity distribution was successfully fitted by means of an expansion of 2 γ-functions. The inverse problem was then solved for

different numbers of basis functions per axis and different values of the regularisation. Good fits of the right-hand side to the left-hand side of the population balance equation were obtained, although no major influence of the number of basis functions and the regularisation were observed.

In the next step, the unscaled aggregation frequency was determined. It was found from the behaviour of the scaling function h(t) that the kernel was not homogeneous and, hence, that the normal procedure presented in Ramkrishna (2000) could not be followed. Instead, a more general approach had to be adopted to calculate the unscaled kernel. It was based on the product of the scaled aggregation kernel found through inversion and the dynamic behaviour of the derivative of the scaling function, i.e. h'(t). The shape of the unscaled aggregation kernel changed for different numbers of basis functions used. When using two basis functions per axis, a monotonic increasing kernel (i.e. aggregation frequencies) was found for increasing particle sizes. Using three basis functions per axis resulted in a saddle surface. However, the shape changed when regularisation was increased. When using four basis functions a similar shape as in the case with two basis functions was obtained, although larger collision frequencies were found and the increase in frequency started only at intermediate floc sizes.

Finally, the quality of the inversion was checked by performing a forward simulation using the obtained kernel structures. This resulted in good results for all cases, taken into account that an additional factor had to be used. Still, when four basis functions were used the best results were obtained. Apart from the lower tail (at small floc sizes), the dynamics of the volume distributions were described accurately. However, the prediction of the number distributions suffered from severe underpredictions in the lower size range, which corresponds to the rather poor prediction of the lower tail in the volume distribution. Again, the prediction improved when the number of basis functions was increased. Not more than four basis functions were investigated at this point, but this is recommended for further research.

Pure breakage

The necessary requirements for the applicability of the similarity analysis for pure breakage, i.e. that breakage can be neglected, could be recovered from a thorough distribution analysis. Similarity analysis showed that the experimental breakage data sets exhibited self-similar behaviour too. The scaling function was found to be dependent on a constant slope of the ln(x) versus ln(t) plot which was found to be -3.7. This means that the breakage rate can be determined up to a constant and by a power law of the floc size using an exponent of 3.7.

Due to the large range of the similarity variable, the expansion with γ-functions was not successful. Alternatively, a Weibul function was fitted to the cumulative similarity distribution. However, due to singular behaviour in the origin (division by zero) the fit of the right-hand side to the left-hand side of the population balance equation was very poor. Therefore, the Legendre polynomials that were used in the expansion of the cumulative daughter distribution, was modified to cure this problem. This resulted in a reasonable fit of the right-hand side to the left-hand side. However, the result deteriorated when the number of basis functions was increased. Therefore, only the case with two basis functions was considered in the remainder.

For this case the remaining unknown constant in the breakage rate β was determined to be 1.5. This resulted in rather large breakage rates for large particles. Furthermore, the plain daughter distribution $\mathrm{P}(\mathrm{x}|\mathrm{x}')$ could be extracted from the cumulative daughter distribution g(u).

In order to check the quality of the inversion, the forward simulation was performed. However, due to the large breakage rates, numerical problems occurred since large dynamics are present which forced

the solver to substantially reduce its step size or even caused failure of convergence. In order to cure this, an additional factor was introduced to artificially decrease the breakage rates. However, the forward simulation did not yield good results as the absolute breakage rates of large particle still seem to be too large compared to those of small particles. Further research is needed here to identify the exact cause of this behaviour and obtain a good description of breakage.

Combined aggregation and breakage

Once the problem with the inverse problem for breakage is solved, the kernels obtained from both inverse problems can be combined and the forward simulation be evaluated. This should be subject of further research.

12.4 Experimental data collection

In a next step, experimental data are needed to study the physico-chemical influences of activated sludge flocculation. Obtaining suitable experimental data has long been the bottleneck in studying and modelling the activated sludge flocculation process. Recent developments have resulted in an on-line measurement technique that allows to follow the floc size distribution in time. However, most researchers attempt to model a summarising parameter of the distribution, e.g. D[4,3], even though distributions contain a lot more information about the proces being studied. The distributions at hand are suitable for modelling by means of population balances. Therefore, some existing data from literature were analysed focusing on the distribution behaviour. New data were collected with the Flocunit and were analysed in a similar fashion.

The different shear rate experiments exhibited different behaviour for different size classes depending on the floc size to Kolmogorov microscale relationship. Flocs smaller than this scale will aggregate, whereas larger flocs will be broken. Hence, the most abundant floc size should have a similar size as this scale. In aggregation experiments size classes larger than the Kolmogorov scale increase monotonously toward an equilibrium, smaller classes reach a maximum and subsequently decrease to reach a steady state, whereas the smallest classes do not exhibit such a peak behaviour. Furthermore, the estimate of the Kolmogorov scale by using the 10-fold of the average energy dissipation seemed to be a reasonable assumption for the literature data studied. This was, however, not found for the Flocunit experiments. Possibly the different reactor configuration is causing this, which could be verified by means of a CFD model.

The literature experiment with the sequence of step changes in average shear rate showed similar results when solely looking at a summarising parameter. However, (de)flocculation behaviour is clearly different when looking at the complete distributions. Comparing the reflocculation after sonication and increased shear rate respectively, showed that the initial number of small particles is much larger in the former case. Whereas all classes smaller than the Kolmogorov scale exhibited a peak in the former case, this was not true for the increased shear rate case. Also, the size class exhibiting the largest vol% was somewhat smaller, suggesting more compact flocs. This leads to an important conclusion: sonication prior to the experiment seems to induce a different kind of flocculation compared to break-up through shear. Hence, sonication is not representative for the flocculation occurring in a real full-scale treatment plant. Lab-scale studies should, therefore, not apply sonication in order to understand the activated sludge flocculation behaviour.

Experiments performed in the Flocunit showed more measurement noise, which might be related to the reactor configuration (different volume and many obstacles), reactor volume and the sampling procedure, which was not based on recirculation. However, when discarding the noise, the main trends could still be distinguished.

The 'standard' initial part of all experiments in the design could not prevent that initial distributions were different. The previously used relationship between average shear intensity and Kolmogorov scale appeared not to be a good assumption here. This was reasoned to be caused by differences in reactor configuration and differences in floc strength (resistance to stress).

The conclusions drawn from the CIS-100 measurements in terms of total number of flocs are the same as those obtained from the Malvern measurements. However, the number distributions are too noisy and cannot be used for model calibration on the basis of particle size distributions. This is merely caused by the fact that this technique is based on counting and is hence more sensitive to noise.

Basically, the conclusions that are drawn based on the evolution of the mass mean diameter or from the complete distributions are the same. However, many details, e.g. moving of fronts (i.e. size distributions moving along the size axis), most abundant floc size, floc size classes that are affected by changes in operational conditions,... are lost when using summarising parameters. Many distributions can exhibit a similar mass mean diameter, and, hence, many models can describe these data without capturing what really is happening. This doesn't mean that summarising parameters are useless. On the contrary, they are very useful for getting a first impression of the dynamics of a process.

To summarise the effects of the different factors that were investigated in the design:

- Shear has an important effect on the activated sludge flocculation. High shear destroys flocs and shifts distributions toward smaller sizes. Low shear allows larger flocs to be present in the system. The addition of calcium confirms the hypothesis of floc strength playing an important role. Even at high shear a partial reflocculation was observed after Ca-addition. From a modeller's point of view, the dynamics at high shear cannot be investigated since the measurement frequency with the available set-up was too low to capture the very fast flocculation dynamics.

- Flocs are not disturbed when temperature is lowered. However, some immediate flocculation occurs when temperature is increased. Addition of calcium results in stronger flocs at lower temperatures.

- Applying anaerobic conditions showed an immediate increase in floc size. However, Ca-addition leads to stronger flocs when the DO-concentration is higher.

- At low sludge concentration, a slow deflocculation can be observed, caused by the smaller collision probability. This can also be observed when Ca is added. The largest concentration results in the largest floc size.

- Ca-addition results in flocculation. However, the results clearly show that the degree of flocculation is not proportional to the amount of Ca added. A slow background flocculation was observed when no Calcium was added.

In order to capture the very fast dynamics that were observed in some cases (and could not be captured by the measuring devices), two strategies can be followed in future work. The measurement frequency could be increased, but this might decrease the statistical soundness of the data and is not recommended.

Alternatively, the design could be adapted in the sense that different factor values are used that limit the speed of the dynamics.

Furthermore, the existing (rich) data set could be further analysed to extract more useful information on the flocculation that could be used in the modelling exercise (e.g. fractal dimension from the image analysis data).

Additional information on the hydrodynamic flow patterns within the Flocunit which are closely related to the flocculation behaviour could be obtained by building a CFD-model.

12.5 Model calibration based on the gathered experimental data

This forms the ultimate step in completing the evaluation of the appropriateness of the population balance framework for the modelling of activated sludge flocculation. Moreover, it should be possible to include descriptions for the effect of the different investigated physico-chemical conditions into the derived kernels. Therefore, the experimental data obtained by the Flocunit that show analogous dynamic behaviour (e.g. in case of Ca-addition) can also be analysed for similarity and if similarity would be found, the inverse problem can also be solved for these experiments, leading to model structures that can capture the behaviour in these very different conditions. The necessary requirements for applicability of the respective similarity analysis for pure aggregation/pure breakage have already been proven in the thorough distribution analysis. This should lead to a model that can be used to optimise the activated sludge flocculation and, hence, the separation step of the wastewater treatment process. However, the time scope of this thesis did not permit to investigate this step. Hence, this is suggested as a perspective for further research.

12.6 Overall conclusion

This work provides a significant step forward in the evaluation of the appropriateness of the population balance framework to describe the activated sludge flocculation process. The moving pivot is suggested to be used as discretised solution method, yielding the best compromise between accuracy and simulation speed. It can be used with a relatively coarse grid, avoiding possible pitfalls that were addressed. A comprehensive calibration methodology was presented that provides specific solutions for data transformation, determination of measurement errors and choice of fitting variable in the case of activated sludge flocculation. The data transformation can be done on the basis of relatively easy to measure sludge properties, i.e. sludge concentration and floc/solid densities. Measurement errors of number distributions can be determined on the basis of a multinomial distribution. Number distributions were found to be more relevant as fitting variable. However, applying this calibration methodology to experimental data for existing literature models revealed that none of them was able to capture the dynamics of the number distribution. An alternative approach based on the solution of the inverse problem and the exploitation of self-similarity was tested. The similarity analysis revealed that sonication induces different flocculation dynamics and is not recommended since it is not representative for flocculation occurring in full-scale. Similarity was found for both aggregation and breakage and was used to extract the respective kernels. The latter was successful for the aggregation case where a forward simulation was able to predict the dynamic behaviour of the experimental data. The forward simulation in the breakage case failed and more work is needed. Finally, additional experimental data were collected that will allow

for future investigation of several physico-chemical factors using the tools that were developed throughout this work. This will eventually lead to a model that is able to capture the flocculation behaviour in these very different conditions that might be present in a real wastewater treatment plant. Such a model would allow for the optimisation of the separation step, either the traditional gravitational or the more recent membrane-based technology and, hence, have a significant impact on the further evolution of this 'separation market'.

APPENDIX A

Turbulence

A.1 The velocity-gradient tensor

A discrete volume element of viscous fluid that is in motion and contains a homogeneous distribution of spherical particles is considered. The volume element is sufficiently small within the fluid domain so that linear velocity-gradients act on the element. The particles are assumed to have neutral buoyancy so that any inertial effects can be ignored. It is also assumed that the fluid element is a continuum and any movement imparted on the fluid also affects the particles. The motion of the fluid element and the forces acting on it generate velocity gradients across the surfaces of the element. This can be described by the velocity-gradient tensor e, given by (Kramer and Clark, 1997):

$$e_{lm} = \frac{\partial u_l}{\partial x_m} = \frac{1}{2}\left(\frac{\partial u_l}{\partial x_m} + \frac{\partial u_m}{\partial x_l}\right) + \frac{1}{2}\left(\frac{\partial u_l}{\partial x_m} - \frac{\partial u_m}{\partial x_l}\right) \tag{A.1}$$

where l and m represent either of the 3 orthogonal directions in the 3-dimensional space. This tensor can be separated into symmetric and anti-symmetric components. The anti-symmetric component $\mathrm{b_{lm}}$ corresponds to rotation

$$b_{lm} = \frac{\partial u_l}{\partial x_m} = \frac{1}{2}\left(\frac{\partial u_l}{\partial x_m} - \frac{\partial u_m}{\partial x_l}\right) \tag{A.2}$$

while the symmetric component $\mathrm{a_{lm}}$ is the strain-rate tensor

$$a_{lm} = \frac{\partial u_l}{\partial x_m} = \frac{1}{2}\left(\frac{\partial u_l}{\partial x_m} + \frac{\partial u_m}{\partial x_l}\right) \tag{A.3}$$

which causes physical distortion of the fluid element. For a constant e, the strain rates are constant within the boundaries of the fluid element. An example of such an element is shown in Fig. A.1. The origin moves with the component velocities $\mathrm{u_1}$, $\mathrm{u_2}$ and $\mathrm{u_3}$. Due to the velocity gradients, the velocities at a distance away from the xy, yz and xz-planes will be changed by an amount $\mathrm{e_{lm}dx_m}$ in the component l

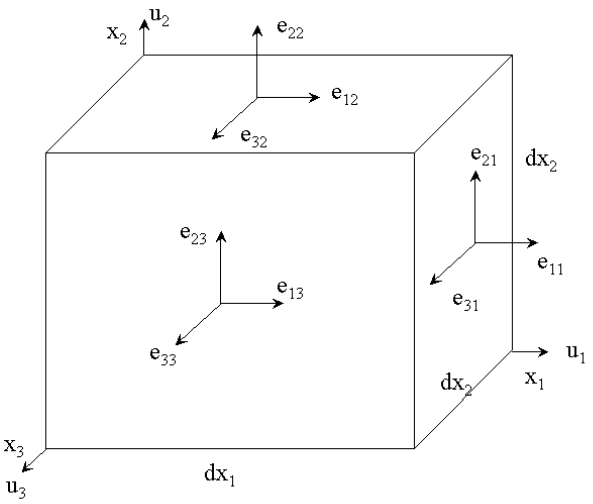

Figure A.1: Fluid element and graphical representation of the velocity-gradient components

direction. Summation on the common index is implied and $\mathrm{dx_m}$ is the distance from the datum in the m direction.

While the velocity gradients cause distortion of the fluid element, the gradients also generate rotations. This occurs when $\mathrm{e_{12}} \neq \mathrm{e_{21}}$, $\mathrm{e_{13}} \neq \mathrm{e_{31}}$ and $\mathrm{e_{32}} \neq \mathrm{e_{23}}$. In collision modelling, the main concern is the relative velocity between points in the element. The strain-rate tensor is established by the velocity gradient tensor, but only the strain-rate tensor results in the physical distortion of the fluid element. This distortion causes points within the fluid element to move towards (or away from) each other. This fluid element distortion and, hence, relative movement of particles within the fluid element was illustrated for pure normal strain motion ($\mathrm{l} = \mathrm{m}$) in Fig.2.22 and pure shear strain motion in Fig.2.23. Fig.2.24 showed that rotation does not contribute to the relative movement of particles.

An important point to consider is the effect of including the rotational component of the velocity gradient on a collision model. When it is accounted for, it will introduce an error in the true relative velocity, which can be large in flows with a large rotational component. Hence, the rotational component should not be taken into account when calculating collisions. The computation of the collision rate should, therefore, only involve the aforementioned normal and shear components.

A.2 Absolute maximum principal strain rate

Incorporating all nine components of the strain-rate tensor in the calculation of the collision rate will result in incorrect estimates and, hence in an inaccurate population balance. The improper counting results from a failure to consider the direction of the strain-rate induced velocities. Negative values will result in velocities toward each other, whereas positive values will have the opposite effect. This error will always occur, since positive and negative strain-rates need to occur to satisfy continuity. Therefore, only the strain rates that induce velocities toward one another must be considered and those resulting in velocities causing movement away from each other must be eliminated.

In order to simplify the calculations, the number of collision equations should be reduced. Since the strain-rate tensor is symmetric, it can be diagonalised

$$\begin{bmatrix} a_{11} & a_{12} & a_{13} \\ a_{21} & a_{22} & a_{23} \\ a_{31} & a_{32} & a_{33} \end{bmatrix} = \begin{bmatrix} a'_{11} & 0 & 0 \\ 0 & a'_{22} & 0 \\ 0 & 0 & a'_{33} \end{bmatrix} \tag{A.4}$$

where the primed values ($\mathrm{a}'_{\mathrm{lm}}$) are the principal strain-rates that act in the principal directions. Also it can be shown that

$$a'_{11} \geq a'_{22} \geq a'_{33} \tag{A.5}$$

$$a'_{11} + a'_{22} + a'_{33} = 0 \tag{A.6}$$

This induces that a'_{11} is always positive, a'_{33} is always negative and a'_{22} is either positive or negative. It can be concluded that the maximum of $|\mathrm{a}'_{11}|$ and $|\mathrm{a}'_{33}|$ should be used to compute the collision rate. This value is called the *absolute maximum strain-rate*.

APPENDIX B

Self-similarity and the inverse problem

This appendix contains some explicit mathematical developments that were mentioned in Section 2.5.6 and should allow better comprehension.

B.1 Self-similar cumulative mass fraction

The equation for the cumulative mass fraction is given by

$$F_1(x,t) = \frac{\int_0^x x' f_1(x',t)dx'}{\int_0^\infty x' f_1(x',t)dx'} \tag{B.1}$$

Taking into account the definition of similarity being

$$f_1(x,t) = g(t)\Psi(\eta) \qquad \eta \equiv \frac{x}{h(t)} \tag{B.2}$$

we obtain

$$F_1(x,t) = \frac{\int_0^x \eta' h(t)^2 g(t)\Psi(\eta')d\eta'}{\int_0^\infty \eta' h(t)^2 g(t)\Psi(\eta')d\eta'} \tag{B.3}$$

resulting in

$$F_1(x,t) = \frac{\int_0^\eta \eta'\Psi(\eta')d\eta'}{\int_0^\infty \eta'\Psi(\eta')d\eta'} \equiv \Phi(\eta) \tag{B.4}$$

B.2 g(t) and h(t) in terms of higher integral moments

The k^{th} integral moment of $\mathrm{f_1(x,t)}$ is expressed as

$$\mu_k(t) = \int_0^\infty x^k f_1(x,t)dx \tag{B.5}$$

Transforming this into the similarity variable yields

$$\mu_k(t) = \int_0^\infty \eta^k h(t)^k g(t)\Psi(\eta)h(t)d\eta = h(t)^{k+1}g(t)\int_0^\infty \eta^k\Psi(\eta)d\eta = h(t)^{k+1}g(t)\mu_k(\eta) \tag{B.6}$$

In a similar fashion $\mu_{k+1}(t)$ can be calculated

$$\mu_{k+1}(t) = h(t)^{k+2}g(t)\mu_{k+1}(\eta) \tag{B.7}$$

Imposing the constraint

$$\mu_k(\eta) = \mu_{k+1}(\eta) = 1 \tag{B.8}$$

leads to the following set of equations

$$\mu_{k+1}(t) = h(t)^{k+2}g(t) \qquad \mu_k(t) = h(t)^{k+1}g(t) \tag{B.9}$$

which can be solved to yield

$$h(t) = \frac{\mu_{k+1}(t)}{\mu_k(t)} \qquad g(t) = \frac{\mu_k(t)^2}{\mu_{k+1}(t)} \tag{B.10}$$

B.3 Derivation of the PBE in terms of the similarity variable for pure breakage

The equation of pure breakage in terms of the cumulative number density $\mathrm{F_1(x,t)}$is given by

$$\frac{\partial F_1(x,t)}{\partial t} = \int_x^\infty b(x')G(x|x')\partial_{x'}F_1(x',t) \tag{B.11}$$

We denote the self-similar cumulative number density as $\Phi(\eta)$ and assume power law breakage

$$b(x) = Kx^\alpha \tag{B.12}$$

and assume that the cumulative daughter distribution is function of the ratio of the breaking particle x' and the particle x, i.e. $\mathrm{G(x|x')} = \mathrm{g}\left(\frac{\mathrm{x}}{\mathrm{x'}}\right)$. The following transformations can be performed

$$\frac{\partial F_1(x,t)}{\partial t} = \frac{d\Phi(\eta)}{d\eta}\frac{d\eta}{dt} = -\Phi(\eta)\eta\frac{h'(t)}{h(t)} \tag{B.13}$$

$$b(x') = Kx'^\alpha = K(\eta' h(t))^\alpha \tag{B.14}$$

$$G(x|x') = g\left(\frac{x}{x'}\right) = g\left(\frac{\eta}{\eta'}\right) \tag{B.15}$$

resulting in

$$-\eta\Phi'(\eta)\frac{h'(t)}{h(t)^{\alpha+1}} = K\int_\eta^\infty \eta'^\alpha g\left(\frac{\eta}{\eta'}\right)d\Phi(\eta') \tag{B.16}$$

The right-hand side is independent of time. Therefore, we should impose the following constraint on the left-hand side to also make it time-independent

$$h'(t) = -ch(t)^{\alpha+1} \tag{B.17}$$

The latter can ultimately be solved to yield a possible similarity variable $\eta = \mathrm{b(x)t}$ for c=K. The PBE then becomes

$$\eta\Phi'(\eta) = \int_{\eta}^{\infty} g\left(\frac{\eta}{\eta'}\right)\eta'\Phi'(\eta')d\eta' \tag{B.18}$$

In practice, however, the similarity variable (η) is unknown. Redefining it as

$$\hat{z} = \frac{\eta}{b(x_0)} \tag{B.19}$$

allows the transformation to be completely known using the experimental data and eq. 2.91. In order to obtain the PBE in the new similarity variable $\hat{z}$, the following transformations need to be used

$$\Phi'(\eta) = \frac{\Phi(\eta)}{d\eta} = \frac{d\Phi(\hat{z}b(x_0))}{d\hat{z}b(x_0)} = \frac{\Phi(\hat{z})}{d\hat{z}} \tag{B.20}$$

$$g\left(\frac{\eta}{\eta'}\right) = g\left(\frac{\hat{z}}{\hat{z}'}\right) \tag{B.21}$$

$$\Phi'(\eta')d\eta' = \frac{d\Phi(\hat{z'}b(x_0))}{d\hat{z'}b(x_0)}d\hat{z'}b(x_0) = b(x_0)\Phi'(\hat{z'})d\hat{z'} \tag{B.22}$$

This results in

$$\hat{z}\Phi'(\hat{z}) = b(x_0)\int_{z}^{\infty} g\left(\frac{\hat{z}}{\hat{z}'}\right)\hat{z}'\hat{\Phi}'(\hat{z}')d\hat{z}' \tag{B.23}$$

Defining

$$u = \frac{\hat{z}}{\hat{z'}} \tag{B.24}$$

and

$$du = \frac{1}{\hat{z'}}d\hat{z} - \frac{\hat{z}}{\hat{z'}^2}d\hat{z'} = -\frac{\hat{z}}{\hat{z'}^2}d\hat{z'} \tag{B.25}$$

the PBE can be rewritten as

$$\hat{z}\hat{\Phi}'(\hat{z}) = b(x_0)\int_{1}^{0} \frac{\hat{z}}{u}g(u)\hat{\Phi}'\left(\frac{\hat{z}}{u}\right)\left(-\frac{\hat{z'}^2}{\hat{z}}\right)du \tag{B.26}$$

Rearranging yields

$$\hat{z}\hat{\Phi}'(\hat{z}) = \beta\int_{0}^{1} \frac{\hat{z}^2}{u^3}\hat{\Phi}'\left(\frac{\hat{z}}{u}\right)g(u)du \tag{B.27}$$

which serves as the starting point for the inverse problem solution.

B.4 Derivation of the PBE in terms of the similarity variable for pure aggregation

The equation of pure aggregation in terms of the cumulative number density $\mathrm{F_1(x,t)}$is given by

$$\frac{\partial F_1(x,t)}{\partial t} = -\int_0^x \partial_\xi F_1(\xi,t) \int_{x-\xi}^{\infty} \frac{a(\xi,u)}{u} \partial_u F_1(u,t) \tag{B.28}$$

We denote the self-similar cumulative number density as $\Phi(\eta)$ and find for the left hand side of eq. B.28

$$\frac{\partial F_1(x,t)}{\partial t} = \frac{\partial \Phi(\eta)}{\partial t} = \frac{d\Phi(\eta)}{d\eta}\frac{d\eta}{dt} = \Phi'(\eta)\frac{d\eta}{dt} \tag{B.29}$$

Derivation of eq. B.2 yields

$$\frac{d\eta}{dt} = \frac{-xh'(t)}{h(t)^2} = \frac{-\eta h'(t)}{h(t)} \tag{B.30}$$

yielding

$$\frac{\partial F_1(x,t)}{\partial t} = \Phi'(\eta)\frac{-\eta h'(t)}{h(t)} \tag{B.31}$$

The right hand side of eq. B.28 can be transformed to

$$-\int_0^\eta \Phi'(\eta')d\eta' \int_{\eta'-\eta''}^{\infty} \frac{a(\eta' h(t), \eta'' h(t))}{\eta'' h(t)} \Phi'(\eta'')d\eta'' \tag{B.32}$$

Eq. B.28 then becomes

$$\Phi'(\eta)\frac{-\eta h'(t)}{h(t)} = -\int_0^\eta \Phi'(\eta')d\eta' \int_{\eta'-\eta''}^{\infty} \frac{a(\eta' h(t), \eta'' h(t))}{\eta'' h(t)} \Phi'(\eta'')d\eta'' \tag{B.33}$$

or

$$\Phi'(\eta)\eta = \frac{1}{h'(t)}\int_0^\eta \Phi'(\eta')d\eta' \int_{\eta'-\eta''}^{\infty} \frac{a(\eta' h(t), \eta'' h(t))}{\eta''} \Phi'(\eta'')d\eta'' \tag{B.34}$$

To impose time-independency, we need to assure

$$\frac{\partial}{\partial t}\left[\frac{a(\eta' h(t), \eta'' h(t))}{h'(t)}\right] = 0 \tag{B.35}$$

or

$$a(\eta' h(t), \eta'' h(t)) = \alpha(\eta', \eta'')H(h(t)) \qquad h'(t) = cH(h(t)) \tag{B.36}$$

which yields the PBE for pure aggregation in terms of the similarity variable η

$$c\eta\Phi'(\eta) = \int_0^\eta d\eta' \Phi'(\eta') \int_{\eta-\eta'}^{\infty} d\eta'' \frac{\Phi'(\eta'')}{\eta''} \alpha(\eta', \eta'') \tag{B.37}$$

B.5 Derivation of the semi-analytical equation for solving the matrix equations for the pure aggregation case

In order to solve the PBE as function of the similarity variable η, it was rewritten in matrix notation. Taking into account the constrained quadratic minimisation, the problem to be solved was reformulated as

$$min\ a^T \left(X^T X + \lambda_{reg} D\right) a - 2a^T X^T g \tag{B.38}$$

where matrix $X_{i,j}$ is formulated as

$$X_{ij} = \int_0^{\eta_i} d\eta' \Phi'(\eta') \int_{\eta_i - \eta'}^{\infty} d\eta'' \frac{\Phi'(\eta'')}{\eta''} l_j(\eta', \eta'') \tag{B.39}$$

By taking advantage of the analytical representation of the similarity distribution $\Phi'(\eta)$ by means of an expansion in γ-functions

$$\Phi'(\eta) = \sum_{k=1}^{n_{term}} A_k \eta^{\alpha_k - 1} exp(-\beta_k \eta) \tag{B.40}$$

and the expansion of the scaled aggregation rate in terms of inner products of Laguerre polynomials

$$l_n(x, y) = L_i(x) L_j(x) \tag{B.41}$$

where $L_i(x)$ is given by

$$\sum_{m=0}^{i} (-1)^m \frac{j!}{(j-m)!m!^2} x^m \tag{B.42}$$

Eq. B.39 can be simplified into a semi-analytical expression which can be solved quite easily.

First, eq. B.39 is rewritten as

$$\bar{X}_{ij}(m) = \int_0^{\eta_m} d\eta' \Phi'(\eta') L_i(\eta') \bar{Y}_j(\eta_m - \eta') \tag{B.43}$$

where η_m is a point of the discretised similarity range and $\bar{Y}_j(\eta_m - \eta')$ is defined by

$$\bar{Y}_j(\eta_m - \eta') = \int_{\eta_i - \eta'}^{\infty} d\eta'' \frac{\Phi'(\eta'')}{\eta''} L_j(\eta'') \tag{B.44}$$

Substitution of the Laguerre polynomial by its explicit form yields

$$\bar{Y}_j(\eta_m - \eta') = \int_{\eta_i - \eta'}^{\infty} d\eta'' \frac{\Phi'(\eta'')}{\eta''} \sum_{m=0}^{j} (-1)^m \frac{j!}{(j-m)!m!^2} \eta''^m \tag{B.45}$$

Including the γ-expansion yields

$$\bar{Y}_j(\eta_m - \eta') = \int_{\eta_i - \eta'}^{\infty} d\eta'' \sum_{k=1}^{n_{term}} A_k \sum_{m=0}^{j} (-1)^m \frac{j!}{(j-m)!m!^2} \eta''^{m-1} \left(\eta''^{\alpha_k - 1} exp(-\beta k \eta'')\right) \tag{B.46}$$

which can be rewritten as

$$\bar{Y}_j(\eta_m - \eta') = \sum_{k=1}^{n_{term}} A_k \sum_{m=0}^{j} (-1)^m \frac{j!}{(j-m)!m!^2} \int_{\eta_i - \eta'}^{\infty} \left(\eta''^{\alpha_k + m - 2} exp(-\beta k \eta'')\right) d\eta'' \tag{B.47}$$

The integral to the extreme right can be rewritten in the integration variable $\beta \mathrm{k}\eta''$

$$\frac{\int_{\beta_k(\eta_i-\eta')}^{\infty}\left((\beta_k\eta'')^{(\alpha_k+m-1)-1}exp(-\beta k\eta'')\right)d(\beta_k\eta'')}{\beta_k^{\alpha_k+m-1}} \tag{B.48}$$

where the integral in the numerator represents the incomplete complementary γ-function γ_{c} given in its general form by

$$\gamma_c(x,a)=\int_x^{\infty}(t)^{a-1}exp(-t)dt \tag{B.49}$$

and is available as pre-programmed function in most mathematical software packages (e.g. Matlab,...), which avoids the need for its numerical integration. Finally, the semi-analytical expression for $\bar{\mathrm{Y}}_{\mathrm{j}}$ becomes

$$\bar{Y}_j(\eta_m-\eta')=\sum_{k=1}^{n_{term}}A_k\sum_{m=0}^{j}(-1)^m\frac{j!}{(j-m)!m!^2}\frac{\gamma_c(\alpha_k+m-1,\beta_k(\eta_i-\eta'))}{\beta_k^{\alpha_k+m-1}} \tag{B.50}$$

APPENDIX C

Experimental data

C.1 Experimental data set from Biggs (2000)

This appendix contains the discussion of the experimental data that were not discussed explicitly in Chapter 6.

Time evolutions of the vol% in the different size classes for the experiments with shear rates G equal to 37, 113 and 346 s^{-1} are given in respectively Fig. C.1, C.2 and C.3.

For the case of G equal to 37 s^{-1}, the Kolmogorov microscale was calculated to be 93 $\mu\mathrm{m}$. This scale coincides with the classes containing the largest volumes (92 and 112 $\mu\mathrm{m}$). It can again be concluded that breakup is not occurring to a large extent throughout the complete experiment since no decrease in the large size classes is observed. The leveling off appears faster compared to the 19.4 s^{-1} case (see section 6.1.1, suggesting smaller aggregation and breakage time-scales. Size classes larger than the Kolmogorov microscale exhibit an increasing behaviour, eventually reaching an equilibrium. Smaller size classes show a maximum before reaching the equilibrium (same reasoning as in the G equal to 19.4 s^{-1} case). However, the peaks for the different size classes are reached sooner than in the 19.4 s^{-1} case, indicating smaller time-scales of aggregation. The drop in volume after the peak is less pronounced, which is either caused by (1) a smaller rate of aggregation of these particles out of the size class (unlikely, since the number of collisions should be higher at higher mixing intensities) or (2) by a larger number of particles aggregating into the size class from smaller particles or (3) due to particles born due to breakage from larger sizes. The observed peak maxima for the same classes are also higher here, which supports the second hypothesis. The smallest size classes don't show a peak. The peak disappears for classes below 23 $\mu\mathrm{m}$.

For the case of G equal to 113 s^{-1} similar observations are found. The calculated Kolmogorov microscale is 53 $\mu\mathrm{m}$. The maximum vol% is indeed observed for particles with sizes between 50 and 75 $\mu\mathrm{m}$. Leveling off starts faster, indicating smaller aggregation and breakage time-scales. Again peaks reach higher

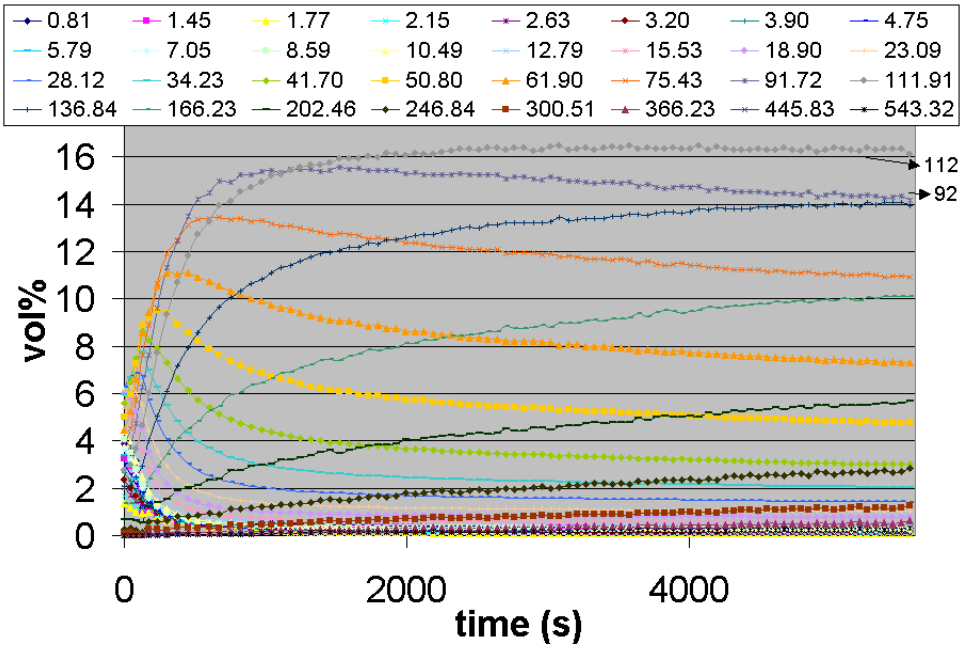

Figure C.1: Time evolutions of vol% in the different size classes for the experiment at a shear rate of $37\,\mathrm{s}^{-1}$

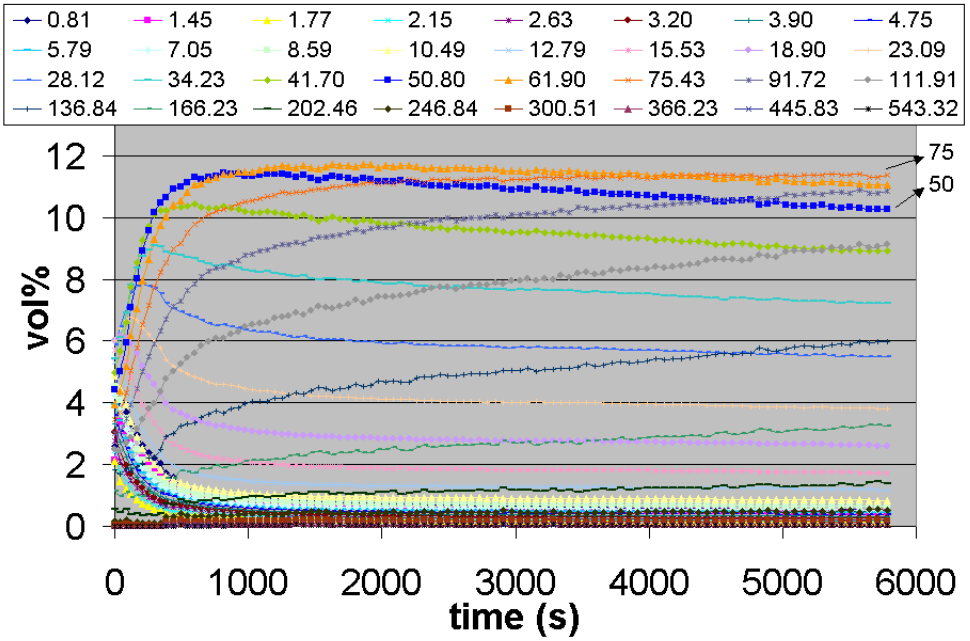

Figure C.2: Time evolutions of vol% in the different size classes for the experiment at a shear rate of $113\,\mathrm{s}^{-1}$

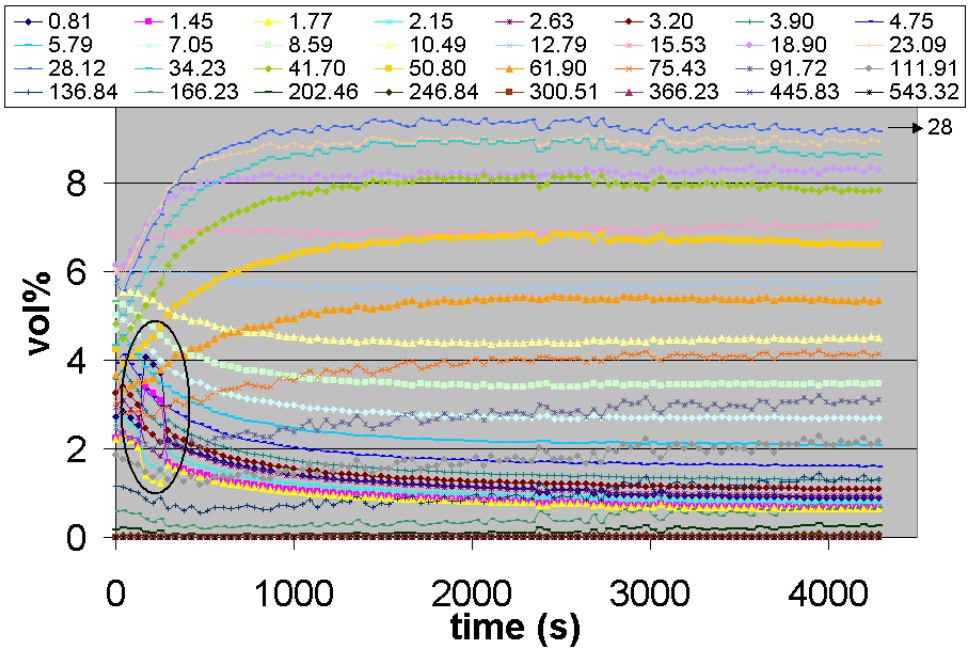

Figure C.3: Time evolutions of vol% in the different size classes for the experiment at a shear rate of $346\,\mathrm{s}^{-1}$

maximum values for the same particle classes and the decrease after the peak is less pronounced, probably due to higher aggregation rates as was argued in the previous case. The peak disappears for classes below 23 μm.

For the case of G equal to $346\,\mathrm{s}^{-1}$ similar observations are found. The calculated Kolmogorov microscale is 30 μm. The maximum is indeed observed between 23 and 34 μm. Leveling off starts faster, indicating smaller aggregation and breakage time-scales. All particle size classes larger than 90 μm exhibit an initial decrease. In this case it would not be sound to neglect breakage and claim that pure aggregation is occurring. Again peaks reach higher maximum values for the same particle classes and the decrease after the peak is less pronounced, probably due to higher aggregation rates as was argued in previous cases in combination with particles being formed from breakage of larger particles. The peak disappears for classes below 11 μm. Note the small measurement error that occurred in the early stages of the experiment (indicated by the oval). Such artefacts can never be noticed in a summarising parameter such as D[4,3], especially when they appear in the small size range as is the case here.

APPENDIX D

Comprehensive procedures for solving the inverse problem

D.1 Pure aggregation

Wright and Ramkrishna (1992) used a Fortran-code to analyse the self-similarity and to solve the inverse problem. For this dissertation, a procedure was developed based on simple manipulations in a spreadsheet (MS Excel was used here) and some coding/scripting in m-files in Matlab (Mathworks Inc., USA). It uses the following steps:

1. Left-hand side of eq. 11.1: A continuous analytical expression for the similarity distribution $\Phi'(\eta)$ was found by means of a γ-function expansion. Two steps are required which can be performed entirely in the spreadsheet:
   (a) Discretisation of the similarity variable range – As mentioned earlier, the behaviour of similarity distributions for different known kernels exhibit differences at low values of η. Therefore, a logarithmic grid for covering the range between $\eta_{\min}$ and $\eta_{\max}$ is recommended. The number of bins $\mathrm{n_e}$ will determine the accuracy of the inversion. Values of 80-100 have proven to be sufficient (Wright and Ramkrishna, 1992). In our case, a geometric grid with a factor 1.223 was used resulting in 100 bins to cover the range between $\eta_{\min} = 7.91\mathrm{E}-7$ and $\eta_{\max} = 352$.
   (b) $\eta\Phi'\eta$ should be evaluated at all discretised η-values. This will result in a vector **L** with dimension $\mathrm{n_e x1}$
2. Right-hand side of eq. 11.1: This will be computed based on eq. 11.12 and eq. 11.14. The following steps are to be taken:
   (a) Choose the number of basis functions per axis. Let this be $\mathrm{n_b}$. The number of γ-functions used for fitting the similarity distribution is denoted $\mathrm{n_{term}}$.

(b) Vectors representing the result of the numerical integration for all elements of the discretised grid for a combination of basis functions $\mathrm{L_i(x)}$ and $\mathrm{L_j(y)}$ need to be calculated. Let these be $\mathrm{I_{i,j}}$ (dimension: $\mathrm{n_e x1}$) and store them as columns in a matrix **AR** (dimension: $\mathrm{n_e x n_b^2}$). This is implemented in a number of m-files in Matlab (Mathworks Inc., USA). The core file used for this calculation *calculation_I.m* is given at the end of this section (for reasons of transparency of the procedure). It contains some parameter declarations and calls quadl, which is a matlab-routine for numerical integration, working on the function *integrandum*.

The integrandum-function is described in a separate m-file *integrandum.m*, which is also given further in this section. It accepts 8 arguments, calculates the product of three function (f_prime,L and II) and returns a vector. It calls three functions, which are given in separate m-files, *f_prime.m, L.m and II.m*, respectively. The files are also given further on this section.

The function f_prime takes 5 arguments, calculates the $\Phi'(\eta_\mathrm{i})$-values based on the γ-expansion calculated before and returns a vector. In order to return a vector with the correct dimension, the storage of elements needs to be based on the storage and size of the x-vector that is received.

The function L takes 2 arguments among which the order of the Laguerre polynomial to be evaluated. Note that this order is a value in the set $0, 1, \ldots, \mathrm{n_b} - 1$. It evaluates the $\mathrm{i^{th}}$-order Laguerre polynomial and returns a vector.

Finally, the function II takes 6 arguments, evaluates $\bar{\mathrm{Y}}$ for different values of the similarity variable and returns a vector. The evaluation includes two summations: one for the parts of the Laguerre polynomial and one for the number of γ-functions used.

3. Constrained quadratic optimisation – Matlab (Mathworks Inc., USA) contains a function called *quadprog* that performs a constrained quadratic optimisation problem given by

$$min_x \frac{1}{2} x^T H x + F^T x \tag{D.1}$$

with the following constraints

$$A \cdot x \leq b \quad A_{eq} \cdot x = b_{eq} \tag{D.2}$$

In the next steps, the matrices H and F, together with the constraint matrices for our specific problem are prepared for use in the quadprog function. The m-file (*inverse_problem_solver.m*) is given later in this section for reasons of transparency of the method.

(a) The matrix H can be calculated based on the previously determined matrix AR as follows:

$$H = 2 * \left(AR^T * AR + \lambda_t I_d \right) \tag{D.3}$$

Compared to the original equation, a factor of 2 needs to be added in order to be compatible with the quadprog-function in Matlab. λ_t represents the regularisation parameter and $\mathrm{I_d}$ is the identity matrix of dimension $\mathrm{n_b^2 x n_b^2}$. The dimension of **H** is also $\mathrm{n_b^2 x n_b^2}$.

(b) The matrix F is calculated based on the previously determined matrices AR and L as follows

$$F = (-1) * 2 * AR^T * L \tag{D.4}$$

The dimension of **F** is $\mathrm{n_b^2 x 1}$.

(c) The first constraint expresses the positivity of the aggregation rate. The scaled version of the latter was expanded in inner products of Laguerre polynomials $\mathrm{l_j(x,y)}$. Hence, the constraint becomes (note that quadprog checks for negativity)

$$(-1)\frac{b(x,y)}{\langle b\rangle} = (-1)\sum_{j=1}^{n_b^2} a_j l_j(x,y) \leq 0 \tag{D.5}$$

In order to evaluate this constraint, we need to calculate the proper matrix A. For this, we need to discretise both x and y into a number of bins, say $\mathrm{n_d}$. For all possible combinations of x and y (i.e. $\mathrm{n_d^2}$), all inner products $\mathrm{l_j(x,y)}$ should be evaluated. These $\mathrm{n_d^2x1}$ vectors are then stored as columns to form the A matrix with dimension $\mathrm{n_d^2xn_b^2}$. Note that the order of storage should be similar as in AR. A null-vector **b**, representing the right-hand side, with dimension $\mathrm{n_d^2x1}$ needs to be defined. The mentioned discretisation should not be the same as the one used for the inversion. $\mathrm{n_d} = 20$ should be sufficient.

(d) The second constraint stems from the symmetric nature of the aggregation rate. Collisions between particles i and j should have the same probability as those between j and i. This means that coefficients for the inner products $\mathrm{L_i(x)L_j(y)}$ and $\mathrm{L_j(x)L_i(y)}$ should be equal. The number of mixed inner products (with $\mathrm{i} \neq \mathrm{j}$) depends on the number of basis functions along each axis and is equal to

$$\frac{n_b^2 - n_b}{2} \tag{D.6}$$

When $\mathrm{n_b} = 3$, the constraint reads

$$0.a_1 + 1.a_2 + 0.a_3 - 1.a_4 + 0.a_5 + 0.a_6 + 0.a_7 + 0.a_8 + 0.a_9 = 0 \tag{D.7}$$
$$0.a_1 + 0.a_2 + 1.a_3 + 0.a_4 + 0.a_5 + 0.a_6 - 1.a_7 + 0.a_8 + 0.a_9 = 0 \tag{D.8}$$
$$0.a_1 + 0.a_2 + 0.a_3 + 0.a_4 + 0.a_5 + 1.a_6 + 0.a_7 - 1.a_8 + 0.a_9 = 0 \tag{D.9}$$

where eq. D.7, eq. D.8 and eq. D.9 respectively express the equality of $\mathrm{a_2} = \mathrm{a_4}$, $\mathrm{a_3} = \mathrm{a_7}$ and $\mathrm{a_6} = \mathrm{a_8}$, respectively representing the inner products (0,1-1,0), (0,2-2,0) and (1,2-2,1). A null-vector $\mathrm{b_{eq}}$ with dimension $\frac{\mathrm{n_b^2 - nb}}{2}\mathrm{x1}$ needs to be defined.

(e) At this stage all necessary matrices and vectors are defined to solve the inverse problem using the quadprog-function in Matlab (Mathworks Inc., USA). The default number of iterations of 200 might be too low in some cases. This can be increased by using the options argument.

(f) Finally, the right-hand side of eq. 11.1 can be calculated from the product of AR and C. The resulting vector has dimension $\mathrm{n_e x1}$ and can be compared with the vector L that represents the left-hand side of eq. 11.1 to evaluate the quality of inversion.

The different pieces of Matlab-code that were mentioned in the above elaboration of the stepwise inversion procedure are given here in order of appearance.

- Calculation_I.m

```
% Calculation_I.m -- routine to calculate vectors I
z=dlmread('Z.txt','\t');
[rows_z,cols_z]=size(z);          % determine number of bins n_e
n_term=2;                         % number of gamma functions
```

```
nb=4;                                % number of basis functions per axis
% results from gamma fit dimension: 1xn_term
A=[0.1631,0.0062];
alfa=[1.7487,2.2483];
beta=[0.3201,0.1015];
% numerical integration procedure
for i=0:nb-1,                        % loop for basis function along x-axis
    for j=0:nb-1,                    % loop for basis function along y-axis
        for m=1:rows_z,
            I(m,j+nb*i+1)=quadl(@integrandum,0,z(m),[],[],z(m),n_term,
            i,j,A,alfa,beta);
            m                        % check progression of calculation
            j
            i
        end
    end
end
dlmwrite('AR.txt',I,'\t');           % write AR to file
```

- integrandum.m

```
% integrandum.m -- routine to calculate the integrandum
% x is a vector passed on by the quadl function in calculation_I.m
function y=integrandum(x,z_m,n_term,i,j,A,alfa,beta)
y=f_prime(x,A,alfa,beta,n_term).*L(x,i)
        .*II(z_m-x,n_term,j,A,alfa,beta);
end
```

- f_prime.m

```
% f_prime.m -- routine to evaluate the similarity distribution
function y=f_prime(x,A,alfa,beta,n_term)
[x_rows,xcols]=size(x);
    for i=1:n_term,
        temp(i,1:xcols)=A(i).*x.^(alfa(i)-1).*exp(-beta(i).*x);
    end
    y=sum(temp);
end
```

- L.m

```
% L.m -- routine to calculate Laguerre polynomials evaluations
function y=L(x,i)
[x_rows,xcols]=size(x);
    for m=0:i,
```

```
        temp(m+1,1:xcols)=(-1).^m.*factorial(i)./factorial(i-m)

    end
    y=sum(temp);
end
```

- II.m

```
% II.m -- routine that evaluates \bar{Y} at different values of simvar
function y=II(x,n_term,j,A,alfa,beta)
[x_rows,xcols]=size(x);
    for k=1:n_term,
            for m=0:j,
                temp(m+1,1:xcols)=A(k).*(-1).^m.*factorial(j)
                ./factorial(m).^2./factorial(j-m).*gammainc(beta(k)
                .*x,alfa(k)+m-1,'upper').*gamma(alfa(k)+m-1)
                ./beta(k).^(alfa(k)+m-1);
            end
            gam(k,1:xcols)=sum(temp);
    end
    y=sum(gam);
end
```

- inverse_problem_solver.m

```
% solver for inverse problem for pure aggregation
nb=4;            % number of basis functions
% left-hand side of PBE(simvar) was calculated in
% excel and stored in L.txt, dimension, ne x 1
L=dlmread('L.txt','\t');
% AR was calculate separately and stored in AR.txt
AR=dlmread('AR.txt','\t');
% constrained quadratic minimisation
% first term, H=AR'*AR+lambda*Id
% regularisation parameter and nb^2 identity matrix
lambda=1E-3
Id=ones(nb*nb,nb*nb);
H=2*(AR'*AR+lambda*Id);
% second term, F=(-1)*2*AR'*L
F=(-1)*2*AR'*L;
% constraints
% 1. Positivity at each x and y
nd=20; %number of discretisation points for x,y
A=-constraint1(nb,nd); %constraint in quadprog evaluates negativity
b=zeros(nd*nd,1);
% 2.Symmetry
```

```
Aeq=dlmread('Aeq.txt','\t');
beq=zeros(6,1);
[C,FVAL,EXITFLAG,OUTPUT]=quadprog(H,F,A,b,Aeq,beq,[],[],[],options)
dlmwrite('C.txt',C,'\t');
RHS=AR*C;
dlmwrite('RHS.txt',RHS,'\t');
```

D.2 Pure breakage

Sathyagal et al. (1995) used a Fortran-code to analyse the self-similarity and to solve the inverse problem. However, here, a procedure was developed based on simple manipulations in a spreadsheet (MS Excel was used here) and some coding/scripting in m-files in Matlab (Mathworks Inc., USA). It uses the following steps:

1. Left-hand side of eq. 2.100: A continuous analytical expression for the cumulative similarity distribution $\Phi(\mathrm{z})$ is needed and was found by means of a Weibul function given by (note that this is a simpler alternative for the expansion in γ-functions)

$$\Phi(z) = a\left\{1 - exp\left[-\left(\frac{log(z) - x_0 + b(ln2)^{1/c}}{b}\right)^c\right]\right\} \tag{D.10}$$

   The logarithmic transform is needed due to the wide range of the similarity variable caused by the similarity transformation.

   Two further steps are required here which can be performed entirely in a spreadsheet:

   (a) Discretisation of the similarity variable range – In contrast to the aggregation case, a much larger number of discretisation bins $\mathrm{n_e}$ is necessary and their location should be chosen such that plenty of bins are present in the regions where steep changes in the volume fraction occur. This can be done by choosing the bin location such that equal areas under the curve are obtained, resulting in a denser grid in steep regions (see Fig. D.1). Alternatively, this choice can be done visually by choosing most of the elements (say 80%) in the steep varying regions. The latter has the advantage of being less time consuming. A number of at least 500 elements is recommended and was used in this work.

   (b) $\mathrm{z}\Phi'\mathrm{z}$ should be evaluated at all discretised η-values. This will result in a vector **L** with dimension $\mathrm{n_e x 1}$.

2. Right-hand side of eq. 2.100: The computation of the right-hand side is somewhat less complicated compared to the aggregation case. The unknown function $\gamma\mathrm{g(u)}$ was expanded according to eq. 2.101.

   (a) Choose the number of basis functions in the expansion. Let this be $\mathrm{n_b}$.

   (b) Calculate the numerical integral $\mathrm{I_{i,j}}$ for every basis function j and for all elements of the discretisation grid $\mathrm{z_i}$. This will result in $\mathrm{n_b}$ vectors of dimension $\mathrm{n_e x 1}$, which are then stored column-wise in a matrix **AR** that has dimension $\mathrm{n_e x n_b}$. The m-file (*RHS_calc.m*) is given later in this section for reasons of transparency of the method.

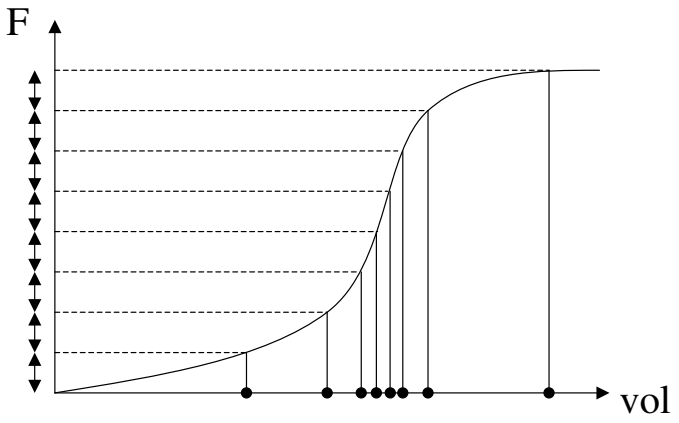

Figure D.1: Grid determination for obtaining equal areas under the curve

3. Constrained quadratic optimisation – Matlab (Mathworks Inc., USA) contains a function called *quadprog* that performs a constrained quadratic optimisation problem given by

$$min_x \frac{1}{2} x^T H x + F^T x \tag{D.11}$$

with the following constraints

$$A \cdot x \leq b \quad A_{eq} \cdot x = b_{eq} \tag{D.12}$$

In the next steps, the matrices H and F, together with the constraint matrices for the specific problem at hand are prepared for use in the quadprog function. The m-file (*inverse_problem_solver.m*) is given later in this section for reasons of transparency of the method.

(a) The matrix H can be calculated based on the previously determined matrix AR as follows

$$H = 2 * \left(AR^T * AR\right) \tag{D.13}$$

Compared to the original equation, a factor of 2 needs to be added in order to be compatible with the quadprog-function in Matlab. The dimension of **H** is $\mathrm{n_b x n_b}$.

(b) The matrix F is calculated based on the previously determined matrices AR and L as follows:

$$F = (-1) * 2 * AR^T * L \tag{D.14}$$

The dimension of **F** is $\mathrm{n_b x 1}$.

(c) The first constraint requires the extracted function to always be positive. To build up the constraint matrix **A**, the interval $\{0 - 1\}$ needs to be discretised in $\mathrm{n_x}$ classes (around 20 should be sufficient). At each of these points, the basis functions are evaluated resulting in $\mathrm{n_b}$ vectors of dimension $\mathrm{n_x x 1}$. These are then stored column-wise to form a matrix **A1**. Since quadprog checks for the negativity constraint, all elements of the matrix should be multiplied by -1.

(d) The second constraint requires the extracted function to be a monotonic rising function. A similar procedure should be followed as was done for constraint 1, except that the differentiated basis functions should now be evaluated at all points in the discretisation. This again

results in n_b vectors of dimension $n_x x1$, which are stored column-wise to form a matrix **A2**. Again, multiplication of all matrix elements by -1 is needed.

Matrices A1 and A2 are then stacked to form matrix A, which has dimension $2n_x x n_b$. A null vector **b** of dimension $2n_x x1$ should be defined to represent the right-hand side of the constraint.

(e) The third constraint requires the derivative at z=1 to be equal to zero. For this, the differentiated basis functions are evaluated at z=1 and the results are stored in a $1xn_b$ vector which is called **Aeq**. A null-vector b_eq of size 1x1 should be defined to represent the right-hand side of the constraint.

(f) At this stage all necessary matrices and vectors are defined to solve the inverse problem using the quadprog-function in Matlab (Mathworks Inc., USA). The default number of iterations of 200 might be too low in some cases. This can be increased by using the options argument.

(g) Finally, the right-hand side of eq. 11.1 can be calculated from the product of AR and C. The resulting vector has dimension $n_e x1$ and can be compared with the vector L that represents the left-hand side of eq. 11.1 to evaluate the quality of inversion.

The different pieces of Matlab-code that were mentioned in the above elaboration of the stepwise inversion procedure are given here in order of appearance.

- RHS_calc.m

```
% rhs_calc.m -- routine to calculate right-hand side
x=dlmread('Z.txt','\t');
a=0.996894654295881
b=129431677.326099
c=45586368.9234719
d=log(2)
x0=23.21092937
for i=1:500,
f_prime_xu=inline('x.^2./u.^3.*0.0913.*u.*(2-u).*a
.*((x./u-x0+b.*d.^(1./c))./b).^c.*c./(x./u-x0+b.*d
.^(1./c)).*exp(-((x./u-x0+b.*d.^(1./c))./b).^c)',
'u','x','a','b','c','d','x0');
rhs(i)=quadl(f_prime_xu,0.05,1,[],[],x(i),a,b,c,d,x0);
end
%x(1:10)
%I_0
DLMWRITE('rhs.txt',transpose(rhs),'\t');
```

- inverse_problem_solver.m

```
% Inverse_problem_solver.m
% Defining the left hand side vector L that was calculated in Excel
% dimension ne x 1
L=dlmread('L.txt','\t');
```

```
% Defining the right hand side vector AR that was calculated in Excel
% number of basis functions
nb=3;
% define vectors containing the integral over the unit interval at the
% discretised values of simvar, for all basis functions, dimension ne x 1
I_0=dlmread('I_0.txt','\t');
I_1=dlmread('I_1.txt','\t');
I_2=dlmread('I_2.txt','\t');
% put these vectors in a matrix, dimension ne x nb
AR=[I_0,I_1,I_2];
% transpose this matrix, dimension nb x ne
AR_trans=transpose(AR);
% Preparing the matrices for the quadratic optimisation
% terms for optimisation (Sathyagal eq.17)
% term 1, dimension nb x nb
H=AR_trans*AR;
%term 2, dimension nb x 1
F=(-1)*2*AR_trans*L;
% constraints
% g(u)>0,g'(u)>0
% discretising the u interval [0,1] into nx classes
nx=50;
step=1/(nx-1);
Nx=transpose(0:step:1);
% define vectors containing values of G_nb at the different discrete points
% nx, dimension nx x 1
% define matrix based on these vectors, dimension nx x nb
A1=dlmread('G.txt','\t');
A2=dlmread('G_prime.txt','\t');
% stack matrices, dimension 2nx x nb, and multiply by -1
A=-1*[A1;A2];
% rhs of constraint
b=zeros(2*nx,1);
% g'(1)=0
% vector, dimension 1 x nb
Aeq=dlmread('G_prime_1.txt','\t');
beq=zeros(1,1);
% quadratic optimisation
C=quadprog(H,F,A,b,Aeq,beq);
```

Bibliography

Adler, P., 1981a. Heterocoagulation in shear flow. J. Col. Int. Sc. 83 (1), 106–115.

Adler, P., 1981b. Streamlines in and around porous particles. J. Col. Int. Sc. 81 (2), 531–535.

Agresti, 1990. Categorical data analysis. Wiley, New York.

Andreadakis, A., 1993. Physical and chemical properties of activated sludge floc. Wat. Res. 27 (12), 1707–1714.

Ardern, E., Lockett, W., 1914. Experiments on the oxidation of sewage without the aid of filters. J. Soc. Chem. Ind. 33, 523.

Barbusinski, K., Koscielniak, H., 1995. Influence of substrate loading intensity on floc size in activated sludge process. Wat. Res. 29 (7), 1703–1710.

Batterham, R., Hall, J., Barton, G., 1981. Pelletizing kinetics and simulation of full-scale balling circuits. In: 3rd Int. Symp. on Agglomeration, Nürnberg, W. Germany. pp. A136–A150.

Biggs, C., 2000. Activated sludge flocculation: Investigating the effect of shear rate and cation concentration on flocculation dynamics. Ph.D. thesis, The University of Queensland, Australia.

Biggs, C., Lant, P., 2000. Activated sludge flocculation: on-line determination of floc size and the effect of shear. Wat. Res. 34 (9), 2542–2550.

Biggs, C., Lant, P., 2001. Modelling activated sludge flocculation using population balances. Powd. Techn. 124 (3), 201–211.

Blake, G., Hartge, K., 1986. Particle Density, 2nd Edition. No. 5 in Soil Science Society of America. Am. Soc. Agron.-Soil Sci. Soc. Am., Madison, WI, USA.

Blatz, P., Tobolsky, A., 1945. Note on the kinetics of systems manifesting simultaneous polymerisation-depolymerisation phenomena. J. Phys. Chem 49, 77–80.

Boeije, G., Corstanje, R., Rottiers, A., Schowanek, D., 1998. Adaptation of the cas test system and synthetic sewage for biological nutrient removal. part i: Development of a new synthetic sewage. Chemosphere 38 (4), 699–709.

Bradshaw, P. (Ed.), 1978. Turbulence. Springer-Verlag Berlin.

Bruus, J., Nielsen, P., Keiding, K., 1992. On the stability of activated sludge flocs with implications to dewatering. Wat. Res. 26, 1597–1604.

Busch, P., Stumm, W., 1968. Chemical interactions in the aggregation of bacteria: bioflocculation in wastewater. Env. Sci. Tech. 2, 49–53.

Bushell, G., Amal, R., 2000. Measurement of fractal aggregates of polydisperse particles using small angle light scattering. J. Col. Int. Sc. 221, 186–194.

Bushell, G., Yan, Y., Woodfield, D., Raper, J., Amal, R., 2002. On techniques for the measurement of the mass fractal dimension of aggregates. Adv. Col. Int. Sci. 95, 1–50.

Bye, C., Dold, P., 1998. Sludge volume index settleability measures: effect of solids characteristics and test parameters. Wat. Env. Res. 70 (1), 87–93.

Camp, T., Stein, P., 1943. Velocity gradients and internal work in fluid motion. J. Boston Soc. Civ. Eng. 30 (4), 219–237.

Capalozza, C., 2001. Design, start-up and monitoring of a pilot sequencing batch reactor for breeding stable nutrient removing sludge. Master's thesis, Ghent University, Belgium.

Chellam, S., Wiesner, M., 1993. Fluid mechanics and fractal aggregates. Wat. Res. 27 (9), 1493–1496.

Chen, W., Fisher, R., Berg, J., 1990. Simulation of particle size distributon in an aggregation-breakuo process. Chem. Eng. Sci. 45 (9), 3003–3006.

Chudoba, J., Grau, P., Ottava, V., 1973. Control of activated sludge filamentous bulking - ii selection of microorganisms by means of a selector. Wat. Res. 7, 1389–1406.

Chung, H., Ju, S., Lee, D., 2003. Hydrodynamic drag force exerted on activated sludge floc at intermediate reynolds number. J. Col. Int. Sc. 263, 498–505.

Clark, M., 1985. Critique of camp and stein's rms velocity gradient. J. Env. Eng. 111 (3), 741–754.

Clark, M., Flora, J., 1991. Floc restructuring in varied turbulent mixing. J. Col. Int. Sc. 147 (2), 407–421.

Cleasby, J., 1984. Is velocity gradient a valid turbulent flocculation parameter? J. Env. Eng. 110 (EE5), 875–897.

Cohen, S., Hindmarsh, A., September 1994. CVODE User Guide. Lawrence Livermore National Laboratory.

Cousin, C., Ganczarczyk, J., 1998. Effects of salinity on physical characteristics of activated sludge flocs. Wat. Qual. Res. J. Can. 33 (4), 565.

Dammel, E., Schroeder, E., 1991. Density of activated sludge flocs. Wat. Res. 25 (7), 841–846.

Das, D., Keinath, T., Parker, D., Wahlberg, E., 1993. Floc breakup in activated sludge plants. Wat. Env. Res. 65 (2), 138–145.

De Clercq, B., 2003. Computational fluid dynamics of settling tanks: development of experiments and rheological, settling, and scraper submodels. Ph.D. thesis, Ghent University.

De Clercq, B., Lant, P., Vanrolleghem, P., 2004. Focused beam reflectance technique for in situ particle sizing in wastewater treatment settling tanks. J. Chem. Technol. Biotechnol. 79, 610–618.

Dick, R., Vesilind, P., 1969. The sludge volume index - what is it? Journal WPCF 41 (7), 1285–1291.

Dobias, B. (Ed.), 1993. Coagulation and flocculation: Theory and Applications. Marcel Dekker, Inc., New York.

Dochain, D., Vanrolleghem, P., 2001. Modelling and estimation in wastewater treatment processes. IWA Publishing, London, UK.

Ducoste, J., 2002. A two-scale pbm for modeling turbulent flocculation in water treatment processes. Chem. Eng. Sci. 57 (12), 2157–2168.

Ducoste, J., Clark, M., 1998a. The influence of tank size and impeller geometry on turbulent flocculation : I experimental. Env. Eng. Sc. 15 (3), 215–224.

Ducoste, J., Clark, M., 1998b. The influence of tank size and impeller geometry on turbulent flocculation: Ii model. Env. Eng. Sc. 15 (3), 225–235.

Ekama, G., Bernard, J., Gunthert, F., Krebs, P., McCorquodale, J., Parker, D., Wahlberg, E., 1997. Secondary settling tanks: Theory, modelling, design and operation. Scientific and technical report series, IWA Publishing, London, UK.

EPA, 2004. Epa water subtopics. http://www.epa.gov/ebtpages/water.html.

Eriksson, L., Steen, I., Tendaj, M., 1992. Evaluation of sludge properties at an activated sludge plant. Wat. Sci. Tech. 25, 251–265.

EU, 2004. Water policy in the european union. http://europa.eu.int/comm/environment/water/index.html.

Flesch, J., Spicer, P., Pratsinis, S., 1999. Laminar and turbulent shear-induced flocculation of fractal aggregates. AIChE J. 45 (5), 1114–1124.

Fowler, H., 1988. Handbook of laboratory model systems for microbial ecosystems. CRC Press, Ch. Microbial adhesion to surface.

Gerald, C., Wheatley, P., 1994. Applied numerical analysis, 5th Edition. Addison-Wesley, Reading, UK.

Govoreanu, R., 2004. Activated sludge flocculation dynamics: on-line measurement methodology and modelling. Ph.D. thesis, Ghent University, Belgium.

Govoreanu, R., Nopens, I., De Clercq, B., Saveyn, H., Van der Meeren, P., Vanrolleghem, P., September 2001. Influence of experimental parameters for on-line determination of floc size distribution. In: 12th Romanian International Conference on Chemistry and Chemical Engineering.

Govoreanu, R., Saveyn, H., Van der Meeren, P., Vanrolleghem, P., 2004. Simulataneous determination of activated sludge floc size distribution by different techniques. Wat. Sci. Tech. 50 (12), 39–46.

Govoreanu, R., Seghers, D., Nopens, I., De Clercq, B., Saveyn, H., Capalozza, C., Van der Meeren, P., Verstraete, W., Top, E., Vanrolleghem, P., 2003. Linking floc structure and settling properties to activated sludge population dynamics in an sbr. Wat. Sci. Tech. 47 (12), 9–18.

Gregory, J., 1997. The density of particle aggregates. Wat. Sci. Tech. 36 (4), 1–13.

Guan, J., Waite, T., Amal, R., 1998. Rapid structure characterization of bacterial aggregates. Env. Sci. Tech. 32 (23), 3735–3742.

Gujer, W., Henze, M., Mino, T., Van Loosdrecht, M., 2000. Activated sludge model no. 3. In: Henze, M., Gujer, W., Mino, T., Van Loosdrecht, M. (Eds.), Activated sludge models ASM1, ASM2, ASM2D and ASM3. IWA Publishing, London, UK.

Han, M., Lawler, D., 1992. The (relative) insignificance of g in flocculation. Journal AWWA, 79–91.

Happel, J., 1958. Viscous flow in multiparticle systems: slow motion of fluids relative to bed of spherical particles. AIChE J. 4, 197–201.

Henze, M., Dupont, R., Grau, P., de la Sota, A., 1993. Rising sludge in secondary settlers due to denitrification. Wat. Res. 27 (2), 231–236.

Henze, M., Grady, C., Gujer, W., Marais, G., Matsuo, T., 1987. Activated sludge model no. 1. Tech. rep., IWA Publishing, London, UK.

Henze, M., Gujer, W., Mino, T., Matsuo, T., Wentzel, M., Marais, G., 1995. Activated sludge model no.2. Tech. rep., IWA Publishing, London, UK.

Hiemenz, P., Rajagopalan, R., 1997. Principles of colloid and surface chemistry. Marcel Dekker, New York, USA.

Higgins, M., Novak, J., 1997. The effect of cations on the settling and dewatering of activated sludges: laboratory experience. Wat. Env. Res. 69, 215–224.

Hill, P., Ng, K., 1995. New discretisation procedure for the breakage equation. AIChE J. 41 (5), 1204–1216.

Hounslow, M., Ryall, R., Marshall, V., 1988. A discretized population balance for nucleation, growth and aggregation. AIChE J. 34 (11), 1821–1832.

Hsu, J., Hsieh, Y., 2003. Drag force on a porous, non-homogeneous spheroidal floc in a uniform flow field. J. Col. Int. Sc. 259, 301–308.

Hulburt, H., Katz, S., 1964. Some problems in particle technology. a statistical mechanical formulation. Chem. Eng. Sci. 19, 555–574.

Jiwani, A., Graham, N., Day, M., 1997. Activated sludge process control via particle monitoring. Wat. Sci. Tech. 36, 269–277.

Jorand, F., Zartarian, F., Thomas, F., Block, J., Bottero, J., Villemin, G., Urbain, V., Manem, J., 1995. Chemical and structural (2d) linkage between bacteria within activated sludge flocs. Wat. Res. 29 (7), 1639–1647.

Keiding, K., Nielsen, P., 1997. Desorption of organic macromolecules frfom activated sludge: effect of ionic compostion. Wat. Res. 31, 1665–1672.

Kinnear, D., 2002. Biological solids sedimentation: a model incorporating fundamental settling parameters. Ph.D. thesis, Department of Civil and Environmental Engineering, University of Utah, USA.

Knocke, W., Zentkovitch, T., 1986. Effect of mean cell residence time and particle size distribution on activated sludge vacuum dewatering characteristics. J. Wat. Pol. Control Fed. 58, 1118–1123.

Koh, P., Andrews, J., Uhlherr, P., 1987. Modelling shear-flocculation by population balances. Chem. Eng. Sci. 42 (2), 353–362.

Konno, M., Aoki, M., Saito, S., 1983. Scale effect on breakup process in liquid-liquid agitated tanks. J. Chem. Eng. Japan 16 (4), 312–319.

Kramer, T., Clark, M., 1997. Influence of strain rate on coagulation kinetics. J. Env. Eng. 123 (5), 444–452.

Kramer, T., Clark, M., 1999. Incorporation of aggregate breakup in the simulation of orthokinetic coagulation. J. Col. Int. Sc. 216, 116–126.

Kumar, S., Ramkrishna, D., 1996a. On the solution of population balance equations by discretisation - i. a fixed pivot technique. Chem. Eng. Sci. 51 (8), 1311–1332.

Kumar, S., Ramkrishna, D., 1996b. On the solution of population balance equations by discretisation - ii. a moving pivot technique. Chem. Eng. Sci. 51 (8), 1333–1342.

Kumar, S., Ramkrishna, D., 1997. On the solution of population balance equations by discretisation - iii nucleation, growth and aggregation of particles. Chem. Eng. Sci. 52 (24), 4659–4679.

Kusters, K., 1991. The influence of turbulence on aggregation of small particles in agitated vessels. Ph.D. thesis, Technische Universiteit Eindhoven, The Netherlands.

Kusters, K., Wijers, J., Thoenes, D., 1997. Aggregation kinetics of small particles in agitated vessels. Chem. Eng. Sci. 52 (1), 107–121.

Lee, D., Bonner, J., Garton, L., Ernest, A., Autenrieth, R., 2000. Modeling coagulation kinetics incorporating fractal theories: a fractal rectilinear approach. Wat. Res. 34 (7), 1987–2000.

Lee, D., Vanrolleghem, P. A., 2002. Monitoring of a sequencing batch reactor using adaptive multiblock principal component analysis. Biotechnol. Bioeng. 82 (4), 489–497.

Lee, D., Vanrolleghem, P. A., 2004. Adaptive consensus principal component analysis for on-line batch process monitoring. Environ. Monit. Assess. 92, 119–135.

Lee, G., Yoon, E., Lim, Y., Lann, J. L., Meyer, X., Joulia, X., 2001. Adaptive mesh method for the simulation of crystallisation processes including agglomeration and breakage: the potassium sulfate system. Ind. Eng. Chem. Res. 40, 6228–6235.

Lee, S., Koopman, B., Bode, H., Jenkins, D., 1983. Evaluation of alternative sludge settleability indices. Wat. Res. 17 (10), 1421–1426.

Li, D., Ganczarczyk, J., 1989. Fractal geometry of fractal aggregates in water and wastewater treatment processes. Env. Sci. Tech. 23, 1385–1389.

Li, D., Ganczarczyk, J., 1990. Structure of activated sludge flocs. Biotechnol. Bioeng. 35, 57–65.

Li, D., Ganczarczyk, J., 1991. Size distribution of activated sludge flocs. Res. J. WPFC 63 (5), 806–814.

Li, D., Ganczarczyk, J., 1993. Factors affecting dispersion of activate sludge flocs. Biotechnol. Bioeng. 35, 57–65.

Li, X., Logan, B., 1997a. Collision frequencies between fractal aggregates and small particles in a turbulently sheared fluid. Env. Sci. Tech. 31, 1237–1242.

Li, X., Logan, B., 1997b. Collision frequencies of fractal aggregates with small particles by differential sedimentation. Env. Sc. tech. 31, 1229–1236.

Li, X., Yuan, Y., 2002. Collision frequencies of microbial aggregates with small particles by differential sedimentation. Env. Sci. Tech. 36, 387–393.

Liao, B., Allen, D., Droppo, I., Leppard, G., Liss, S., 2000. Bound water content of activated sludge and its relationship to solids retention time, floc structure and surface properties. Wat. Env. Res. 72 (6), 722–730.

Liao, B., Allen, D., Droppo, I., Leppard, G., Liss, S., 2001. Surface properties of sludge and their role in bioflocculation and settleability. Wat. Res. 35 (2), 339–350.

Liou, J., Srienc, F., Frecerickson, A., 1997. Solutions of population balance models based on a successive generations approach. Chem. Eng. Sci. 52 (9), 1529–1540.

Liss, S., Droppo, I., Flannigan, D., Leppard, G., 1996. Floc architecture in wastewater and natural riverine systems. Env. Sci. Tech. 30, 680–686.

Litster, J., Smit, D., Hounslow, M., 1995. Adjustable discretised population balance for growth and aggregation. AIChE J. 41 (3), 591–603.

Liu, Y., Cameron, I., 2001. A new wavelet-based method for the solution of the population balance equation. Chem. Eng. Sci. 56 (18), 5283–5294.

Liu, Y., Fang, H., 2003. Influences of extracellular polymeric substances (eps) on flocculation, settling and dewatering of activated sludge. Crit. Rev. Env. Sci. Technol. 33 (3), 237–273.

Lu, C., Spielman, L., 1984. Kinetics of floc breakage and aggregation in liquid suspensions. J. Col. Int. Sci. 103 (1), 95–105.

Mandelbrot, B., 1987. The fractal geometry of nature. Freeman, New York, USA.

Marchisio, D., Vigil, R., Fox, R., 2003. Quadrature method of moments for aggregation-breakage processes. J. Col. Int. Sc. 258 (2), 322–334.

Marshall, K., 1981. Microbial adhesion of surfaces. Ellis Horwood, Chichester, UK, Ch. Bacterial adhesion in natural environments.

Mikkelsen, L., 2001. The shear sensitivity of activated sludge: Relations to filterability, rheology and surface chemistry. Coll. Surf. A 182, 1–14.

Mikkelsen, L., Gotfredsen, A., Agerbaek, M., Nielsen, P., Keiding, K., 1996. Effects of colloidal stability on clarification and dewatering of activated sludge. Wat. Sci. Tech. 34, 449–457.

Mikkelsen, L., Keiding, K., 2002. Physico-chemical characteristics of full scale sewage sludges with implication to dewatering. Wat. Res. 36 (10), 2451–2462.

Morgan-Sagastume, F., Allen, D., 2003. Effects of temperature transient conditions on aeroboc biological treatment of wastewater. Wat. Res. 37, 3590–3601.

Narsimhan, G., Ramkrishna, D., Gupta, J., 1980. Analysis of drop size distributions in liquid-liquid dispersions. AIChE J. 26, 991–1000.

Nelder, J., Mead, R., 1965. A simplex method for function minimalization. Computer Journal 7, 308–313.

Pandya, J., Spielman, L., 1983. Floc breakage in agitated suspensions: effect of agitation rate. Chem. Eng. Sci. 38 (12), 1983–1992.

Parker, D., Kaufman, W., Jenkins, D., 1970. Characteristics of biological flocs in turbulent regimes. Tech. Rep. 70-5, Sanit. Eng. Res. Lab., Univ. Calif. Berkeley.

Parker, D., Kaufman, W., Jenkins, D., 1972. Floc breakup in turbulent flocculation processes. J. Sanitary Div. A.S.C.E. 1, 79–99.

Ramkrishna, D., 2000. Population Balances: Theory and Applications to Particulate Systems in Engineering. Academic Press, London, UK.

Ramkrishna, D., Mahoney, A., 2002. Population balance modeling. promise for the future. Chem. Eng. Sci. 57, 595–606.

Rogak, S., Flagan, R., 1990. Stokes drag on self-similar clusters of spheres. J. Col. Int. Sc. 134 (1), 206–218.

Saffman, P., Turner, J., 1956. On the collision of drops in turbulent clouds. J. Fluid Mech. 1 (16), 16–30.

Samimi, A., Ghadiri, M., Boerefijn, R., Groot, A., Kohlus, R., 2003. Effect of structural characteristics on impact breakage of agglomerates. Powd. Techn. 130, 428–435.

Sathyagal, A., Ramkrishna, D., Narsimhan, G., 1995. Solution of inverse problems in population balances — ii particle break-up. Comp. Chem. Eng. 19 (4), 437–451.

Scott, W., 1968. Analytical studies in cloud droplet coalescence i. J. Atmos. Sci. 25, 54–65.

Selomulya, C., Amal, R., Bushell, G., Waite, T., 2001. Evidence of shear rate dependence on restructuring and breakup of latex aggregates. J. Col. Int. Sci. 236, 67–77.

Serra, T., Casamitjana, X., 1998. Modelling the aggregation and break-up of fractal aggregates in a shear flow. Applied Scientific Research 59, 255–268.

Serra, T., Colomer, J., Casamitjana, X., 1997. Aggregation and break-up of particles in a shear flow. J. Col. Int. Sc. 187, 466–473.

Serra, T., Logan, B., 1999. Collision frequencies of fractal bacterial aggregates with small particles in a sheared fluid. Env. Sc. Techn. 33, 2247–2251.

Sezgin, M., Jenkins, D., Parker, D., 1978. A unified theory of filamentous activated sludge bulking. J. Wat. Pol. Control Fed. 50, 362–381.

Smoluchowski, M., 1917. Versuch einer mathematischen theorie der koagulationskinetik kolloider lsungen. Z. Phys. Chem. 92, 129–168.

Sobeck, D., Higgins, M., 2002. Examination of three theories for mechanisms of cation-induced bioflocculation. Wat. Res. 36, 527–538.

Spicer, P., Pratsinis, S., 1996a. Coagulation and fragmentation: universal steady-state particle size distribution. AIChE J. 42 (6), 1612–1620.

Spicer, P., Pratsinis, S., 1996b. Shear-induced flocculation: the evolution of floc structure and the shape of the size distribution at steady state. Wat. Res. 30 (5), 1049–1056.

Stanley, S., Smith, D., 1995. Measurement of turbulent flow in standard jar test apparatus. J. Env. Eng. 121 (12), 902–910.

Starkey, E., Karr, P., 1984. Effect of low dissolved oxygen concentration on effluent turbidity. Journal WPCF 56 (7), 837–843.

Stobbe, C., 1964. ber das verhalten des belebten schlammes in aufsteigender wasserbewegung. In: Verffentlichungen des Institutes fr Siedlungswasserwirtschaft der Technischen Hochschule Hannover. Vol. 18.

STOWa, 2002. Optimalisatie van ronde nabezinktanks: Ontwikkeling nabezinktankmodel en evaluatie stora-ontwerprichtlijn. Tech. rep., Stichting Toegepast Onderzoek Waterbeheer (STOWA), Utrecht, The Netherlands.

Sürücü, G., Cetin, F., 1989. Effect of temperature, ph and do concentration on filterability and compressibility of activated sludge. Wat. Res. 23, 1389–1395.

Tambo, N., Hozumi, H., 1979. Physical aspects of flocculation process: – ii. contact flocculation. Wat. Res. 13, 441–448.

Tambo, N., Watanabe, Y., 1979. Physical characteristics of flocs – i. the floc density function and aluminum floc. Wat. Res. 13, 409–419.

Tchobanoglous, G., Burton, F., Stensel, H., 2003. Wastewater Engineering: Treatment and reuse, 4th Edition. Metcalf and Eddy. McGraw - Hill, New York, USA.

Thill, A., Moustier, S., Aziz, J., Wiesner, M., Bottero, J., 2001. Flocs restructuring during aggregation: experimental evidence and numerical simulation. J. Col. Int. Sc. 243, 171–182.

Thomas, D., Judd, S., Fawcett, N., 1999. Flocculation modelling: a review. Wat. Res. 33 (7), 1579–1592.

Urbain, V., Block, J., Manem, J., 1993. Bioflocculation in activated sludge: an analytical approach. Wat. Res. 27 (5), 829–838.

Vanhooren, H., Meirlaen, J., Amerlinck, Y., Claeys, F., Vangheluwe, H., Vanrolleghem, P., 2003. West: Modelling biological wastewater treatment. J. Hydroinformatics 5, 27–50.

Vanni, M., 2000. Approximate population balance equations for aggregation-breakage processes. J. Coll. Int. Sc. 221, 143–160.

Vanrolleghem, P., Van Der Schueren, D., Krikilion, G., Grijspeerdt, K., Willems, P., Verstraete, W., 1996. On-line quantification of settling properties with in-sensor-experiments in an automated settlometer. Wat. Sci. Techn. 33 (1), 37–51.

Veerapaneni, S., Wiesner, M., 1996. Hydrodynamics of fractal aggregates with radially varying permeability. J. Col. Int. Sc. 177, 45–57.

Verwey, E., Overbeek, J., 1948. Theory of the stability of lyophobic colloids. Elsevier, The Netherlands.

Wahlberg, E., Keinath, T., Parker, D., 1994. Influence of flocculation time on secondary clarification. Wat. Env. Res. 66 (6), 779–786.

Wahlberg, E., Merill, D., Parker, D., 1995. Troubleshooting activated sludge secondary clarifier performance using simple diagnostic tests. In: Proceedings of the 68th Annual WEF Conference and Exposition, Miami. Vol. 1. WEF, Alexandria, Virginia, USA, pp. 435–444.

Waite, T., 1999a. Measurement and implications of floc structure in water and wastewater treatment. Colloids and Surf. 151, 27–41.

Waite, T., 1999b. Measurement and implications of floc structure in water and wastewater treatrment. Colloids and Surfaces A 151, 27–41.

Wang, C., Friedlander, S., 1967. The self-preserving particle size distribution for coagulation by brownian motion: Ii. small particle slip correction and simulaneous shear flow. J. Col. Int. Sci. 24, 170–179.

Wanner, J., 1994. Activate sludge bulking and foaming control. Technomic Publishing.

Weiner, B., Tscharnuter, W., Karasikov, N., 1998. Improvements in accuracy and speed using the time-of-transition method and dynamic image analysis for particle sizing. In: Provder, T. (Ed.), Symposium Series 693, Particle Size Distribution III. American Chemical Society.

White, M., 1975. Settling of activated sludge. Tech. Rep. 11, Water research centre, Stevenage, UK.

Wilén, B., Balmér, P., 1999. The effect of dissolved oxygen concentration on the structure, size and size distribution of activated sludge flocs. Wat. Res. 33 (2), 391–400.

Wilén, B., Jin, B., Lant, P., 2003. Relationship between flocculation of activated sludge and composition of extracellular polymeric substances. Wat. Sci. Tech. 47 (12), 95–103.

Wilén, B., Keiding, K., Nielsen, P., 2000. Anaerobic deflocculatin and aerobic reflocculation of activated sludge. Wat. Res. 34 (16), 3933–3942.

Wright, H., Ramkrishna, D., 1992. Solutions of inverse problems in population balances — i aggregation kinetics. Comp. Chem. Eng. 16 (12), 1019–1038.

Wu, R., Lee, D., Waite, T., Guan, J., 2002. Multilevel structure of sludge flocs. J. Col. Int. Sc. 252, 383–392.

Wynn, E., 2003. Relationship between particle-size and chord-length distributions in focused beam reflectance measurement: stability of direct inversion and weighting. Powd. Tech. 133, 125–133.

Yoo, C., Lee, D., Vanrolleghem, P. A., 2004. Application of multiway ica for on-line process monitoring of a sequencing batch reactor. Wat. Res. 38, 1715–1732.

Ziff, R., McGrady, E., 1985. The kinetics of cluster fragmentation and depolymerisation. J. Phys. A: Math. Gen. 18, 3027–3037.

Zita, A., Hermansson, M., 1994. Effects of ionic strength on bacterial adhesion and stability of flocs in a wastewater activated sludge system. Appl. Env. Microbiol. 60 (9), 3041–3048.

List of abbreviations and symbols

Abbreviations

BOD	biochemical oxygen demand	$[\mathrm{M.L^{-3}}]$
BW	bound water	
CFD	computational fluid dynamics	
CFS	coalesced fractal sphere	
COD	chemical oxygen demand	$[\mathrm{M.L^{-3}}]$
CWA	clean water act	
DCB	divalent cation bridging	
DGGE	denaturing gradient gel electrophoresis	
DO	dissolved oxygen concentration	$[\mathrm{M.L^{-3}}]$
DSS	dispersed suspended solids	$[\mathrm{M.L^{-3}}]$
DSVI	diluted sludge volume index	$[\mathrm{L^3.L^{-3}}]$
EPA	environmental protection agency	
EPS	exocellular polymeric substances	
ESS	effluent suspended solids	$[\mathrm{M.L^{-3}}]$
FSS	flocculated suspended solids	$[\mathrm{M.L^{-3}}]$
HGE	hierarchical graphical editor	
HRT	hydraulic residence time	[T]
MLSS	mixed liquor suspended solids	$[\mathrm{M.L^{-3}}]$
MSL	model specification language	
NPDES	National Pollution Discharge Elimination System	
ORP	oxidation-reduction potential	$[\mathrm{V}]$
PBE	population balance equation	
PBM	population balance model	
PCA	principal component analysis	
PSD	particle size distribution	
SBR	sequencing batch reactor	
SCM	shell core model	
SPA	state point analysis	
SRT	sludge residence time	[T]
SS	suspended solids	$[\mathrm{M.L^{-3}}]$
SST	secondary settling tank	

Abbreviations - continued

SSVI	stirred sludge volume index	$[L^3.L^{-3}]$
$SSVI_{3.5}$	stirred sludge volume index at a SS concentration of 3.5 $g.l^{-1}$	$[L^3.L^{-3}]$
SVI	sludge volume index	$[L^3.L^{-3}]$
TMDL	total maximum daily load	
WML	WEST model library	
z	vector of internal and external coordinates	

English letters

a_0	primary particle radius	$[L]$
a'_{max}	maximum principal strain rate	$[T^{-1}]$
A_{ham}	Hamaker constant	$[M.L^2.T^{-2}]$
b(x,r,Y,t)	specific breakage rate	$[T^{-1}]$
d_m	metastable floc diameter	[L]
d_{max}	maximum stable floc diameter	[L]
D_f	fractal dimension	[-]
$r \equiv (r_1, r_2, r_3)$	vector of external coordinates	
$f_1(x, r, t)$	number density function	$[L^{-3}]$
$f_2(x, r; x', r', t)$	particle pair density function	$[L^{-6}]$
$F_1(x, r, t)$	cummulative number density function	$[L^{-3}]$
g	gravity constant	$[L.T^{-2}]$
G	absolute velocity gradient	$[T^{-1}]$
$h(x, r, Y, t)$	net birth rate	$[T^{-1}.L^{-3}]$
$h^+(x, r, Y, t)$	source term of net birth rate	$[T^{-1}.L^{-3}]$
$h^+_{agg}(x, r, Y, t)$	source term from aggregation	$[T^{-1}.L^{-3}]$
$h^+_{break}(x, r, Y, t)$	source term from breakage	$[T^{-1}.L^{-3}]$
$h^-(x, r, Y, t)$	sink term of net birth rate	$[T^{-1}.L^{-3}]$
$h^-_{agg}(x, r, Y, t)$	sink term from aggregation	$[T^{-1}.L^{-3}]$
$h^-_{break}(x, r, Y, t)$	sink term from breakage	$[T^{-1}.L^{-3}]$
I	light intensity	
l	turbulent length scale	[L]
L	length of a scattering body	[L]
m	relative refractive index	[-]
n	refractive index	[-]
n_b	number of basis functions (to solve inverse problem	[-]
N_a	agitation speed	$[T^{-1}]$
N_i	number concentration in class i	$[L^{-3}]$
N_p	dimensionless impeller power number	$[L^{-3}]$
$P(x, r\|x', r', Y, t)$	probability density function or daughter size distribution	
Q	wave vector	
r	particle radius	[L]
r_G	radius of gyration	[L]
r_{Gi}	radius of gyration of aggregate i	[L]

English letters - continued

$\mathrm{r_H}$	hydraulic radius	[L]
$\dot{\mathrm{R}}\left(\mathrm{x,r,Y,t}\right)$	rate of change of external coordinates	$[\mathrm{T^{-1}}]$
$\mathrm{R_p}$	primary particle size	[L]
t	time	T
T	absolute temperature	K
$\mathrm{T_a}$	torque	F.L
$\Delta\mathrm{u(l)}$	differential velocity	$[\mathrm{L.T^{-1}}]$
$\bar{\mathrm{v}}_\mathrm{e}$	mean volume of all erosion product particles	$[\mathrm{L^3}]$
$\mathrm{v_p}$	mean volume of all erosion product particles $<$ parent floc	$[\mathrm{L^3}]$
$\mathrm{V_{ZS}}$	zone settling velocity	$[\mathrm{L.T^{-1}}]$
$\mathrm{x} \equiv (\mathrm{x_1}, \mathrm{x_2}, \ldots, \mathrm{x_d})$	d-dimensional vector of internal coordinates	
$\dot{\mathrm{X}}\left(\mathrm{x,r,Y,t}\right)$	rate of change of internal coordinates	$[\mathrm{T^{-1}}]$
$\mathrm{Y}\left(\mathrm{r,t}\right)$	continuous phase vector	

Greek symbols

$\alpha_{\mathrm{i,j}}$	collision efficiency of particles of sizes i and j	[-]
$\beta_{\mathrm{i,j}}$	collision frequency of particles of sizes i and j	$[\mathrm{L^3.T^{-1}}]$
ϵ	energy dissipation rate	$[\mathrm{L^2.T^{-3}}]$
η	Kolmogorov length scale	[L]
η	similarity variable (only in section 2.5.6)	[L]
$\phi\left(\mathrm{x,r,t}\right)$	volume fraction	[-]
$\varphi)$	floc density	[-]
$\varphi_0)$	packing density	[-]
κ	permeability	$[\mathrm{L^2}]$
λ	wavelength of radiation in vacuum	[L]
λ_H	ratio of hydraulic particle radii	$[-]$
λ_reg	regularisation parameter	$[-]$
μ	dynamic viscosity	$[\mathrm{M.L^{-1}.T^{-1}}]$
$\mu_\mathrm{r}\left(\mathrm{t}\right)$	$\mathrm{r^{th}}$ integral moment	
$\mu_\mathrm{r}^{(\mathrm{i})}\left(\mathrm{t}\right)$	$\mathrm{r^{th}}$ sectional moment	
ν	kinematic viscosity	$[\mathrm{L^2.T^{-1}}]$
Ω_r	domain of external coordinates	
Ω_x	domain of internal coordinates	
ρ_l	fluid density	$[\mathrm{M.L^{-3}}]$
ρ_p	particle density	$[\mathrm{M.L^{-3}}]$
τ	pulse width	[T]
θ	scattering angle	$[-]$
$\upsilon\left(\mathrm{x'},\mathrm{r'},\mathrm{Y},\mathrm{t}\right)$	average number of particles formed through breakage	
ξ	Debye's shielding ratio	[-]

Summary

The separation of activated sludge and purified wastewater still remains a delicate issue in wastewater treatment. In both the traditional separation by means of gravitation in a secondary settling tank and the more recent membrane technology, it has been accepted that floc size and, hence, activated sludge flocculation plays an important role.

This dissertation deals with the investigation of the applicability of a population balance framework for modelling the activated sludge flocculation process. This analysis consists of several separate issues which should be treated in a logical order.

A first issue is related to the *numerical solution methods for population balance models*. To this end, three discretisation methods (Hounslow algorithm, fixed pivot and moving pivot) were taken from literature and subjected to a detailed simulation study in which several aspects like ease of implementation, accuracy, stability, ... were investigated for three distinct mechanisms (pure aggregation, pure breakage and the combined case) when using different initial conditions and grid densities. It was concluded that the moving pivot was superior in most cases. However, the choice is often a trade-off between accuracy and simulation speed.

In a second stage, a *comprehensive calibration methodology* was developed which deals with several issues related to the fitting of a population balance model to an experimental data set, i.e. the selection of the solution method, data transformation, determination of measurement errors and choice of fitting variable. The former was already investigated in the first part. Data transformations should be avoided, but are sometimes necessary, e.g. to determine the initial particle size distribution for the model. A new method based on the sludge concentration and the densities of water, flocs and solids was presented. Preliminary experiments for the measurement of the floc and solids densities were also conducted, where the former is based on pyknometry and the latter on a linear Percoll gradient. Initial results showed floc densities of 1.02-1.06 $\mathrm{g.ml^{-1}}$, whereas solids densities were found in the range of 1.60 $\mathrm{g.ml^{-1}}$. A method to determine measurement errors in the different size classes of a distribution was presented based on the variance of a multinomial distribution. Finally, the choice of fitting variable was investigated. Volume-based variables were able to capture the dynamics of the volume percentage distribution rather well. However, they completely failed at predicting the dynamics of the number distribution. Fitting on number-based variables resulted in poor predictions of the volume distribution dynamics, whereas a better prediction of the dynamic number distribution was found. The choice should be determined by the goal of the research. In this case, the number of small particles is of interest as it are the small particles that end up in the effluent and determine its quality.

In the previous steps, no attention was paid to finding an adequate *structure of the model*. Two different approaches were used to find one: evaluate existing kernels from literature and extracting the kernel structures from the experimental data.

In the first approach, different relevant kernels for aggregation and breakage were selected from literature. These were combined into four models that were subsequently fitted to the dynamic number distribution using a least squares method. The knowledge-based models incorporated mechanisms like shear-based orthokinetic aggregation, fractal dimension, hydrodynamic and Van der Waals interactions, turbulent breakage. However, none of the investigated models was able to describe the evolution of the number distributions. The best model was found to be composed of a constant collision efficiency, a shear-based orthokinetic aggregation frequency and power law breakage with an exponent of 1/9.

The second approach aims at solving the inverse problem to reconstruct the unknown aggregation and breakage kernels from the experimental data. Prior to applying this technique, a similarity analysis is performed since this can simplify the inversion problem.

In the pure aggregation case, the aggregation data obtained from a sonicated sludge did not exhibit self-similar behaviour. However, aggregation from a sludge that was previously exposed to a high shear environment did exhibit self-similar behaviour. This leads to the important conclusion that sonication is apparently not representative for the dynamic flocculation behaviour of an activated sludge in a full-scale plant. It should, therefore, be avoided in lab-scale studies on activated sludge flocculation.

Since flocculation behaviour was found to be different for the non-sonicated sludge, the previous approach using models from literature was repeated first. However, the optimisation algorithm was found to be sensitive to initial parameter values and also resulted in very high parameter variances. An investigation based on a scenario analysis showed that the objective function consisted of a large plateau and only exhibited a minumum around the origin. This would imply that the dynamic data could best be described by a static model (i.e. no aggregation or breakage) which is not consistent with the observations.

Continuing the second approach, the inverse problem was solved. In the scope of reconstructing the unscaled aggregation frequency, it was found that the kernel was not homogeneous and that an alternative method based on the derivative of the scaling function h(t) was to be used. The reconstructed unscaled aggregation kernels exhibited a different shape depending on the number of basis function that was used in the inversion. The regularisation parameter did not influence the results a lot, except in the case where three basis functions were used.

The quality of the inversion was checked by performing a so-called forward simulation. The case using four basis functions in the inversion yielded the best results and was able to capture the evolution of the complete volume distribution, except for the lower tail. However, in order to obtain this result, an additional factor had to be introduced. The origin of this factor is unclear. It causes the small size classes of the number distribution to be underestimated, whereas the remainder of the distribution is captured quite well.

The inversion was also investigated for the pure breakage case. Self-similar behaviour was found and resulted in a breakage rate described by a power law with exponent 3.7. The constant and the daughter distribution have to be recovered from the inverse problem. However, the basis functions had to be modified due to a singularity near the origin. This resulted in a solution of the inverse problem that was best for the lowest number of basis functions. The remaining constant of the breakage rate was determined to be 1.5. The daughter distribution could be extracted from the cumulative daughter distribution.

Unfortunately, the forward simulation was impossible to complete due to the high breakage rates that

prohibited the solver to converge to a solution. Multiplying by a small factor allowed to perform the simulation, but resulted in poor predictions of the dynamic volume distribution.

Finally, existing *experimental data* and new experimental data from the newly built Flocunit were analysed with focus on the dynamic behaviour of the distributions instead of a summarising parameter such as the weighted average diameter. No universal relationship between the most abundant floc size and the Kolmogorov microscale was found for the different experiments. For the literature data, the Kolmogorov scale, calculated based on the assumption that the maximum energy dissipation rate near the impeller is tenfold of the average energy dissipation rate, was in good agreement with the most abundant floc size. The latter was not found for the Flocunit experiments. This is possibly due to differences in reactor configuration (larger volume, different impeller) and floc strength. On the other hand, the analysis revealed that in the dynamic part of aggregation/breakage experiments the assumption of neglecting the other mechanism (breakage/aggregation respectively) was valid. This assumption is an important requirement for conducting the similarity analysis.

The new experimental data investigated the influence of 5 possible influencing physico-chemical factors by means of a fractional factorial design, i.e. temperature, shear rate, dissolved oxygen, sludge concentration and Ca-addition. Shear has an important effect on the activated sludge flocculation. High shear destroys flocs and shifts distributions toward smaller sizes. Low shear allows larger flocs to be present in the system. Flocs are not disturbed when temperature is lowered. However, some immediate flocculation occurs when temperature is increased. Applying anaerobic conditions showed an immediate increase in floc size. At low sludge concentration, a slow deflocculation can be observed, caused by the smaller collision probability. Ca-addition results in flocculation.

Samenvatting

De scheidingsstap van het actief slib en het gezuiverde water blijft nog steeds een delicate kwestie binnen de afvalwaterzuivering. Zowel in de traditionele gravitaire bezinking in een secundaire nabezinktank als bij de meer recente membraantechnologie wordt algemeen aangenomen dat de vlokgrootte en dus de actief slib flocculatie een belangrijke rol speelt.

Dit werk onderzoekt de toepasbaarheid van een populatiebalansmodel voor het modelleren van het actief slib flocculatieproces. De analyse behelst verscheidene zaken die in een logische volgorde dienen te worden behandeld.

Een eerste zaak is gerelateerd met de *numerieke oplossingsmethoden voor populatiebalmansmodellen*. Met dit doel voor ogen werden drie discretisatiemethoden (het Hounsloalgortime, de fixed pivot en de moving pivot) uit de literatuur onderworpen aan een gedetailleerde simulatiestudie waarin verschillende aspecten zoals moeilijkheidsgraad van implementatie, accuraatheid, stabiliteit,... werden belicht voor drie mechanismen (zuivere aggreggatie, zuivere breking en het gecombineerde geval) en voor verschillende initiële condities en griddichtheden. Het moving pivot algoritme bleek in de meeste gevallen superieur te zijn. De keuze blijft echter steeds een afweging tussen accuraatheid en rekensnelheid.

In een tweede luik werd een *uitgebreide calibratiemethodologie* ontwikkeld die verschillende punten aanraakt die belangrijk zijn bij de calibratie van een populatiebalansmodel met experimentele meetgegevens zoals de selectie van een oplossingsmethode, datatransformatie, het bepalen van meetfouten en schattingsvariabele. Het eerste punt werd reeds voorheen uitvoerig behandeld. Datatransformaties worden best vermeden maar zijn soms onafwendbaar om vb. een initiële partikelgroottedistributie voor het model te genereren. Een nieuwe methode gebaseerd op de slibconcentratie en de densiteiten van water, vlokken en vaste stof werd ontwikkeld. Ook werden preliminaire experimenten voor de bepaling van de vlok- en vaste stof densiteiten uitgevoerd, waarbij de eerste steunt op pyknometrie en de laatste op een lineaire Percoll-gradiënt. Initiële resultaten toonden vlokdensiteiten van 1.02-1.06 $\mathrm{g.ml^{-1}}$, terwijl vaste stof densiteiten in de buurt van 1.60 $\mathrm{g.ml^{-1}}$ lagen. Een methode ter bepaling van meetfouten in de verschillende klassen gebaseerd op op de variantie van een multinomiale verdeling werd voorgesteld. Tenslotte werd de keuze van de schattingsvariabele onderzocht. Volumegebaseerde variabelen konden de dynamica van de volume distributies behoorlijk goed beschrijven. Anderzijds faalden zij volledig bij het voorspellen van de dynamica van de aantallen-verdelingen. Aantalgebaseerde variabelen konden de dynamica van de volumedistributies niet beschrijven, maar konden de dynamica van de aantallendistributies dan weer beter voorspellen. De keuze wordt dan ook in grote mate bepaald door het doel van het onderzoek. In dit geval is het aantal kleine partikels van primordiaal belang aangezien het net deze kleine partikels zijn die in het effluent zullen terechtkomen en de kwaliteit ervan bepalen.

In wat vooraf ging werd nog geen aandacht besteed aan het vinden van een adequate *modelstructuur*. Twee verschillende aanpakken werden gebruikt om deze te vinden: evaluatie van bestaande functies uit de literatuur en het extraheren van de functiestructuren uit de experimentele data.

Voor de eerste benadering werden verschillende aggregatie- en brekingsfuncties uit de literatuur geselecteerd. Deze werden gecombineerd in vier modellen die vervolgens werden gefit aan de dynamische aantallendistributies met behulp van een kleinste kwadratenmethode. Deze kennisgebaseerde modellen incorporeerden concepten zoals orthokinetische aggregatie, fractale dimensie, hydrodynamische en Van der Waals interacties en turbulente breking. Geen van de modellen was echter in staat om een goede beschrijving te geven van de dynamische evolutie van de aantallendistributie. Het beste model bestond uit een constante botsingsefficiëntie, een orthokinetische aggregatiefrequentie en een machtsfunctie voor breking met een exponent gelijk aan 1/9.

De tweede benadering trachtte het invers probleem op te lossen om zo de onbekende aggregatie- en brekingsfuncties te reconstrueren uitgaande van de experimentele data. Alvorens deze techniek toe te passen werd een similariteitsanalyse uitgevoerd aangezien deze de oplossing van het invers probleem aanzienlijk kan vergemakkelijken.

In het geval van zuivere aggregatie werd geen similariteit gevonden voor de gesoniceerde data. In tegenstelling hiermee werd wel similariteit gevonden bij slib dat aggregeerde uitgaande van een slib dat voordien aan een hogere mengintensiteit werd blootgesteld. Dit leidt tot de belangrijke conclusie dat het toepassen van sonicatie niet representatief is voor het bestuderen van slibflocculatiedynamica in een volschalige installatie. Het wordt dan ook afgeraden om sonicatie in laboschaalexperimenten voor het bestuderen van actief slib flocculatie te gebruiken.

Aangezien het flocculatiegedrag met of zonder sonicatie verschillende bleek te zijn, werd de vorige aanpak met de modellen uit de literatuur herhaald. Er werd gevonden dat het optimalisatie-algoritme gevoelig was voor de initiële parameterwaarden en de resulterende parametervarianties waren zeer groot. Een diepgaandere studie van de parameterruimte met behulp van een scenario-analyse toonde aan dat de objectieffunctie bestond uit een groot plateau dat enkel bij de oorspong een minimum vertoonde. Dit impliceert dat de dynamische data het best beschreven worden door een statisch model (maw. geen aggregatie of breking) wat duidelijk niet consistent is met de observaties.

Verderbouwend op de tweede benadering werd het invers probleem opgelost. Vervolgens diende de ongeschaalde aggregatiefrequentie worden gereconstrueerd. Hierbij bleek dat deze niet homogeen bleek te zijn en dat een alternatieve methode steunend op de afgeleide van de schalingsfunctie h(t) diende gebruikt te worden. De gereconstrueerde, ongeschaalde aggregatiefrequentie vertoonde een verschillende vorm afhankelijk van het aantal basisfuncties dat werd gebruikt bij de inversie. De regularisatieperameter beïnvloedde de resultaten nauwelijks behalve in het geval waar drie basisfuncties werden gebruikt.

De kwaliteit van de inversie werd gecontroleerd door het uitvoeren van een zogenaamde voorwaartse simulatie gebruik makende van de gevonden aggregatiefrequentie in het model. Het geval waarbij vier basisfuncties in de inversie werden gebruikt leverde het beste resultaat en was in staat om de evolutie van de gehele volumedistributie te beschrijven met uitzondering van de staart bij de kleine partikels. Om dit resultaat te bekomen diende echter een additionele factor te worden ingevoerd in het model. De reden hiervoor is vooralsnog onduidelijk. De kleine partikels van de aantallendistributie worden opnieuw onderschat, maar de rest van de distributie wordt goed beschreven.

De mogelijkheid voor inversie werd ook onderzocht voor zuivere breking. Ook hier werd similariteit gevonden, wat in dit geval reeds de exponent van de machtsfunctie oplevert, nl. 3.7. Zowel de tweede

constante van de machtsfunctie als de dochterdistributie dienen vervolgens bepaald te worden uit het invers probleem. In dit geval dienden andere basisfuncties te worden gebruikt wegens het optreden van een singulariteit in de buurt van de oorsprong. Dit resulteerde in een oplossing voor het invers probleem dat het beste bleek te zijn voor het kleinste aantal basisfuncties. De overblijvende constante in de machtsfunctie werd bepaald op 1.5. De dochterdistributie kon worden afgeleid van de cumulatieve dochterdistributie.

De voorwaartse simulatie bleek echter niet uitvoerbaar wegens de te hoge brekingssnelheden wat de solver niet toeliet om naar een oplossing te convergeren. Vermenigvuldigen met een kleine factor liet wel toe om de simulatie uit te voeren, maar dit resulteerde niet in goede voorspellingen van de dynamische volumedistributies.

Tenslotte werden ook bestaande *experimentele data* en nieuwe data van de Flocunit geanalyseerd waarbij de aandacht vooral werd toegespitst op het dynamisch gedrag van de distributies in plaats van op een samenvattende parameter zoals de gewogen gemiddelde diameter. Er werd geen eenduidige relatie gevonden tussen de meest voorkomende vlokgrootte en de Kolmogorov microschaal van turbulentie voor de verschillende experimenten. Voor de data uit de literatuur was de Kolmogorovschaal, berekend op basis van de assumptie dat de energiedissipatiesnelheid in de buurt van het roerblad tien keer hoger is dan de gemiddelde energiedissipatiesnelheid, vergelijkbaar met de meest voorkomende vlokgroottes. Dit laatste werd echter niet teruggevonden voor de Flocunit-experimenten. Dit is waarschijnlijk toe te schrijven aan het verschil in reactorconfiguratie (ander volume en mengblad) en vloksterkte. Anderzijds onthulde de analyse dat zuivere aggregatie/breking kan worden verondersteld in de dynamische fase van de experimenten. Dit laatste is een belangrijke voorwaarde voor het toepassen van similariteitsanalyses op de experimentele data.

De nieuwe experimentele data onderzocht de invloed van 5 mogelijke fysico-chemische invloeden door middel van een fractioneel factorieel ontwerp. Deze invloeden waren temperatuur, mengintensiteit, opgeloste zuurstofconcentratie, slibconcentratie en Ca-additie. Mengintensiteit had een belangrijke impact op actief-slib flocculatie. Hoge mengintensiteiten vernietigen de vlokken en verschuift de distributie naar kleinere vlokgroottes. Lage mengintensiteiten laten toe dat de vlokken groter worden. Vlokken blijken niet gevoelig te zijn voor temperatuursverlagingen. Anderzijds, werd een onmiddellijke flocculatie vastgesteld bij een toename van de temperatuur. Hetzelfde werd gevonden bij het aanleggen van anaërobe omstandigheden. Bij lage slibconcentraties werd een trage deflocculatie vastgesteld, te wijten aan lagere botsingsprobabiliteiten. Ca-toevoeging resulteerde in flocculatie.

Curriculum Vitae

Personal data

Ingmar Nopens	Gustaaf Van Heckelaan 1
Lokeren, November 17, 1976	9042 Sint-Kruis-Winkel (Gent)
Belgian	0478/42.77.95
Male	Ingmar.Nopens@UGent.be

Education

Bio-engineer in Environmental Technology, Ghent University *MSc. Thesis*: Estimation of activated sludge kinetic parameters using combined respirometric-titrimetric experimental data' conducted at the Department of Applied Mathematics, Biometrics and Process Control	1994-1999
PhD Training, Ghent University	2003

Additional courses with examination

Statistical data analysis (UGent)	2001
Easy PC-logging and data acquisition using LabView (UGent)	2001
Experimental Design (UGent)	2002
R&D Management (UGent)	2003

Additional courses without examination

PHP and MySQL (UGent)	2001
C and C++ (UGent)	2002
Membrane Technology: From theory to practice (VITO)	2003

Employment

OECD-criteria for ready biodegradability: environmental interpretation and study of alternatives. The 10 Day Window project. Project financed by AISE/CESIO (Detergent industry)	09-1999 until 06-2000
PhD, Department of Applied Mathematics, Biometrics and Process Control (Biomath): *Modelling the Activated Sludge Flocculation Process: a Population Balance Approach*. Research assistant on FWO-projects G.0032.00 and G.0184.04 and IWT-WEST 030449	07-2000 until now

Long-term stays abroad

February-April 2004. School of Chemical Engineering, Purdue University, USA.

Teaching activities

Practical exercises for courses on *Process Control* and *Bioprocess Control* (LabView)	2000-2003
Trends in R&D: Easy PC-logging and control with LabView.	Yearly since 2000
Teaching Assistant for the course *Process Control*	2004-2005

M.Sc Thesises supervised

Capalozza, C., 2001. Design, startup and monitoring of a pilot sequencing batch reactor for breeding stable nutrient removal sludge. MSc thesis, Ghent University, 146p.

Mahieu, K., 2002. Modelbouw van actief slib flocculatie d.m.v. een populatiebalansmodel. MSc thesis, Ghent University, 103p.

Koegst, T., 2002. Issues related to the calibration of a PBM for activated sludge flocculation. MSc thesis, Ghent University, 111p.

Beheydt, D., 2003. Vergelijking van verschillende numerieke technieken voor het oplossen van een populatiebalansmodel. MSc thesis, Ghent University, 53p.

International Conferences/Symposia/Workshops attended

European Union COST action 624, Work Group 4

- Unbalanced growth. April 6-7, 2000, Delft, The Netherlands. Attendee
- Microbial tools: Application in wastewater treatment (WWTP) processes. May 3-4, 2001, Lisbon, Portugal. Attendee
- Biodegradation of toxic and biorefractory compounds and their impact on wastewater treatment plants. November 29-30, 2001, Rome, Italy. Oral presentation (guest lecture).
- Optimal management of wastewater systems: Workshop on secondary clarifiers. 14-15, November 2002, Prague, Czech Republic. Attendee

European Union COST action 624, Management Committee Meetings

- May 4, 2001, Lisbon, Portugal
- November 30, 2001, Rome, Italy
- November 16, 2002, Prague, Czech Republic

International Conferences

- 3rd SETAC World Conference, May 21-25, 2000. Brighton, UK. Poster presentation.
- 5th International Symposium on Systems Analysis and Computing in Water Quality Management (WATERMATEX). September 18-20, 2000. Gent, Belgium. Attendee.
- 6th Ph.D Symposium, Gent, Belgium, October 11, 2000. Attendee.
- WEFTEC - 73rd Annual Conference & Exposition on Water Quality and Wastewater Treatment. October 14 - 18, 2000. Anaheim, California, USA. Attendee.
- 3rd IWA International Specialised Conference on Microorganisms in Activated Sludge and Biofilm Processes. June 13-15, 2001. Rome, Italy. Poster presentation.
- Activated Sludge Modelling: Fifth Kollekolle seminar. September 10-12, 2001. KolleKolle, Denmark. Oral presentation.
- 4th MathMod - Fourth International Symposium on Mathematical Modelling. February 5-7, 2003. Vienna, Austria. Oral presentation.
- WEFTEC 76th Annual Conference & Exposition on Water Quality and Wastewater Treatment. October 11-15, 2003, Los Angeles, California, USA. Oral presentation.
- PBM2004 - 2nd International Conference on Population Balance Modelling, May 5-7, 2004, Valencia, Spain. Oral and poster presentation.

Organization of conferences/workshops

- 5th International Symposium on Systems Analysis and Computing in Water Quality Management (WATERMATEX). September 18-20, 2000, Ghent, Belgium. Member of organizing committee.
- 2nd International Conference on Population Balance Modelling, May 5-7, 2004, Valencia, Spain. Member of organizing committee - General Responsible, together with Dr. C. Biggs (University of Sheffield, UK) and Dr. Joel Ducoste (NC State, US)
- Workshop on Recent Advances in Activated Sludge Flocculation (RAASF), September 27-28, 2004, Ghent, Belgium. Member of organizing committee.

Attended technical workshops

- Goffin Meyvis seminar for Particle characterization instruments, June 14, 2000, Bergen-op-Zoom, The Netherlands
- National Instruments Technical Roadshow: High-speed Data Acquisition, November 2001.
- National Instruments Technical Roadshow. Improving Productivity with PC-based Data Logging Solutions, November 2001.
- Stowa Optimisation of circular clarifiers, July 2002, DHV Amersfoort, Holland.
- Annual workshop on secondary clarifiers for German speaking researchers, January 2005, Hannover, Germany.

Publications (chronological per section)

Peer-reviewed Papers

De Clercq, J., Jacobs, F., Kinnear, D., Nopens, I., Dierckx, R., Defrancq, J., Vanrolleghem, P.A. Detailed spatio-temporal solids concentration profiling during batch settling of activated sludge using a radiotracer. Wat. Res. (accepted).

Nopens, I., Vanrolleghem, P. Comparison of discretisation methods to solve a population balance model of activated sludge flocculation including aggregation and breakage. Mathematical and Computer Modelling of Dynamical Systems (accepted).

Nopens, I., Beheydt, D., Vanrolleghem, P., 2005. Comparison and pitfalls of different discretised solution methods for population balance models: a simulation study. Comp. Chem. Eng., 29(2), 367-377.

Nopens, I., Koegst, T., Mahieu, K., Vanrolleghem, P. Population Balance Model and activated sludge flocculation: from experimental data to a calibrated model. AIChE Journal, 51(5), 1548-1557.

Beheydt, D., Nopens, I., 2004. Studie van actief slib flocculatie met behulp van een populatiebalansmodel: theoretische en praktische aspecten. Afvalwaterwetenschap, 3(1), 41-62.

Govoreanu, R., Seghers, D., Nopens, I., De Clercq, B., Saveyn, H., Capalozza, C., Van der Meeren, P., Verstraete, W., Top, E., Vanrolleghem P., 2002. Linking floc structure and settling properties to activated sludge population dynamics in an SBR. Wat. Sci. Tech., 47(12), 9-18.

Gernaey, K., Petersen, B., Nopens, I., Comeau, Y., Vanrolleghem, P., 2002. Modelling aerobic carbon source degradation processes using titrimetric data and combined respirometric-titrimetric data: I. Experimental data and model structure. Biotechn. Bioeng., 79(7), 741-753.

Nopens, I., Biggs, C., De Clercq, B., Govoreanu, R., Wilén, B., Lant, P., Vanrolleghem P., 2002. Modelling the activated sludge flocculation process combining laser diffraction particle sizing and population balance modelling (PBM). Wat. Sci. Tech., 45(6), 41-49.

Nopens, I., Hopkins, L., Vanrolleghem P., 2001. An overview of the posters presented at Watermatex 2000. III: Model selection and calibration / Optimal experimental design. Wat. Sci. Tech. 43(7), 387-389.

Carvalho, G., Nopens, I., Novais, J., Vanrolleghem, P., Pinheiro, H., 2001. Modelling of activated sludge acclimatisation to a non-ionic surfactant. Wat. Sci. Tech., 43(7), 9-17.

Papers without peer-review

Köster, S., Armbruster, M., Günther, N., Hollenstein, R., Nopens, I., Patzinger, M. and Schumacher, S., 2005. Quo vadis Nachklärbecken? Korrespond. Abw. (accepted).

Edited books

Nopens, I., Malisse, K., Biggs, C.A. and Ducoste, J., 2004. Advances in Population Balance Modelling. Book of abstracts of the 2nd International Conference on Population Balance Modelling, Valencia, Spain. Eurosis, Gent, Belgium. ISBN: 90-77381-10-4.

Nopens, I., Biggs C. Special Issue on PBM. Chem. Eng. Sci. (in preparation).

Proceedings

De Clercq, B., Nopens, I., Govoreanu, R., Vanrolleghem, P.A., Van Der Meeren P., 2000. Sludge (de)-flocculation dynamics in secondary clarifiers. Med. Fac. Landbouww. Univ. Gent, 65/4, 235-240.

Van Vooren, L., Van De Steene, M., Nopens, I., Ottoy, J.P., Vanrolleghem, P.A., 2000. Buffer capacity based multipurpose hard- and software sensor for environmental applications. In: Proceedings 7th International Conference on Chemometrics in Analytical Chemistry (CAC2000). Antwerp, Belgium, October 16-20, 2000.

Nopens, I., Biggs, C., De Clercq, B., Govoreanu, R., Wilén, B., Lant, P., Vanrolleghem, P.A., 2001. Modelling the activated sludge flocculation process combining laser diffraction particle sizing and population balance modelling (PBM). In: Proceedings 5th IWA Seminar on Modelling of Activated Sludge Processes in Theory and Practise. Kollekolle, Denmark, September 10-12, 2001.

Govoreanu, R., Nopens, I., De Clercq, B., Saveyn, H., Van der Meeren, P., Vanrolleghem P.A., 2001.

Influence of experimental parameters for on-line determination of floc size distribution. In: Proceedings 12th Romanian International Conference on Chemistry and Chemical Engineering. Bucharest, Romania, September 13-15, 2001.

Govoreanu, R., Seghers, D., Nopens, I., De Clercq, B., Saveyn, H., Capalozza, C., Van der Meeren, P., Verstraete, W., Top, E., Vanrolleghem P.A., 2002. Linking floc structure and settling properties to activated sludge population dynamics in an SBR. In: Proceedings 3rd IWA World Water Congress. Melbourne, Australia, April 7-12, 2002.

Govoreanu, R., Vandegehuchte, K., Saveyn, H., Nopens, I., De Clercq, B., Van Der Meeren, P., Vanrolleghem P.A., 2002. An automated image analysis system for on-line structural characterization of the activated sludge flocs. Med. Fac. Landbouww. Univ. Gent, 67/4, 175-178.

Nopens, I., Vanrolleghem, P.A., 2003. Comparison of discretisation methods to solve a population balance model of activated sludge flocculation including aggregation and breakage. In: Proceedings IMACS 4th MATHMOD Conference. Vienna, Austria, February 5-7, 2003.

Vanrolleghem, P.A., Insel, G., Petersen, B., Sin, G., De Pauw, D., Nopens, I., Doverman, H., Weijers, S., Gernaey, K., 2003. A comprehensive model calibration procedure for activated sludge models. In: Proceedings 76th Annual WEF Conference and Exposition. Los Angeles, USA, October 11-15, 2003.

Nopens, I., Koegst, T., Mahieu, K., Vanrolleghem P.A., 2004. PBM and activated sludge flocculation: From experimental data to a calibrated model. In: Proceedings 9th IFAC Conference on Computer Applications in Biotechnology CAB9. Nancy, France, March 28-31, 2004.

Nopens, I., Beheydt, D., Vanrolleghem P.A., 2004. Comparison of discretisation techniques to solve PBMs including aggregation and/or breakage: a simulation study. In Proceedings 2nd International Conference on Population Balance Modelling. Valencia, Spain, May 5-7 2004.

Nopens, I., Koegst, T., Vanrolleghem, P.A., 2004. Comparison of different aggregation and breakage kernels for PBMs of the activated sludge flocculation process. In: Proceedings 2nd International Conference on Population Balance Modelling, Valencia, Spain, May 5-7, 2004.

M.Sc Thesis

Nopens, I., 1999. Schatten van actief slib kinetische parameters via gecombineerde respirometrisch-titrimetrische experimenten, Afstudeerwerk, Universiteit Gent, 112p.

Posters

Nopens, I., Verbrugge, T., Seghers, D., Krzanowska, A., Vanrolleghem, P., ERASM M&MV Task Force, 2000. OECD criteria for ready biodegradability: Environmental interpretation and study of alternatives. Poster presented at the Tenth Annual Meeting of SETAC-Europe (Society of Environmental Toxicology and Chemistry), Brighton, United Kingdom, May 22-25, 2000.

De Clercq, B., Nopens I., Govoreanu R., Vanrolleghem P.A. and Van Der Meeren P., 2000. Sludge (de)flocculation dynamics in secondary clarifiers. Poster presented at the 6th Ph.D Symposium, Gent, Belgium, October 11, 2000.

Van Vooren, L., Van De Steene, M., Nopens, I., Ottoy, J-P., Vanrolleghem P., 2000. Buffer capacity based multipurpose hard- and software sensor for environmental applications. Poster presented at 7th International Conference on Chemometrics in Analytical Chemistry (CAC2000). Antwerp, Belgium, October 16-20, 2000.

Govoreanu, R., Vandegehuchte, K., Saveyn, H., Nopens, I., De Clercq, B., Van Der Meeren, P., Vanrolleghem P., 2002. An automated image analysis system for on-line structural characterization of the activated sludge flocs. Poster presented at the 8th Ph.D Symposium, Gent, Belgium, October 9,2002.

De Pauw, D., Carvalho, G., Nopens, I. , Verdonck, F., Meirlaen, J., Vanrolleghem, P., 2002. WEST, a general tool for dynamic modelling and simulation .(e.g. biodegradation processes). Poster presented at the 12th Annual Meeting of SETAC-Europe (Society of Environmental Toxicology and Chemistry). Vienna, Austria, May 12-16, 2002.

Nopens, I., Koegst, T., Mahieu, K., Vanrolleghem P., 2004. PBM and activated sludge flocculation: From experimental data to a calibrated model. Poster presented at 9th IFAC Conference on Computer Applications in Biotechnology CAB9. Nancy, France, March 28-31, 2004.

Nopens, I., Beheydt, D. and Vanrolleghem P., 2004. Comparison of discretisation techniques to solve PBMs including aggregation and/or breakage: a simulation study. Poster presented at the 2nd International Conference on Population Balance Modelling. Valencia, Spain, May 5-7, 2004.

Technical Reports

Nopens, I., Capalozza, C., Vanrolleghem, P., 2001. Stability analysis of a synthetic municipal wastewater. Technical report, 22p.

Oral contributions to international and national conferences/workshops

Nopens, I., Biggs, C., De Clercq, B., Govoreanu, R., Wilén, B., Lant, P., Vanrolleghem, P., 2001. Modelling the activated sludge flocculation process combining laser diffraction particle sizing and population balance modelling (PBM). 5th IWA Seminar on Modelling of Activated Sludge Processes in Theory and Practise. Kollekolle, Denmark, September 10-12, 2001.

Nopens, I., Vanrolleghem, P.A., 2001. Biodegradation of toxic and biorefractory compounds and their impact on wastewater treatment plants. European Union COST action 624, Work Group 4. Rome, Italy, November 29-30, 2001.

Nopens, I., Vanrolleghem, P., 2003. Comparison of discretisation methods to solve a population balance model of activated sludge flocculation including aggregation and breakage. IMACS 4th MATHMOD Conference. Vienna, Austria, February 5-7, 2003.

Vanrolleghem, P., Insel, G., Petersen, B., Sin, G., De Pauw, D., Nopens, I., Doverman, H., Weijers, S., Gernaey, K., 2003. A comprehensive model calibration procedure for activated sludge models. 76th Annual WEF Conference and Exposition. Los Angeles, USA, October 11-15, 2003.

Nopens, I., Koegst, T., Vanrolleghem, P. 2004. Comparison of different aggregation and breakage kernels

for PBMs of the activated sludge flocculation process. 2nd International Conference on Population Balance Modelling. Valencia, Spain, May 5-7, 2004.

Nopens, I., Vanrolleghem, P. 2004. Integratie van investerings- en werkingskosten voor waterzuivering met behulp van modelsimulaties. Facultaire Themanamiddag FBW. Gent, België, 3 december 2004.

Computer skills

Operating Systems

- Windows 95, NT, 2000
- Red Hat Linux 9.0, Fedora 1.0

Applications

- MS Office (Word, Excel, Powerpoint, Access)
- WEST (simulation/optimisation platform)
- Matlab
- Sigmaplot (data analysis tool)
- S-Plus, SPSS (statistics)
- Latex (word processor)
- LabView and Measurement & Automation Explorer (DAQ software)
- NI Vision builder (image analysis software)
- MySQL (database)
- Apache (webserver)
- PhpMyAdmin (open source dbase administration tool)

Computer languages

- C, C++
- G (LabView graphical programming language)
- Turbo Pascal
- Fortran77
- HTML
- PHP

- SQL
- MSL (model specification language)

Miscellaneous

- Member of the faculty scientific research board (CWO-FBW) since May 2003
- Introduction of BIOMATH lab at faculty open door day (2003)
- Representative of Biomath at IFEST exhibition (2004)
- Promotion of educational program of faculty of Bio-science engineering at K.A. Lokeren (2004,2005)
- Member of Koninklijke Vlaamse Ingenieursvereniging (KVIV) since 1999
- Member of Verbond afgestudeerde Bio-ingenieurs Gent since 1999
- Member of International Water Association (IWA) since 2000
- Responsible organiser BIOMATH seminars
- Member of SYSADMIN BIOMATH (System Administration Team). Responsible web- and database server, webmaster
- Member of the board of Lokerse Badminton Club since 1997. Functions: Vice-president, webmaster, international tournament organizer.